

# Organization, Manipulation and Motion of Brush Polymers and Low Molecular Weight Amphiphiles at Interfaces

VON DER FAKULTÄT FÜR MATHEMATIK, INFORMATIK UND  
NATURWISSENSCHAFTEN DER RHEINISCH-WESTFÄLISCHEN TECHNISCHEN  
HOCHSCHULE AACHEN ZUR ERLANGUNG DES AKADEMISCHEN GRADES EINES  
DOKTORS DER NATURWISSENSCHAFTEN GENEHMIGTE DISSERTATION

VORGELEGT VON

BERND TARTSCH

AUS

GIENGEN/BRENTZ

BERICHTER: PROF. DR. MARTIN MÖLLER

PROF. DR. WALTER RICHTERING

TAG DER MÜNDLICHEN PRÜFUNG: 25. AUGUST 2005

Diese Dissertation ist auf den Internetseiten der Hochschulbibliothek online verfügbar



# Contents

<b>1</b>	<b>Introduction</b>	<b>1</b>
<b>2</b>	<b>Literature Review</b>	<b>3</b>
2.1	Scanning force microscopy - History, state of the art and future . . . . .	3
2.1.1	The beginning . . . . .	3
2.1.2	The scanning force microscope . . . . .	4
2.1.3	Scanning force microscopy probes . . . . .	6
2.1.4	Resolution and errors in scanning force microscopy . . . . .	7
2.1.5	Environmental control . . . . .	8
2.1.6	Force measurements . . . . .	9
2.1.7	Manipulation and nanolithography . . . . .	9
2.1.8	Outlook . . . . .	11
2.2	Molecular motion, motors and devices . . . . .	11
2.2.1	Top-down and bottom-up approach . . . . .	11
2.2.2	The switch . . . . .	12
2.2.3	Motion and Motors . . . . .	12
<b>3</b>	<b>Nanomanipulation and thermal equilibration of monodendron jacketed polymers</b>	<b>23</b>
3.1	Introduction . . . . .	23
3.2	Experimental . . . . .	24
3.2.1	Materials . . . . .	24
3.2.2	Methods . . . . .	24
3.2.3	Synthesis of 12-ABG-4EO-PMA . . . . .	25
3.3	Results and discussion . . . . .	30
3.3.1	Epitaxial adsorption of 12-ABG-4EO-PMA on HOPG . . . . .	30
3.3.2	Nanomanipulation of 12-ABG-4EO-PMA . . . . .	35
3.3.3	Thermal equilibration . . . . .	41
3.4	Conclusions . . . . .	41
<b>4</b>	<b>Stimulated motion of monodendron jacketed polymers on HOPG</b>	<b>49</b>
4.1	Introduction . . . . .	49
4.2	Experimental . . . . .	49
4.2.1	Materials . . . . .	49
4.2.2	Methods . . . . .	49
4.3	Results and discussion . . . . .	50
4.4	Conclusions . . . . .	66
4.5	Appendix . . . . .	67

<b>5</b>	<b>Monodendron jacketed polymers modified with photo-switchable spiropyran</b>	<b>83</b>
5.1	Introduction . . . . .	83
5.2	Experimental part . . . . .	84
5.2.1	Materials . . . . .	84
5.2.2	Methods . . . . .	84
5.3	Results and discussion . . . . .	86
5.4	Conclusions . . . . .	88
<b>6</b>	<b>Reversible collapse of polymer brushes</b>	<b>93</b>
6.1	Introduction . . . . .	93
6.2	Experimental . . . . .	94
6.2.1	Materials . . . . .	94
6.2.2	Scanning force microscopy in vapor atmospheres . . . . .	95
6.3	Results and discussion . . . . .	95
6.3.1	Collapse/decollapse dynamics of short PMA- <i>g</i> -PBuA brush molecules on mica in ethanol/water atmosphere . . . . .	95
6.3.2	Collapse/decollapse dynamics of long PMA- <i>g</i> -PBuA brush molecules on mica in ethanol/water atmosphere . . . . .	97
6.3.3	Collapse/decollapse experiments of PMA- <i>g</i> -PBuA brush molecules on HOPG, SrTiO <sub>3</sub> and silicon substrates in ethanol/water atmosphere . . . . .	99
6.3.4	The role of water in the rod-globule transition . . . . .	102
6.3.5	Collapse/decollapse experiments of PMA- <i>g</i> -PBuA brush molecules on mica in different solvent vapors . . . . .	107
6.3.6	Model explanation . . . . .	112
6.4	Conclusions . . . . .	113
<b>7</b>	<b>Self-assembly of eicosylperfluorotetradecane</b>	<b>119</b>
7.1	Introduction . . . . .	119
7.2	Experimental part . . . . .	119
7.2.1	Materials . . . . .	119
7.2.2	Methods . . . . .	120
7.3	Results and discussion . . . . .	121
7.3.1	SFM Imaging . . . . .	121
7.3.2	X-ray reflectivity . . . . .	126
7.3.3	Gracing incidence x-ray reflectivity . . . . .	128
7.4	Conclusions . . . . .	130
<b>8</b>	<b>Micellization of 16-arm star-block copolymers</b>	<b>133</b>
8.1	Introduction . . . . .	133
8.2	Experimental . . . . .	135
8.2.1	Materials . . . . .	135
8.2.2	Methods . . . . .	136
8.2.3	Sample preparation . . . . .	136
8.3	Results and discussion . . . . .	136
8.3.1	Micellization from octane solutions . . . . .	136
8.3.2	Micellization from cyclohexane solutions . . . . .	137
8.3.3	Micellization from solvent mixtures . . . . .	139
8.4	Conclusions . . . . .	140

<b>A</b>	<b>Visualization of the gelation process of semicarbazide-organogelators by SFM</b>	<b>147</b>
A.1	Introduction . . . . .	147
A.2	Experimental part . . . . .	149
A.2.1	Methods . . . . .	149
A.2.2	Gel preparation . . . . .	149
A.2.3	Materials . . . . .	150
A.2.4	Synthesis of bis[(alkoxy)benzoyl]semicarbazides . . . . .	150
A.3	Results and discussion . . . . .	150
A.3.1	Thermal transitions . . . . .	150
A.3.2	Gelation tests . . . . .	151
A.3.3	Cold gelation . . . . .	151
A.3.4	Gel morphology . . . . .	153
A.3.5	Modelling . . . . .	159
A.4	Conclusions . . . . .	159
<b>B</b>	<b>Gold nanoparticles with covalently attached polymer chains</b>	<b>165</b>
B.1	Introduction . . . . .	165
B.2	Experimental . . . . .	165
B.2.1	Materials . . . . .	165
B.2.2	Methods . . . . .	166
B.3	Results and discussion . . . . .	166
B.4	Conclusions . . . . .	169
<b>C</b>	<b>Sterically terminated polymerization</b>	<b>173</b>
C.1	Introduction . . . . .	173
C.2	Experimental part . . . . .	175
C.2.1	Materials . . . . .	175
C.2.2	Methods . . . . .	175
C.3	Results and discussion . . . . .	176
C.4	Conclusions . . . . .	178
	<b>Summary</b>	<b>183</b>
	<b>Zusammenfassung</b>	<b>187</b>
	<b>Dankwort</b>	<b>191</b>
	<b>Lebenslauf</b>	<b>193</b>

## *Contents*

# List of Figures

2.1	An example of a surface profiler made in 1929 . . . . .	3
2.2	Principle of the scanning force microscope . . . . .	5
2.3	Illustration of the magnetic acoustic mode . . . . .	6
2.4	Bar and V-shaped SFM probes . . . . .	7
2.5	Spatial resolution of spikes, rigid and soft spheres . . . . .	8
2.6	Force distance curve . . . . .	10
2.7	Pulsed Force Mode . . . . .	10
2.8	Fluctuation induced transport of particles in an asymmetric potential . . . . .	13
2.9	Principle of Feynman's Ratchet . . . . .	14
3.1	Synthesis of Poly(2-[2-{2-(2-(methacryloyloxy)ethoxy)ethoxy}ethoxy]ethyl 3,4,5-tris[(4-( <i>n</i> -dodecan-1-yloxy)benzyl)oxy]benzoate) . . . . .	26
3.2	SFM images of 12-ABG-4EO-PMA on mica, spin-coated from xylene and THF solutions . . . . .	30
3.3	SFM images of 12-ABG-4EO-PMA on HOPG, spin-coated from chloroform solution . . . . .	31
3.4	STM micrographs of the mono-layer structure of the minidendritic side groups on HOPG . . . . .	32
3.5	SFM images of 12-ABG-4EO-PMA on mica at 26 °C and 170 °C . . . . .	33
3.6	SFM images of 12-ABG-4EO-PMA on HOPG at 30 °C and 35 °C . . . . .	34
3.7	SFM image of 12-ABG-4EO-PMA on HOPG, spin-coated from THF solution after annealing at 65 °C for 4 hours . . . . .	34
3.8	Nanomanipulation of 12-ABG-4EO-PMA on HOPG . . . . .	36
3.9	Separating of two molecules of 12-ABG-4EO-PMA on HOPG . . . . .	37
3.10	Cutting of 12-ABG-4EO-PMA on mica . . . . .	38
3.11	Structure of the topmost layer of muscovite mica, HOPG and tungsten selenide . . . . .	39
3.12	Nanomanipulation of 12-ABG-4EO-PMA on WSe <sub>2</sub> . . . . .	40
3.13	Thermal equilibration of 12-ABG-4EO-PMA on HOPG . . . . .	42
3.14	Thermal equilibration of 12-ABG-4EO-PMA on HOPG (heating and cooling) . . . . .	43
4.1	Heating accessory for multimode scanning force microscope . . . . .	50
4.2	Diffusion like motion of 12-ABG-4EO-PMA on HOPG at 45 °C . . . . .	52
4.3	Center of mass traces of clusters of 12-ABG-4EO-PMA on HOPG at 40 °C . . . . .	53
4.4	Center of mass traces of clusters of 12-ABG-4EO-PMA on HOPG at 45 °C . . . . .	54
4.5	Center of mass traces of clusters of 12-ABG-4EO-PMA on HOPG at 48 °C . . . . .	55
4.6	Logarithm diffusion coefficient over the mass of the clusters for experiment series 1 . . . . .	59

4.7	[Logarithm diffusion coefficient over the mass of the clusters for experiment series 2 . . . . .	60
4.8	Two clusters of 12-ABG-4EO-PMA showing diffusion independent of the scanning direction of the SFM tip . . . . .	62
4.9	Guided motion of a cluster of 12-ABG-4EO-PMA along a step in the graphite	63
4.10	Two stick shaped clusters of 12-ABG-4EO-PMA undergoing directed diffusion	63
4.11	Segment motion mechanism . . . . .	64
4.12	Single molecule on WSe <sub>2</sub> showing segmental motion . . . . .	65
4.13	Diffusion like motion of 12-ABG-4EO-PMA on HOPG at 30 °C . . . . .	68
4.14	Diffusion like motion of 12-ABG-4EO-PMA on HOPG at 35 °C . . . . .	69
4.15	Diffusion like motion of 12-ABG-4EO-PMA on HOPG at 40 °C . . . . .	70
4.16	Center of mass traces of clusters of 12-ABG-4EO-PMA on HOPG at 30 °C	71
4.17	Center of mass traces of clusters of 12-ABG-4EO-PMA on HOPG at 35 °C	72
4.18	Center of mass traces of clusters of 12-ABG-4EO-PMA on HOPG at 40 °C	73
4.19	Diffusion like motion of 12-ABG-4EO-PMA on HOPG at 40 °C . . . . .	74
4.20	Diffusion like motion of 12-ABG-4EO-PMA on HOPG at 45 °C . . . . .	75
4.21	Diffusion like motion of 12-ABG-4EO-PMA on HOPG at 48 °C . . . . .	76
4.22	Center of mass traces of clusters of 12-ABG-4EO-PMA on HOPG at 40 °C	77
4.23	Center of mass traces of clusters of 12-ABG-4EO-PMA on HOPG at 45 °C	78
4.24	Center of mass traces of clusters of 12-ABG-4EO-PMA on HOPG at 48 °C	79
5.1	Photoswitching of spiropyrans . . . . .	83
5.2	Photo-controllable membrane . . . . .	84
5.3	Synthesis of Spiran-MA monomer . . . . .	85
5.4	Structure and composition of Poly(12-ABG-4EO-MA-co-Spiran-MA) . . . .	86
5.5	GPC spectra of Poly(12-ABG-4EO-MA-co-Spiran-MA) detected with R <sub>i</sub> and UV <sub>366 nm</sub> . . . . .	87
5.6	UV spectra of the Spiran-MA monomer and (Poly(12-ABG-4EO-MA-co-Spiran-MA) . . . . .	88
5.7	SFM images of Poly(12-ABG-4EO-MA-co-Spiran-MA) on mica and HOPG	89
5.8	SFM images of Poly(12-ABG-4EO-MA-co-Spiran-MA) before and after UV illumination ( $\lambda = 254$ nm) . . . . .	89
5.9	SFM images of Poly(12-ABG-4EO-MA-co-Spiran-MA) before and after UV illumination ( $\lambda = 366$ nm) . . . . .	90
6.1	Molecular Imaging PicoSPM with environmental chamber . . . . .	95
6.2	High-resolution SFM image of PMA- <i>g</i> -PBuA(l) brush molecules on mica . .	96
6.3	Collapse/decollapse dynamics of PMA- <i>g</i> -PBuA(s) brush molecules on mica in ethanol/water atmosphere . . . . .	98
6.4	Collapse dynamics of PMA- <i>g</i> -PBuA(l) brush molecules on mica in ethanol vapor . . . . .	100
6.5	Decollapse dynamics of PMA- <i>g</i> -PBuA(l) brush molecules on mica in water vapor . . . . .	101
6.6	Collapse/decollapse dynamics of PMA- <i>g</i> -PBuA(l) brush molecules on SrTiO <sub>3</sub> substrate in ethanol/water atmosphere . . . . .	103
6.7	Collapse/decollapse dynamics of PMA- <i>g</i> -PBuA(l) brush molecules on silicon substrate in ethanol/water atmosphere . . . . .	104



6.8	Fast Collapse/decollapse dynamics of PMA- <i>g</i> -PBuA(1) brush molecules on mica in 80%/20% ethanol/water mixtures . . . . .	105
6.9	Collapsed and partially collapsed PMA- <i>g</i> -PBuA(1) brush molecules after equilibration under ethanol/water vapor of different composition . . . . .	106
6.10	Surface tension of ethanol/water mixtures . . . . .	107
6.11	Collapse/decollapse dynamics of PMA- <i>g</i> -PBuA(s) brush molecules on mica in ethyl acetate/ethylene glycol atmosphere . . . . .	108
6.12	Collapse/decollapse dynamics of PMA- <i>g</i> -PBuA(1) brush molecules on mica in isopropanol/DMSO atmosphere . . . . .	109
6.13	Collapse/decollapse dynamics of PMA- <i>g</i> -PBuA(1) brush molecules on mica in diethylether/DMF atmosphere . . . . .	110
6.14	Collapse/decollapse dynamics of PMA- <i>g</i> -PBuA(1) brush molecules on mica in ethylacetate/cyclohexanone atmosphere . . . . .	111
7.1	SFM images of F <sub>14</sub> H <sub>20</sub> prepared from HFX solution by spin-coating and LB-film deposition . . . . .	122
7.2	Ribbons are rolled up to toroids . . . . .	122
7.3	SFM images of F <sub>14</sub> H <sub>20</sub> prepared from decalin solution by spin-coating and LB-film deposition . . . . .	123
7.4	SFM images of F <sub>14</sub> H <sub>20</sub> prepared from perfluorohexane and perfluorodecalin solution on mica . . . . .	124
7.5	SFM images of F <sub>14</sub> H <sub>20</sub> on mica as cast from decalin solution and after exposure to HFX vapor . . . . .	125
7.6	SFM images of F <sub>14</sub> H <sub>20</sub> on mica as cast from HFX solution and after exposure to perfluorodecalin vapor . . . . .	125
7.7	X-ray results for a monolayer of semi-fluorinated alkane F <sub>14</sub> H <sub>20</sub> . . . . .	126
7.8	Scheme illustrating the packing of the semi-fluorinated molecules . . . . .	127
7.9	Packing of the semi-fluorinated alkanes perpendicular to the plane defined by the kink . . . . .	127
7.10	Comparison of the experimental GIXD-curves for samples with ‘donut’- and ‘ribbon’-structure . . . . .	129
7.11	Fitting of Lorentzians to the GIXD intensities of a ‘ribbon’- and a ‘donut’-sample . . . . .	129
7.12	Crystalline peak in the ‘ribbon’-sample . . . . .	130
8.1	Volume occupied by a single molecule in spherical and cylindrical micelles . . . . .	134
8.2	Miktoarm star-copolymers of the A <sub>8</sub> B <sub>8</sub> -type . . . . .	135
8.3	Spherical micelles of VS1, VS2, VS3 spin-coated from octane solutions . . . . .	137
8.4	SFM images of micelles of polymer VS1 formed in cyclohexane solutions . . . . .	138
8.5	SFM images of aggregates of polymer VS2 formed in cyclohexane solutions . . . . .	138
8.6	SFM images of aggregates of polymer VS3 formed in cyclohexane solutions . . . . .	139
8.7	SFM image of polymer VS2 on mica prepared by dipping from a cyclohexane solution . . . . .	140
8.8	SFM images of aggregates formed from polymer VS2 in cyclohexane/toluene mixtures . . . . .	141
8.9	SFM images of aggregates formed from polymer VS2 in cyclohexane/MEK mixtures . . . . .	141

List of Figures

A.1	Schematic sketch of elementary fibril formation with wedge- and dumb-bell shaped organogelators . . . . .	148
A.2	General structure of bis[{(alkoxy)benzoyl}semicarbazides] . . . . .	150
A.3	SFM micrographs of 1,4-PDI-8/DMAc/toluene systems deposited on mica .	155
A.4	SFM micrographs of a 1,4-PDI-8/DMAc/toluene gel spin-coated on HOPG	156
A.5	Time evolution of the gelation process of a 0.4 wt% 1,4-PDI-8, 2.0 wt% DMAc/toluene mixture . . . . .	157
A.6	Time evolution of the gelation process of a 0.25 wt% 1,4-PDI-8/0.5 wt% DMAc/toluene mixture . . . . .	158
A.7	SFM micrographs of 1,8-NDI-12/ <i>n</i> -hexane systems deposited on mica . . .	159
A.8	Proposed model of the molecular arrangement of 14 molecules in the elementary fibrils . . . . .	160
B.1	Synthesis of thiol-initiator . . . . .	166
B.2	Generation of a polymer shell around the Au-NPs . . . . .	167
B.3	TEM images of dodecanethiol-stabilized, and polymer-coated Au-NPs . . .	167
B.4	SFM images of Au-NPs with tethered polymer chains on mica . . . . .	168
B.5	GPC chromatograms of polymer-grafted Au-NPs, cleaved polymer, and dodecanethiol-stabilized Au-NPs . . . . .	168
C.1	Molecular modelling of P(345-345-ON) with different degree of polymerization	174
C.2	Polymerization of 345-345-ON stops after formation of a sphere, the encapsulated reactive center is able to react with a small monomer . . . . .	175
C.3	Chemical structure of P(345-345-ON) and P(345-345-ON-Et <sub>2</sub> -ON) . . . . .	176
C.4	SFM images of P(345-345-ON) spin-coated from hexane solution on HOPG	177
C.5	SFM images of P(345-345-ON-Et <sub>2</sub> -ON) spin-coated from THF solution on mica . . . . .	178
C.6	SFM images of P(345-345-ON-Et <sub>2</sub> -ON) spin-coated from toluene solution on mica . . . . .	179

# List of Tables

3.1	Crystallographic data of mica, graphite and tungsten selenide . . . . .	39
4.1	Diffusion Coefficient of 12-ABG-4EO-PMA in nm <sup>2</sup> /s at 30–40 °C . . . . .	56
4.2	Diffusion Coefficient of 12-ABG-4EO-PMA in nm <sup>2</sup> /s at 40–48 °C . . . . .	57
5.1	Molecular weight of Poly(12-ABG-4EO-MA-co-Spiran-MA) . . . . .	87
6.1	Molecular characterization of poly(methacrylate)- <i>graft</i> -poly( <i>n</i> -butyl acrylate) brush molecules . . . . .	94
6.2	Surface tension of the solvents used for the collapse and decollapse dynamics of the brush molecules . . . . .	112
7.1	Fitting parameters corresponding to the mono-layer structure of F <sub>14</sub> H <sub>20</sub> . . . . .	128
8.1	Molecular characterization of the miktoarm star-copolymers . . . . .	136
8.2	Dimensions of the micelles in octane by SFM . . . . .	137
A.1	Realized applications of organogels and possible future directions . . . . .	148
A.2	Synthesised bis(semicarbazides) . . . . .	150
A.3	Thermal properties of the bis(semicarbazides) . . . . .	151
A.4	Dissolution and gelation of bis(semicarbazide)/solvent mixtures . . . . .	152
A.5	‘Cold’ gelation of toluene, <i>n</i> -hexane, and 1,3,5-tri(isopropyl)benzene by mixing with solutions of 1,4-PDI-8 in DMAc . . . . .	153
C.1	Molecular weight of P(3,4,5-3,4,5-G <sub>2</sub> -ON) determined by SFM, SEC, and MALDI-TOF-MS . . . . .	177

*List of Tables*

# List of Abbreviations

1,4-PDI	1,4-phenyl diisocyanate
1,8-NDI	1,8-naphthyl diisocyanate
AFM	atomic force microscope
AIBN	2,2'-azobisisobutyronitrile
ATP	Adenosine Triphosphate
ATRP	atom transfer radical polymerization
Au-NPs	gold nanoparticles
cgc	critical gelation concentration
CHCl <sub>3</sub>	chloroform
cmc	critical micelle concentration
CPK	Corey-Pauling-Kultun model
DCC	1,3-dicyclohexylcarbodiimide
DLS	dynamic light scattering
DMAc	N,N-dimethyl acetamide
DMAP	4-(dimethylamino)pyridine
DMF	N,N-dimethylformamide
DMSO	dimethyl sulfoxide
DNA	deoxyribonucleic acid
DP	degree of polymerization
DPN	dip pen nanolithography
DPTS	4-(dimethylamino)pyridinium <i>p</i> -toluenesulfonate
DSC	differential scanning calorimetry
GIXD	Grazing incidence x-ray diffraction
GPC	gel permeation chromatography
HEMA	2-hydroxy-ethyl methacrylate
HFX	hexafluoroxylene
HMA	<i>n</i> -hexyl methacrylate
<sup>1</sup> H-NMR	nuclear magnetic resonance
HOPG	highly ordered pyrolytic graphite
LALLS	low angle laser light scattering
LB	Langmuir-Blodgett
LCM	large compound micelle
LCV	large compound vesicle
LFM	lateral force microscopy
MALDI-TOF-MS	matrix assisted laser desorption/ionization-time of flight-mass spectrometry
MEK	methyl ethyl ketone
MMFF	Merck Molecular Force Field
M <sub>n</sub>	number average molecular weight
M <sub>w</sub>	weight average molecular weight
PAA	poly(acrylic acid)

## List of Abbreviations

pBPEM	poly(2-(2-bromo propionyloxy)ethyl methacrylate)
PD	polydispersity index
PEO	poly(ethylene oxide)
PI	polyisoprene
PS	polystyrene
$R_f$	retardation factor (chromatography)
$R_i$	refractive index
RNA	ribonucleic acid
ROMP	ring opening metathesis polymerization
SEC	size exclusion chromatography
SFM	scanning force microscopy
Si	Silicon (wafer)
SNOM	scanning near-field optical microscopy
SPM	scanning probe microscopy
SrTiO <sub>3</sub>	strontium titanate
STM	scanning tunneling microscopy
TBDMSCl	<i>tert</i> -butyldimethylsilyl chloride
<i>t</i> -BuAc	<i>tert</i> -butyl acetate
TEM	transmission electron microscopy
TGA	thermogravimetric analysis
THF	tetrahydrofuran
TiPrB	1,3,5-tri(isopropyl)benzene
TLC	thin layer chromatography
TMS	tetramethylsilane
TOA	thermo optical analysis
UHV	ultra high vacuum
UV/VIS	ultraviolet spectroscopy

# 1 Introduction

In the following an outline is given of the content of this thesis:

*Chapter 2* gives a general introduction to the field of scanning force microscopy. The emphasis was to show the versatility of SFM and in which direction future developments might lead. The second part of the literature review gives an insight in molecular machines: what is the definition, the basic devices and already realized machines?

*Chapter 3* to *Chapter 5* deal with monodendron jacketed polymers – a linear polymer with a minidendritic side group at each repeating unit. *Chapter 3* describes the synthesis and the manipulation of single polymer chains on three different substrates by means of the SFM tip. Furthermore the molecules have been completely stretched out using the nano-manipulation technique and then their thermal equilibration was studied by in situ scanning force microscopy.

*Chapter 4* discusses the stimulated motion of monodendron jacketed molecules on highly ordered pyrolytic graphite in detail. Stimulation is done thermally and additionally by the tapping tip of the SFM. Diffusion coefficients are calculated and special motion modes are described. The series of in situ SFM images are assembled to animations that can be accessed from the supporting material on the CD version of this thesis or directly in the pdf-document (images with red frame).

In *Chapter 5* the modification of these jacketed molecules with the photoswitchable spiropyran is shown. The incorporation of the switchable dye was successful and the dye was still active in the polymer. First results showing the influence on the molecular structure by illumination with UV-light are presented.

In *Chapter 6* the influence of solvent vapors on brush or comb polymers on mica substrates is investigated. The polymer brushes consist of *n*-butylacrylate side-chains and a polymer backbone on methacrylate basis. It is shown that it is possible to transfer the molecules from an extended state to a collapsed globular state by saturating the surrounding atmosphere with e. g. ethanol vapor. Removing the ethanol and exposure of the polymer to a strongly humid environment resulted in spreading and recovering of the extended state. This process was repeated several times and found to be completely reversible.

*Chapter 7* describes the self-assembly of perfluoroalkyl alkanes. These small diblock molecules possess an enormous tendency to self-assemble in two distinct structures: a stripe-structure and a rolled up toroidal one. The ordering is a consequence of the strongly incompatible blocks and could be controlled by the solvent quality: either selective for one block or non-selective.

*Chapter 8* investigates the micellization of PS-PI star block-copolymers. The aim was to get cylindrical micelles and to compare the results with linear diblock copolymers.

These eight chapters are followed by an appendix containing three short reports. In all cases the main work, as concept development or synthesis, have been performed by other groups, and they were interested in SFM visualization of their compounds. Depending on the time spent on these side-projects or the beauty of the results the following three projects found their way into this thesis: In *Appendix A* the gels formed from bis(semicarbazides) are visualized and the time evolution of gelation was followed. *Appen-*

## 1 Introduction

*dir B* shows SFM images of *n*-butylacrylate side chains polymerized from gold nanoparticles. Finally in *Appendix C* the tiny tadpole shaped molecules formed by a sterically terminated polymerization reaction are imaged.



## 2 Literature Review

### 2.1 Scanning force microscopy - History, state of the art and future

#### 2.1.1 The beginning

Typically, when we think of microscopes, we think of optical or electron microscopes. Such microscopes create a magnified image of an object by focusing electromagnetic radiation, such as photons or electrons, on its surface. Optical and electron microscopes can easily generate two-dimensional magnified images of an object's surface with a magnification as great as  $1000\times$  for an optical microscope, and as large as  $100,000\times$  for an electron microscope.

Although these are powerful tools, the images obtained are typically in the plane horizontal to the surface of the object. Such microscopes do not readily supply the vertical dimensions of an object's surface, the height and depth of the surface features.

The atomic force microscope (AFM), developed in the mid 1980s, uses a sharp probe to magnify surface features. With the AFM, it is possible to image an object's surface topography with extremely high magnification, up to  $1,000,000\times$ . Further, the magnification of an AFM is made in three dimensions, the horizontal x-y plane and the vertical z dimension.

As acknowledged by Binnig and Rohrer [1], the inventors of the tunnelling microscope, such a powerful technique has its origin in the stylus profiler.

An example of an early profiler is shown in Figure 2.1. This profiler, invented by Schmalz in 1929, utilized an optical lever arm to monitor the motion of a sharp probe mounted at the end of a cantilever. A magnified profile of the surface was generated by recording the motion of the stylus on photographic paper. This type of "microscope" generated profile "images" with a magnification of greater than  $1000\times$ .

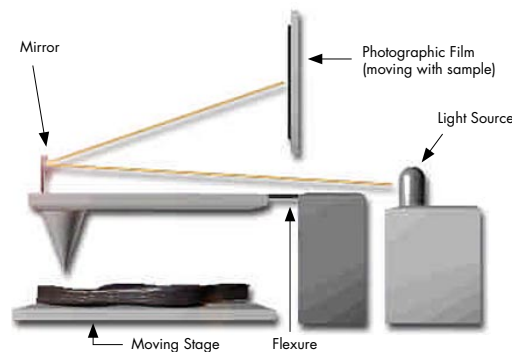


Figure 2.1: An example of a surface profiler made in 1929

A common problem with stylus profilers was the possible bending of the probe from collisions with surface features. Such probe bending was a result of horizontal forces on the probe caused when the probe encountered large features on the surface. This problem was first addressed by Becker in 1950 and later by Lee. Both suggested oscillating the probe from a null position above the surface to contact with the surface. Becker remarked that when using this vibrating profile method for measuring images, the detail of the images would depend on the sharpness of the probe.

In 1971 Russell Young [2] demonstrated a non-contact type of stylus profiler. In his profiler, called the Topographiner, Young used the fact that the electron field emission current between a sharp metal probe and a surface is very dependent on the probe sample distance for electrically conductive samples. In the Topographiner, the probe was mounted directly on a piezoelectric ceramic used to move the probe in a vertical direction above the surface. An electronic feedback circuit monitoring the electron emission was then used to drive the piezoceramic and thus keep the probe sample spacing fixed. Then, with piezoelectric ceramics, the probe was used to scan the surface in the horizontal (x-y) dimensions. By monitoring the x-y and z position of the probe, a 3-D image of the surface was constructed. The resolution of Young's instrument was controlled by the instrument's vibrations.

In 1981 researchers at IBM were able to utilize the method of Young to create the scanning tunneling microscope (STM) [3]. Binnig and Rohrer demonstrated that by controlling the vibrations of an instrument very similar to Young's Topographiner, it was possible to monitor the tunnelling current between a sharp probe and a sample. Since electron tunnelling is more sensitive than field emissions, the probe could be used to scan very close to the surface. The result was astounding: Binnig and Rohrer were able to see individual silicon atoms on a surface. Although the STM was considered a fundamental advancement for scientific research, it had limited applications, because it worked only on electrically conductive samples.

A major advancement in profilers occurred in 1986 when Binnig and Quate [4] demonstrated the atomic force microscope. Using an ultra-small probe tip at the end of a cantilever, the atomic force microscope could achieve extremely high resolutions. Initially, the motion of the cantilever was monitored with an STM tip. It was soon realized that a light-lever, similar to the technique first used by Schmalz, could be used for measuring the motion of the cantilever. In their paper, Binnig and Quate proposed that the AFM could be improved by vibrating the cantilever above the surface.

The first practical demonstration of the vibrating cantilever technique in an atomic force microscope was made by Wickramasinghe [5] in 1987 with an optical interferometer to measure the amplitude of the cantilever's vibration.

Using this optical technique, oscillation amplitudes of between 0.3 nm and 100 nm were achieved. Because of the probe coming into contact with the surface upon each oscillation, Wickramasinghe was able to sense the materials on a surface. The differences between photoresist and silicon were readily observed.

### 2.1.2 The scanning force microscope

The scanning force microscope belongs to the family of the scanning probe microscopes. The commonness of the scanning probe microscopes is the sensing of the sample's surface with a fine probe. Depending on the type of microscope different interactions between probe and sample are exploited and therefore different probes are used. In the case of

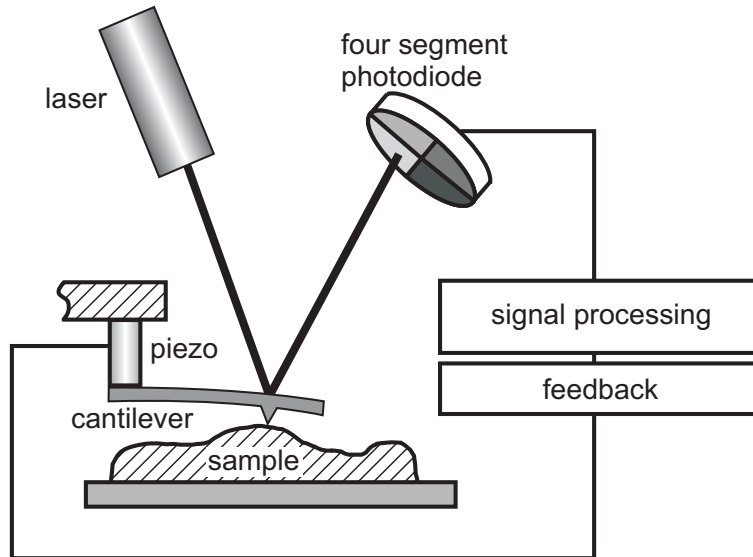


Figure 2.2: Principle of the scanning force microscope with light-lever detection. A laser beam is reflected from the backside of the cantilever and the bending is detected by a four segment photodiode

the SFM the forces between a fine tip and the sample's surface are measured. The probe consists of a pyramidal or cone shaped tip at the end of a small bar, the so called cantilever.

Figure 2.2 shows the principle of a SFM using the light-lever detection method. This is the standard design of a modern SFM.

The cantilever is mounted on a tube shaped piezo ceramics that scans over the sample surface. The tube piezo can bend in x and y direction and it can extend and retract to accomplish the z motion of the cantilever. The bending of the cantilever is detected by a laser beam that is reflected from the backside of the cantilever and hits a four segment photodiode. The signal of the photodiode is read from the feedback control and gives the appropriate voltage to the scanning piezo in order to keep the tip sample distance constant.

There are two types of imaging modes:

1. Contact Mode

In this mode the tip is in contact with the substrate and the bending of the cantilever according to the tip sample forces is measured (deflection signal). The feedback moves the cantilever up and down in order to keep the force and therefore the tip sample distance constant. This provides the topography of the sample. If the scanning direction is orthogonal to the cantilever the cantilever experiences torsional forces because of protruding features of the surface or because of areas with different friction. The torsion is measured by the left minus right signal of the photodiode and gives the friction signal [6, 7]. One speaks of lateral force microscopy (LFM).

2. Oscillation modes [8]

Here the tip is stimulated at the resonant frequency of the cantilever and the amplitude of the oscillation is measured. Far away from the surface oscillates the cantilever with its free amplitude. As soon as the tip touches the surface the amplitude

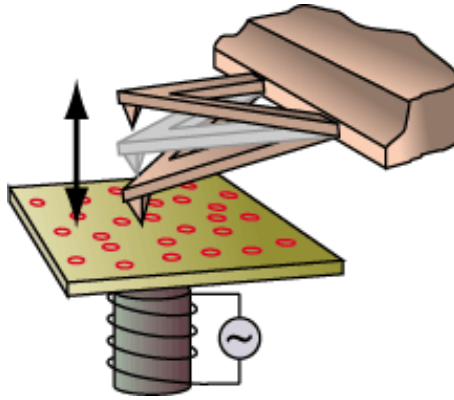


Figure 2.3: Illustration of the magnetic acoustic mode (MAC-Mode). A solenoid mounted underneath the sample provides the alternating magnetic field for the oscillation of a magnetic cantilever.

is reduced and the feedback controls the piezo in  $z$  direction in the way that the amplitude is kept at a certain setpoint. The amplitude is here the equivalent to the deflection in contact mode. The topography is again given by the movement of the piezo along the  $z$ -axes. The third signal gained in the oscillation mode is the phase shift between the excitation of the cantilevers vibration and the oscillation measured at the photo diode. The phase signal can sense differences in material composition because it depends on the stiffness of the sample.

The big advantage of the oscillation mode is the reduced force exerting on the sample. Especially the lateral forces are almost completely suppressed [9, 10].

Most common is the excitation of the cantilever with an additional small piezo ceramics in direct contact with the cantilever. But it is also possible to do the excitation by a oscillating magnetic field in combination with cobalt covered cantilevers (magnetic acoustic mode, MAC-mode, Figure 2.3).

Commonly the term tapping mode is used for the oscillation mode. Other terms are non-contact mode, acoustic mode (AC-mode), and magnetic acoustic mode (MAC-mode). Most terms are trademarks of companies producing scanning probe microscopes.

In comparison to the introduced typical design of SFM some manufacturers apply an inverse approach. They mount the sample on a piezo tube and scan the sample under a fixed tip. Also combined versions that scan the sample in the horizontal  $x$  and  $y$  direction and the tip along the  $z$ -axes are available. Here the piezo tube is usually replaced by stacks of piezo ceramics.

### 2.1.3 Scanning force microscopy probes

AFM probes consist out of three parts: the chip which allows the handling of the probe, the cantilever (a leaf spring), and the tip itself (Figure 2.4a). The terms are not used consistently: tip and cantilever are sometimes used for the whole SFM-probe and sometimes for a specific part of the probe. Generally, SFM probes exist in two forms: bar-shaped and V-shaped (Figure 2.4b and c) and are made out of silicon-nitride or silicon single crystals.

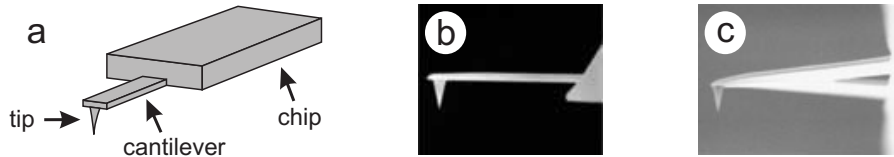


Figure 2.4: SFM probes: a) sketch b) and c) electron microscopy images of bar- and V-shaped cantilevers

There exists a broad variety of SFM probes tailored for the respective application. Characteristic parameters for the probes are the cantilever's length, width and thickness, the spring constant and the resonant frequency, the coating and the height of the tip and the tip apex radius. Probes for force measurements possess the lowest spring constants (0.01 N/m to ca. 2 N/m), contact mode probes follow with several N/m and probes used for oscillation modes have spring constants of 3–50 N/m and higher. The resonant frequencies are in the range of 30–500 kHz.

There are also special probes for particular purposes: tips with high aspect ratios, gold and diamond covered tips, tips covered with magnetic materials, super sharp tips, tips with special shapes, reflex coated tips . . .

#### 2.1.4 Resolution and errors in scanning force microscopy

The lateral resolution of the SFM images depends on the characteristic of the instrument (tip shape, sensitivity of the photodiode, registration principle, electronic noise), on the scanning conditions (medium, distance, forces) and on the inherent properties of the sample (roughness, softness, composition). Although theories of image formation exist [11], there is no general definition of resolution in force microscopy, especially for soft materials.

One can distinguish atomic and nanometer resolution. The atomic resolution can be obtained at a certain superposition of tip shape and the substrate lattices when so-called Moire images appear. In this case, the sharpness of the tip does not affect the resolution but the ratio between the lattice periodicity of the tip and the surface is important. Thus, lattice images with pseudo atomic resolution are obtained, however, atomic defects stay unrevealed. During the last few years the real atomic resolution was achieved using sharp tips and sophisticated feedback control under UHV conditions [12].

In contrast the nanometer resolution which is responsible for the visualization of single polymer and biological molecules depends strongly on the sharpness of the tip. The resolution is in the order of  $\frac{R+D}{\kappa}$ , where  $R$  is the effective probe size,  $D$  is the effective interaction distance and  $\frac{1}{\kappa}$  the decay length of the interaction [13]. Whether the distinct features of a given object can be resolved depends, besides the effective probe size  $R$ , on the context of each feature in the object. If we take for example two sharp spikes (Figure 2.5a) separated by a distance  $d$ ; the spikes can be imaged with some limited resolution because the sample is sharper than the tip and the height of the spikes is equal. If the height of the spikes is not equal it might be that the spikes could never be resolved. The minimum separation distance  $d$ , that will result in a dimple of depth  $z$  for spikes with equal height imaged by a parabolic tip is given by  $d = 2\sqrt{2Rz - z^2}$ . For a tip radius of 10 nm and a dimple depth of 0.3 nm a minimum resolved separation is  $d = 4.9$  nm. For densely packed rigid spheres the minimum  $d$  at which they will be resolved with a tip of radius 10 nm is given by  $d = 4(z + \sqrt{Rz})$  and results in  $d = 8.1$  nm (Figure 2.5b). The flattening

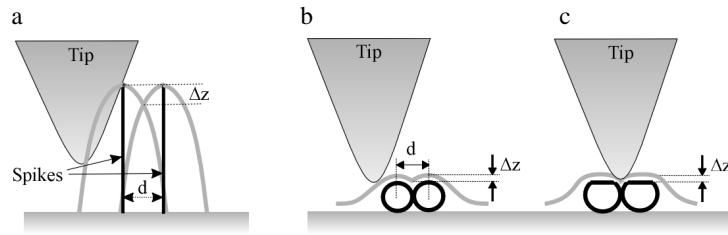


Figure 2.5: Spatial resolution of a) spikes b) rigid spheres c) soft spheres

of soft spheres reduces the resolution considerably. A typical deformation of 0.5 nm results in a minimum sphere distance of  $d = 14.5$  nm that can be resolved by a 10 nm tip.

To summarize, the nanoscopic resolution is determined by the tip geometry and the surface deformation. Sharper tips and smaller deformation are recommended to resolve three dimensional objects of nanometer size. However, these requirements are controversial: as the tip radius is reduced, the local pressure on the sample increases inversely to the radius. This dependence arises because the contact area is proportional to the square of the radius, whereas the interaction forces scale roughly with the tip dimension. Therefore, the resolution can only be improved if sharper tips will be used in combination with lower forces.

As the lateral resolution of the SFM strongly depends on the sharpness of the tip, several approaches to build sharp tips exist. One approach is to use carbon nanotubes on top of a standard tip as probe [14–18]. Additionally, the characterization of the tip size and shape becomes very important. In general, rigid spheres, sharp crystalline steps and saw-tooth surfaces [19, 20] can be used for tip characterization. There exist also commercially available standards with sharp peaks for tip shape visualization.

Most of the scanning artifacts belong to the tip itself. Even a perfect tip is because of its parabolic shape not able to visualize the real surface features but only the convolution of sample features with the tips' shape. Even worse is the situation for a dull, broken or contaminated tip. A tip with several peaks multiplies the surface features. Other typical artifacts come from the non-perfectness of the scanning piezo ceramics: non-linearity, cross coupling of the scanning directions, creep and hysteresis. Most of the piezos' deficits can be overcome by sophisticated position control of the scanners. Scanners with optical, capacitive or inductive sensors in order to measure the scanner's position are commercially available.

### 2.1.5 Environmental control

SFM is a method that is not restricted to ambient conditions and working in air. Especially biologists use the possibility to work in liquids because their main object of interest, the cells, need liquid surroundings in order to survive. The experimental setup can be very easy by just adding a drop of liquid on the sample substrate or by means of the commercially available liquid cells. These cells allow a continuous flow of the solvent and by this also a change of solvent or for example the adjustment of the ionic strength.

By means of environmental chambers it is also possible to control the gas phase. This enables working in inert gases as nitrogen or helium, working with controlled humidity [21] and even in atmospheres saturated with organic solvents.

The most sophisticated SFMs allow to work in UHV [6, 22, 23]. Here no gas or surface contamination is present and the tip-sample interaction can be controlled most precisely, allowing real atomic resolution.

SFM microscopy is also not necessarily a “room temperature method”. A variety of small heaters and cooling devices are available to work in the temperature regime from  $-50^{\circ}\text{C}$  up to  $250^{\circ}\text{C}$ .

Finally, the combination of the environmental control is possible. For example studying cells in nutrition solution with defined pH at  $38^{\circ}\text{C}$ , observation of a polymer phase transition at  $170^{\circ}\text{C}$  in dry nitrogen atmosphere in order to prevent oxidation, or working at  $5.2\text{K}$  in UHV was realized [24].

### 2.1.6 Force measurements

Besides scanning and imaging the SFM can be used to measure forces in the pico-Newton range. The standard way is to make a so called force distance curve where you plot the deflection voltage over the piezo voltage [25]. Figure 2.6 shows a typical force distance curve on a hard substrate in air.

There are significant differences for the approach (A–C) and the withdraw (D–E) of the force curve. At the beginning of the approach (A) the tip is far away from the surface and the deflection stays constant. When the tip is very close to the substrate (B) it feels attractive forces, e. g. electrostatic or surface tension (capillary) forces, and the tip snaps on the surface. By further extending of the piezo (C) the cantilever bends up and the deflection increases linear with the piezo-voltage.

Starting the withdraw of the force curve the bending is released and the deflection decreases linear with the retracting piezo. But then the tip sticks to the substrate and the cantilever is bent down (D) until the snap-off (E) happens. Now the deflection is zero and stays constant on further withdraw.

To overcome the capillary forces and to measure smaller forces it is usually necessary to work in liquids. In the same way it is also possible to pull on long molecules, e. g. DNA, when one end is attached to the tip and the other to the substrate [26, 27].

For the recording of a force-distance curve for each point of an AFM image the term force volume was established. With this method the most detailed information of the substrate is available. Disadvantages are the huge amount of data and the time to acquire all this data. A much faster way to get the same results is the pulsed-force mode. Here you excite a soft tip, similar to tapping mode, but at much lower frequencies than the resonant frequency to a sinusoidal oscillation. With this oscillating tip the surface is scanned doing continuous fast force curves. Figure 2.7 shows the typical signal. From these curves a variety of measurands additionally to the topography can be obtained: adhesion, stiffness, phase energy dissipation, contact time.

### 2.1.7 Manipulation and nanolithography

The AFM was also already used to manipulate objects, such as polymers [28] or carbon nanotubes [29–32], on surfaces. Crucial for these processes is the positioning of the tip. Therefore scanners with implemented position control mechanisms, also called hardware linearization or closed loop, have been designed. The position of the tip is not only given by a certain piezo voltage but is controlled and corrected by means of inductive, capacitive or optical sensors. Thus piezo hysteresis and creep can be avoided. To enhance the control over

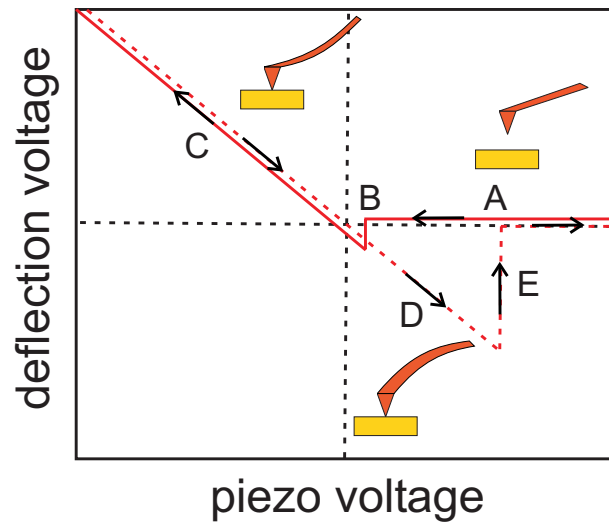


Figure 2.6: Force distance curve, A: approach, B: “snap on”, C: bending of the cantilever, D: adhesion, E: “snap off”

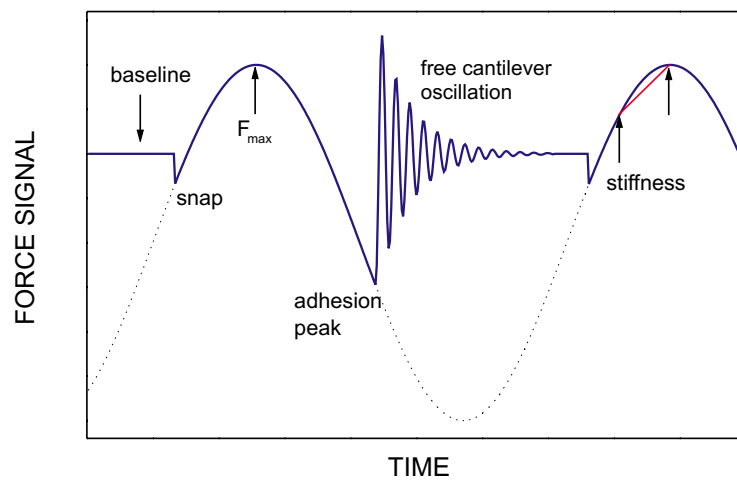


Figure 2.7: Pulsed Force Mode



the manipulation process several homebuilt [33] and even commercially available haptic input devices have been developed. The operator performs a move in the macroscopic space and the tip is doing the same move down scaled to nano-space. In the most advanced devices the operator can even feel the forces acting on the tip (force feedback).

Also lithographical processes similar to writing with a pen have been demonstrated and named dip pen nanolithography (DPN) [34–40]. To enhance the speed AFM probes with hundreds of parallel cantilevers were used [41].

### 2.1.8 Outlook

The main issue after the invention of the scanning force microscope was the visualization of nano-sized objects.

Today SFM is used, besides imaging, at non-ambient conditions or in combination with other methods to get more information about the sample and to probe the objects properties. I would like to mention here the combination with optical microscopy for biological applications [23], the scanning near-field optical microscopy (SNOM) [42] and the possibility to do spectroscopy on the nanometer-scale [43–48]. From the technical point of view the basic concept of SFM is still the same since its beginning and big effort is put in enhancing the imaging speed from minutes to seconds [49–51]. Also the application as data storage device [52] or as analytical tool in the uncrewed spaceflight is discussed.

What will the future bring? – Combining the SFM with spectroscopic and other analytical methods will continue and improve. In future it might be possible to do the standard analytical methods as IR, UV-spectroscopy and others on a nanometer resolution. The second challenging field will be the observation of nanoscale processes in situ at various conditions.

So the eras of SFM can be described as visualization – properties – processes.

## 2.2 Molecular motion, motors and devices

### 2.2.1 Top-down and bottom-up approach

In modern day technology there is a constantly increasing demand for fast processing and miniaturization. Recent advances in information technology are reached by what is called a top-down approach. In this approach, usually silicon-based electronic components are miniaturized to smaller and smaller dimensions to allow more rapid data processing and more dense data storage. The same technique was used to fabricate miniaturized devices as pumps [53], mixers [54, 55] or gears [56]. The limits of miniaturization in such a top-down approach are dependent on the limitations of the lithographic techniques used. It can be estimated that these limits will be reached at some point in the near future.

An alternative route to devices and storage units of smaller dimensions is named the bottom-up approach. Instead of decreasing dimensions of known macroscopic entities, here the aim is to use the smallest thinkable building blocks, molecules, or even atoms, and from this utter limit of miniaturization build up materials that can fulfill the same functions as their macroscopic counterparts. This approach calls for functional molecules as, for example, molecular motors or switches that by self-assembly form supramolecular materials that can function as data storage units or as parts of complex molecular scale devices.

Considering the dimensions of a molecule it is save to predict that eventually devices, developed by this bottom-up approach, would have dimensions in the nanometer ( $10^{-9}$  m) range. This size should also be the approximate limit of the top-down approach, where already devices with 80 nm features are presently known [57]. Therefore both approaches are part of a field of research that is named nanotechnology. But whereas in the top-down approach a single feature has the size of 80 nm, this is the size of the whole device in the bottom-up approach.

### 2.2.2 The switch

An essential component is a simple switch that can differentiate between an on- and an off-state. The basic requirement for a molecular counterpart of a switch is bistability. Bistability is the existence of two different forms of a molecule, which can be interconverted by means of an external stimulus. In practice, this bistability can be based on a variety of properties of molecules like electron transfer, isomerization, conformation changes [58, 59] and difference in complexation behavior whereas light [58, 60], heat, pressure [61], magnetic or electric fields, pH change or chemical reactions can be used to achieve the interconversion, i. e. the actual switching, of the bistable states. Photoreversible or photochromic compounds [62, 63], where the reversible switching process is based on photochemically induced interconversions, are particularly attractive. Photochemical switching of nanoscale architectures [64–66], mechanical devices [67–70], catalysts [71], transport systems [72], sensors [73], surface properties of materials [74–78] and target directed delivery systems [79] are only a few applications that can be envisioned. Next to this possible switching or triggering function which might offer intriguing prospects in the design of new photonic materials, a bistable molecular system itself already constitutes a potential binary data storage system. Defining the two forms of the photochromic system as a 0 and a 1 state this system constitutes one bit of information, provided that writing and reading-out are possible.

### 2.2.3 Motion and Motors

Another important function that can be controlled by light is molecular motion. Motion can be subdivided in two categories: translation and rotation. The major objective in designing a molecular motor is to generate controlled motion, different from random Brownian thermal motions present in every molecular system. Although one might argue on the true definition of the term motor, in current nanotechnological pursuits towards these types of systems, a motor is defined as a device that can convert any form of energy into controlled motion. This controlled motion should eventually be translated into any kind of work. Although driving some other function is theoretically possible in most existing molecular systems, this has not yet been established.

As often in science nature is a good teacher and big efforts have been made to elucidate the movement of kinesin [80] and myosin [81] along the filament fibres in muscles. Although the energy source is already known (ATP) [82–84], forces are measured [85] and the width of one single step is determined to 5.3 nm, [86] the mechanism of the movement is still discussed. Models discussed are porter and rower mechanism [87], collective transport in asymmetric periodic structures [88], fluctuation induced transport on a periodic potential [89–91] and different ratchet mechanism [92, 93].

A nice visualization of fluctuation induced transport of particles can be found in [94]

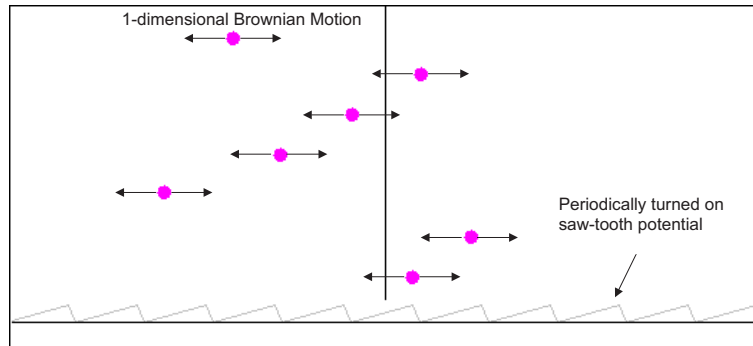


Figure 2.8: Fluctuation induced transport of particles in an asymmetric saw-tooth potential (grey line). The particles undergo 1-dimensional left-right Brownian Motion. Periodical cycles of turning on and off of the potential leads to an overall motion of the particles to the left [94]

and is shown in Figure 2.8. The particles undergo a one-dimensional left-right Brownian motion. In a potential free case the particles would spread symmetrically to the vertical center line. Turning on an asymmetric saw-tooth potential periodically (illustrated by the grey line) forces an overall motion of the particles to the left.

In Figure 2.9 the principle of Feynman's ratchet is shown. Because of the asymmetry of the ratchet's teeth, it might seem that even thermal fluctuations acting on a paddlewheel attached to the ratchet could be used to do work. However, the behavior of the spring is also influenced by collisions with molecules which cause it to vibrate. When the spring is down, molecular collisions with the paddlewheel indeed tend to cause the cog to turn only in the planned direction. However, in the rare event that the spring is up, disengaging the one-way mechanism, the random molecular forces on the paddle cause forward and backward motion with equal probability. It only takes a very tiny movement of the wheel backwards to set the device back one tooth, whereas to send it forward by a tooth requires a much greater motion. If the paddle and the pawl are at the same temperature so that the fluctuations on the pawl are as strong as those driving the paddlewheel, the ratchet, despite appearances will not turn. The equations are approximate formulae for the frequency of moving a step in the clockwise (cw) and counter-clockwise (ccw) direction.  $\Delta U = \kappa h^2$  where  $\kappa$  is the spring constant and  $h$  is the height of a tooth on the cog.

The movement of the Proteins along the filament is directed translation, synthetic systems dealing with translation are mostly not directed, examples are the motion of DNA on fluid membranes [95] or in a defined array [96], diffusion of Lenard-Jones clusters [97] or DNA [98], diffusion of large organic molecules at metal surfaces [99], the motion of nanorods [100] and monodendron jacketed linear polymers [101].

Especially controlled unidirectional rotation is essential for the development of nanomechanical devices. A large number of macroscopic devices make use of rotation behavior, as for example cars or jet engines. In developing machinery on a molecular scale, which has to function as molecular equivalent of these macroscopic entities, full control of movement and especially unidirectional rotation is essential. Although discussions on whether this type of molecular systems will lead to nano-equivalents of cars or robots that will eventually be developed and function as macroscopic devices, nowadays lies in between actual science and science fiction. The research on controlled motion on a molecular level

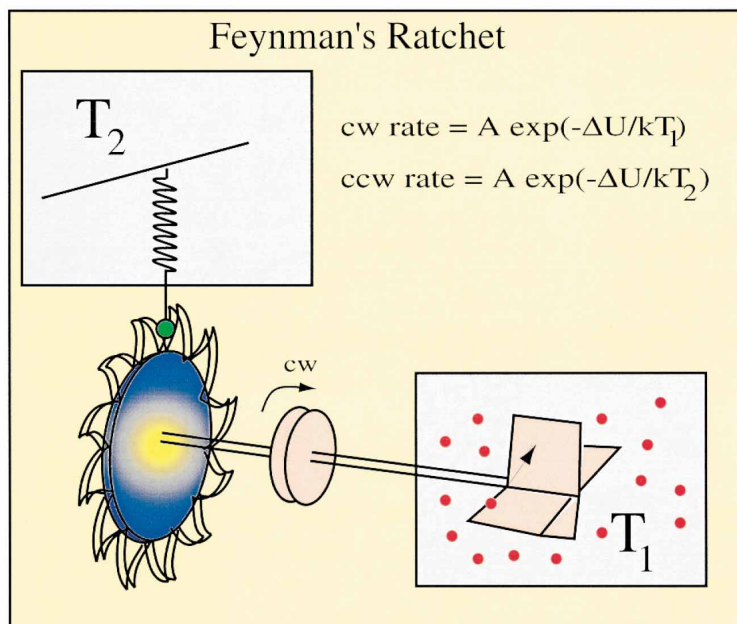


Figure 2.9: Principle of Feynman's Ratchet [90]

is extremely challenging. In these nanotechnological pursuits for true molecular devices, a variety of different functions have to be addressed on a molecular level. Next to molecular switches [60], molecular rotors and ratchets [102–105], brakes [106], gears [107], turnstiles [108], organic/inorganic hybrid devices [109] and muscles [26, 110–112] have, for example, been developed over the years. All are examples of control over molecular action that is molecular geometry or molecular movement.

# Bibliography

- [1] G. Binnig and H. Rohrer. Scanning tunneling microscopy – from birth to adolescence. *Rev. Mod. Phys.*, 59:615–625, 1987.
- [2] R. Young, J. Ward, and F. Scire. The Topografiner: An instrument for measuring surface microtopography. *Rev. Sci. Instrum.*, 43:999–1011, 1972.
- [3] G. Binnig, H. Rohrer, C. Gerber, and E. Weibel. Surface studies by scanning tunneling microscopy. *Phys. Rev. Lett.*, 49:57–61, 1982.
- [4] G. Binnig, C. F. Quate, and C. Gerber. Atomic force microscopy. *Phys. Rev. Lett.*, 56:930–933, 1986.
- [5] Y. Martin, C. C. Williams, and H. K. Wickramasinghe. Atomic force microscope – force mapping and profiling on a sub 100 Å scale. *J. Appl. Phys.*, 61:4723–4729, 1987.
- [6] R. W. Carpick, N. Agrait, D. F. Ogletree, and M. Salmeron. Measurement of interfacial shear (friction) with an ultrahigh vacuum atomic force microscope. *J. Vac. Sci. Technol. B*, 14:1289–1295, 1996.
- [7] J. E. Sader. Susceptibility of atomic force microscope cantilevers to lateral forces. *Rev. Sci. Instrum.*, 74:2438–2443, 2003.
- [8] J. P. Spatz, S. Sheiko, M. Möller, R. G. Winkler, P. Reinecker, and O. Marti. Tapping scanning force microscopy in air Theory and experiment. *Langmuir*, 13:4699–4703, 1997.
- [9] J. P. Spatz, S. Sheiko, M. Möller, R. G. Winkler, P. Reinecker, and O. Marti. Forces affecting the substrate in resonant tapping force microscopy. *Nanotechnology*, 6: 40–44, 1995.
- [10] G. Couturier, R. Boisgard, L. Nony, and J. P. Aimé. Noncontact atomic force microscopy: Stability criterion and dynamical responses of the shift of frequency and damping signal. *Rev. Sci. Instrum.*, 74:2726–2734, 2003.
- [11] D. J. Keller and F. S. Franke. Envelope reconstruction of probe microscope images. *Surf. Sci.*, 294:409–419, 1993.
- [12] M. Bammerlin, R. Lüthi, E. Meyer, A. Baratoff, J. Lü, M. Guggisberg, C. Loppacher, C. Gerber, and H.-J. Güntherodt. Dynamic SFM with true atomic resolution on alkali halide surfaces. *Appl. Phys. A*, 66:S293–S294, 1998.
- [13] H. Rohrer. Scanning tunneling microscopy: a surface science tool and beyond. *Surf. Sci.*, 299/300:956–964, 1994.

- [14] J. H. Hafner, C.-L. Cheung, A. T. Wooley, and C. M. Lieber. Structural and functional imaging with carbon nanotube AFM probes. *Prog. Biophys. Molec. Biology*, 77:73–110, 2001.
- [15] Q. M. Hudspeth, K. P. Nagle, Y.-P. Zhao, T. Karabacak, C. V. Nguyen, M. Meyyappan, G.-C. Wang, and T.-M. Lu. How does a multiwalled carbon nanotube atomic force microscopy probe affect the determination of surface roughness statistics. *Surf. Sci.*, 515:453–461, 2002.
- [16] C. V. Nguyen, R. M. D. Stevens, J. Barber, J. Han, and M. Meyyappan. Carbon nanotube scanning probe for profiling of deep-ultraviolet and 193 nm photoresist patterns. *Appl. Phys. Lett.*, 81:901–903, 2002.
- [17] C. V. Nguyen, K.-J. Chao, R. M. D. Stevens, L. Delzeit, A. Cassell, J. Han, and M. Meyyappan. Carbon nanotube tip probes: stability and lateral resolution in scanning probe microscopy and application to surface science in semiconductors. *Nanotechnology*, 12:363–367, 2001.
- [18] R. Stevens, C. Nguyen, A. Cassell, L. Delzeit, M. Meyyappan, and J. Han. Improved fabrication approach for carbon nanotube probe devices. *Appl. Phys. Lett.*, 77:3453–3455, 2000.
- [19] J. P. Spatz, S. S. Sheiko, and M. Möller. Shape and quality control of modified scanning force tips. *Ultramicroscopy*, 75:1–4, 1998.
- [20] S. S. Sheiko, M. Möller, E. M. C. M. Reuvekamp, and H. W. Zandbergen. Evaluation of the probing profile of SFM tips. *Ultramicroscopy*, 53:371–380, 1994.
- [21] J. M. Maxwell and M. G. Hudson. Using the scanning probe microscope to measure the effect of relative humidity on sample stiffness. *Rev. Sci. Instrum.*, 73:3520–3524, 2002.
- [22] Q. Dai, R. Vollmer, R. W. Carpick, D. F. Ogletree, and M. Salmeron. A variable temperature ultrahigh vacuum atomic force microscope. *Rev. Sci. Instrum.*, 66:5266–5271, 1995.
- [23] A. Radenović, E. Bystrenová, L. Libioulle, M. Taborrelli, J. A. DeRose, and G. Dietler. A low-temperature ultrahigh vacuum atomic force microscope for biological applications. *Rev. Sci. Instrum.*, 74:1022–1026, 2003.
- [24] M. Liebmann, A. Schwarz, S. M. Langkat, and R. Wiesendanger. A low-temperature ultrahigh vacuum scanning force microscope with a split-coil magnet. *Rev. Sci. Instrum.*, 73:3508–3514, 2002.
- [25] B. Capella and G. Dietler. Force-distance curves by atomic force microscopy. *Surf. Sci. Rep.*, 34:1–103, 1999.
- [26] N. B. Holland, T. Hugel, G. Neuert, A. Cattani-Scholz, C. Renner, D. Oesterhelt, L. Moroder, M. Seitz, and H. E. Gaub. Single molecule force spectroscopy of azobenzene polymers: Switching elasticity of single photochromic macromolecules. *Macromolecules*, 36:2015–2023, 2003.

- [27] T. Hugel and M. Seitz. The study of molecular interactions by AFM force spectrometry. *Macromol. Rapid Commun.*, 22:989–1016, 2001.
- [28] L. Shu, A. D. Schlüter, C. Ecker, N. Severin, and J. P. Rabe. Extremely long dendronized polymers: Synthesis, quantification of structure perfection, individualization, and SFM manipulation. *Angew. Chem.*, 113:4802–4805, 2001.
- [29] M. R. Falvo, R. M. Taylor II, A. Helser, V. Chi, F. P. Brooks Jr., S. Washburn, and R. Superfine. Nanometre-scale rolling and sliding of carbon nanotubes. *Nature*, 397:236–238, 1999.
- [30] M. R. Falvo, G. Clary, A. Helser, S. Paulson, R. M. Taylor II, V. Chi, F. P. Brooks Jr., S. Washburn, and R. Superfine. Nanomanipulation experiments exploring frictional and mechanical properties of carbon nanotubes. *Microsc. Microanal.*, 4:504–512, 1999.
- [31] M. R. Falvo, F. Steele, R. M. Taylor II, and R. Superfine. Gearlike rolling motion mediated by commensurate contact: Carbon nanotubes on HOPG. *Phys. Rev. B*, 62:10665–10667, 2000.
- [32] M. R. Falvo and R. Superfine. Mechanics and friction at the nanometer scale. *J. Nanoparticle Res.*, 1:237–248, 2000.
- [33] M. Guthold, M. R. Falvo, W. G. Matthews, S. Paulson, S. Washburn, D. Erie, R. Superfine, F. P. Brooks Jr., and R. M. Taylor II. Controlled manipulation of molecular samples with the nanoManipulator. *IEEE/ASME Transaction on Mechatronics*, 5:189–197, 2000.
- [34] B. M. Maynor, Y. Li, and J. Liu. Au ink for AFM dip-pen nanolithography. *Langmuir*, 17:2575–2578, 2001.
- [35] S. Hong and C. A. Mirkin. A nanoplotter with both parallel and serial writing capabilities. *Science*, 288:1808–1811, 2000.
- [36] S. Hong, J. Zhu, and C. A. Mirkin. Multiple ink nanolithography: Toward a multiple-pen nano-plotter. *Science*, 286:523–525, 1999.
- [37] R. D. Piner, J. Zhu, F. Xu, S. Hong, and C. A. Mirkin. Dip-pen nanolithography. *Science*, 283:661–663, 1999.
- [38] C. A. Mirkin, S. Hong, and L. Demers. Dip-pen nanolithography: Controlling surface architecture on the sub-100 nanometer length scale. *Chemphyschem*, 2:37–39, 2001.
- [39] L. M. Demers, D. S. Ginger, S.-J. Park, Z. Li, S.-W. Chung, and C. A. Mirkin. Direct patterning of modified oligonucleotides on metals and insulators by dip-pen nanolithography. *Science*, 296:1836–1838, 2002.
- [40] P. V. Schwartz. Molecular transport from an AFM tip: A comparative study of DPN. *Langmuir*, 18:4041–4046, 2002.
- [41] H. Kawakatsu, D. Saya, A. Kato, K. Fukushima, H. Toshiyoshi, and H. Fujita. Millions of cantilevers for atomic force microscopy. *Rev. Sci. Instrum.*, 73:1188–1192, 2002.

- [42] A. Jau, J. Koenen, K. Weishaupt, and O. Hollricher. Scanning near-field optical microscopy in life science. *Single Mol.*, 3:232–235, 2002.
- [43] R. Hillenbrand, T. Taubner, and F. Keilmann. Phonon-enhanced light-matter interaction at the nanometer scale. *Nature*, 418:159–162, 2002.
- [44] R. Hillenbrand and F. Keilmann. Material-specific mapping of metal/semiconductor/dielectric nanosystems at 10 nm resolution by backscattering near-field optical microscopy. *Appl. Phys. Lett.*, 80:25–27, 2002.
- [45] B. Knoll and F. Keilmann. Near-field probing of vibrational absorption for chemical microscopy. *Nature*, 399:134–137, 1999.
- [46] F. F. Schrey, E. E. Chaban, M. J. Matthews, and J. W. P. Hsu. A microscope for imaging, spectroscopy, and lithography at the nanometer scale: Combination of a two-photon laser scanning microscope and an atomic force microscope. *Rev. Sci. Instrum.*, 74:1211–1261, 2003.
- [47] A. Noy and T. R. Huser. Combined force and photonic probe microscope with single molecule sensitivity. *Rev. Sci. Instrum.*, 74:1217–1221, 2003.
- [48] E. J. Thoreson and N. A. Burnham. Apparatus for illuminating the tip-sample interface of an atomic force microscope. *Rev. Sci. Instrum.*, 74:94–99, 2003.
- [49] T. Sulchek, G. G. Yaralioglu, C. F. Quate, and S. C. Minne. Characterization and optimization of scan speed for tapping-mode atomic force microscopy. *Rev. Sci. Instrum.*, 73:2928–2936, 2002.
- [50] T. Akiyama, U. Staufer, and N. F. de Rooij. Fast driving technique for integrated thermal bimorph actuator toward high-throughput atomic-force microscopy. *Rev. Sci. Instrum.*, 73:2643–2646, 2002.
- [51] H. Kawakatsu, S. Kawai, D. Saya, M. Nagashio, D. Kobayashi, and H. Toshiyoshi. Towards atomic force microscopy up to 100 MHz. *Rev. Sci. Instrum.*, 73:2317–2320, 2002.
- [52] P. Vettiger, M. Despont, U. Drechsler, U. Dürig, W. Hberle, M. I. Lutwyche, H. E. Rothuizen, R. Stutz, R. Widmer, and G. K. Binnig. The "millipede" more than one thousand tips for future afm data storage. *IBM J. Res. Develop.*, 44:323–340, 2000.
- [53] D. Maillefer, S. Gamper, B. Frehner, and P. Balmer. A high-performance silicon micropump for disposable drug delivery systems. In *International Conference MEMS 2002, Interlaken, Switzerland*, pages 413–417, 2001.
- [54] V. Haverkamp, W. Ehrfeld, K. Gebauer, V. Hessel, H. Löwe, T. Richter, and C. Wille. The potential of micromixers for contacting of disperse liquid phases. *Fresenius J. Anal. Chem.*, 364:617–624, 1999.
- [55] W. Ehrfeld, K. Golbig, V. Hessel, H. Lwe, and T. Richter. Characterization of mixing in micromixers by a test reaction: Single mixing units and mixer arrays. *Ind. Eng. Chem. Res.*, 38:1075–1082, 1999.



- [56] J. J. Sniegowski and E. J. Garcia. Surface micromachined gear trains driven by an on-chip electrostatic microengine. *IEEE Electron Device Lett.*, 17:366–369, 1996.
- [57] S. Eisenberg and D. Cunningham. Optical lithography used to make smallest working device – with 80 nm features. Bell Labs Innovations website <http://www.bell-labs.com>, 1999.
- [58] P. Uznanski. UV-assisted formation of nanoaggregates from photochromic spiropyrans in nonpolar solvents. *Langmuir*, 19:1919–2022, 2003.
- [59] E. Zahavy, S. Rubín, and I. Willner. Conformational dynamics associated with photoswitchable binding of spiropyran modified Concanavlin A. *Mol. Cryst. Liq. Cryst.*, 246:195–199, 1994.
- [60] D. V. McGrath, D. M. Junge, J. R. McElhanon, and M. Hashemzadeh. Driving dendrimers with light. *Polym. Prepr.*, 39:281–282, 1998.
- [61] S. S. Sheiko, S. A. Prokhorova, K. L. Beers, K. Matyjaszewski, I. I. Potemkin, A. R. Khokhlov, and M. Möller. Single molecule rod-globule transition of brush molecules at a flat interface. *Macromolecules*, 34:8354–8360, 2001.
- [62] M. R. Wasielewski. Photoinduced electron transfer in supramolecular systems for artificial photosynthesis. *Chem. Rev.*, 92:435–461, 1992.
- [63] D. Gosztola, M. P. Niemczyk, and M. R. Wasielewski. Picosecond molecular switch based on bidirectional inhibition of photoinduced electron transfer using photogenerated electric fields. *J. Am. Chem. Soc.*, 120:5118–5119, 1998.
- [64] D. M. Junge and D. V. McGrath. Photoresponsive dendrimers. *Chem. Commun.*, pages 857–858, 1997.
- [65] A. Archut, F. Vögtle, L. De Cola, G. C. Azzellini, V. Balzani, P. S. Ramanujam, and R. H. Berg. Azobenzene-functionalized cascade molecules: Photoswitchable supramolecular systems. *Chem. Eur. J.*, 4:699–706, 1998.
- [66] D.-L. Jiang and T. Aida. Photoisomerization in dendrimers by harvesting of low-energy photons. *Nature*, 388:454–456, 1997.
- [67] P. L. Anelli, N. Spencer, and J. F. Stoddart. A molecular shuttle. *J. Am. Chem. Soc.*, 113:5131–5133, 1991.
- [68] A. Livoreil, C. O. Dietrich-Buchecker, and J.-P. Sauvage. Electrochemically triggered swinging of a [2]-Catenate. *J. Am. Chem. Soc.*, 116:9399–9400, 1994.
- [69] A. Credi, V. Balzani, S. J. Langford, and J. F. Stoddart. Logic operations at the molecular level. An XOR gate based on a molecular machine. *J. Am. Chem. Soc.*, 119:2679–2681, 1997.
- [70] F. G. Gatti, D. A. Leigh, S. A. Nepogodiev, A. M. Z. Slawin, S. J. Teat, and J. K. Y. Wong. Stiff, and sticky in the right places: The dramatic influence of preorganizing guest binding sites on the hydrogen bond-directed assembly of rotaxanes. *J. Am. Chem. Soc.*, 123:5983–5989, 2001.

- [71] F. Würthner and J. Rebek. Photoschaltbare Katalyse mit synthetischen Rezeptoren. *Angew. Chem.*, 107:503–505, 1995.
- [72] F. Vögtle. *Supramolecular Chemistry*. Wiley, New York, 1991.
- [73] T. D. James, K. R. A. S. Sandanayake, and S. Shinkai. Chiral discrimination of monosaccharides using a fluorescent molecular sensor. *Nature*, 374:345–347, 1995.
- [74] M. Lion-Dagan, E. Katz, and I. Willner. A bifunctional monolayer electrode consisting of 4-pyridyl sulfide and photoisomerizable spiropyran: Photoswitchable electrical communication between the electrode and Cytochrome C. *J. Chem. Soc. Chem. Commun.*, pages 2741–2742, 1994.
- [75] H. Tachibana, T. Nakamura, M. Matsumoto, H. Komizu, E. Manda, H. Niino, A. Yabe, and Y. Kawabata. Photochemical switching in conductive Langmuir-Blodgett films. *J. Am. Chem. Soc.*, 111:3080–3081, 1989.
- [76] R. C. Ahuja, J. Maack, and H. Tachibana. Unconstrained cis-trans isomerization of azobenzene moieties in designed mixed monolayers at the air/water interface. *J. Phys. Chem.*, 99:9221–9229, 1995.
- [77] J. Maack, R. C. Ahuja, and H. Tachibana. Resonant and nonresonant investigations of amphiphilic azobenzene derivatives in solution and in monolayers at the air/water interface. *J. Phys. Chem.*, 99:9210–9220, 1995.
- [78] M. Lahav, K. T. Ranjit, E. Katz, and I. Willner. A  $\beta$ -amino-cyclodextrin monolayer-modified Au electrode: a command surface for the amperometric and microgravimetric transduction of optical signals recorded by a photoisomerizable bipyridiniumazobenzene diad. *Chem. Commun.*, pages 259–260, 1997.
- [79] T. Nagasaki, S. Tamagaki, and K. Ogino. Syntheses and characterization of photochromic dendrimers including a 1,3-alternate calix[4]arene as core and azobenzene moieties as branches. *Chem. Lett.*, pages 717–718, 1997.
- [80] G. S. Bloom and S. A. Endow. Motor proteins 1: Kinesins. *Protein Profile*, 2: 1109–1111, 1995.
- [81] J. R. Sellers and H. V. Goodson. Motor proteins 2: Myosins. *Protein Profile*, 2: 1323–1423, 1995.
- [82] A. L. Wells, A. W. Lin, L.-Q. Chen, D. Safer, S. M. Cain, T. Hasson, B. O. Carragher, R. A. Milligan, and H. L. Sweeney. Myosin VI is an actin-based motor that moves backwards. *Nature*, 401:505–508, 1999.
- [83] M. Schliwa. Myosin steps backwards. *Nature*, 401:431–432, 1999.
- [84] Y. Okada and N. Hirokawa. A processive single-headed motor: Kinesin superfamily protein KIF1A. *Science*, 283:1152–1157, 1999.
- [85] M. J. Schnitzer, K. Visscher, and S. M. Block. Force production by single kinesin motors. *Nature Cell Biol*, 2:718–723, 2000.

- [86] K. Kitamura, M. Tokunaga, A.H. Iwane, and T. Yanagida. A single myosin head moves along an actin filament with regular steps of 5.3 nanometers. *Nature*, 397: 129–134, 1999.
- [87] S. Leibler and D. A. Huse. Porters versus rowers: A unified stochastic model of motor proteins. *J. Cell Biol.*, 121:1357–1368, 1993.
- [88] I. Derényi, P. Tegzes, and T. Vicsek. Collective transport in locally asymmetric periodic structures. *Chaos*, 8:657–664, 1998.
- [89] R. D. Astumian. Adiabatic theory for fluctuation-induced transport on a periodic potential. *J. Phys. Chem.*, 100:19075–19081, 1996.
- [90] R. D. Astumian and I. Derényi. Fluctuation driven transport and models of molecular motors and pumps. *Eur. Biophys. J.*, 27:474–489, 1998.
- [91] R. D. Astumian. Thermodynamics and kinetics of a Brownian Motor. *Science*, 276: 917–922, 1997.
- [92] A. van Oudenaarden and S. G. Boxer. Brownian ratchets: Molecular separations in lipid bilayers supported on patterned arrays. *Science*, 285:1046–1048, 1999.
- [93] R. D. Vale and F. Oosawa. Protein motors and Maxwell’s Demons: Does mechanochemical transduction involve a thermal ratchet? *Adv. Biophys.*, 26:97–134, 1990.
- [94] R. Ketzmerick, M. Weiß, and F.-J. Elmer. Brownian motor. Java-applet at <http://monet.physik.unibas.ch/~elmer/bm/>, 2002.
- [95] B. Maier and J. O. Rädler. DNA on fluid membranes: A model polymer in two dimensions. *Macromolecules*, 33:7185–7194, 2000.
- [96] D. Nykypanchuk, H. H. Strey, and D. A. Hoagland. Brownian motion of DNA confined within a two-dimensional array. *Science*, 297:987–990, 2002.
- [97] P. Deltour, J.-L. Barrat, and P. Jensen. Fast diffusion of a Lennard-Jones cluster on a crystalline surface. *Phys. Rev. Lett.*, 78:4597–4600, 1997.
- [98] B. Maier and J. O. Rädler. Conformation and self-diffusion of single DNA molecules confined to two dimensions. *Phys. Rev. Lett.*, 82:1911–1914, 1999.
- [99] J. Weckesser, J. V. Barth, and K. Kern. Direct observation of surface diffusion of large organic molecules at metal surfaces: PVBA on Pd(110). *J. Chem. Phys.*, 113: 5351–5354, 1999.
- [100] S. K. St. Angelo, C. C. Waraksa, and T. E. Mallouk. Diffusion of gold nanorods on chemically functionalized surfaces. *Adv. Mater.*, 5:400–402, 2003.
- [101] S. S. Sheiko and M. Möller. Visualization of macromolecules - A first step to manipulation and controlled response. *Chem. Rev.*, 101:4099–4123, 2001.
- [102] N. Koumura, R. W. J. Zijlstra, R. A. van Delden, N. Harada, and B. L. Feringa. Light-driven unidirectional molecular motor. *Nature*, 401:152–154, 1999.

## Bibliography

- [103] T. R. Kelly, J. P. Sestelo, and I. Tellitu. New molecular devices: In search of a molecular ratchet. *J. Org. Chem.*, 63:3655–3665, 1998.
- [104] L. P. Faucheux, L. S. Bourdieu, P. D. Kaplan, and A. J. Libchaber. Optical thermal ratchet. *Phys. Rev. Lett.*, 74:1504–1507, 1995.
- [105] M. O. Magnasco. Forced thermal ratchets. *Phys. Rev. Lett.*, 71:1477–1481, 1993.
- [106] T. R. Kelly, M. C. Bowyer, K. V. Bhaskar, D. Bebbington, A. Garcia, F. Lang, M. H. Kim, and M. P. Jette. A molecular brake. *J. Am. Chem. Soc.*, 116:3657–3658, 1994.
- [107] J. Clayden and J. H. Pink. Konzertierte Rotation in einem tertiären aromatischen Amid: auf dem Weg zu einem einfachen molekularen Getriebe. *Angew. Chem.*, 110:2040–2043, 1998.
- [108] T. C. Bedard and J. S. Moore. Design and synthesis of a “molecular tumstile”. *J. Am. Chem. Soc.*, 117:10662–10671, 1995.
- [109] C. Montemagno and G. Bachand. Constructing nanomechanical devices powered by biomolecular motors. *Nanotechnology*, 10:225–231, 1999.
- [110] M. C. Jiménez, C. Dietrich-Buchecker, and J.-P. Sauvage. Towards synthetic molecular muscles: Contraction and stretching of a linear rotaxane dimer. *Angew. Chem.*, 112:3422–3425, 2000.
- [111] B. L. Feringa. In control of molecular motion. *Nature*, 408:151–154, 2000.
- [112] T. Hugel. *Towards Synthetic Molecular Motors Interfaced by AFM*. PhD thesis, Ludwig-Maximilians-Universität München, 2002.

# 3 Nanomanipulation and thermal equilibration of monodendron jacketed polymers

## 3.1 Introduction

Scanning force microscopy (SFM) has been shown to enable imaging of single biological and synthetic macromolecules. Examples are globular and cylindrical or worm-like molecules such as DNA and RNA [1], nucleosomes [2], viruses [3], dendrimers, arborescent graft polymers [4], polymacromonomers [5], monodendron jacketed linear polymers [6] and poly(*p*-phenylene)s [7]. The examples listed above have in common that they all represent rather thick molecules which do not interpenetrate each other but exist as segregated species.

This chapter will deal with one species of monodendron jacketed linear polymers: 12-ABG-4EO-PMA (Figure 3.1). The polymer was synthesized to create self-assembling structures analogous to the rod-like viruses such as tobacco mosaic virus. The minidendritic side groups mimic the shape of the protein subunits of the viral coat. Diameters of 5 nm and more, a defined shape and strong adsorption on common substrates as mica and HOPG makes this type of molecules to model compounds similar to DNA strands but with an order of magnitude smaller sizes.

In the field of scanning probe microscopy (SPM) already many years ago the idea was born that this technique can not only be used for imaging procedures but also for creating and manipulating objects on surfaces. In 1990 Eigler started to deposit xenon atoms on nickel surfaces with the scanning tunnelling microscope [8]. Later scanning force microscopy was used to scratch patterns into substrates and more recently dip pen lithography [9–11] was used successfully to write on substrates. Although all of these techniques use the same procedures that are necessary for well directed manipulation of objects, this area was less developed. Only in the last two years several people [12–15] started to address this field. The manipulation of nano-objects can also be used to probe complex surface properties as the friction or adhesion of molecules on surfaces. This method can also help to create artificial model systems which otherwise can only be created with bigger efforts. One example is the polymer crystallization: the understanding of the early stage of chain folding is of primary importance. One way is to prepare monodispers oligomer samples and study the properties of an ensemble [16, 17], another way is to prepare an artificial model system with completely stretched molecules and study the chain folding by scanning force microscopy.

In this chapter the synthesis of 12-ABG-4EO-PMA is described and the adsorbed monodendron jacketed polymers on different substrates are visualized. Furthermore the manipulation of these molecules is used to judge how strong is the adsorption of these molecules on mica, HOPG and tungsten selenide. In the last part of this chapter the initial steps of chain folding starting from a completely straight molecule on HOPG is followed by in situ

SFM experiments.

## 3.2 Experimental

### 3.2.1 Materials

Methyl 4-hydroxybenzoate (99 %), 1-bromododecane (97 %), 4-(dimethylamino)pyridine (DMAP, 99 %), hydrogen fluoride-pyridine, methyl 3,4,5-trihydroxybenzoate (98 %), *tert*-butyldimethylsilyl chloride (TBDMSCl, 99 %), thionyl chloride (99 %), SiO<sub>2</sub> thin layer chromatography sheets with fluorescent indicator, neutral chromatographic Al<sub>2</sub>O<sub>3</sub> (all from Aldrich), 1,3-dicyclohexylcarbodiimide (DCC, 99 %, Fluka), *p*-toluenesulfonic acid (99 %, Alfa), chloroform-*d* (Cambridge Isotope Laboratories), chromatographic SiO<sub>2</sub> (Silicycle), acetone, methanol, dimethylformamide (DMF), ethanol, ethyl acetate, hexanes (technical grade, all six from Fisher), and other conventional reagents were used as received.

Tetraethylene glycol (99 %, Aldrich) was stored over 4 Å molecular sieves for more than 24 h. Methacryloyl chloride (98 %), pyridine (99 %) and triethylamine (99.5 %, all three from Aldrich) were distilled before use. Diethylether, tetrahydrofuran (THF), methylene chloride, benzene (technical grade, all four from Fisher) were dried by passing with pressure through a column of chromatographic Al<sub>2</sub>O<sub>3</sub>. 2,2'-Azobisisobutyronitrile (AIBN, Kodak) was recrystallized from methanol at 4 °C.

4-(Dimethylamino)pyridinium *p*-Toluenesulfonate (DPTS) was prepared according to literature procedures [18].

### 3.2.2 Methods

<sup>1</sup>H-NMR (250 MHz) spectra were recorded on a Bruker AC-250 FT NMR spectrometer at 20 °C using CDCl<sub>3</sub> as solvent and tetramethylsilane (TMS) as an internal standard. Relative molecular weight of the polymer was measured by size exclusion chromatography (SEC) with a Perkin Elmer Series 200 pump equipped with a LC100 column oven (40 °C), a Perkin Elmer 785A UV/VIS detector, a Varian Star 9040 differential refractive index detector, and a Nelson 900 series integration data station. A set of two Polymer Laboratories PL gel columns with 5·10<sup>2</sup> and 10<sup>4</sup> Å pores and THF as eluent at 1 ml/min were used. Polystyrene standards were used for calibration.

Scanning force microscopy (SFM) was performed using a Digital Instruments Dimension Series 3100 scanning force microscope equipped with a Nanoscope IV controller and a capacitive controlled closed loop scanner. The closed loop scanner combined with the new nanoman software from Digital Instruments allowed precise positioning and controlled movement of the SFM-tip. Imaging and manipulation was done in tapping mode. For the comparison of the adhesion on mica and HOPG a silicon single crystal cantilever (Digital Instruments OTESP) with triangular shape and force constant of ca. 40 N/m and a resonance frequency of ca. 300 kHz was used. For the other experiments a standard silicon cantilever (Nanoworld FM,  $k = 2.8$  N/m and  $f_0 = 70$  kHz) was used. In order to get less noisy images in some cases the closed loop control was turned off. For scanning at elevated temperatures a home made heating stage with a Lakeshore temperature controller was used.

STM was performed with an RHK Technology Inc. microscope operating in constant current mode. The tunneling current was 20–30 pA at a bias voltage of -200 to +500 mV.

STM images of the monodendron mono-layers were obtained on HOPG in a saturated solution of the monodendrons in 1,2,4-trichlorobenzene.

### 3.2.3 Synthesis of 12-ABG-4EO-PMA (**10**)

Figure 3.1 outlines the synthesis of the monomer **9** and of the poly(methacrylate) **10**. The sequence of reactions is almost similar to a series of similar compounds prepared before [19, 20]. Almost all reaction steps were accomplished in high yields. To introduce the ethylene glycol spacer one hydroxy group of the tetraethylene glycol was protected with *tert*-butyldimethylsilyl chloride [21].

Radical polymerization of **9** was carried out in bulk at 80 °C for 30 min [22]. The polymer was purified by column chromatography (SiO<sub>2</sub>, 2:1 hexanes/ethyl acetate). The molecular weight determined by SEC is  $M_n = 462,000$  g/mol and the polydispersity is 2.06.

#### Synthesis of methyl 4-(*n*-dodecan-1-yloxy)benzoate (**1**)

A 1 l round-bottom flask equipped with a Teflon-coated stirring bar was charged with 290 ml of DMF and 110.0 g (0.796 mol) of anhydrous K<sub>2</sub>CO<sub>3</sub>. The mixture was sparged with nitrogen for 10 min and then 58.0 g (0.381 mol) of methyl 4-hydroxybenzoate were added. The solution was sparged for another 10 min and then 67 ml (0.280 mol) of 1-bromododecane were added. The mixture was heated at 70 °C and poured into 2 l of cold tap water. Hydrochloric acid (10 %) was added until CO<sub>2</sub> evolution ceased. The product was filtered and recrystallized from methanol giving 85.0 g (94,8 %) of white crystals.

<sup>1</sup>H-NMR,  $\delta$  (CDCl<sub>3</sub>, TMS, ppm): 0.88 (t, 3H, CH<sub>3</sub>), 1.26 (overlapped m, 18H, (CH<sub>2</sub>)<sub>9</sub>), 1.80 (m, 2H, CH<sub>2</sub>CH<sub>2</sub>OPh), 3.88 (s, 3H, CO<sub>2</sub>CH<sub>3</sub>), 4.00 (t, 2H, CH<sub>2</sub>OPh), 6.90 (d, 2H, ArH ortho to CH<sub>2</sub>O), 7.97 (d, 2H, ArH ortho to CO<sub>2</sub>CH<sub>3</sub>).

#### Synthesis of 4-(*n*-dodecan-1-yloxy)benzyl alcohol (**2**)

A 1 l round-bottom flask containing a Teflon-coated magnetic stirring bar and equipped with an addition funnel was charged with 60 ml of dry THF and 6.19 g (0.163 mol) of LiAlH<sub>4</sub>. The flask was flushed with nitrogen and cooled in an ice bath. 47.5 g (0.148 mol) of **1** were dissolved in 210 ml of dry THF and added in drops over a period of 1 h. The ice bath was removed and the reaction mixture was stirred for an additional hour. The reaction mixture was again cooled in an ice bath and 6.2 ml of water were added cautiously drop by drop. The ice bath was removed and 6.2 ml of NaOH (15 %) were added. Finally water was added until a white precipitation occurred. During the addition of water and NaOH further THF was added in order to keep the solution stirrable. The reaction was filtered, the solvent evaporated and the product was recrystallized from acetone resulting in 38.4 g (88.7 %) of white solid.

<sup>1</sup>H-NMR,  $\delta$  (CDCl<sub>3</sub>, TMS, ppm): 0.88 (t, 3H, CH<sub>3</sub>), 1.27 (overlapped m, 18H, (CH<sub>2</sub>)<sub>9</sub>), 1.79 (m, 2H, CH<sub>2</sub>CH<sub>2</sub>OPh), 3.95 (t, 2H, CH<sub>2</sub>OPh), 4.62 (d, 2H, CH<sub>2</sub>OH), 6.89 (d, 2H, ArH ortho to CH<sub>2</sub>O), 7.28 (d, 2H, ArH ortho to CH<sub>2</sub>OH).

#### Synthesis of 4-(*n*-dodecan-1-yloxy)benzyl chloride (**3**)

A 1 l round-bottom flask equipped with an addition funnel and a Teflon-coated magnetic stirring bar was charged with 72.95 g (0.249 mol) of **2**, 600 ml of dry CH<sub>2</sub>Cl<sub>2</sub>, and 1 ml of DMF. The flask was flushed with nitrogen then cooled in an ice bath followed by drop

### 3 Nanomanipulation and thermal equilibration of monodendron jacketed polymers

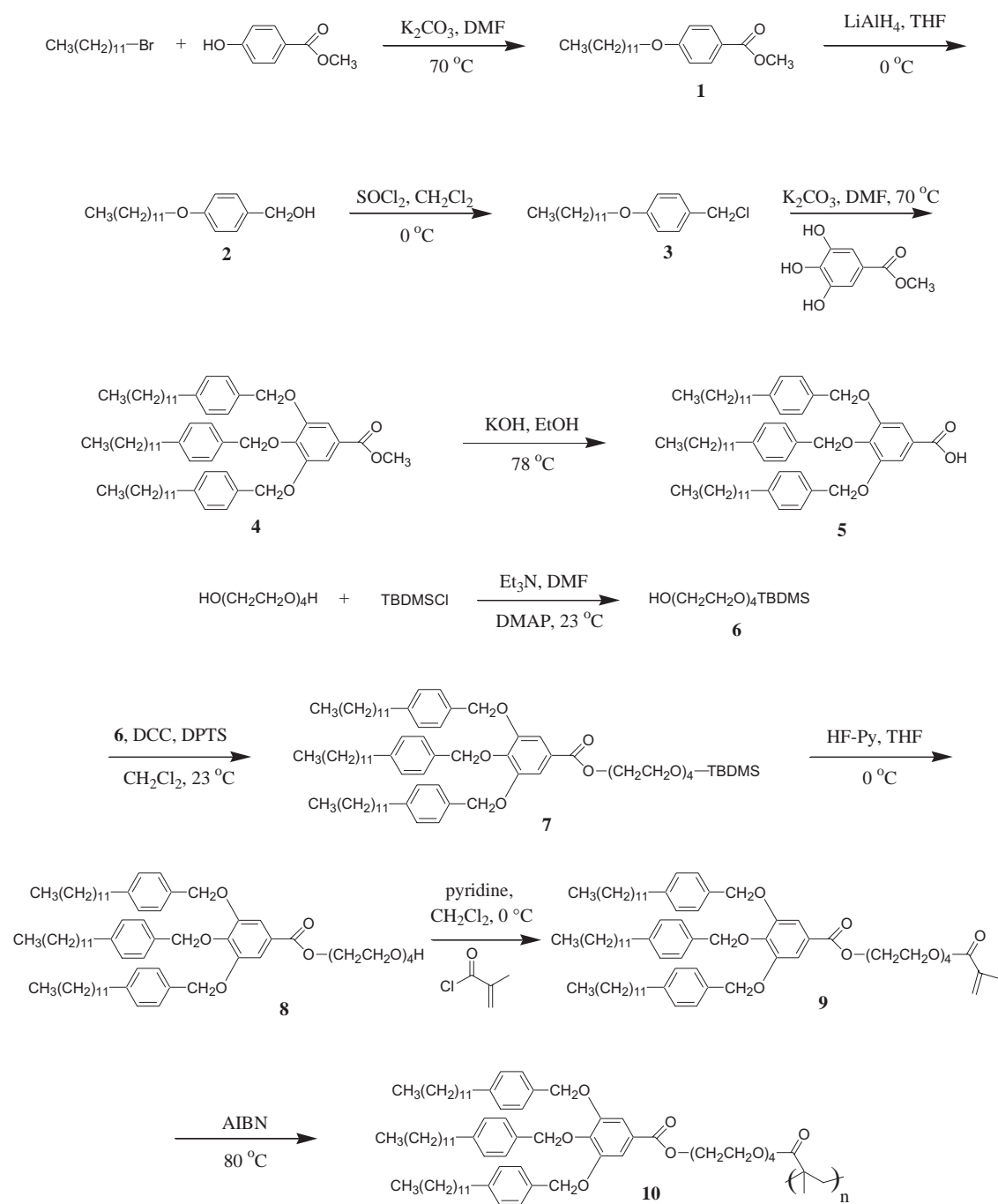


Figure 3.1: Synthesis of Poly(2-[2-{2-(2-(methacryloyloxy)ethoxy)ethoxy}ethoxy]ethyl 3,4,5-tris[(4-(*n*-dodecan-1-yloxy)benzyl)oxy]benzoate)



by drop addition of 32.6 ml (0.274 mol) of  $\text{SOCl}_2$  over 15 min. The ice bath was removed and the reaction mixture stirred for an additional 1 h. The solvent and excess  $\text{SOCl}_2$  were evaporated. The crude product was dissolved in 300 ml of diethylether, and washed two times with 300 ml of water. The organic phase was dried over  $\text{MgSO}_4$ , filtered, and the solvent evaporated. The product was recrystallized from acetone, giving 49.11 g (63.4 %) of light yellow crystals.

$^1\text{H-NMR}$ ,  $\delta$  ( $\text{CDCl}_3$ , TMS, ppm): 0.88 (t, 3H,  $\text{CH}_3$ ), 1.27 (overlapped m, 18H,  $(\text{CH}_2)_9$ ), 1.79 (m, 2H,  $\text{CH}_2\text{CH}_2\text{OPh}$ ), 3.95 (t, 2H,  $\text{CH}_2\text{OPh}$ ), 4.56 (s, 2H,  $\text{CH}_2\text{Cl}$ ), 6.87 (d, 2H, ArH ortho to  $\text{CH}_2\text{O}$ ), 7.29 (d, 2H, ArH ortho to  $\text{CH}_2\text{Cl}$ ).

TLC:  $R_f = 0.95$  (3:1 hexanes/ethyl acetate).

### Synthesis of methyl 3,4,5-tris[(4-(*n*-dodecan-1-yloxy)benzyl)oxy]benzoate (**4**)

A 1 l round-bottom flask equipped with a Teflon-coated magnetic stirring bar was charged with 420 ml of DMF and 43.66 g (0.316 mol) of anhydrous  $\text{K}_2\text{CO}_3$ . The mixture was sparged with nitrogen for 30 min and then 9.70 g (52.7 mmol) of methyl 3,4,5-trihydroxybenzoate was added. The solution was sparged for another 10 min and then 49.11 g (0.158 mol) of **3** were added. The mixture was stirred for 12 h at 70 °C under nitrogen atmosphere. The reaction was cooled to about 40 °C and poured into 2 l of cold tap water. The precipitate was filtered, washed with 2 l water, and filtered again. The solid was dissolved in  $\text{CH}_2\text{Cl}_2$ , dried over  $\text{MgSO}_4$  and the solvent evaporated. The crude product was passed through a neutral  $\text{Al}_2\text{O}_3$  column using  $\text{CH}_2\text{Cl}_2$  as eluent. The product was recrystallized from acetone giving 36.54 g (68.8 %) of white solid.

$^1\text{H-NMR}$ ,  $\delta$  ( $\text{CDCl}_3$ , TMS, ppm): 0.88 (t, 9H,  $\text{CH}_3$ ), 1.27 (overlapped m, 54H,  $(\text{CH}_2)_9$ ), 1.78 (m, 6H,  $\text{CH}_2\text{CH}_2\text{OPh}$ ), 3.88 (s, 3H,  $\text{CO}_2\text{CH}_3$ ), 3.91–3.98 (overlapped t, 6H,  $\text{CH}_2\text{OPh}$ ), 5.00–5.04 (overlapped s, 6H,  $\text{PhCH}_2\text{OPh}$ ), 6.75 (d, 2H, ArH ortho to  $\text{CH}_2\text{OPh}$ , para to  $\text{PhCO}_2\text{CH}_3$ ), 6.89 (d, 4H, ArH ortho to  $\text{CH}_2\text{OPh}$ , meta to  $\text{PhCO}_2\text{CH}_3$ ), 7.24 (d, 2H, ArH meta to  $\text{CH}_2\text{OPh}$ , para to  $\text{PhCO}_2\text{CH}_3$ ), 7.33 (d, 4H, ArH meta to  $\text{CH}_2\text{OPh}$ , meta to  $\text{PhCO}_2\text{CH}_3$ ), 7.36 (s, 2H, ArHCO<sub>2</sub>CH<sub>3</sub>).

TLC:  $R_f = 0.80$  ( $\text{CH}_2\text{Cl}_2$ ).

### Synthesis of 3,4,5-tris[(4-(*n*-dodecan-1-yloxy)benzyl)oxy]benzoic acid (**5**)

A 500 ml round-bottom flask equipped with a Teflon-coated magnetic stirring bar was charged with 28.16 g (27.95 mmol) of **4**, 13.64 g (0.243 mol) of KOH and 230 ml of 95 % ethanol. The reaction mixture was refluxed for 1 h and then cooled to room temperature. The resulting precipitate was filtered and washed with ethanol. The solid and 330 ml THF were placed in a 1 l Erlenmeyer flask and 1 M hydrochloric acid was added in drops until pH = 1 was reached. The THF solution was poured in 650 ml of diethylether and washed two times with 330 ml portions of water and then with 200 ml of saturated NaCl solution. The organic phase was separated and dried over  $\text{MgSO}_4$ . The mixture was filtered and the solvent evaporated. The product was recrystallized from acetone, resulting in 25.82 g (93.0 %) of white solid.

$^1\text{H-NMR}$ ,  $\delta$  ( $\text{CDCl}_3$ , TMS, ppm): 0.88 (t, 9H,  $\text{CH}_3$ ), 1.27 (overlapped m, 54H,  $(\text{CH}_2)_9$ ), 1.78 (m, 6H,  $\text{CH}_2\text{CH}_2\text{OPh}$ ), 3.92–3.99 (overlapped t, 6H,  $\text{CH}_2\text{OPh}$ ), 5.00–5.05 (overlapped s, 6H,  $\text{PhCH}_2\text{OPh}$ ), 6.75 (d, 2H, ArH ortho to  $\text{CH}_2\text{OPh}$ , para to  $\text{PhCO}_2\text{CH}_3$ ), 6.89 (d, 4H, ArH ortho to  $\text{CH}_2\text{OPh}$ , meta to  $\text{PhCO}_2\text{CH}_3$ ), 7.25 (d, 2H, ArH meta to  $\text{CH}_2\text{OPh}$ ,

para to PhCO<sub>2</sub>CH<sub>3</sub>), 7.33 (d, 4H, ArH meta to CH<sub>2</sub>OPh, meta to PhCO<sub>2</sub>CH<sub>3</sub>), 7.42 (s, 2H, ArHCO<sub>2</sub>CH<sub>3</sub>).

TLC: R<sub>f</sub> = 0 (CH<sub>2</sub>Cl<sub>2</sub>).

### Synthesis of 2-[2-{2-(2-(tert-butyldimethylsiloxy)ethoxy)ethoxy}ethoxy]ethanol (**6**)

A 250 ml round-bottom flask equipped with an addition funnel and a Teflon-coated magnetic stirring bar was charged with 5.99 g (39.7 mmol) of *tert*-butyldimethylsilyl chloride and 30 ml of dry DMF. The flask was flushed with nitrogen and 68.9 ml (0.397 mol) of dry tetraethylene glycol and 6.09 ml (43.7 mmol) of dry Et<sub>3</sub>N were added. Finally 200 mg (1.6 mmol) of DMAP were added to the emulsion. The reaction was stirred for 12 h at room temperature under nitrogen. The reaction mixture was poured into 350 ml of CH<sub>2</sub>Cl<sub>2</sub> and washed three times with 200 ml of water and then with 100 ml of saturated NH<sub>4</sub>Cl solution. The organic phase was dried over NaSO<sub>4</sub> and the solvent evaporated. The product was dissolved in 350 ml of diethylether and washed twice with 100 ml water and then with 70 ml of saturated NaCl solution. The organic phase was dried over NaSO<sub>4</sub> and the solvent evaporated. The product was dried over night under high vacuum and yielded 10.14 g (82.8 %) of a light yellow liquid.

<sup>1</sup>H-NMR, δ (CDCl<sub>3</sub>, TMS, ppm): 0.04 (s, 6H, OSi(CH<sub>3</sub>)<sub>2</sub>), 0.89 (s, 9H, C(CH<sub>3</sub>)<sub>3</sub>), 3.52–3.78 (overlapped m, 16H, (CH<sub>2</sub>CH<sub>2</sub>O)<sub>4</sub>H).

### Synthesis of 2-[2-{2-(2-(tert-butyldimethylsiloxy)ethoxy)ethoxy}ethoxy]ethyl 3,4,5-tris[(4-(*n*-dodecan-1-yloxy)benzyl)oxy]benzoate (**7**)

A 250 ml round-bottom flask equipped with a Teflon-coated stirring bar was charged with 20.61 g (21.12 mmol) of **5**, 8.47 g (27.46 mmol) of **6**, 130 ml of CH<sub>2</sub>Cl<sub>2</sub>, 5.66 g (27.46 mmol) of DCC, and 621 mg (2.11 mmol) of DPTS. The flask was flushed with nitrogen and stirred at room temperature for 15 h, after which <sup>1</sup>H-NMR analysis indicated complete reaction. The reaction mixture was filtered and the solvent evaporated. The residue was dissolved in hexanes and filtered again. The crude product was chromatographed on silica gel (4:1 hexanes/ethyl acetate) resulting in 19.44 g (71.7 %) of white solid.

<sup>1</sup>H-NMR, δ (CDCl<sub>3</sub>, TMS, ppm): 0.04 (s, 6H, OSi(CH<sub>3</sub>)<sub>2</sub>), 0.88 (overlapped m, 9H, CH<sub>3</sub>, 9H, OSi(CH<sub>3</sub>)<sub>2</sub>(CH<sub>3</sub>)<sub>3</sub>), 1.27 (overlapped m, 54H, (CH<sub>2</sub>)<sub>9</sub>), 1.78 (m, 6H, CH<sub>2</sub>CH<sub>2</sub>OPh), 3.53 (t, 2H CH<sub>2</sub>OSi), 3.64–3.88 (overlapped m, 12H, CH<sub>2</sub>O(CH<sub>2</sub>CH<sub>2</sub>O)<sub>2</sub>CH<sub>2</sub>), 3.91–3.99 (overlapped t, 6H, CH<sub>2</sub>OPh), 4.45 (t, 2H, CO<sub>2</sub>CH<sub>2</sub>), 5.00–5.04 (overlapped s, 6H, PhCH<sub>2</sub>OPh), 6.75 (d, 2H, ArH ortho to CH<sub>2</sub>OPh, para to PhCO<sub>2</sub>CH<sub>3</sub>), 6.88 (d, 4H, ArH ortho to CH<sub>2</sub>OPh, meta to PhCO<sub>2</sub>CH<sub>3</sub>), 7.24 (d, 2H, ArH meta to CH<sub>2</sub>OPh, para to PhCO<sub>2</sub>CH<sub>3</sub>), 7.33 (d, 4H, ArH meta to CH<sub>2</sub>OPh, meta to PhCO<sub>2</sub>CH<sub>3</sub>), 7.37 (s, 2H, ArHCO<sub>2</sub>CH<sub>3</sub>).

TLC: R<sub>f</sub> = 0.53 (3:1 hexanes/ethyl acetate).

### Synthesis of 2-[2-{2-(2-hydroxyethoxyethoxy)ethoxy}ethoxy]ethyl 3,4,5-tris[(4-(*n*-dodecan-1-yloxy)benzyl)oxy]benzoate (**8**)

A polypropylene flask containing a Teflon-coated magnetic stirring bar was charged with 19.44 g (15.14 mmol) of **7** and 225 ml of dry THF. The flask was flushed with nitrogen and closed with a rubber stopper. The solution was cooled in an ice bath and 15 ml of hydrogen fluoride-pyridine was added drop by drop. The ice bath was removed and the reaction stirred for an additional 1 h. TLC (2:1 hexanes/ethyl acetate) indicated complete

deprotection. The reaction solution was diluted with 500 ml diethylether and saturated NaHCO<sub>3</sub> solution was added cautiously until CO<sub>2</sub> evolution ceased. The two phases were separated and the organic phase was washed three times with 500 ml water and then with 250 ml saturated NaCl solution. The organic phase was dried over MgSO<sub>4</sub> and the solvent evaporated. The crude product was recrystallized from 1:1 hexanes/diethylether and dried in high vacuum resulting in 15.15 g (85.54 %) of light brown solid.

<sup>1</sup>H-NMR,  $\delta$  (CDCl<sub>3</sub>, TMS, ppm): 0.88 (t, 9H, CH<sub>3</sub>), 1.27 (overlapped m, 54H, (CH<sub>2</sub>)<sub>9</sub>), 1.79 (m, 6H, CH<sub>2</sub>CH<sub>2</sub>OPh), 3.55–3.71 (overlapped m, 12H (CH<sub>2</sub>CH<sub>2</sub>O)<sub>3</sub>H), 3.82 (t, 2H, CO<sub>2</sub>CH<sub>2</sub>CH<sub>2</sub>), 3.91–3.99 (overlapped t, 6H, CH<sub>2</sub>OPh), 4.46 (t, 2H, CO<sub>2</sub>CH<sub>2</sub>), 5.00–5.04 (overlapped s, 6H, PhCH<sub>2</sub>OPh), 6.75 (d, 2H, ArH ortho to CH<sub>2</sub>OPh, para to PhCO<sub>2</sub>CH<sub>3</sub>), 6.88 (d, 4H, ArH ortho to CH<sub>2</sub>OPh, meta to PhCO<sub>2</sub>CH<sub>3</sub>), 7.19 (d, 2H, ArH meta to CH<sub>2</sub>OPh, para to PhCO<sub>2</sub>CH<sub>3</sub>), 7.33 (d, 4H, ArH meta to CH<sub>2</sub>OPh, meta to PhCO<sub>2</sub>CH<sub>3</sub>), 7.37 (s, 2H, ArHCO<sub>2</sub>CH<sub>3</sub>).

### Synthesis of 2-[2-{2-(2-(methacryloyloxy)ethoxy)ethoxy}ethoxy]ethyl 3,4,5-tris[(4-(*n*-dodecan-1-yloxy)benzyl)oxy]benzoate (**9**)

A 250 ml round-bottom flask equipped with a Teflon-coated magnetic stirring bar was charged with 9.88 g (8.45 mmol) of **8**, 145 ml of dry CH<sub>2</sub>Cl<sub>2</sub>, and 3.4 ml (42.23 mmol) of distilled pyridine. The flask was flushed with nitrogen and cooled in an ice bath. 0.98 ml (10.14 mmol) of methacryloyl chloride were added in drops. The ice bath was removed and the reaction was stirred for an additional 1 h, when TLC analysis (2:1 hexanes/ethyl acetate) indicated complete conversion. The solvent was evaporated and the crude product was chromatographed on silica gel (2:1 hexanes/ethyl acetate) resulting in 6.94 g (66.4 %) of white solid.

<sup>1</sup>H-NMR,  $\delta$  (CDCl<sub>3</sub>, TMS, ppm): 0.88 (t, 9H, CH<sub>3</sub>), 1.27 (overlapped m, 54H, (CH<sub>2</sub>)<sub>9</sub>), 1.79 (m, 6H, CH<sub>2</sub>CH<sub>2</sub>OPh), 1.94 (s, 3H, –COC(CH<sub>3</sub>)=CH<sub>2</sub>), 3.65–3.74 (overlapped m, 10H (CH<sub>2</sub>CH<sub>2</sub>O)<sub>2</sub>OCH<sub>2</sub>), 3.82 (t, 2H, CO<sub>2</sub>CH<sub>2</sub>CH<sub>2</sub>), 3.89–3.98 (overlapped t, 6H, CH<sub>2</sub>OPh), 4.27 (t, 2H, CH<sub>2</sub>OCOC(CH<sub>3</sub>)=CH<sub>2</sub>), 4.45 (t, 2H, PhCO<sub>2</sub>CH<sub>2</sub>), 5.00–5.04 (overlapped s, 6H, PhCH<sub>2</sub>OPh), 5.56 (s, 1H, COC(CH<sub>3</sub>)=CH<sub>2</sub>), 6.12 (s, 1H, COC(CH<sub>3</sub>)=CH<sub>2</sub>), 6.75 (d, 2H, ArH ortho to CH<sub>2</sub>OPh, para to PhCO<sub>2</sub>CH<sub>3</sub>), 6.88 (d, 4H, ArH ortho to CH<sub>2</sub>OPh, meta to PhCO<sub>2</sub>CH<sub>3</sub>), 7.24 (d, 2H, ArH meta to CH<sub>2</sub>OPh, para to PhCO<sub>2</sub>CH<sub>3</sub>), 7.33 (d, 4H, ArH meta to CH<sub>2</sub>OPh, meta to PhCO<sub>2</sub>CH<sub>3</sub>), 7.37 (s, 2H, ArHCO<sub>2</sub>CH<sub>3</sub>).

TLC: R<sub>f</sub> = 0.40 (2:1 hexanes/ethyl acetate).

### Synthesis of Poly(2-[2-{2-(2-(methacryloyloxy)ethoxy)ethoxy}ethoxy]ethyl 3,4,5-tris[(4-(*n*-dodecan-1-yloxy)benzyl)oxy]benzoate) (**10**)

A 25 ml Schlenk tube containing a Teflon-coated magnetic stirring bar was charged with 1.732 g (1.399 mmol) of **9**, 33.4 mg (0.203 mmol) of AIBN, and 1 ml of benzene. The tube was sealed with a rubber septum, the compounds mixed and the benzene was evaporated using a high vacuum pump. The mixture was heated for 30 min at 80 °C. After cooling to room temperature the crude reaction mixture was passed through a silica gel column (2:1 hexanes/ethyl acetate). The product was dissolved in THF and precipitated in methanol, filtered and dried in high vacuum, resulting in 1.06 g (61.2 %) of white polymer.

SEC: M<sub>n</sub> = 462,000 g/mol, DP = 373, M<sub>w</sub>/M<sub>n</sub> = 2.06.

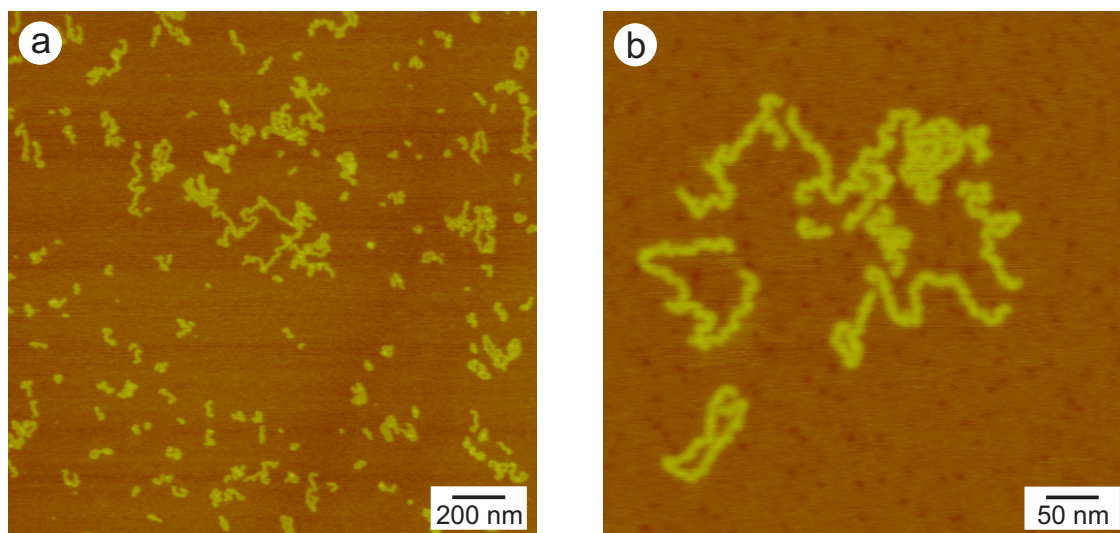


Figure 3.2: SFM tapping mode topography images of 12-ABG-4EO-PMA on mica, spin-coated from a) xylene solution  $c = 0.025$  g/l and b) THF solution  $c = 0.01$  g/l

### 3.3 Results and discussion

#### 3.3.1 Epitaxial adsorption of 12-ABG-4EO-PMA on HOPG

Figure 3.2 shows SFM images of 12-ABG-4EO-PMA on mica spin-coated from diluted xylene and THF solutions. Single macromolecules can be seen as worm-like objects lying flat on the substrate with a height of 1.3–1.7 nm and a width of 4–7 nm. The contour length of the molecules is in the range of ca. 20 nm up to several hundred nm, reflecting the polydispersity of 2.06.

In Figure 3.3 12-ABG-4EO-PMA was spin-coated from chloroform solution on HOPG substrates. The same worm-like objects could be identified, the dimensions – height: 1.2–1.5 nm and width: 5–8 nm – are comparable to the ones measure on mica. But here the molecules showed one speciality: the molecules show straight segments of 20–100 nm which make sharp kinks. The angle of these kinks is almost exclusively  $60^\circ$  or  $120^\circ$ . Also the straight segments do not show arbitrary orientations on the substrate. Even the segments of molecules separated by several hundred nanometers are parallel and lay on three main directions which differ by  $60^\circ$ .

Similar observations have been made in highly ordered mono-layers of linear alkanes and cycloalkanes [23, 24], catenanes with linear hydrocarbon segments [25], polymers with alkyl side chains [26] as well as for comblike molecules with alkyl substituents as oligo(thiophenes) [27, 28] due to the preferential orientation of the hydrocarbon chains with respect to the graphite lattice. It is tempting to ascribe the ordering of monodendron-jacketed polymers to the epitaxial adsorption of the alkyl tails on the graphite, where the repeat length  $l = 0.254$  nm of a  $-(\text{CH}_2)-(\text{CH}_2)-$  sequence in the all-trans planar zigzag conformation matches the crystallographic spacing  $a = 0.246$  nm of the graphite surface. To verify this hypothesis STM studies on mono-layers of monomeric dendrons were performed. Figure 3.4a depicts the monolayer structure of 3,4,5-tris[(4-(*n*-dodecan-1-yloxy)-benzyl)oxy]benzoic acid (**5**). A drop of a saturated solution of the monodendrons in 1,2,4-trichlorobenzene was placed on HOPG and the in this way adsorbed monolayer was imaged

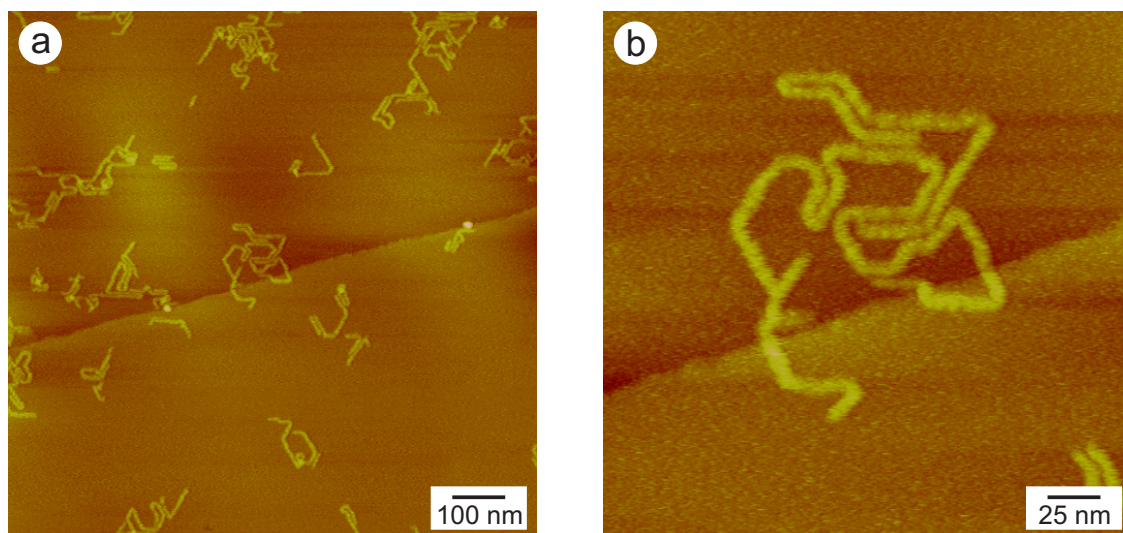


Figure 3.3: SFM tapping mode topography images of 12-ABG-4EO-PMA on HOPG, spin-coated from chloroform solution  $c = 0.02$  g/l

in situ. The image shows domains of parallel aligned stripes with a mean periodicity of  $3.9 \pm 0.1$  nm. Again the stripes align only in three directions differing by  $60^\circ$ . The high resolution image in Figure 3.4b depicts the individual monodendrons within the stripes. The three benzyl groups and the gallic acid core are depicted as bright spots forming a triple leaf structure. The alkyl chains could be identified as straight lines between the rows aligned at an angle of  $65^\circ$  with respect to the stripes and parallel to the crystalline axes of the HOPG. A schematic representation of the adsorbed molecules laying head to head with the carboxylic acid group is also given in this figure. The STM images indicate that the alkyl chains are arranged in an interdigitating comb structure. The length of the alkyl chains was measured to 1.5 nm which is consistent with the length of a dodecane molecule in its all-trans conformation. The main periodicity along the stripes was measured to 1.9 nm per adsorbed molecule. Within this distance only four interdigitated alkyl tails can be arranged tightly adsorbed on the surface with an average distance between the chains of at least 0.46 nm. It must be concluded that only two alkyl chains per molecule are adsorbed along the main direction of the HOPG surface, while the third alkyl chain dangles into the solution above the adsorbed layer. This interpretation could be confirmed by computer simulations based on simple force-field calculations.

In the next series of experiments the influence of the temperature on the polymer fixed to the substrate was investigated. Figure 3.5 shows the experiment on mica whereas Figure 3.6 shows the corresponding experiment on a HOPG substrate. The left images show the initial state at or close to room temperature, whereas on the right side the images at elevated temperature are displayed. The heating was conducted in form of an in situ SFM heating experiment and the temperature was stepwise increased. Above  $100^\circ\text{C}$  the measurement was conducted in helium atmosphere to prevent the polymer from oxidation.

In the case of mica as substrate the position and the shape of the molecules does not change at all. On the image on the right side at  $170^\circ\text{C}$  all molecules and aggregates could be still identified in their original state. The only change that takes place is that the molecules get thinner most probably due to thermal decomposition. This effect of thinning

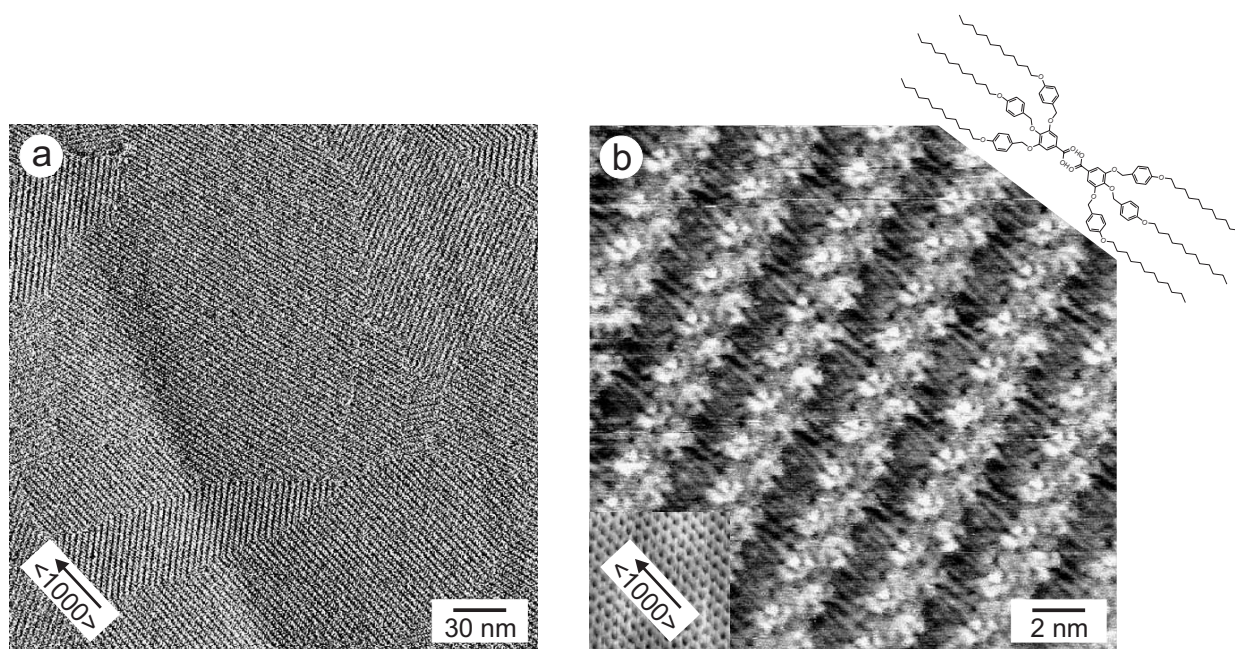


Figure 3.4: STM micrographs of the mono-layer structure of the minidendritic side groups on HOPG obtained by adsorption from a saturated solution in trichlorobenzene. The inset in a) shows the graphite substrate which was measured at higher currents

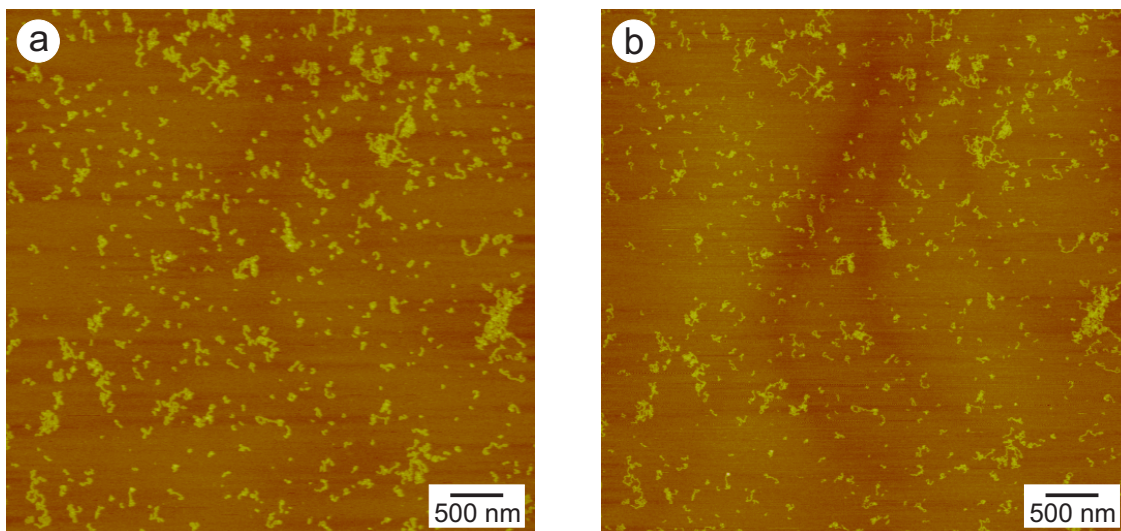


Figure 3.5: SFM tapping mode topography images of 12-ABG-4EO-PMA on mica, spin-coated from xylene solution  $c = 0.025$  g/l. a)  $T = 26$  °C b)  $T = 170$  °C in helium atmosphere

could be followed up to the experimental limit of 250 °C. Still the contours of the molecules did not change but became barely visible.

Completely different was the situation on the graphite substrate. Already at temperatures as low as 35 °C the molecules left their original places on the substrate in order to form bigger two-dimensional aggregates (Figure 3.6). Figure 3.7 shows a high resolution of one aggregate. Here the annealing time was 4 hours and also the temperature was higher: 65 °C. Nicely the parallel alignment of the molecules can be seen. The average length of the straight segments is increased compared to the state direct after spin-coating. Exclusively kink angles of 60°, 120° and hairpin folds with 180° could be observed. The number of kinks with 60° has been dramatically reduced.

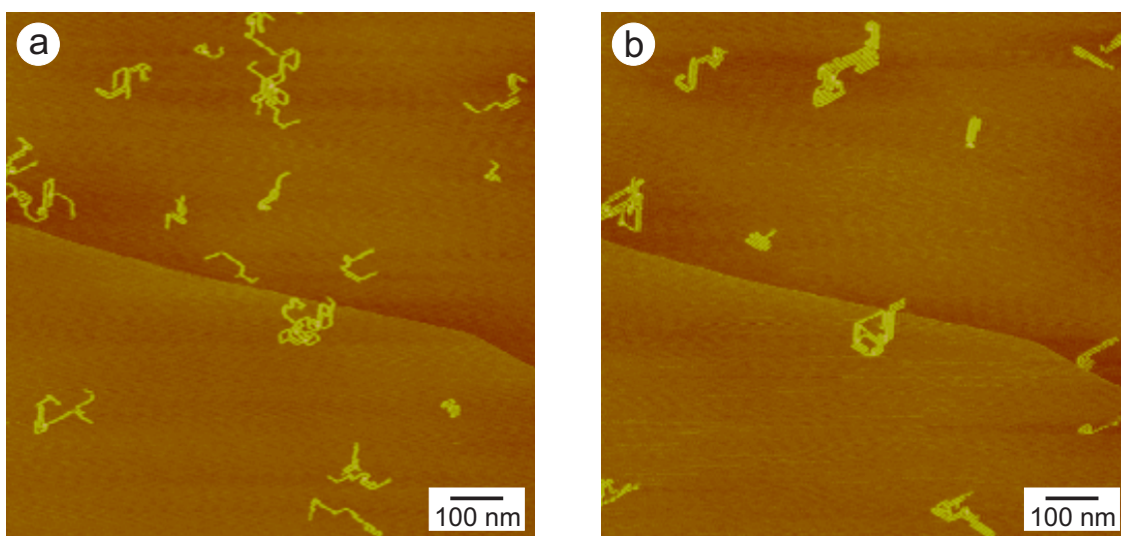


Figure 3.6: SFM tapping mode topography images of 12-ABG-4EO-PMA on HOPG, spin-coated from THF solution  $c = 0.01$  g/l. a)  $T = 30$  °C b)  $T = 35$  °C

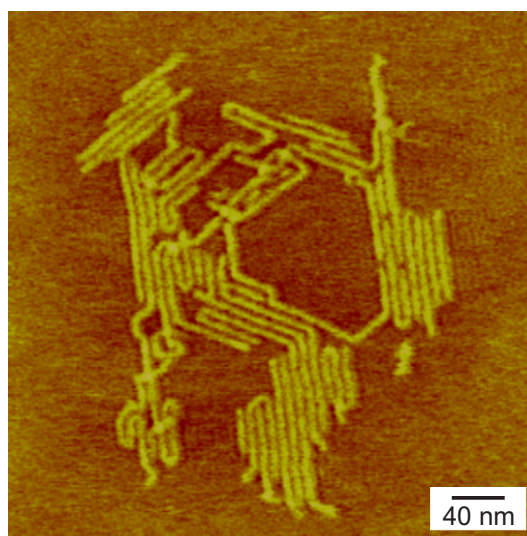


Figure 3.7: SFM tapping mode topography image of 12-ABG-4EO-PMA on HOPG, spin-coated from THF solution  $c = 0.01$  g/l and annealed at  $65$  °C for 4 hours. The image was taken at room temperature



### 3.3.2 Nanomanipulation of 12-ABG-4EO-PMA

From the completely different thermal behavior of 12-ABG-4EO-PMA on mica and graphite substrates arises the question what happens if we try to manipulate the molecules mechanically on the substrate with a SFM-tip.

The standard scheme of nanomanipulation was the following: First the substrate was scanned in tapping mode and the appropriate molecules for manipulation were selected. Then the scanning was stopped and the tip was moved to the starting point of the manipulation step. This was done under tapping feed-back control. Then the feedback was turned off and the tip was lowered down several nanometers (3–10 nm) towards the substrate. This is further on called z-move. Now the actual manipulation was performed with a speed of 1–50 nm/s. In the final step the same area was imaged again to control the effect of the nanomanipulation. It should be mentioned that the tip was kept tapping all over the whole procedure and usually did not get affected by the manipulation making it possible to do a series of manipulation steps.

Figure 3.8 shows SFM images of a successful manipulation of 12-ABG-4EO-PMA on graphite. In this case the z-move was 3 nm and the lateral speed of the tip during manipulation was 50 nm/s. Initial experiments which have been performed with a z-move of 1 nm did not show any effect at all. Increasing the z-move to 2 nm resulted in about 50 % of the attempts in an at least partially successful displacement of the molecules. With a z-move of 3 nm almost each manipulation was successful in a quite predictable way. Another important factor for the manipulation is the lateral speed of the tip. It turned out that at high speeds of several hundred nm/s the tip easily jumped over the molecules and was not able to affect the polymers. Also with a z-move of 2 nm the chance of successful manipulation was greatly improved with lower speeds. Thus the value of the z-move at constant speed can be used as a rough measure of the adhesion of the polymer molecules to the respective substrate. For all these measurements the speed was set to 10 nm/s even when the manipulation steps in the shown images were performed with different velocities.

Additionally, two further effects could be evaluated. The first concerns the defects (i. e. steps) in the HOPG. To move a part of the polymer over a step, or to pull a molecule away from a step, significant stronger conditions are necessary: z-move 5–7 nm. The second concerns the overlapping of the polymers. In Figure 3.8a the molecule which was manipulated crosses itself in the left upper corner identifiable by the bright spot. An overlapping like this was never resolvable by means of a manipulation step. It looks like the minidendritic side groups are strongly entangled into each other, so that they can not be resolved. To displace such a crossing point also higher z-moves in the order of 5–7 nm have been necessary.

The first effect of gluing to the steps can be explained in the increased contact area of the polymer to the substrate. It does not only adhere to the bottom but also on the side to the wall formed by the step. The impeded displacement of the crossing points is due to the increased number of simultaneously moved monomeric units. If we try to move a linear fragment of the polymers only the adjacent monomers on the left and right side have to detach from the substrate in order to change their position. In the case of the crossovers there are four adjacent parts of the polymer chain which have to loose at once from the substrate.

In Figure 3.9 another example with a more practical application is shown. Here in a three step sequence an aggregate of three polymer molecules was separated into three free molecules. This proves the capability of nanomanipulation to arrange objects on a

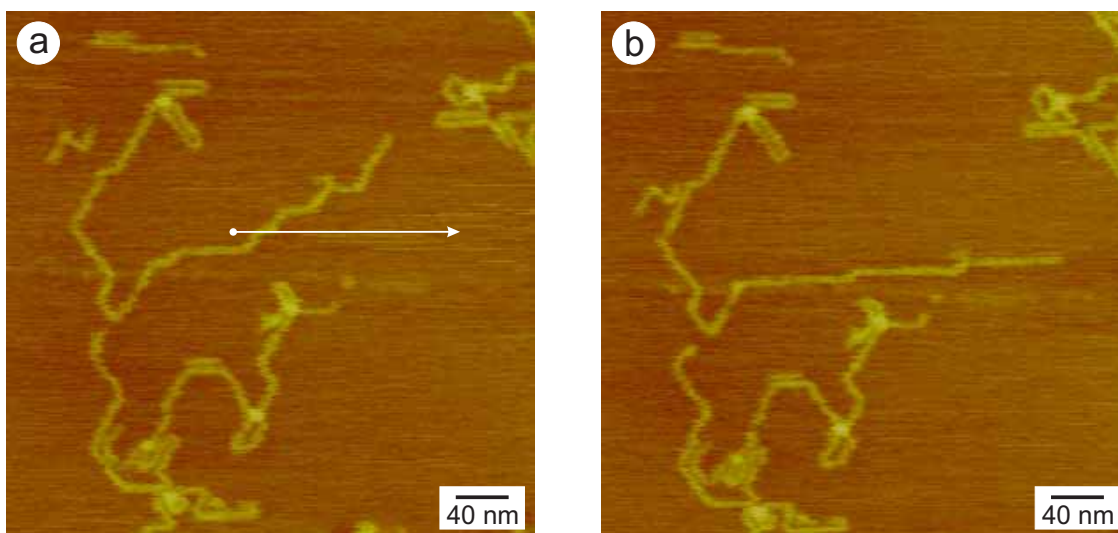


Figure 3.8: Nanomanipulation of 12-ABG-4EO-PMA on HOPG, the white arrow indicates the manipulation step:  $z\text{-move} = 3\text{ nm}$ ,  $v = 50\text{ nm/s}$  a) before and b) after manipulation

substrate in a desired configuration.

If we try to manipulate the polymers on mica using the same parameters as on graphite nothing happens at all. The tip is just jumping over the molecules and we see no effect. When the  $z\text{-move}$  was increased to 5 nm the molecules showed in some cases a small distortion where the tip crossed the polymer chain, but no displacement took place. Further increase of the  $z\text{-move}$  to 7 nm resulted in, what is shown in Figure 3.10, the cutting of the molecules in two parts. The created gap is in the range of 18–25 nm what is consistent with a tip apex radius of ca. 10 nm given by the producer. Most impressive is the result which is shown in Figure 3.10b–c. Here a molecule with a total length of only 45 nm was cut in two parts. The two left over pieces did not change their position at all.

Now having a working tool that allows to judge the adhesion of molecules on substrates, we decided to stay with the same polymer and expanded the experiments to a third substrate: tungsten selenide. Tungsten selenide ( $\text{WSe}_2$ ) is a semiconductor and characterized by a two dimensional crystal structure with strong chemical bonding in two dimensional sandwich type layers and only weak interaction between the layers themselves. The sandwich layers are formed by Se–W–Se repetition units. Cleaving these crystals leads to (0001) surface planes which consist of a hexagonally close-packed selenide lattice with the hexagonally packed tungsten ions in the trigonal position of the plane below.

The first unexpected result after spin-coating of 12-ABG-4EO-PMA on the surface was the same epitaxial adsorption which we know already from HOPG. The question arises what are the differences and similarities of mica, HOPG and  $\text{WSe}_2$  which cause the same behavior for HOPG and  $\text{WSe}_2$  and different behavior for mica. Table 3.1 gives the crystallographic data for the three substrates. Graphite is unpolar,  $\text{WSe}_2$  is a polar substrate, whereas muscovite mica even exhibits ionic interactions. Also the crystal structure of muscovite is monoclinic, whereas the two other substrates have a hexagonal lattice. Nevertheless the topmost layer of all three substrates (Figure 3.11) consist out of condensed hexagons, which are in the case of  $\text{WSe}_2$  occupied in the center with another Se atom .

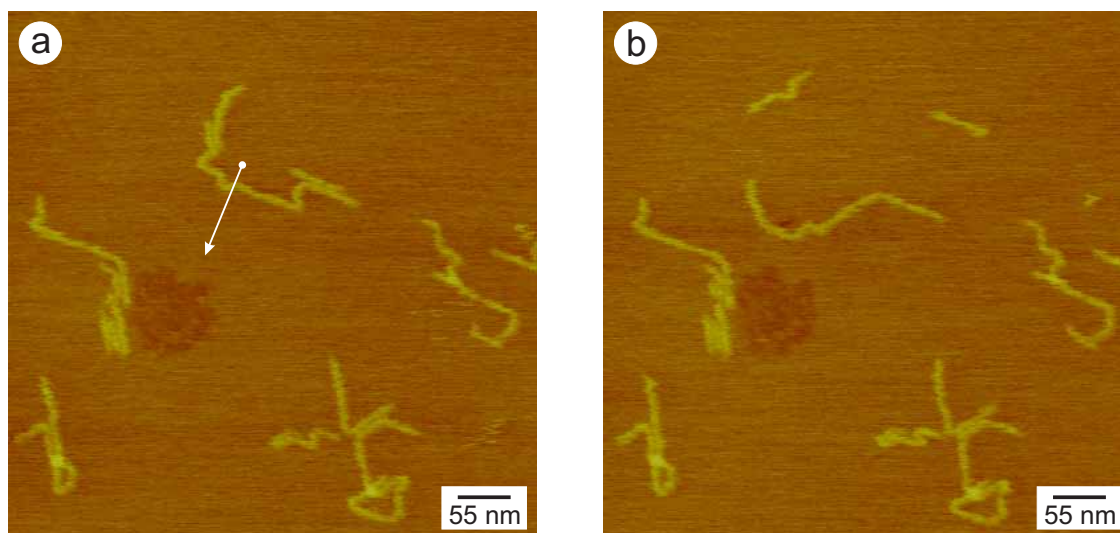


Figure 3.9: Separating of two molecules of 12-ABG-4EO-PMA on HOPG, the white arrows indicate the manipulation steps:  $z$ -move = 3 nm,  $v$  = 10 nm/s a) before and b) after manipulation

The flat topmost layer of graphite with a C–C distance of 142 pm matches almost the C–C bond length of the alkyl chains (154 pm), leading to good conditions for epitaxial adsorption as already mentioned in section 3.3.1.

In the case of  $\text{WSe}_2$  the topmost layer is also flat, but the Se–Se distance (190 pm) is 23 % larger than the C–C bond length. In semiconductor research the epitaxial growth of films on  $\text{WSe}_2$  with lattice mismatches of up to 50 % was reported [29, 30]. This unveils why the epitaxial adsorption of alkyl chains with lattice mismatch of 23 % still works.

For muscovite mica the Si–O distance of 150 pm matches perfectly the C–C bond length but the top layer is not flat like in the other two cases: the silicon atoms lay deeper than the oxygen atoms. This would either result in a vertical orientation of the alkyl zigzag chains unlike to a horizontal orientation or in an effective atom–atom distance of 260 pm of the oxygen atoms. Both cases seem to impede the epitaxial adsorption of the alkyl chains. Additionally from the strong binding of the polymers on mica a quite fast adsorption kinetic is expected. This might be too fast and too strong to allow reorganization after initial random adsorption.

The manipulation on  $\text{WSe}_2$  (Figure 3.12) worked also similar to graphite. A  $z$ -move of 5 nm was necessary to obtain reliable results. From this a stronger adsorption to  $\text{WSe}_2$  compared to HOPG is concluded. This is also confirmed by in situ annealing SFM experiments: to achieve the same mobility of the molecules on  $\text{WSe}_2$  the sample must be heated 10–20 °C higher than graphite as substrate.

Also the tendency to stay in epitaxy with the substrate is more pronounced. The molecule on HOPG in Figure 3.9 showed a bow after manipulation. On  $\text{WSe}_2$  a completely straight molecule was moved down in Figure 3.12a–b. The molecule kept almost straight and even the small step in the molecule was in one of the three preferred directions. After the molecule was straightened again (b–c) the same manipulation was performed in the opposite direction (c–d) with the same result.

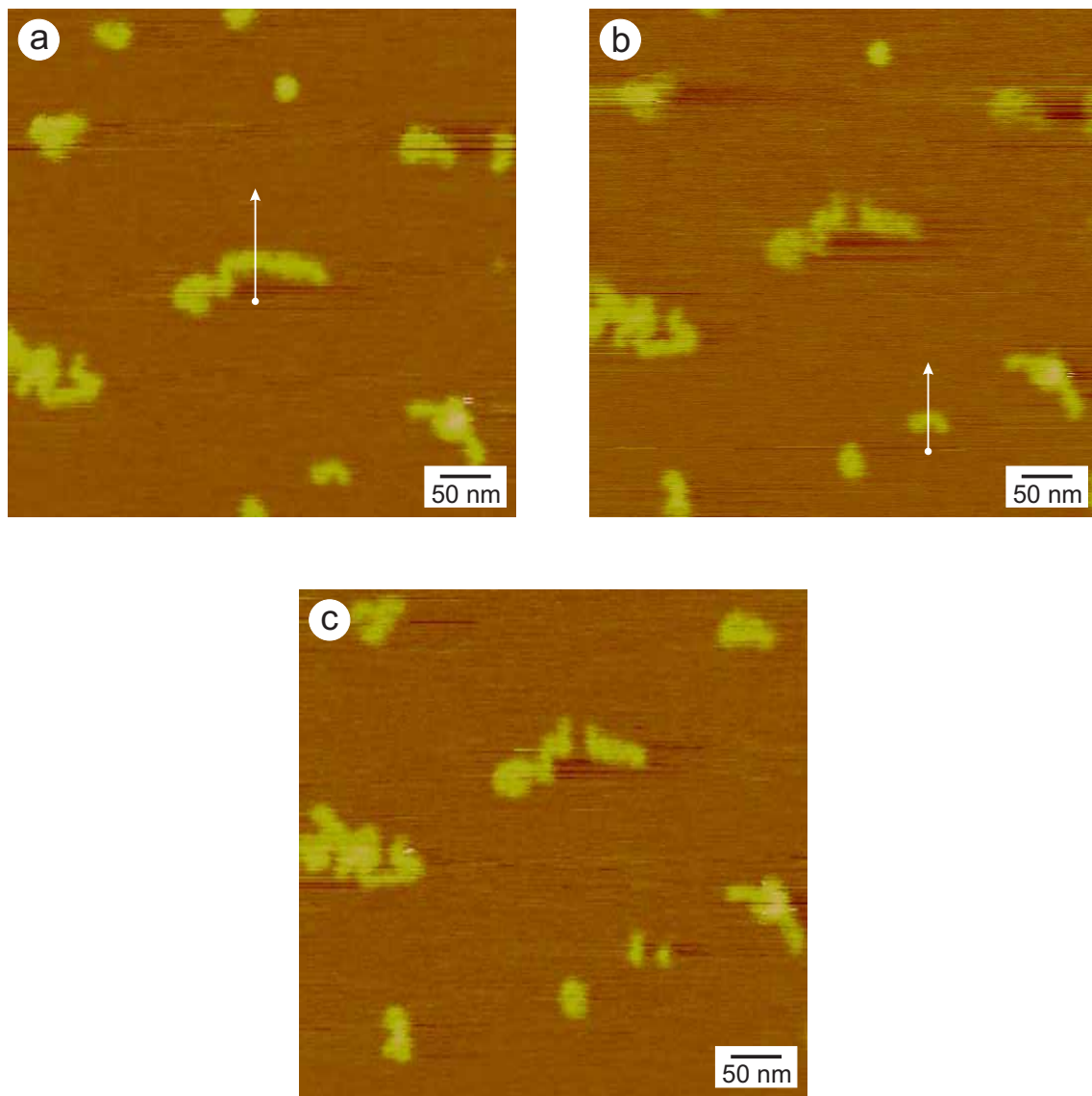
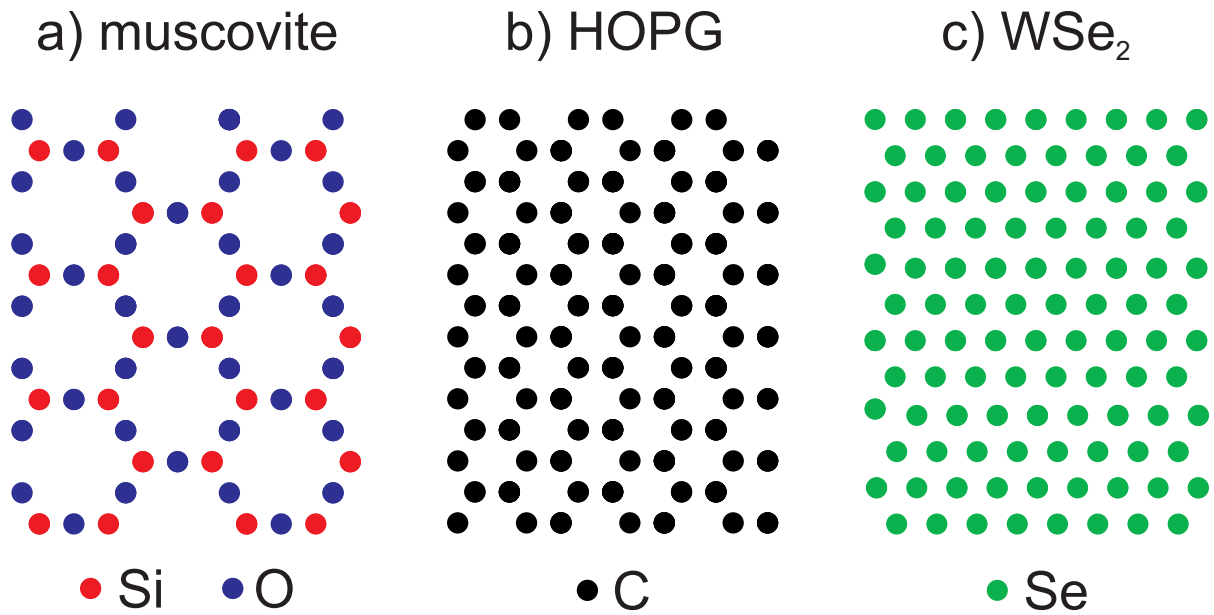


Figure 3.10: Cutting of 12-ABG-4EO-PMA on mica, the white arrows indicate the manipulation steps:  $z\text{-move} = 7 \text{ nm}$ ,  $v = 10 \text{ nm/s}$

Table 3.1: Crystallographic data of mica (muscovite), graphite (HOPG) and tungsten selenide  $\text{WSe}_2$ 

	<b>muscovite</b> [31]	<b>HOPG</b> [31]	<b>tungsten selenide</b> [29]
<b>formula</b>	$\text{KAl}_2(\text{OH})_2[\text{AlSi}_3\text{O}_{10}]$	C	$\text{WSe}_2$
<b>crystal system</b>	monoclinic	hexagonal	hexagonal
<b>space group</b>	C2/c	C6/mmc	P6 <sub>3</sub> /mmc
<b>Z</b>	4	4	4
<b>a</b>	520 pm	246 pm	329 pm
<b>b</b>	900 pm		
<b>c</b>	200 pm	671 pm	1298 pm
<b><math>\beta</math></b>	94.5°		

Figure 3.11: Structure of the topmost layer of a) muscovite mica, Si–O: 150 pm O–O: 260 pm, the silicon atoms lay deeper than the oxygen atoms b) HOPG, C–C: 142 pm c)  $\text{WSe}_2$ , Se–Se: 190 pm

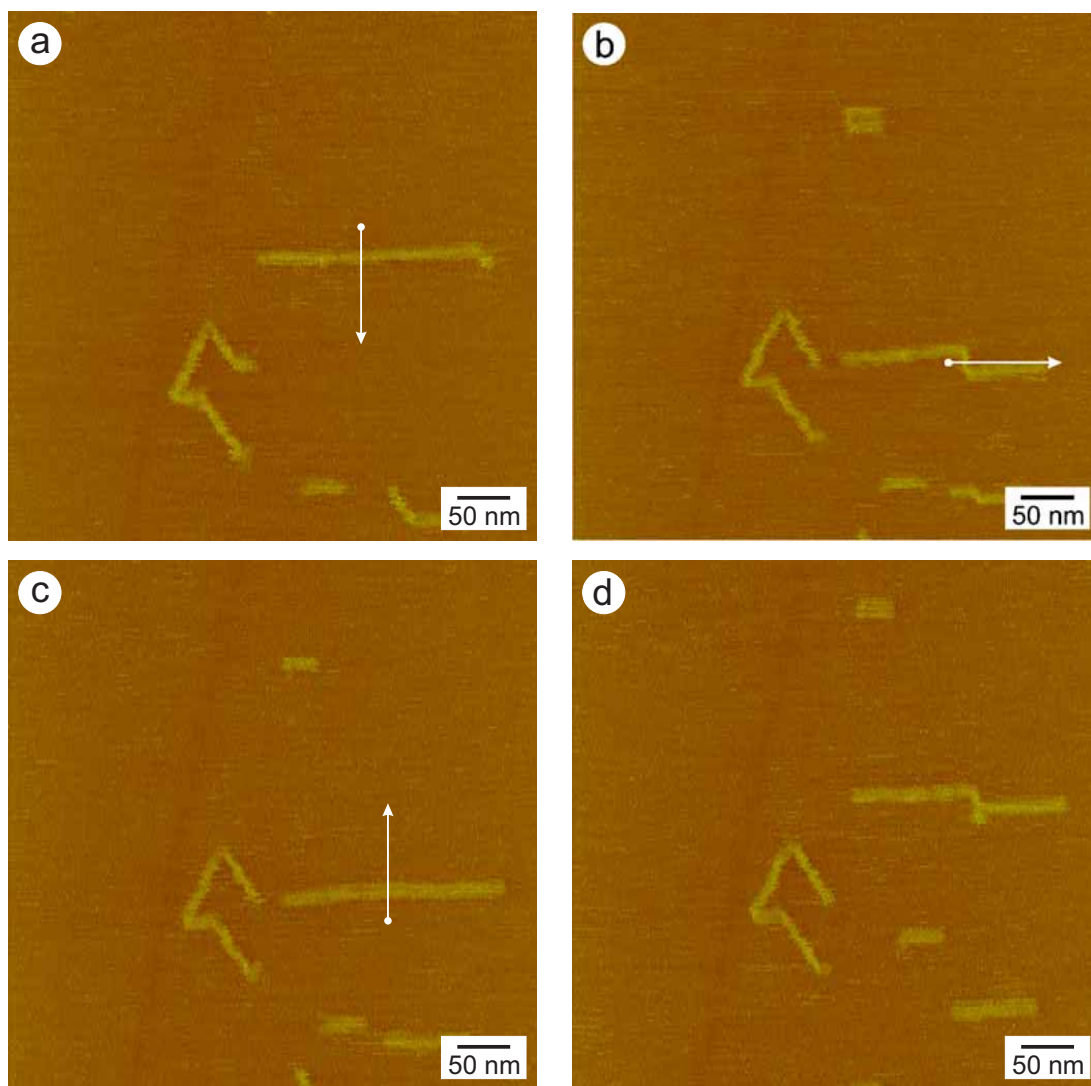


Figure 3.12: Nanomanipulation of 12-ABG-4EO-PMA on  $WSe_2$ , the white arrows indicate the manipulation steps:  $z\text{-move} = 5\text{ nm}$ ,  $v = 10\text{ nm/s}$

### 3.3.3 Thermal equilibration

The manipulation technique described in the previous section allowed to change the initial conformation of the polymer after the spin-coating procedure into a completely stretched conformation (Figure 3.13a). For this a series of ca. 50 single manipulation steps was necessary. In the same way molecules nearby have been moved further apart in order to have a free area of at least 1  $\mu\text{m}$  in each direction. The completely stretched conformation of the macromolecule is expected to be meta-stable and should relax to an entropically more favored structure. Thermal energy is supposed to deliver the activation energy for the system to undergo the transformation. Heating up the sample in steps up to 45 °C led to high mobility of the polymer chain (Figure 3.13b-d). This is visible in the images by the different cutouts in which the substrate underneath has different defect structures. Increasing the temperature from room temperature to 45 °C does not change the fashion of motion, only the speed. Because of the comparable slow SFM imaging process (scanning rate 1 Hz, 256 lines) the molecule or parts of the molecule are changing their location during scanning and the molecule looks distorted. But it can still be seen that the polymer chain stayed in a mainly elongated conformation. It bent a little and formed some kinks, but it never adopted a condensed state. When the molecule hit a group of already assembled molecules, exhibiting only very slow diffusion (figure 5e), it got trapped and started to fold (Figure 3.13f). The arrangement of the polymer segments in accordance to the three directions of the hexagonal crystal lattice of the graphite can be nicely seen. In the final state the molecules showed two kinks with 120° and a hairpin fold.

In the next experiment the starting point of a completely stretched molecule (figure 6a) was prepared in the same way as before. This experiment differs from the previous in two ways:

1. The sample was heated to a certain temperature and when some conformational change was indicated the sample was cooled down to room temperature in order to freeze the actual state and increase the quality of the imaging procedure.
2. The molecule lays across a smaller step of the HOPG which served as a support of the molecule and inhibited the polymer from leaving its position.

In the initial stage the sample was heated up in steps to 45 °C and the molecule formed kinks with angles of 120° (Figure 3.14b-c). These kinks were not stable and could be released and formed on a new site. Higher temperatures of about 50 °C have been necessary that the molecule started to form hairpin folds which resulted in parallel alignment of segments of the polymer (d-f). Once these hairpin folds have been formed they have never been released. Bending to the 180° angle in the hairpin folds itself is energetically not favored and explains why the molecule initially is not forming these strong bends. But if the thermal motion of the segments is high enough that the hairpin folds are formed this structure is stabilized by the enthalpy gain of the parallel segments coming along with the reduced line tension.

## 3.4 Conclusions

12-ABG-4EO-PMA, a polymer with dense packed mini-dendritic side groups and therefore with defined cylindrical shape could be easily visualized by tapping mode scanning force microscopy on different substrates as mica, HOPG and tungsten selenide.

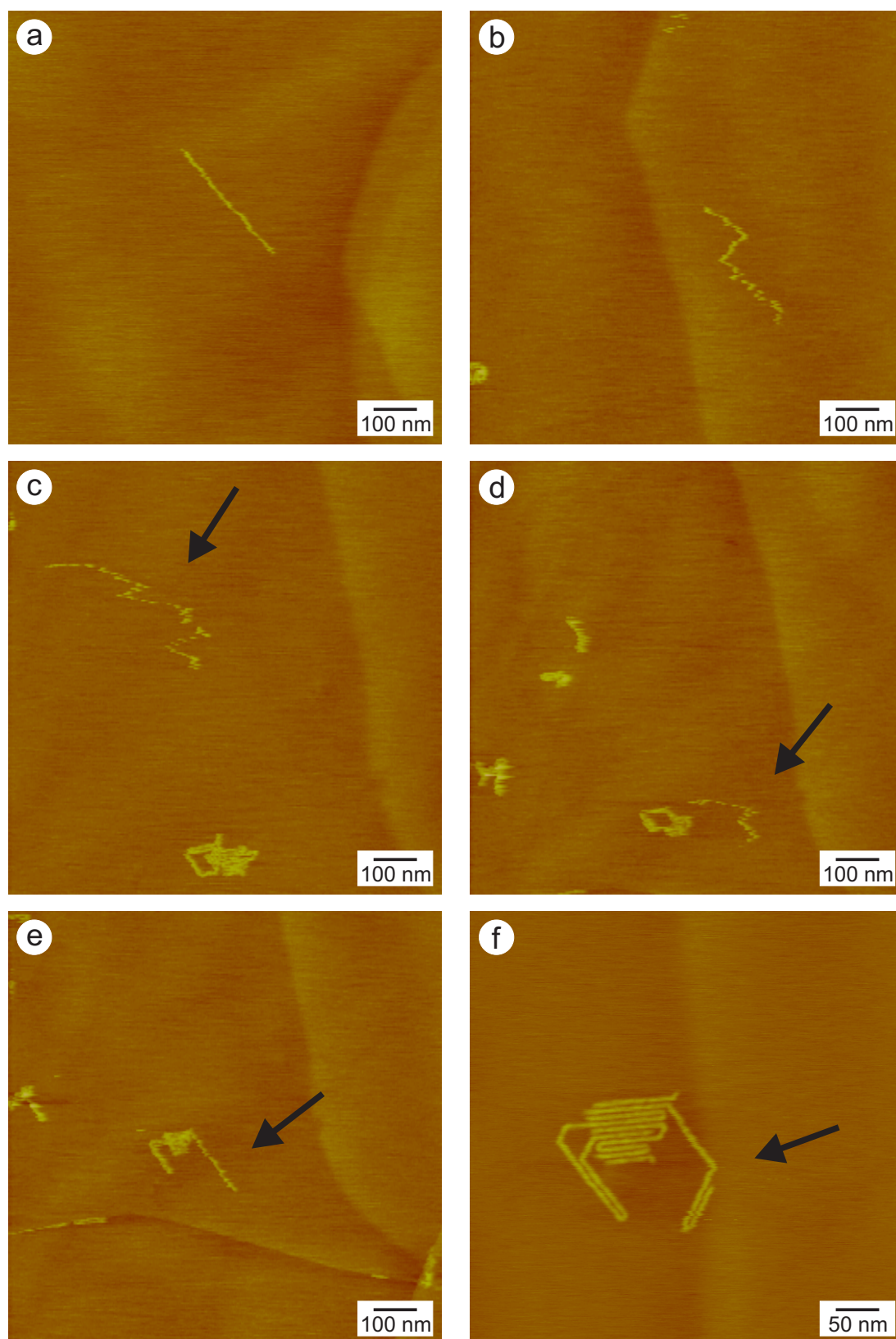


Figure 3.13: Thermal equilibration of 12-ABG-4EO-PMA on HOPG. a) initial state b–d) thermal motion of the molecule at 45 °C. The molecule looked distorted and formed kinks but did not fold. e) fusion with a large aggregate f) final state with hairpin fold



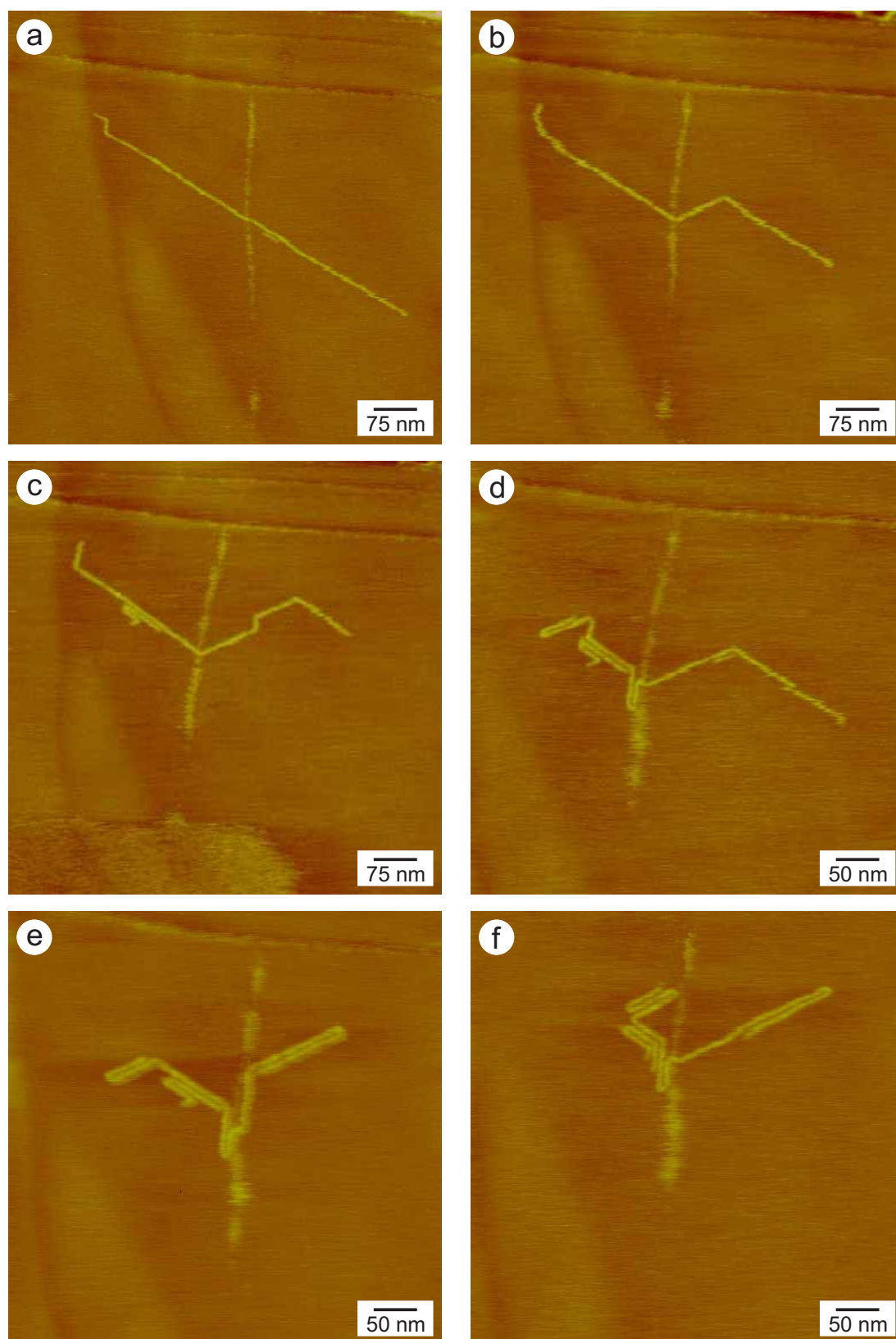


Figure 3.14: Thermal equilibration of 12-ABG-4EO-PMA on HOPG (heating and cooling).  
a) initial state b–c) formation of kinks at 45°C d–f) folding at 50°C

The polymer molecules adsorb on mica in a random worm-like conformation. The polymer molecules adsorb on HOPG and WSe<sub>2</sub> epitaxially with straight segments oriented according to the three preferential directions of the hexagonal surface layer and bending angles of 60° and 120°. The top layers of HOPG and WSe<sub>2</sub> are flat and the inter-atom distance of the crystal lattice matches fairly good the C–C distance of the outer alkyl-chains of the polymer. In the case of mica the Si–O distance of the surface layer matches the C–C distance, but the surface is not flat: the Si atoms lay deeper than the O atoms. This seems to impede the epitaxial crystallization.

Nanomanipulation performed on all three substrates showed that in the case of HOPG and WSe<sub>2</sub> the displacement of molecules was possible. On mica all manipulations led either to no effect or the cutting of polymer molecules in several pieces. From these experiments the adhesion of the polymers on the substrate could be judged: The molecules adsorb weakest on HOPG, stronger on WSe<sub>2</sub> and orders of magnitude stronger on mica.

The same results could be gained by in situ annealing SFM experiments. The molecules showed on HOPG already at 40 °C quite high mobility. On WSe<sub>2</sub> a temperature 10–20 K higher was necessary to reach the same mobility. The results after annealing are bigger aggregates of molecules with increased order, longer straight segments and a decrease in 60° angles. On mica heating up to 250 °C did not result in any displacement of the molecules, instead thermal decomposition started.

The method of nanomanipulation was also used successfully to study the initial folding process of polymer chains. Here an artificially starting situation of a completely straight molecule of 12-ABG-4EO-PMA on HOPG was created. Heating of the sample was chosen as the energetic supply to undergo the transition from straight to an entropically more favored conformation. Heating to 45 °C led to high mobility of the polymer chain and the formation of 120° kinks, which could be released and formed again on new sites. Slightly higher temperatures of ca. 50 °C have been necessary for the formation of hairpin folds with 180° angle. Here the attraction of the two parallel aligned chain segments was so strong that under these conditions the hairpin fold was never released.

# Bibliography

- [1] S. Kasas, N. H. Thomson, B. L. Smith, H. G. Hansma, X. Zhu, M. Guthold, C. Bustamante, E. T. Kool, M. Kashlev, and P. K. Hansma. Escherichia coli RNA polymerase activity observed using atomic force microscopy. *Biochemistry*, 36:461–468, 1997.
- [2] W. Fritzsche and E. Henderson. Chicken erythrocyte nucleosomes have a defined orientation along the linker DNA – a scanning force microscopy study. *Scanning*, 19: 42–47, 1997.
- [3] H. Maeda. An atomic force microscopy study for the assembly structures of tobacco mosaic virus and their size evaluation. *Langmuir*, 13:4150–4161, 1997.
- [4] S. S. Sheiko, M. Gauthier, and M. Möller. Monomolecular films of arborescent graft polystyrenes. *Macromolecules*, 30:2343–2349, 1997.
- [5] S. S. Sheiko, M. Gerle, K. Fischer, M. Schmidt, and M. Möller. Wormlike polystyrene brushes in thin films. *Langmuir*, 13:5368–5372, 1997.
- [6] V. Percec, C.-H. Ahn, G. Ungar, D. J. P. Yearley, M. Möller, and S. S. Sheiko. Controlling polymer shape through the self-assembly of dendritic side-groups. *Nature*, 391:161–164, 1998.
- [7] B. Karakaya, W. Claussen, K. Gessler, W. Saenger, and A.-D. Schlüter. Toward dendrimers with cylindrical shape in solution. *J. Am. Chem. Soc.*, 119:3296–3301, 1997.
- [8] J. Kumaki, Y. Nishikawa, and T. Hashimoto. Visualization of single-chain conformation of a synthetic polymer with AFM. *J. Am. Chem. Soc.*, 118:3321–3322, 1996.
- [9] S. Hong and C. A. Mirkin. A nanoplotter with both parallel and serial writing capabilities. *Science*, 288:1808–1811, 2000.
- [10] S. Hong, J. Zhu, and C. A. Mirkin. Multiple ink nanolithography: Toward a multipen nano-plotter. *Science*, 286:523–525, 1999.
- [11] R. D. Piner, J. Zhu, F. Xu, S. Hong, and C. A. Mirkin. Dip-pen nanolithography. *Science*, 283:661–663, 1999.
- [12] M. R. Falvo, R. M. Taylor II, A. Helsen, V. Chi, F. P. Brooks Jr., S. Washburn, and R. Superfine. Nanometre-scale rolling and sliding of carbon nanotubes. *Nature*, 397: 236–238, 1999.
- [13] M. R. Falvo, G. Clary, A. Helsen, S. Paulson, R. M. Taylor II, V. Chi, F. P. Brooks Jr., S. Washburn, and R. Superfine. Nanomanipulation experiments exploring frictional and mechanical properties of carbon nanotubes. *Microsc. Microanal.*, 4:504–512, 1999.

- [14] M. R. Falvo and R. Superfine. Mechanics and friction at the nanometer scale. *J. Nanoparticle Res.*, 1:237–248, 2000.
- [15] L. Shu, A. D. Schlüter, C. Ecker, N. Severin, and J. P. Rabe. Extremely long dendronized polymers: Synthesis, quantification of structure perfection, individualization, and SFM manipulation. *Angew. Chem.*, 113:4802–4805, 2001.
- [16] S. J. Organ, G. Ungar, and A. Keller. Rate minimum in solution crystallization of long paraffins. *Macromolecules*, 22:1995–2000, 1989.
- [17] S. J. Organ and A. Keller. The onset of chain folding in ultralong *n*-alkanes: An electron microscopy study of solution-grown crystals. *J. Polym. Sci. B: Polym. Phys.*, 25:2409–2430, 1987.
- [18] J. S. Moore and S. I. Stupp. Room temperature polyesterification. *Macromolecules*, 23:65–70, 1990.
- [19] V. Percec, D. Schlueter, Y. K. Kwon, J. Blackwell, M. Möller, and P. J. Slangen. Dramatic stabilization of a hexagonal columnar mesophase generated from supramolecular and macromolecular columns by the semifluorination of the alkyl groups of their tapered building blocks. *Macromolecules*, 28:8807–8818, 1995.
- [20] V. Percec, J. Heck, D. Tomazos, F. Falkenberg, H. Blackwell, and G. Ungar. Self-assembly of taper-shaped monoesters of oligo(ethylene oxide) with 3,4,5-tris(*p*-dodecyloxybenzyloxy)benzoic acid and of their polymethacrylates into tubular supramolecular architectures displaying a columnar mesophase. *J. Chem. Soc. Perkin Trans. 1*, pages 2799–2811, 1993.
- [21] V. Percec, D. Schlueter, G. Ungar, S. Z. D. Cheng, and A. Zhang. Hierarchical control of internal superstructure, diameter, and stability of supramolecular and macromolecular columns generated from tapered monodendritic building blocks. *Macromolecules*, 31:1745–1762, 1998.
- [22] V. Percec, C.-H. Ahn, and B. Barboiu. Self-encapsulation, acceleration and control in the radical polymerization of monodendritic monomers via self-assembly. *J. Am. Chem. Soc.*, 119:12978–12979, 1997.
- [23] J. P. Rabe and S. Buchholz. Direct observation of molecular structure and dynamics at the interface between a solid wall and an organic solution by scanning tunneling microscopy. *Phys. Rev. Lett.*, 66:2096–2099, 1991.
- [24] A. Wawkuschewski, H.-J. Cantow, S. N. Magonov, M. Möller, W. Liang, and M.-H. Whangbo. A scanning tunneling microscopy study of cyclooctatetracontane,  $(\text{CH}_2)_{48}$ , and cyclodoheptacontane,  $(\text{CH}_2)_{72}$ , adsorbed on graphite. *Adv. Mater.*, 5:821–826, 1993.
- [25] P. Samori, F. Jäckel, Ö. Ünsal, A. Godt, and J. P. Rabe. Ordered nanostructures of a [2]catenane through self-assembly at surfaces - an STM study with sub-molecular resolution. *Chemphyschem*, 7:461–464, 2001.
- [26] P. Samori, N. Severin, K. Müllen, and J. P. Rabe. Macromolecular fractionation of rod-like polymers at atomically flat solid-liquid interfaces. *Adv. Mater.*, 12:579–582, 2000.

- [27] P. Bäuerle, T. Fischer, B. Bidlingmeier, A. Stabel, and J. P. Rabe. Oligothiophene – immer länger? Synthese, Charakterisierung und rastertunnelmikroskopische Abbildung von homologen isomerenreinen Oligo(alkylthiophenen). *Angew. Chem.*, 107: 335–339, 1995.
- [28] E. Mena-Osteritz, A. Meyer, B. M. W. Langeveld-Voss, R. A. J. Janssen, E. W. Meijer, and P. Bäuerle. Two-dimensional crystals of poly(3-alkylthiophene)s: Direct visualization of polymer folds in submolecular resolution. *Angew. Chem.*, 112:2791–2796, 2000.
- [29] T. Löher, Y. Tomm, A. Klein, D. Su, and C. Pettenkofer. Highly oriented layers of the three-dimensional semiconductor CdTe on the two-dimensional layered semiconductors MoTe<sub>2</sub> and WSe<sub>2</sub>. *J. Appl. Phys.*, 80:5718–5722, 1996.
- [30] T. Löher, Y. Tomm, C. Pettenkofer, A. Klein, and W. Jaegermann. Structural dipoles at interfaces between polar II-VI semiconductors CdS and CdTe and non-polar layered transition metal dichalcogenide semiconductors MoTe<sub>2</sub> and WSe<sub>2</sub>. *Semicond. Sci. Technol.*, 15:1–9, 2000.
- [31] D. R. Lide, editor. *CRC Handbook of Chemistry and Physics*. CRC press, Boston, 72<sup>nd</sup>, special student edition, 1991–1992.

## *Bibliography*

# 4 Stimulated motion of monodendron jacketed polymers on HOPG

## 4.1 Introduction

The most common and best known transport phenomena occur in systems where macroscopic driving forces exist. These are typically external fields or concentration gradients. In contrast are random-walk motion processes like Brownian motion and self-diffusion. These processes were studied for a broad variety of particles because of experimental reasons mostly in 2-D systems. Starting from metal atoms and clusters of atoms [1–3], nanocrystals [4, 5] over large organic molecules [6] and fullerenes [7], ending up with DNA-molecules on fluid layers [8, 9]. Even complicated 2-D arrays have been created to study the Brownian motion of DNA in confined media [10].

Recently there has been considerable interest in various transport processes, often referred to as fluctuation driven transport, that take place in systems with no macroscopic driving forces [11–17]. These processes seem to be essential for the operation of molecular combustion motors that are responsible for many kinds of biological motion like cellular transport or muscle contraction.

In the case of biological motion complex protein molecules as kinesin or myosin undergo directed movement along cytoskeletal filaments based on conformational changes inducing adsorption and detachment of molecular fragments on the filament surface [18–21]. The movement is a collective process of many proteins performing a cycle of elementary steps driven by ATP hydrolysis. The steps take place stochastically and some can even be directed backwards [22–24].

Here the stimulated motion of monodendron jacketed linear chains on HOPG is presented. The stimuli are the temperature and the mechanical influence of the scanning tip.

## 4.2 Experimental

### 4.2.1 Materials

THF (Uvasolv, 99,9%) from Merck was used as received. Freshly cleaved highly ordered pyrolytic graphite (HOPG) from Plano was chosen as substrate for the SFM experiments.

### 4.2.2 Methods

Scanning force microscopy (SFM) was performed using a Digital Instruments Multimode scanning force microscope equipped with a Nanoscope IIIa controller. Imaging was done in tapping mode using standard silicon cantilevers: Nanoworld Pointprobe NCH ( $k = 42 \text{ N/m}$ ,  $f_0 = 330 \text{ kHz}$ ).

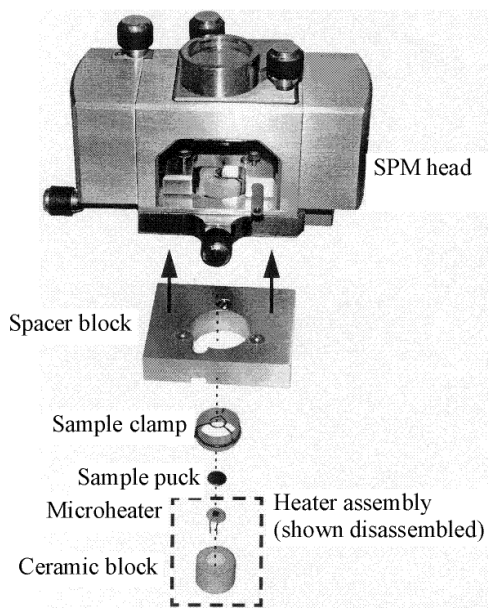


Figure 4.1: Heating accessory for multimode scanning force microscope

Samples for the SFM experiments were prepared by spin casting of a dilute tetrahydrofuran (THF) solution with a concentration of 0.05 mg/ml. The spin coating was done at room temperature at 2000 rpm on HOPG as a substrate. The heating experiment was performed on-line during the scan using a specially designed heating cell (Digital Instruments) (Figure 4.1).

### 4.3 Results and discussion

Two series of SFM experiments are discussed here. The first series show the motion at 30 °C, 35 °C and 40 °C. The second series shows another experiment that was conducted at 40 °C, 45 °C and 48 °C. In the appendix (Chapter 4.5) a full presentation of the two series is given in Figures 4.13–4.18 and Figures 4.19–4.24, together with the corresponding center of mass traces.

These experiments can be followed in much more detail in the movies, which are either included in the PDF-version of this document or are supplied as supporting material. The file names of the movies are: *Movie1C30.avi*, *Movie1C35.avi*, *Movie1C40.avi*, *Movie2C40.avi*, *Movie2C45.avi*, and *Movie2C48.avi*.

Figure 4.2 shows six snapshots from a series of 105 images showing the general appearance of the diffusion like motion of 12-ABG-4EO-PMA on HOPG at 45 °C. The invariance of the defects in the graphite assures that always the same area was observed and allows to follow the movement of clusters of aggregated molecules. In Figure 4.4 the corresponding center of mass traces of most of the clusters are displayed. The figures 4.3 and 4.5 show the center of mass traces of the same experiment performed at 40 °C and 48 °C.

There are three main observations found from these Movies:

1. Small molecules or cluster of molecules move faster than bigger ones.



2. Increasing the temperature increases the velocity of an individual cluster.
3. Molecules that meet each other usually stick together and move further as one bigger cluster.
4. Molecules hitting a defect, e. g. a step in the graphite, stick to it and either quit moving or start doing guided 1-D linear diffusion.

These characteristics have several consequences for the experiment. At the beginning of the experiment the surface was covered with single molecules or small clusters. Their fast diffusion increases the chances dramatically to encounter another cluster or an defect in the graphite. By this the molecule gets either trapped by the defect or slowed down by joining another cluster. All over this leads to a slowed down dynamics at constant temperature. Increasing the temperature increases the velocity of the clusters and again fast diffusion can be observed. Therefore at low temperatures the diffusion of small clusters is observed whereas at higher temperatures the cluster size increases progressively. Only a few medium sized clusters which by chance did not come in contact with others could be evaluated over longer periods.

The observed motion of the molecules and clusters resembles very much the random walks of particles undergoing 2-dimensional Brownian motion. Diffusion coefficients have been calculated for each cluster (Table 4.1 and 4.2) using the Formula of Einstein and Smoluchowski:

$$\overline{x^2} = nDt \tag{4.1}$$

$\overline{x^2}$  = average squared distance from origin,

$n$  = Dimension, here surface motion  $\Rightarrow n = 2$ ,

$D$  = diffusion coefficient,

$t$  = time

4 Stimulated motion of monodendron jacketed polymers on HOPG

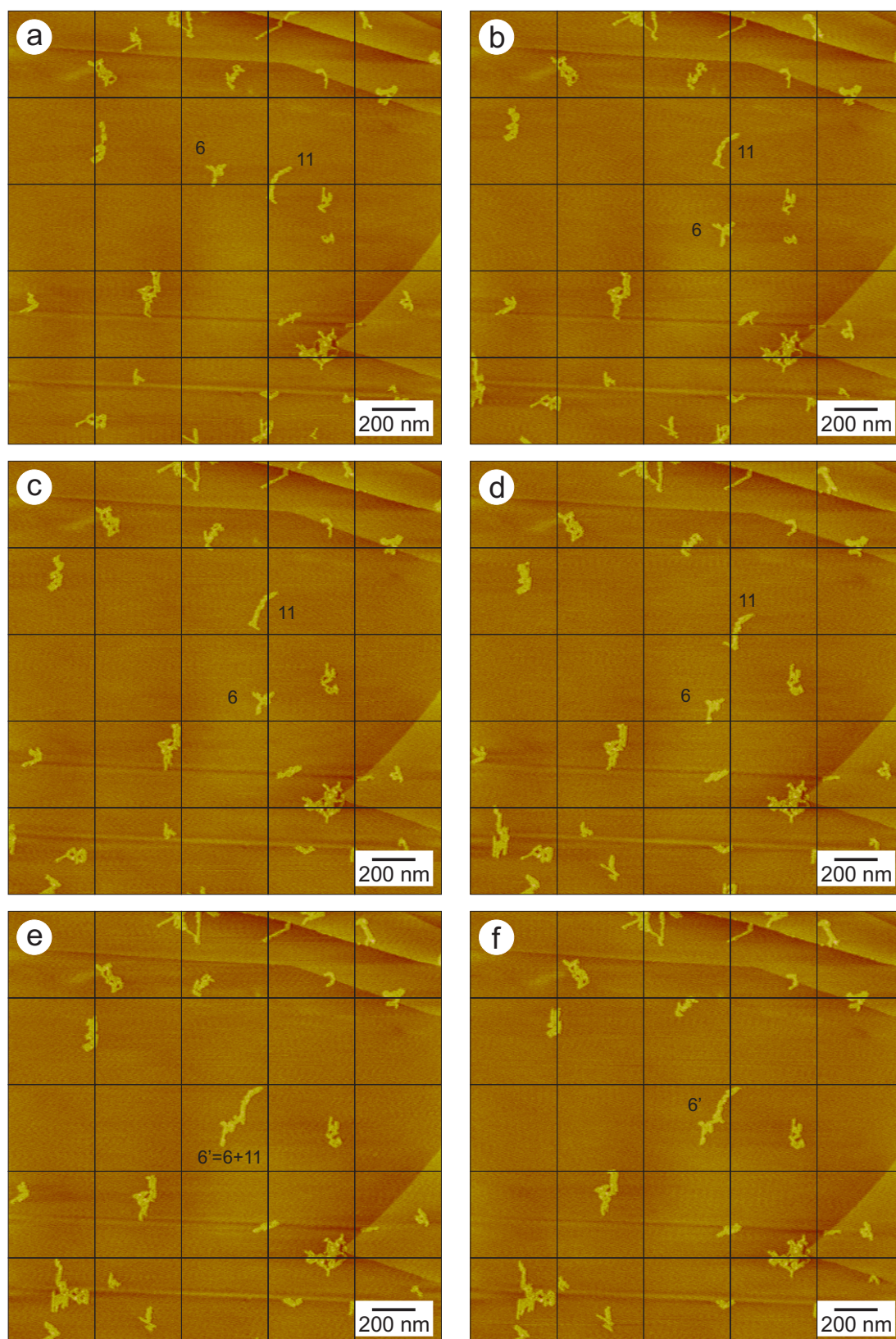


Figure 4.2: Six snapshots out of a series of 105 images (recorded in 420 min) of the diffusion like motion of 12-ABG-4EO-PMA on HOPG at 45 °C. The snapshots show the situation after a) 0 b) 80 c) 160 d) 240 e) 320 f) 400 min

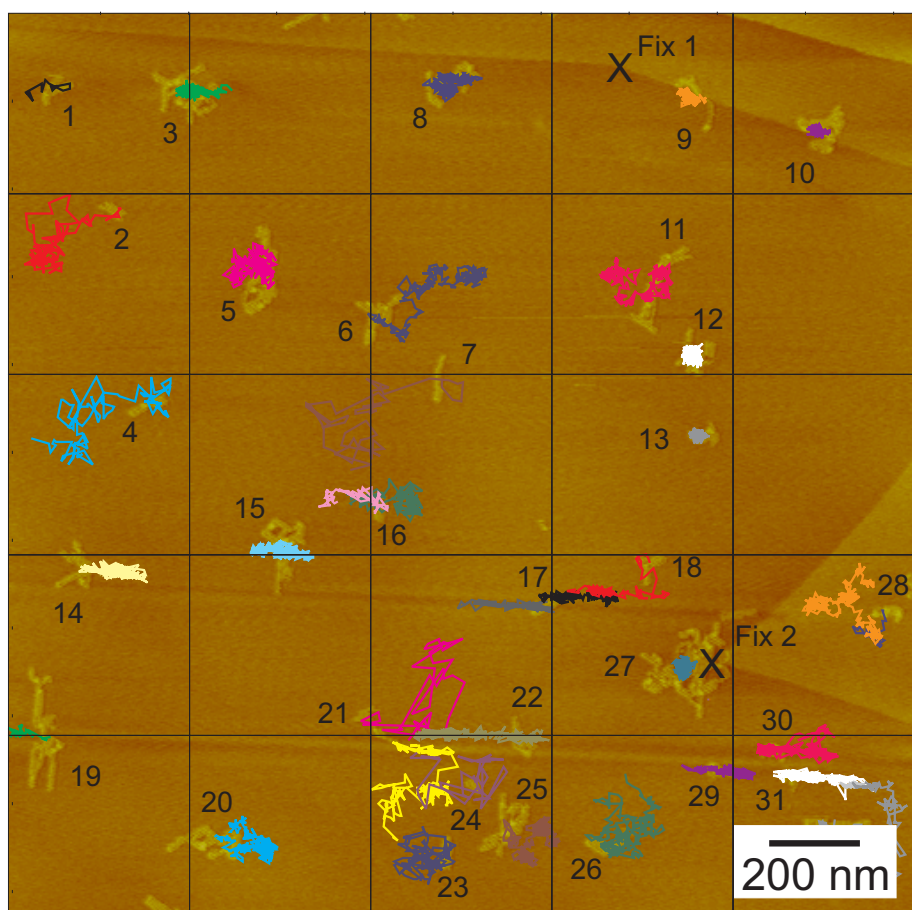


Figure 4.3: Center of mass traces of clusters of 12-ABG-4EO-PMA on HOPG at 40 °C

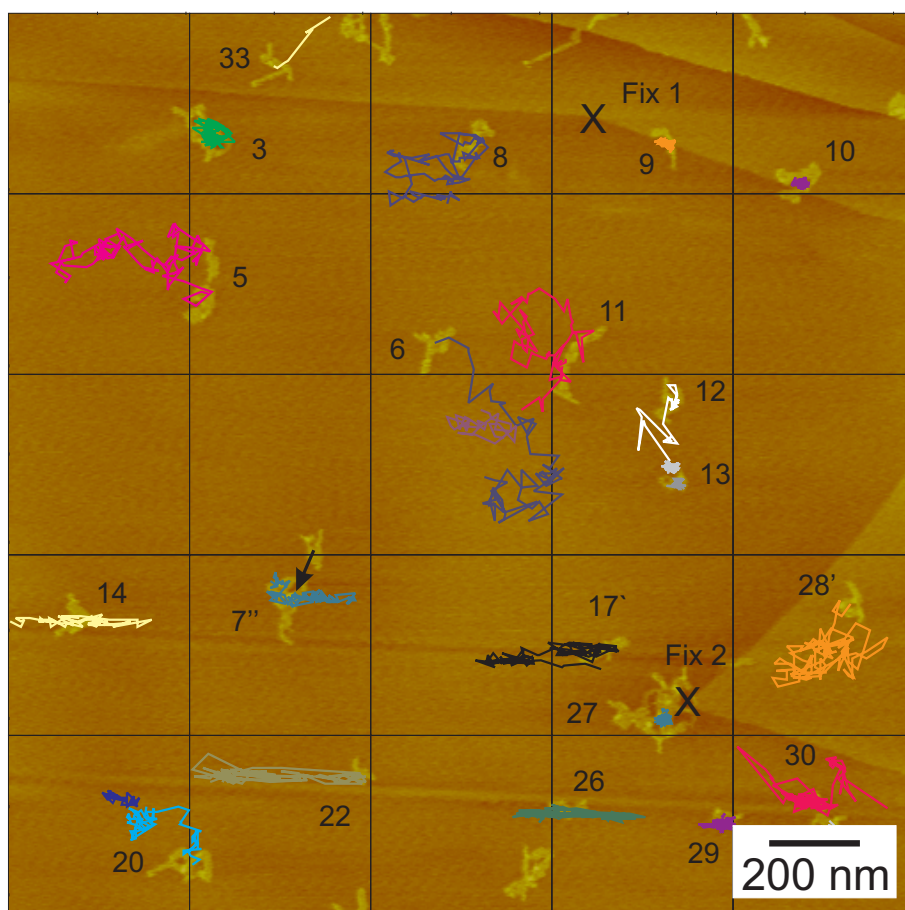


Figure 4.4: Center of mass traces of clusters of 12-ABG-4EO-PMA on HOPG at 45 °C

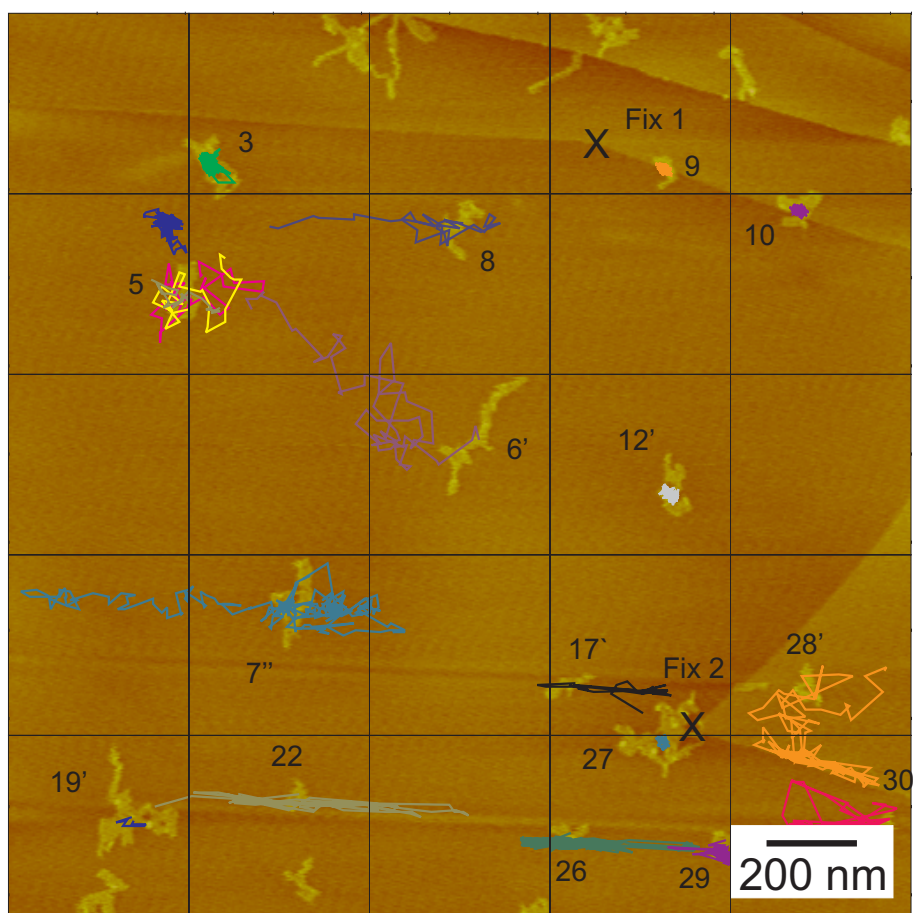


Figure 4.5: Center of mass traces of clusters of 12-ABG-4EO-PMA on HOPG at 48 °C

Table 4.1: Diffusion Coefficient of 12-ABG-4EO-PMA in  $\text{nm}^2/\text{s}$  at 30–40 °C

molecule no.	mass [kg/mol]	30 °C	35 °C	40 °C
1	1010	0,28	–	–
1'=1+2	1850	0,06	0,09	–
1''=1'+3'	3190	–	–	0,51
2	910	0,30	–	–
3	870	0,06	–	–
3'=3+4	1440	0,04	0,09	–
4	530	0,38	–	–
5	480	1,33	–	–
6	3970	0,03	0,04	0,37
7	1860	0,05	0,08	0,55
8	920	0,04	–	–
8'=fraction of 8	490	–	2,10	–
8''=8'+11	1260	–	0,08	–
9	530	0,09	–	–
10	4150	0,02	0,03	0,34
11	1080	0,05	0,12	2,62
12	690	0,49	–	–
12'=12+fraction of 8	1060	–	0,12	1,24
13	1130	0,15	0,34	–
14	510	0,29	–	–
14'=14+15	940	0,02	0,38	–
15	560	0,25	–	–
16	670	0,27	–	–
16'=16+17	1210	0,05	0,38	0,67
17	600	0,39	–	–
18	1090	0,16	–	–
18'=18+19'	3560	–	0,05	0,54
19	560	0,11	–	–
19'=19+20	2420	0,05	–	–
20	2070	0,03	–	–
21	770	0,30	–	–
21'=21+22	1230	0,16	–	–
22	430	4,08	–	–
23	2770	0,02	–	–
23'=23+24	3990	–	0,02	0,17
24	790	0,05	–	–
25	1420	0,06	0,16	1,60
26	1460	0,09	–	–
26'=26+42	1930	0,05	0,16	–
26''=26'+28	2830	–	–	0,19
27	1060	0,03	0,13	0,20

Diffusion Coefficient of 12-ABG-4EO-PMA in nm<sup>2</sup>/s at 30–40 °C (continued)

molecule no.	mass [kg/mol]	30 °C	35 °C	40 °C
28	1150	0,02	0,07	–
29	1190	0,09	–	–
29'=29+30	2730	0,03	0,07	0,40
29''=29'+32	3220	–	0,05	–
30	1520	0,06	–	–
31	3110	0,03	0,02	0,22
32	600	0,14	0,45	–
33	3270	0,02	0,05	0,22
34	1200	0,20	0,43	–
34'=34+47	2220	–	0,36	–
34''=34'+50	2640	–	0,05	0,29
35	460	1,94	–	–
35'=35+new	5190	–	0,06	–
36	1550	0,03	0,10	–
36'=36+37	2320	–	0,06	0,34
37	930	0,87	2,22	–
38	880	0,06	0,20	–
38'=38+39	2610	–	0,05	–
38''=38'+41'	3900	–	0,02	0,05
39	1890	0,02	0,04	–
40	1800	0,02	0,08	0,25
41	550	0,52	–	–
41'=41+43	1280	0,06	0,07	–
42	410	1,05	–	–
43	1110	0,05	–	–
44	510	0,81	–	–
44'=44+45	2250	0,02	0,04	0,36
45	1680	0,02	–	–
46	1380	0,01	0,13	2,48
47	1140	0,06	0,69	–
48	630	0,03	0,13	2,80
49	2520	–	0,09	–
49'=fraction of 49	1640	–	–	0,33
50	790	–	1,35	–

Table 4.2: Diffusion Coefficient of 12-ABG-4EO-PMA in nm<sup>2</sup>/s at 40–48 °C

molecule no.	mass [kg/mol]	40 °C	45 °C	48 °C
1	1460	0,45	–	–
2	1000	0,41	–	–
3	4750	0,05	0,14	0,09

4 Stimulated motion of monodendron jacketed polymers on HOPG

Diffusion Coefficient of 12-ABG-4EO-PMA in nm<sup>2</sup>/s at 40–48 °C (continued)

molecule no.	mass [kg/mol]	40 °C	45 °C	48 °C
3'=3+5''	18170	–	–	0,13
4	1340	0,40	–	–
5	4510	0,09	0,82	1,10
5'=5+8	7330	–	–	0,95
5''=5'+6'	14680	–	–	0,35
6	2940	0,11	1,24	–
6'=6+11	6880	–	0,38	3,02
7	960	0,90	–	–
7'=7+16	1880	0,14	–	–
7''=7'+15	5950	–	0,21	0,83
8	3040	0,08	0,81	2,41
9	2020	0,03	0,02	0,02
10	2940	0,03	0,03	0,02
11	3760	0,07	0,72	–
12	2420	0,04	0,51	–
12'=12+13	3580	–	0,03	0,03
13	1210	0,03	0,03	–
14	2280	0,09	0,69	–
15	4390	0,08	–	–
16	1160	0,15	–	–
17	870	0,32	–	–
17'=17+18	1950	0,11	0,88	1,06
18	1450	0,21	–	–
19	4900	0,16	–	–
19'=19+20	9540	–	0,12	0,14
20	3370	0,08	0,40	–
21	1040	1,44	–	–
21'=21+24	1300	0,46	–	–
22	1400	0,12	1,27	10,06
23	1030	0,36	–	–
24	510	0,72	–	–
25	3760	0,09	–	–
26	1320	0,20	1,50	1,77
27	10130	0,04	0,03	0,04
28	870	0,41	–	–
28'=28+new	1890	0,09	0,84	1,06
29	1290	0,09	0,08	0,07
30	620	0,16	0,50	1,94
31	580	0,16	–	–
31'=31+32	1800	0,09	0,17	0,21
32	1410	0,36	–	–
33	1770	–	3,69	–



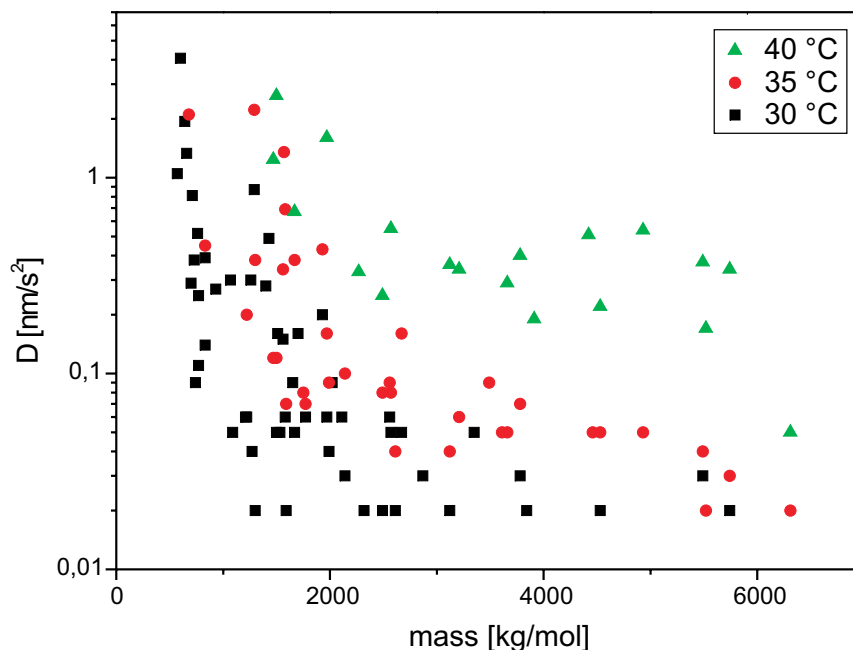


Figure 4.6: Plot of logarithm diffusion coefficient over the mass of the clusters for experiment series 1 at 30, 35 and 40 °C

Another remarkable fact is the high shape persistence of the molecules and clusters. Even after aggregation of two molecules or clusters together a stable configuration is found within several scanned images (minutes) and can then be retained for hours. Taking for example clusters 6 and 11 in Figure 4.2: both clusters diffused on the surface for over 240 minutes and could easily be identified by their characteristic shape (Figure 4.2a–d). Then both clusters met and formed a new larger cluster named 6' with its own characteristic shape (Figure 4.2e–f). The cluster 6' diffused then without significant changes till the end of the experiment when it joined cluster 5'. Additionally the dynamics can be easily followed: For cluster 6 and 11 the diffusion coefficients are 0.11 and 0.07 nm<sup>2</sup>/s at 40 °C (Table 4.2). Increasing the temperature to 45 °C enhances the diffusion, the diffusion coefficients are 1.24 and 0.72 nm<sup>2</sup>/s. Forming a larger cluster the diffusion of 6' is slowed down to 0.38 nm<sup>2</sup>/s. When the temperature was raised to 48 °C the diffusion increases again significantly to 3.02 nm<sup>2</sup>/s and fell down to 0.35 nm<sup>2</sup>/s when it aggregated with cluster 5'.

The mass of the molecules or aggregates was calculated from the volume, determined from the SFM-images, by assuming a density of 1 g/cm<sup>3</sup>. In Figure 4.6 the diffusion coefficient of the molecules or aggregates is shown for the first series of experiments from 30 °C to 40 °C. The same plot for the second series of experiments from 40 °C to 48 °C is shown in 4.7.

The qualitative observations concerning the velocity is confirmed quantitatively. At each studied temperature the diffusion coefficient is decreasing with increasing molecular weight. The lower the temperature is the more pronounced is this observation. At 30 °C only the very smallest molecules are able to undergo motion whereas for bigger aggregates the diffusion decreases virtually to zero.

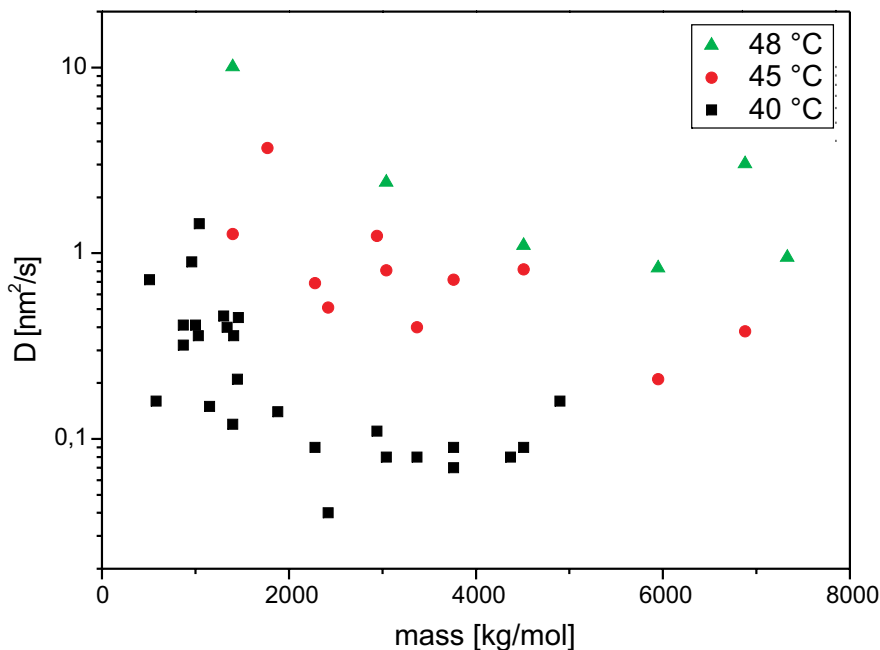


Figure 4.7: Plot of logarithm diffusion coefficient over the mass of the clusters for experiment series 2 at 40, 45 and 48 °C

Also the overall diffusion for aggregates of comparable size increases with temperature in each series, although there is a notable variance of diffusion coefficients. Many data points which have been present in the graphs at low temperature disappear because of aggregation of the clusters. Therefore the new aggregated clusters could be observed at higher temperatures doing slower diffusion, resulting in new marks in the graphs.

Comparing the two series of experiments it is obvious that the diffusion is slower in the second series. Taking the values at 40 °C that was studied in both series the diffusion coefficients calculated from the first series for molecules with masses larger than 2000 kg/mol are in the range of 0.2–0.5 nm<sup>2</sup>/s. In contrast the diffusion coefficients from the second series at the same temperature are about 0.1 nm<sup>2</sup>/s. From this it is obvious that besides the size of the clusters and the temperature there is another variable that influences dramatically the diffusion rate. The less controlled parameters in the system are the scanning tip and the scanning conditions. Each tip has its own characteristic dimensions, spring constant and resonance frequency. Depending on that and the adjusted scanning parameters the forces acting on the sample are changing. It was shown that the tip is able to move single molecules on the surface in Chapter 3. The conditions used for imaging are far from the forces acting in the case of manipulating the molecules but nevertheless the tapping tip transfers energy to the polymer clusters supporting the positional change and therefore the diffusion of the clusters. The forces acting on the molecules in the first series of experiments must have been stronger compared to the second series explaining the different diffusion velocities at 40 °C.

The influence of the tip in imaging conditions never showed an influence on the direction of diffusion. In Figure 4.8 the scanning direction of the tip was rotated by 90°. Figure 4.8a shows the starting position and in Figure 4.8b the center of mass traces of the clusters

are shown. Cluster 1 undergoes a diffusion that mainly lays in the left-right orientation. For cluster 2 no preferred direction could be observed. Figure 4.8c shows the position of the clusters when the scanning direction was rotated by 90 °C and Figure 4.8d the corresponding center of mass trace. Cluster 1 still shows diffusion in the left-right orientation and Cluster 2 without a preferred orientation.

Nevertheless the clusters can undergo directed motion under certain circumstances. In figure 4.9 the more trivial of two cases is shown. A small cluster sticks to a barely visible tiny step in the graphite (marked by the dotted line). The step is not large enough to fix the molecule and exclude it from diffusion. But the attraction is strong enough to force the cluster to move along the step. The motion does not go straight forward into one direction but back and forth. This type of directed motion is referred to as guided motion.

In Figure 4.10 the more tricky case of diffusion in a preferred direction is shown. Here the two clusters sit on an atomically flat area on the graphite without any defects. Thus, the substrate can be excluded as being the origin for the directional motion. The overall diffusion of cluster 1 is from bottom left to top right, for cluster two from top left to bottom right. That means two clusters undergo diffusion in perpendicular directions to each other and all in the same experiment. Again, if there would be a preferred orientation of the diffusion due to the scanning direction of the tip this could not happen. The origin for this directed diffusion is found in the intrinsic properties of the two clusters. Both clusters have a stick like shape and the preferred motion is perpendicular to the main axis of the stick-shaped cluster.

All observed types of motion and differences in velocity can be explained by a segment motion mechanism. The segments are in the range of several monomer units corresponding to a length of several nanometer of a straight part of the molecule chain. Three examples of motion are shown in Figure 4.11. Taking one of the easiest cases: the straight molecule. By moving a few segments and forming two kinks a part of the molecule is translated. If this process goes on through the rest of the molecule the whole molecule is translated perpendicular to its main axes. For each of the basic steps only the energy to release a few segments at the same time from the substrate is necessary. The energy source is the thermal energy and the tip scanning over the molecule. These basic steps are on the atomic level, what we usually observe in the SFM experiments is the result of tens or hundreds of these steps. Each of these basic steps can go forward and backward, as well as the whole molecule can move forward and backward. What would be necessary for a movement parallel to the main axes of the molecule? In this case all segments of the molecule are coupled to each other and to do one basic step all segments have to release from the substrate. This explains the directed motion of highly oriented clusters as shown in 4.10.

As a second example two parallel aligned molecules are shown in Figure 4.11. The situation is almost the same as in the case discussed before the only difference is that the two molecules are coupled together and we have the case of coupled segments. But again for movements perpendicular to the main axis the number of segments that have to move in a basic step is much lower than for movements parallel to the main axis. But the motion is slowed down compared to one single molecule because the number of moved segments in a basic step is doubled because of the strong interaction between the two chains, leading to coupled segments.

The third example in Figure 4.11 shows a molecule with a crossover. The crossover was observed to be a very stable configuration that again couples together several segments. As a consequence much higher energies are needed to desorb all the coupled segments around

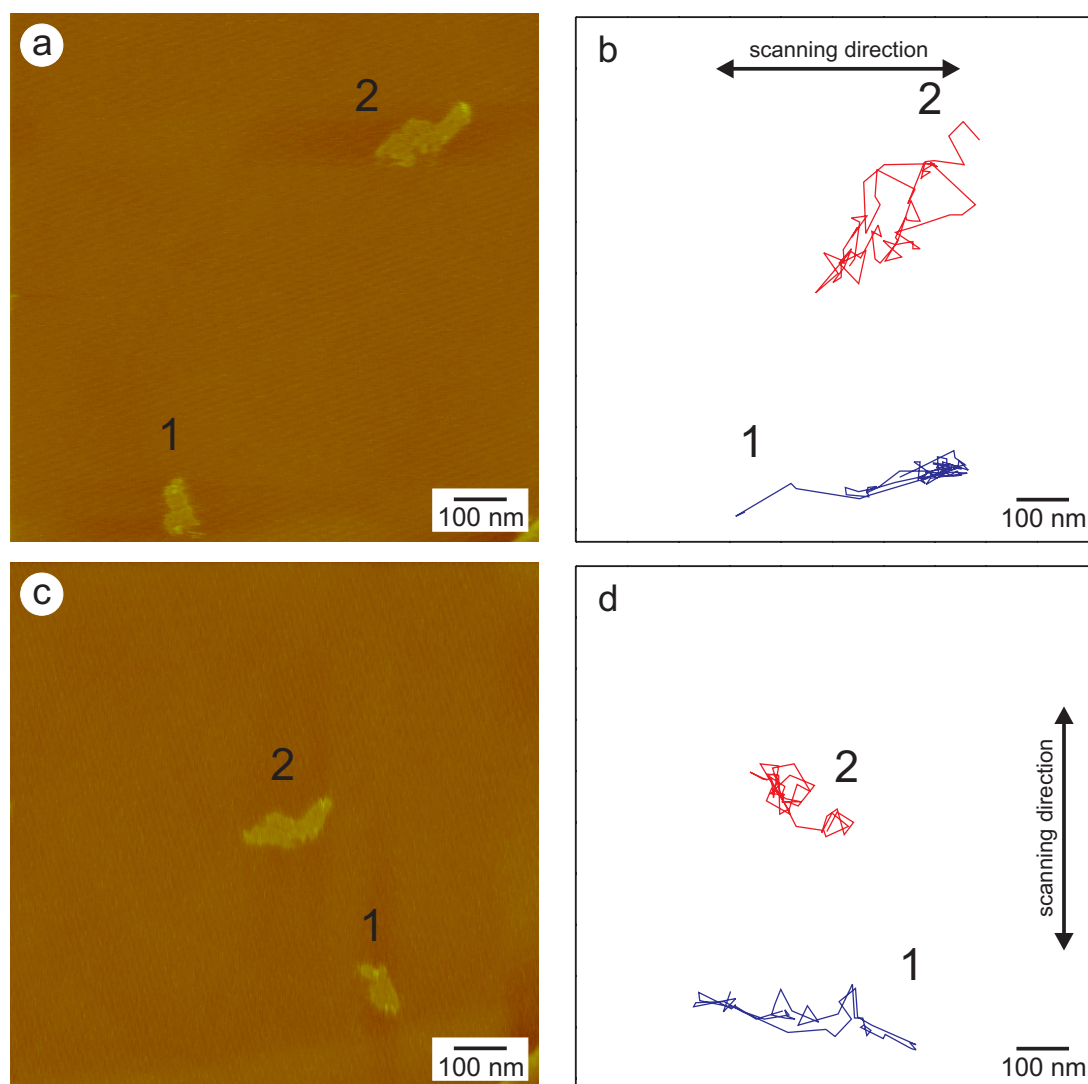


Figure 4.8: SFM images of two clusters of 12-ABG-4EO-PMA showing diffusion independent of the scanning direction of the SFM tip. a) position of the clusters when starting left-right scanning b) corresponding center of mass traces c) position of the clusters when starting up-down scanning d) corresponding center of mass traces. Cluster 1 shows in both cases left-right diffusion and cluster 2 does not show any preferential orientation of the diffusion

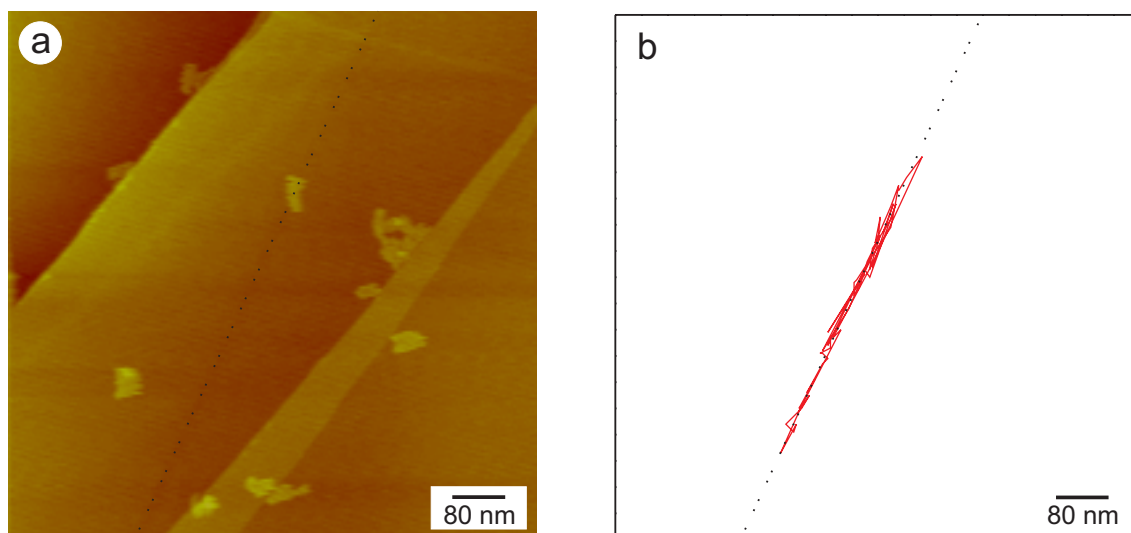


Figure 4.9: Guided motion of a cluster of 12-ABG-4EO-PMA along a barely visible step in the graphite, visualized by the dotted line a) SFM image b) corresponding center of mass trace

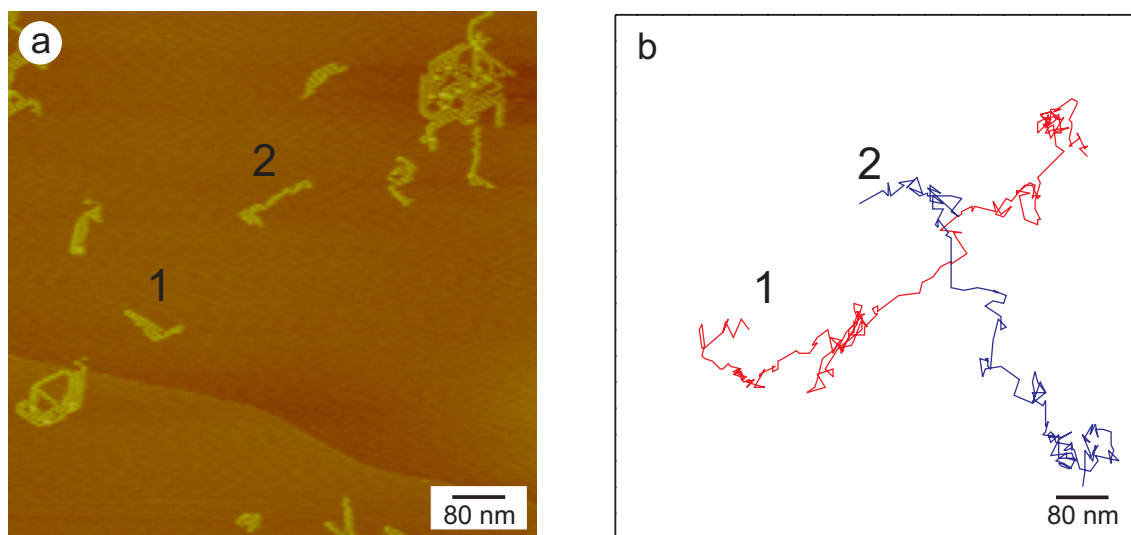


Figure 4.10: Two stick shaped clusters of 12-ABG-4EO-PMA undergoing directed diffusion perpendicular to the main axis of the clusters

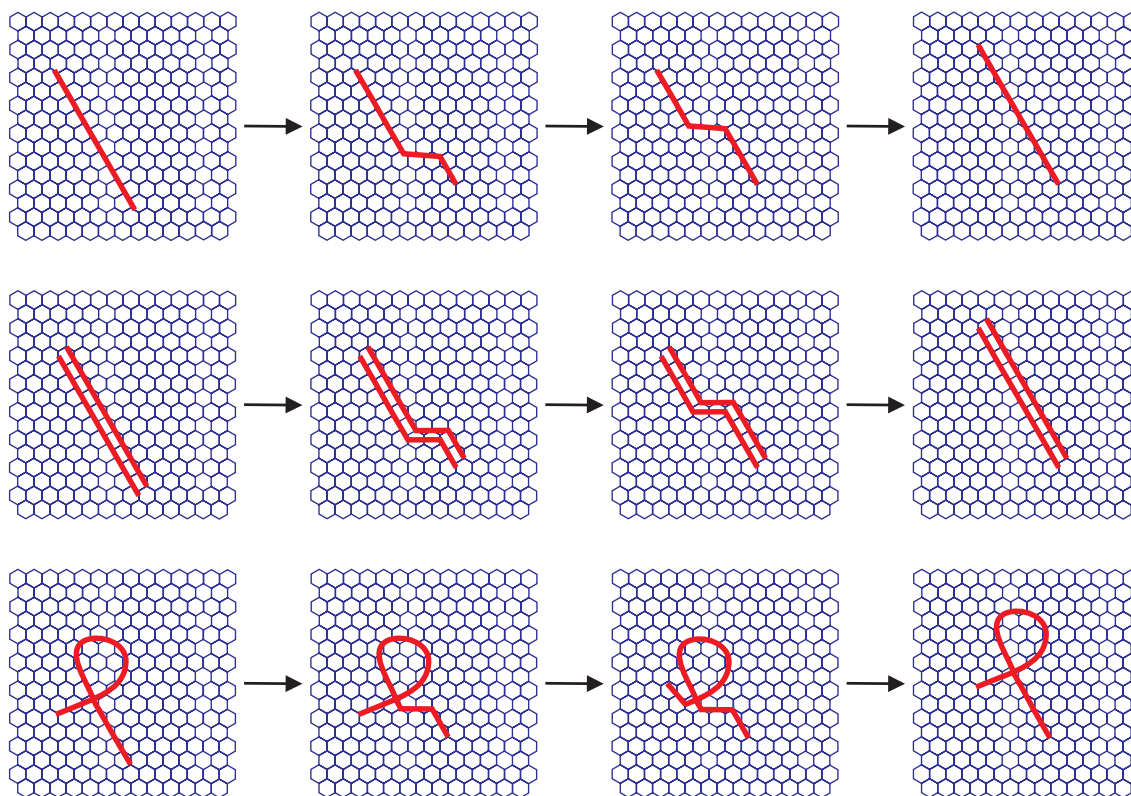


Figure 4.11: Segment motion mechanism for a linear chain, two aligned linear chains and a chain with crossover

the crossover from the substrate in order to translate it. A directional influence from the crossover itself was not observed and therefore depends on the rest of the molecule or molecular cluster.

In large clusters several of the described cases come together and lead to complex behavior. Two or more parts of the cluster might show movement in a preferred direction leading to an overall displacement of the cluster. Also the inner arrangement in the cluster and the overall shape might lead to different numbers of coupled segments and therefore for different behavior or velocity. In a completely compacted cluster almost all segments have to desorb at the same time to undergo a basic step. In contrast a cluster of same size that has some leftover flexibility by connecting two parts with a single molecular chain shows much faster diffusion. Here only half of the cluster has to release from the substrate to undergo a basic step.

Finally, a last example of diffusion of a single molecule of 12-ABG-4EO-PMA on  $\text{WeSe}_2$  as substrate is shown in Figure 4.12. As discussed in the previous chapter  $\text{WeSe}_2$  behaves in the same way as HOPG in adsorption and manipulation experiments. The same was confirmed for diffusion experiments and as in the manipulation experiments higher forces were required here higher temperatures are necessary to observe comparable diffusion. In the given example nicely the same behavior of forming kinks and moving parts of the molecule can be seen as described in the segment motion model. The molecule then soon forms an aggregate with another cluster.

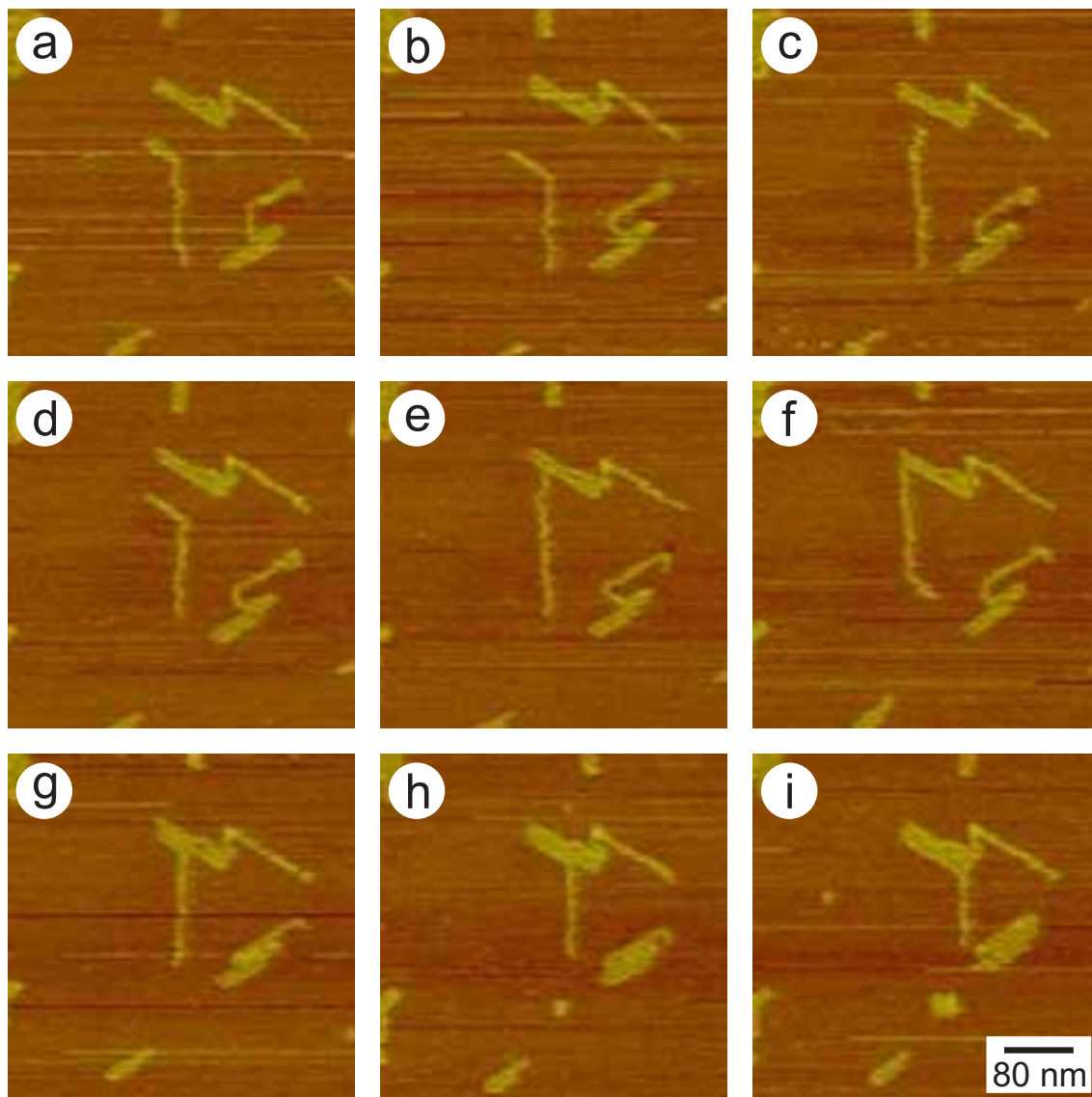


Figure 4.12: Single molecule of 12-ABG-4EO-PMA on WSe<sub>2</sub> showing motion according to the segment motion mechanism

## 4.4 Conclusions

Spin-coated molecules of 12-ABG-4EO-PMA on HOPG show already at room temperature diffusion-like motion. The velocity increases with temperature and the motion could be followed by long time SFM imaging series in the temperature range up to 48 °C. The motion at higher temperature is too fast to be followed by SFM.

The SFM imaging conditions, e. g. the force applied with the tip to the sample, given by the oscillation amplitude, excitation frequency, and amplitude setpoint, influence the diffusion speed of the molecules and clusters. But under the used tapping mode imaging conditions, in contrast to the conditions used for the manipulation in chapter 3.3.2, the tip does not push the molecules in a certain direction but is an additional energy source that helps to excite the molecules. Therefore only experiments performed with the same cantilever and similar parameters can be compared directly.

The diffusion is influenced by two attractive interactions:

1. interaction molecule — graphite
2. interaction molecule — molecule (much stronger)

This has several effects on the observed motion and could be followed in the SFM movie series.

Molecules diffuse freely, but when they encounter a step in the graphite they stick there and either quit moving or undergo guided linear 1-D diffusion. If molecules meet each other they stick together and do almost never release. The strong molecule-molecule interaction is also responsible for the parallel alignment of the chains and that the clusters get more compact by time. The shape-persistent diffusion of the molecular clusters is also an effect of the strong molecule-molecule interaction which keeps certain segments together and by this freezing the freedom of the rest of the molecule chain.

The molecules are flexible in the near range, as a consequence the molecules or clusters can move segment per segment. What we observe is the multi-segment motion when usually all segments moved several steps. The segments move not necessarily independently like in linear chains. Parallel alignment of several chains, hairpin folds and crossovers couples several segments together making it necessary that all these segments move in one step. As a consequence the energy necessary for the displacement of coupled segments is larger explaining their slower speed and therefore the reduced speed of the whole aggregate. Therefore small aggregates with only a few segments and little chance of coupled segments show fast diffusion.

The orientation and coupling of the segments can induce a preferred direction of motion. For example a completely linear molecule the displacement perpendicular to its axis can take place segment per segment inducing kinks in the chain. The displacement in direction of the axis of the molecule needs the movement of all segments at the same time and is therefore less preferred. This effect is more complex and levelled in bigger clusters.

The size, arrangement of segments and position on the substrate makes each cluster an individual with its own specific way of diffusion. Nevertheless the basic common concept behind the motion of each cluster is the same and could be extracted from the performed experiments.



## 4.5 Appendix

The results shown in Chapter 4 are the results of two series of SFM images. In series 1 the same area on the substrate has been observed at 30, 35 and 40 °C. In a second series another experiment was performed at 40, 45 and 48 °C.

For each temperature in both series a representative of six images was taken out (Figures 4.13–4.15 and 4.19–4.21) to give an impression what happened during the experiment. Additionally, the center of mass traces for each cluster are given in Figures 4.16–4.18 and 4.22–4.24. By clicking on these images a movie starts showing the full experiment. The movies are also found in the supporting material: `Movie1C30.avi`, `Movie1C35.avi`, `Movie1C40.avi`, `Movie2C40.avi`, `Movie2C45.avi`, and `Movie2C48.avi`.

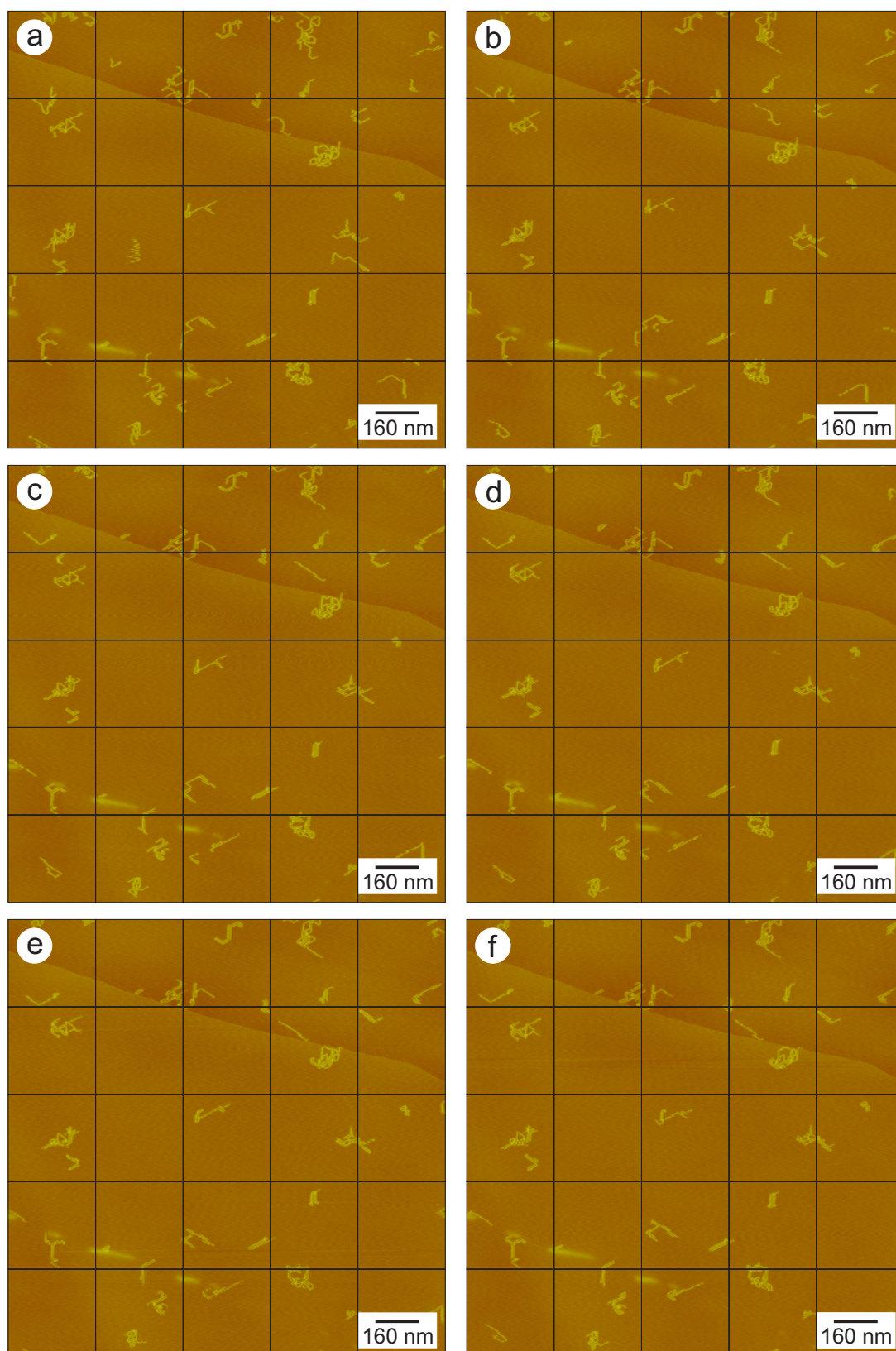


Figure 4.13: Six snapshots out of a series of 53 images (recorded in 212 min) of the diffusion like motion of 12-ABG-4EO-PMA on HOPG at 30°C. The snapshots show the situation after a) 24 b) 64 c) 96 d) 136 e) 168 f) 208 min

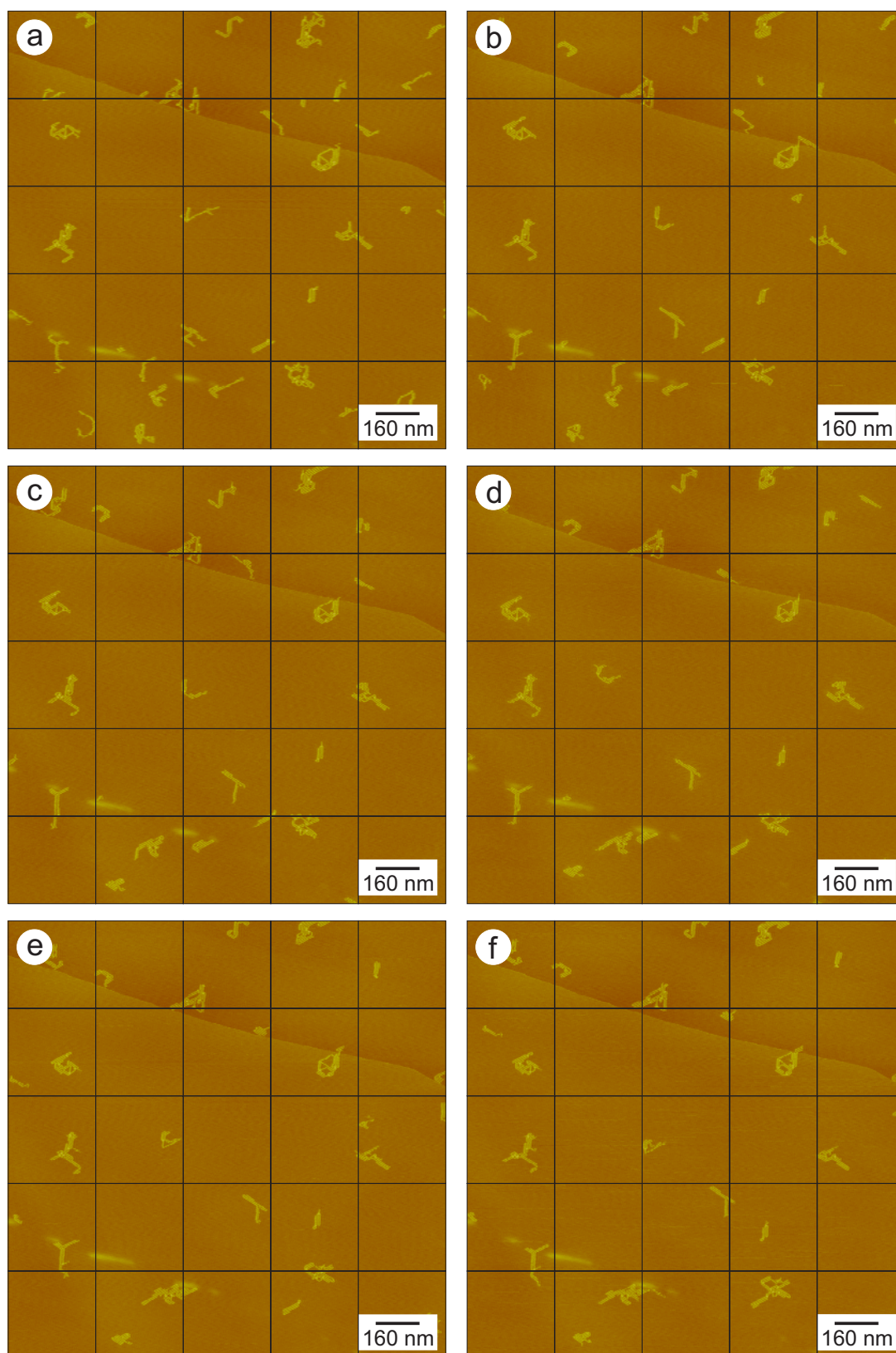


Figure 4.14: Six snapshots out of a series of 225 images (recorded in 900 min) of the diffusion like motion of 12-ABG-4EO-PMA on HOPG at 35 °C. The snapshots show the situation after a) 0 b) 184 c) 368 d) 552 e) 736 f) 896 min

4 Stimulated motion of monodendron jacketed polymers on HOPG

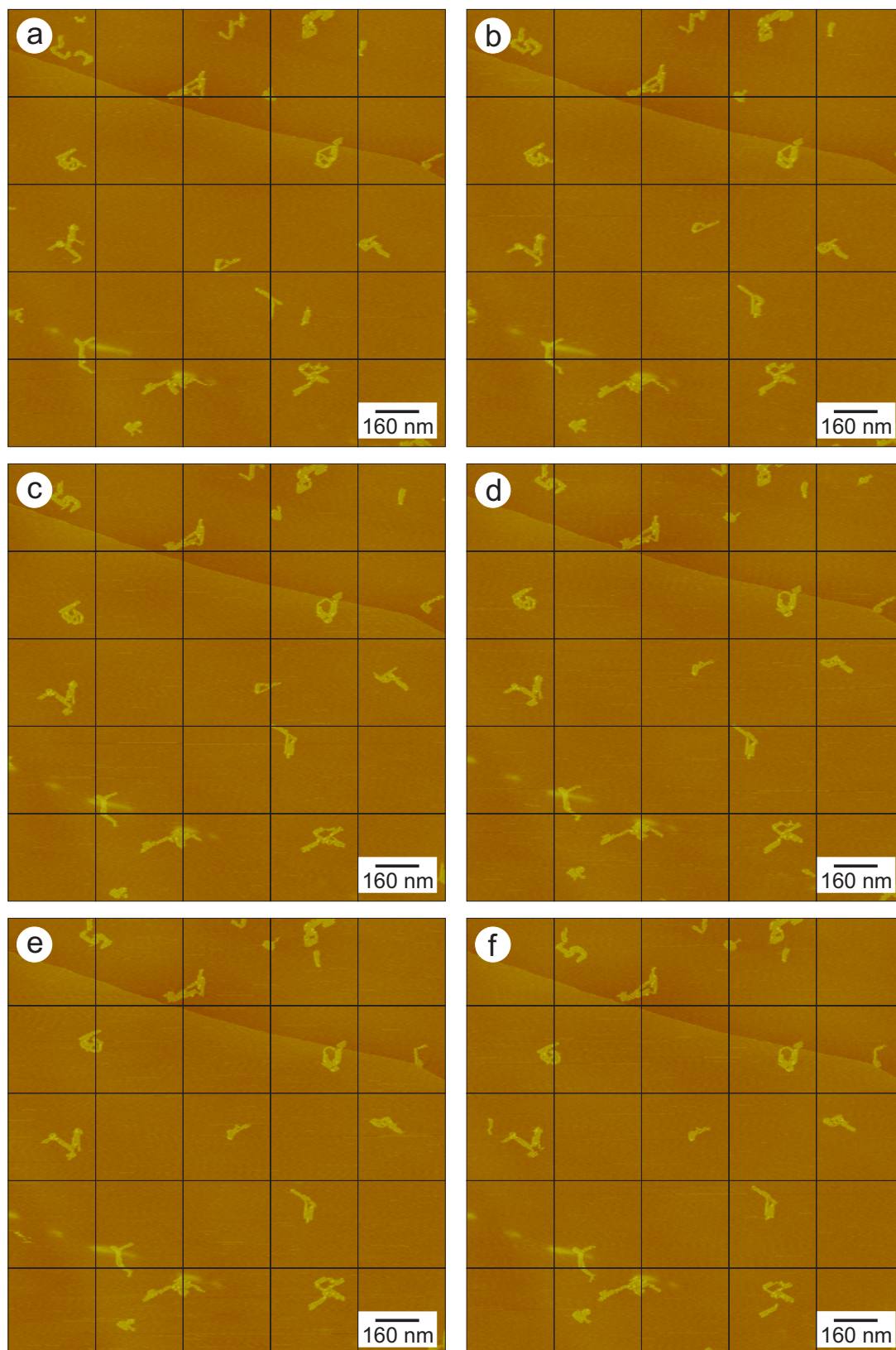


Figure 4.15: Six snapshots out of a series of 49 images (recorded in 196 min) of the diffusion like motion of 12-ABG-4EO-PMA on HOPG at 40°C. The snapshots show the situation after a) 8 b) 32 c) 72 d) 112 e) 152 f) 192 min

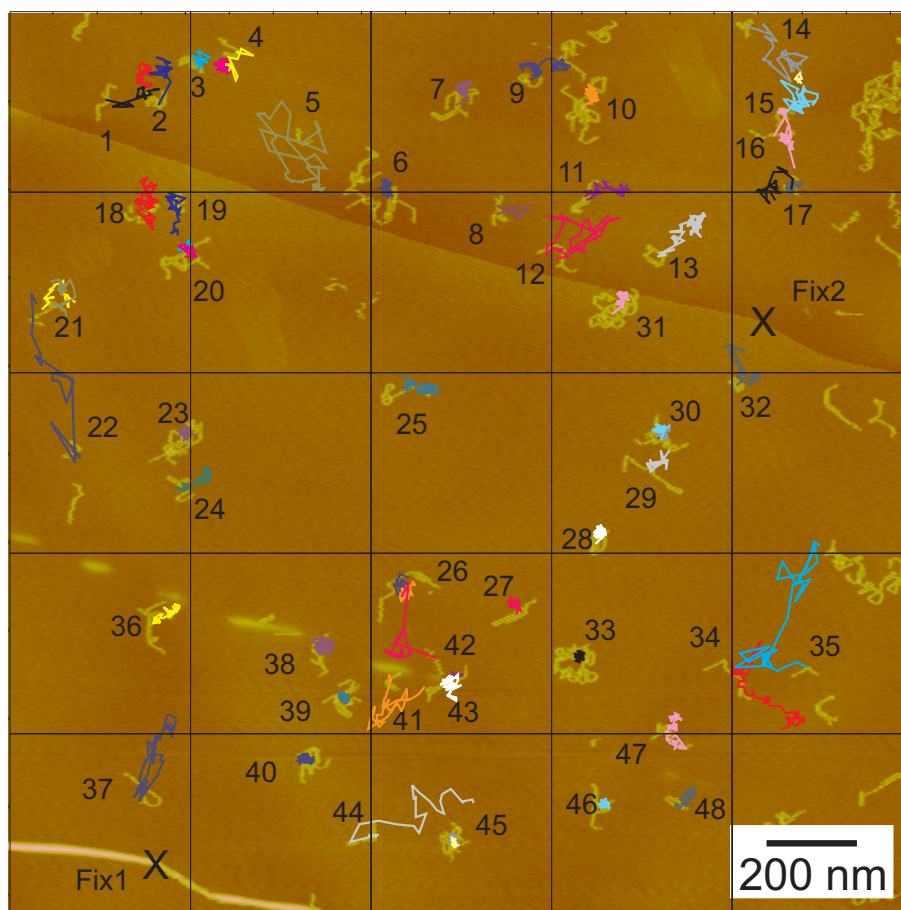


Figure 4.16: Center of mass traces of clusters of 12-ABG-4EO-PMA on HOPG at 30 °C

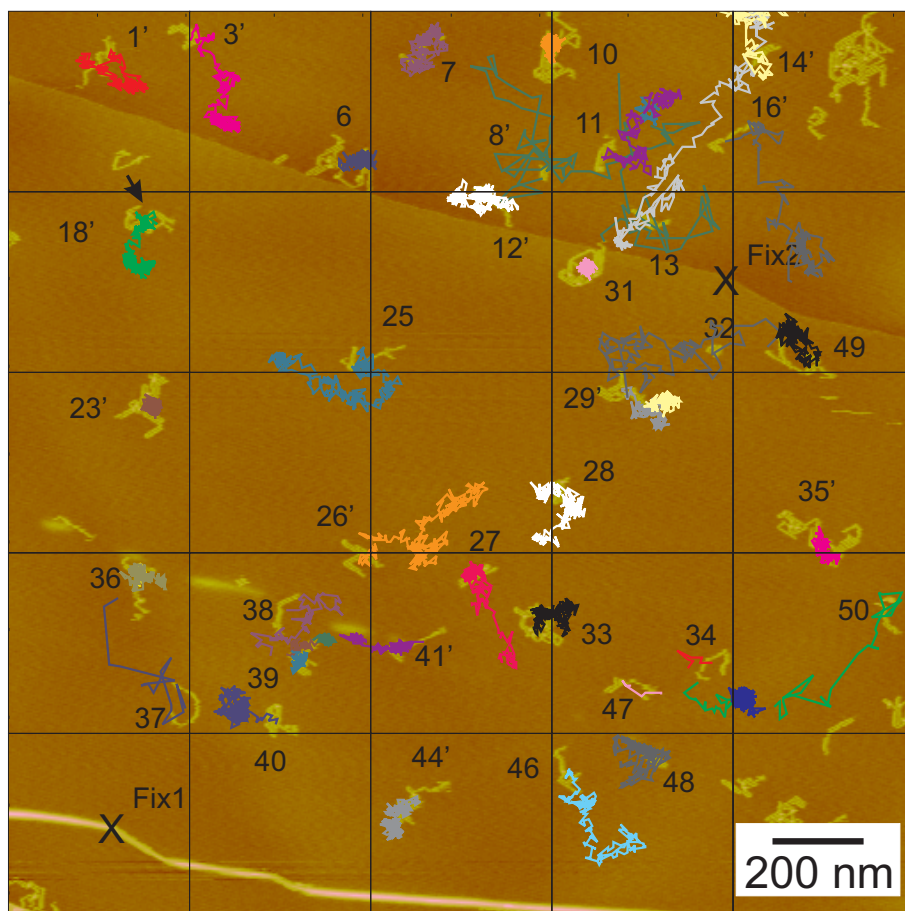


Figure 4.17: Center of mass traces of clusters of 12-ABG-4EO-PMA on HOPG at 35 °C

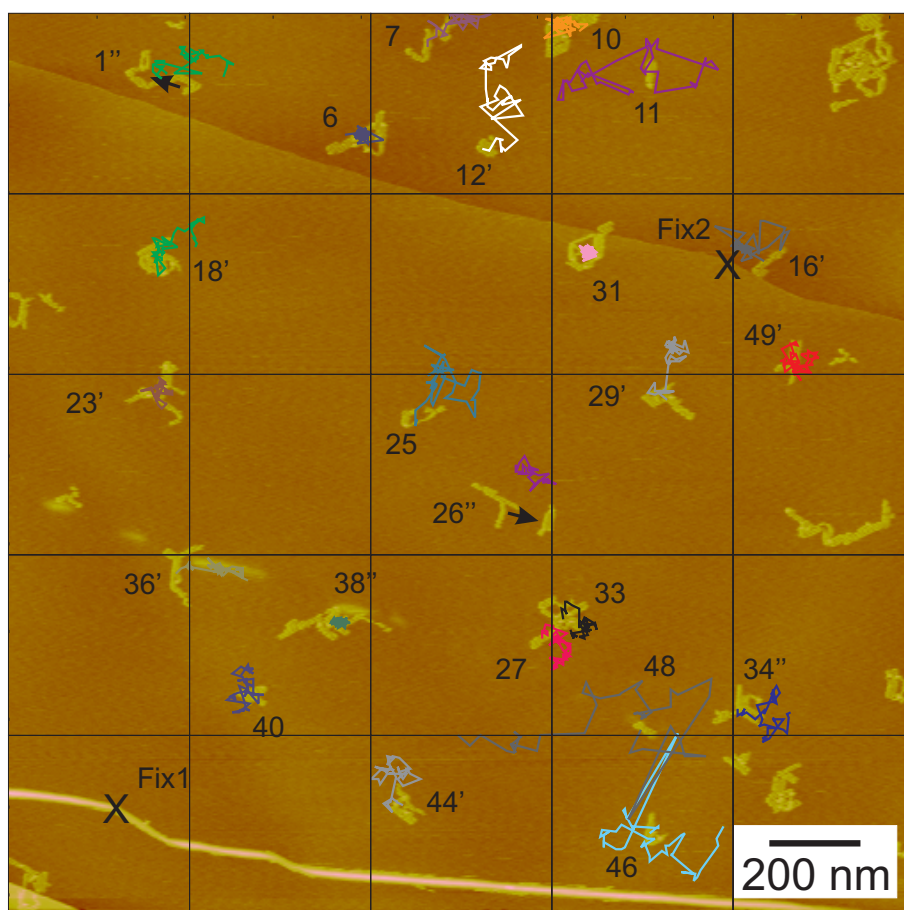


Figure 4.18: Center of mass traces of clusters of 12-ABG-4EO-PMA on HOPG at 40 °C

4 Stimulated motion of monodendron jacketed polymers on HOPG

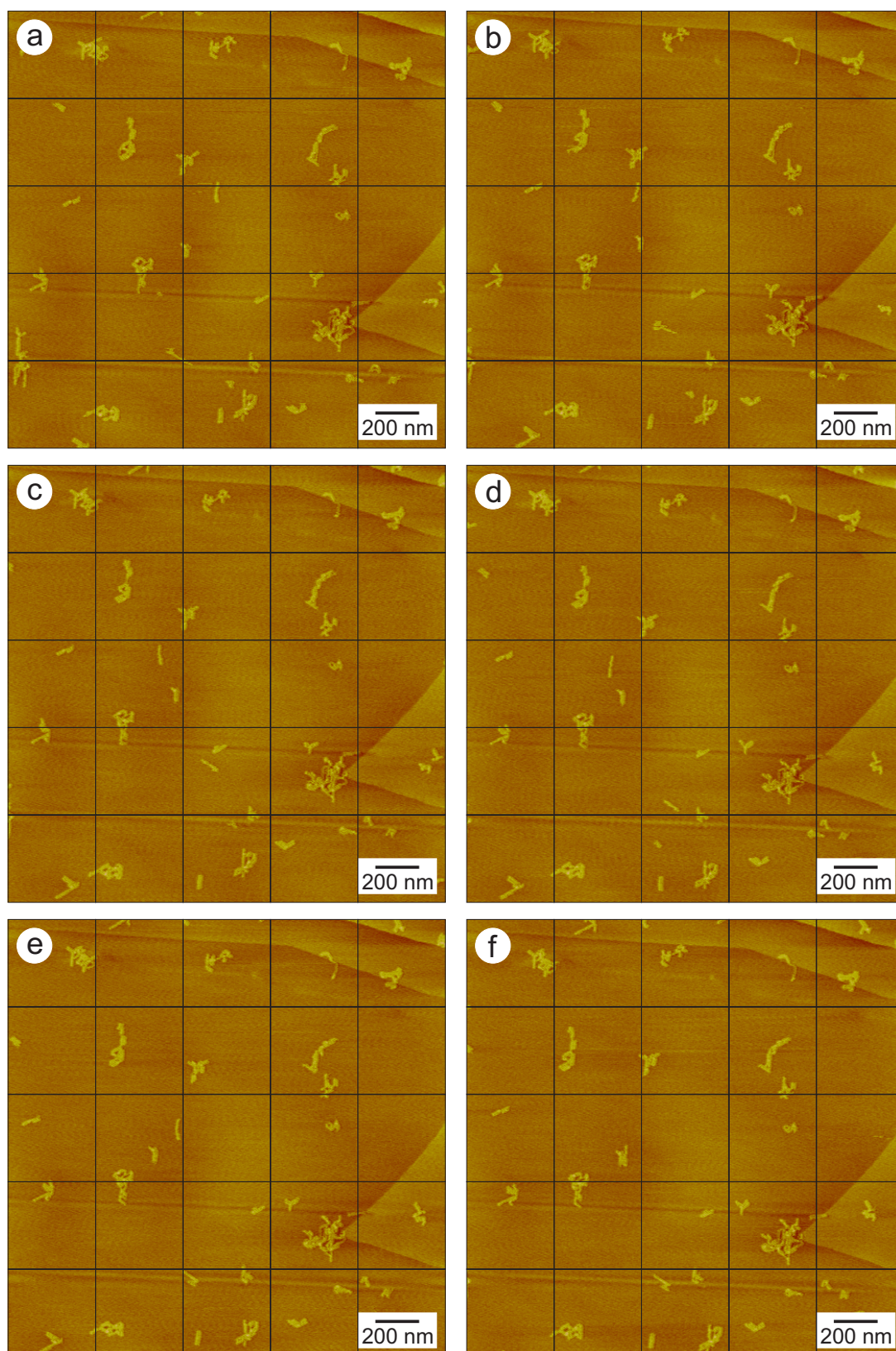


Figure 4.19: Six snapshots out of a series of 235 images (recorded in 940 min) of the diffusion like motion of 12-ABG-4EO-PMA on HOPG at 40 °C. The snapshots show the situation after a) 8 b) 56 c) 104 d) 152 e) 200 f) 248 min



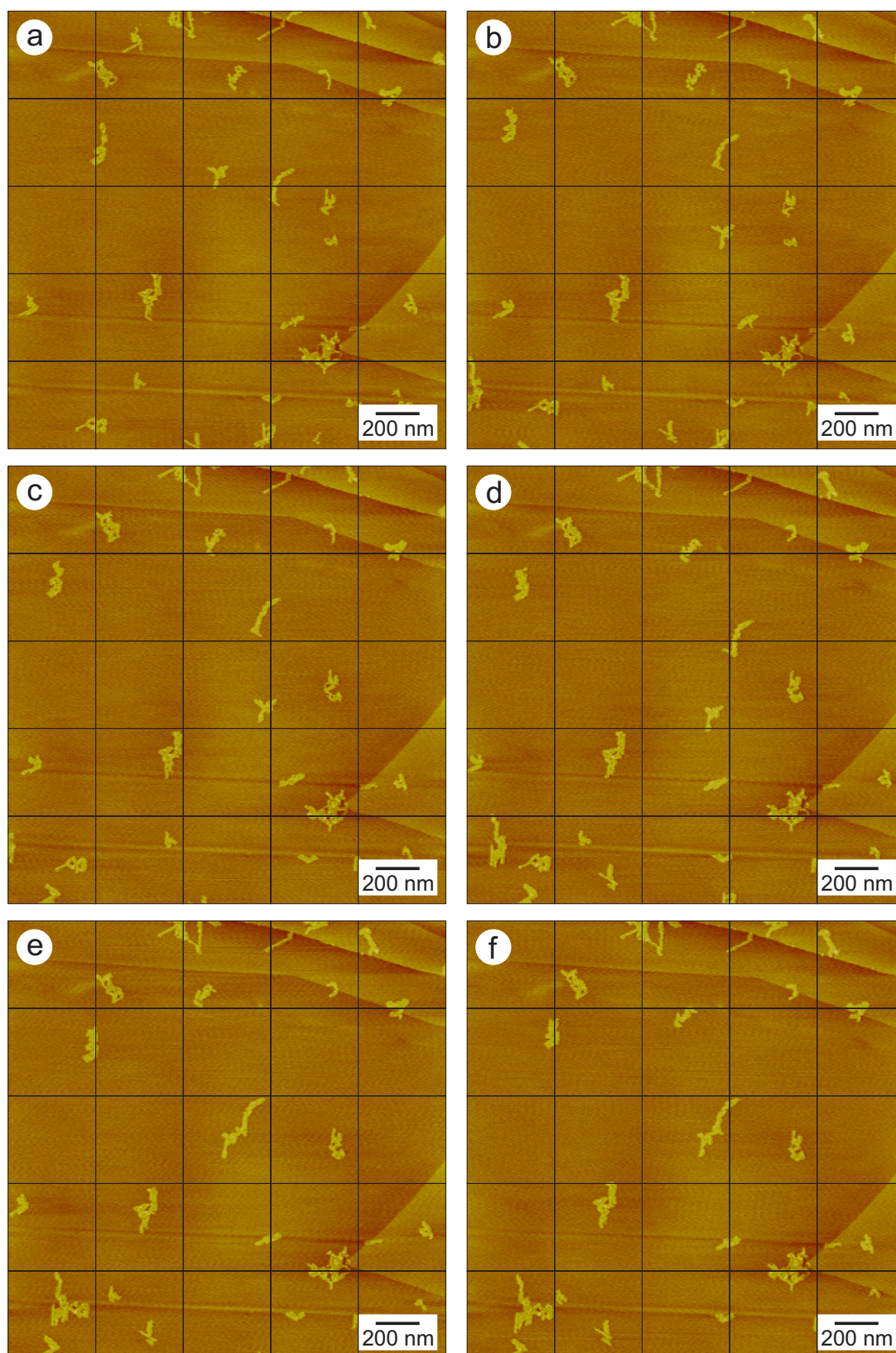


Figure 4.20: Six snapshots out of a series of 105 images (recorded in 420 min) of the diffusion like motion of 12-ABG-4EO-PMA on HOPG at 45 °C. The snapshots show the situation after a) 0 b) 80 c) 160 d) 240 e) 320 f) 400 min

4 Stimulated motion of monodendron jacketed polymers on HOPG

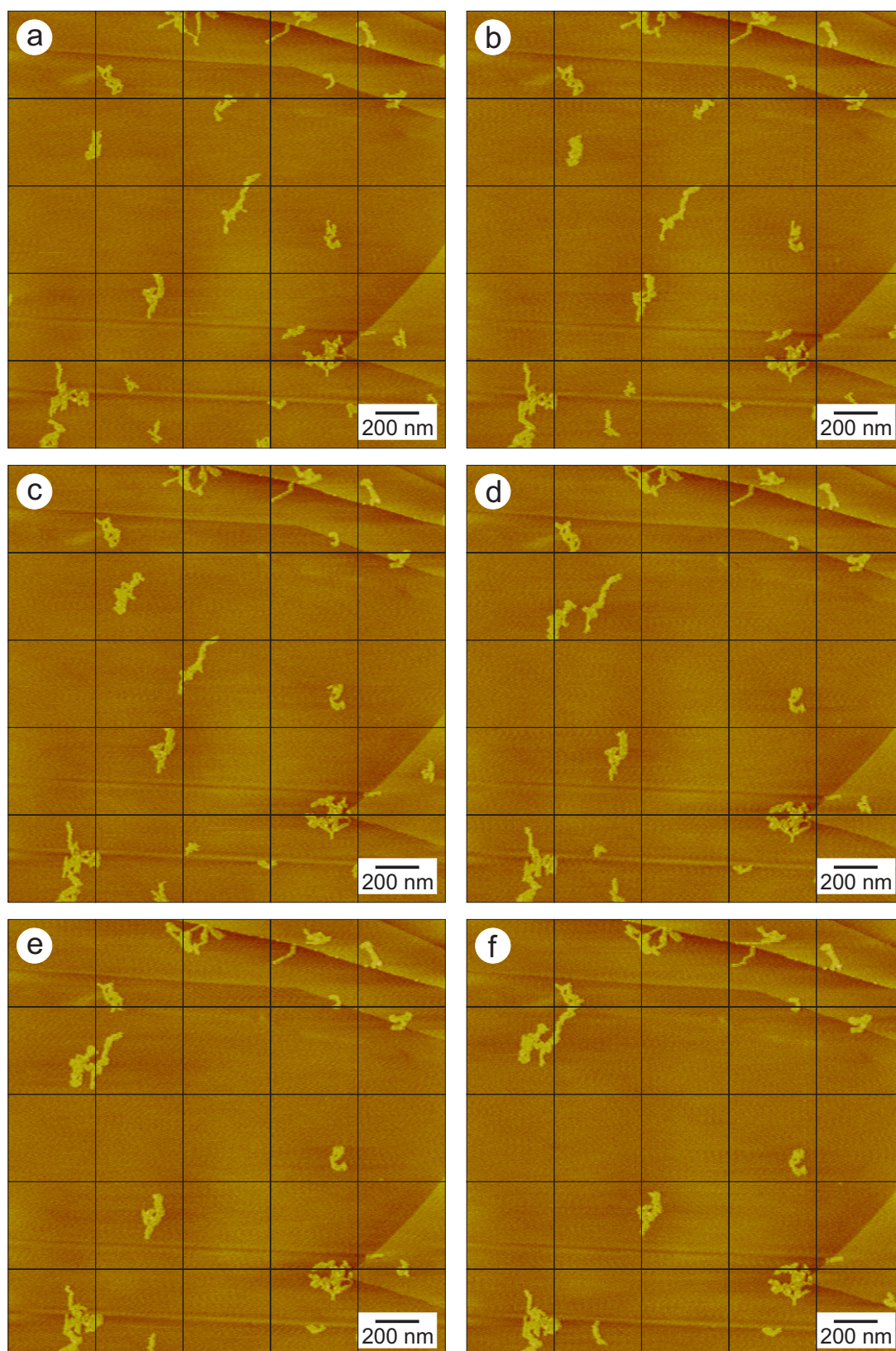


Figure 4.21: Six snapshots out of a series of 220 images (recorded in 880 min) of the diffusion like motion of 12-ABG-4EO-PMA on HOPG at 48 °C. The snapshots show the situation after a) 4 b) 84 c) 164 d) 244 e) 324 f) 404 min

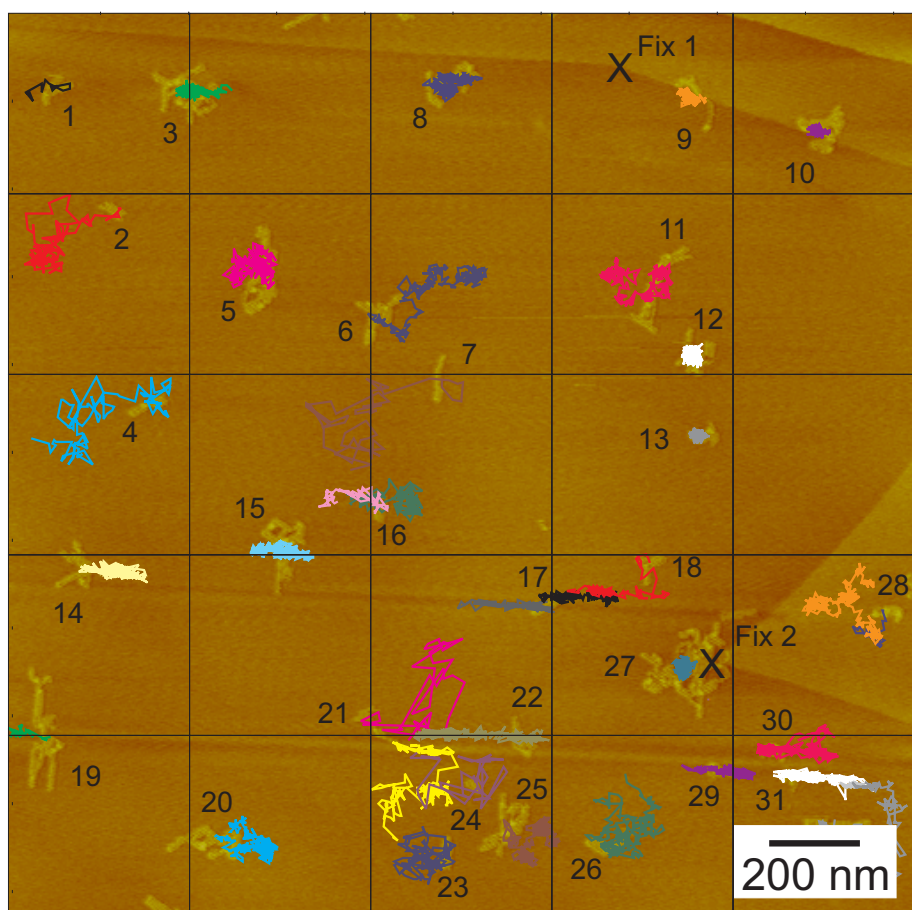


Figure 4.22: Center of mass traces of clusters of 12-ABG-4EO-PMA on HOPG at 40°C

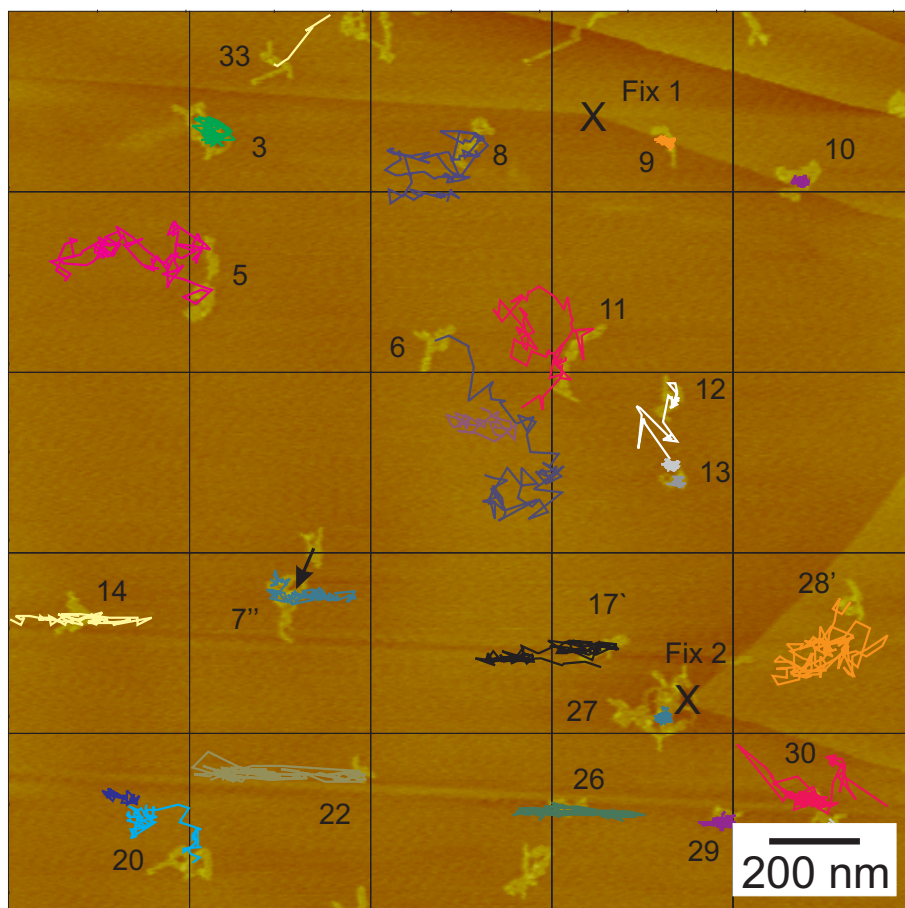


Figure 4.23: Center of mass trace of 12-ABG-4EO-PMA on HOPG at 45 °C

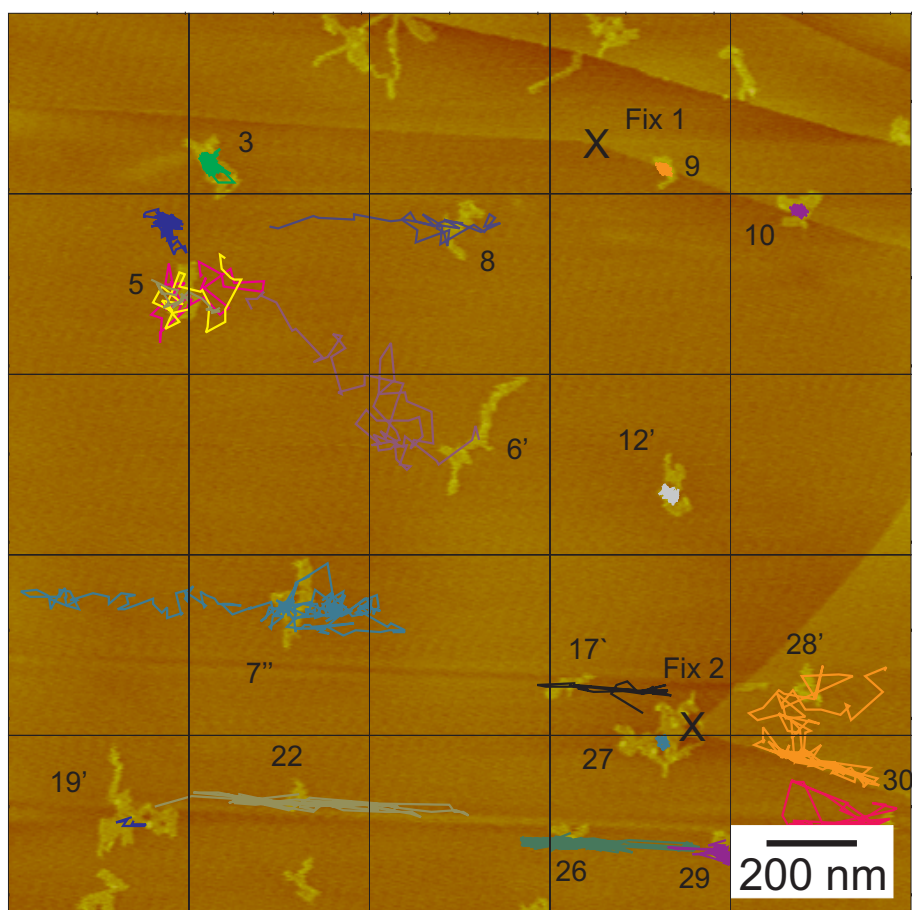


Figure 4.24: Center of mass traces of clusters of 12-ABG-4EO-PMA on HOPG at 48 °C



# Bibliography

- [1] W. D. Luedtke and U. Landman. Slip diffusion and Lévy flights of an adsorbed gold nanocluster. *Phys. Rev. Lett.*, 82:3835–3838, 1999.
- [2] P. Deltour, J.-L. Barrat, and P. Jensen. Fast diffusion of a Lennard-Jones cluster on a crystalline surface. *Phys. Rev. Lett.*, 78:4597–4600, 1997.
- [3] L. Bardotti, P. Jensen, A. Hoareau, M. Treilleux, and B. Cabaud. Experimental observation of fast diffusion of large antimony clusters on graphite surfaces. *Phys. Rev. Lett.*, 74:4694–4697, 1995.
- [4] G. Ge and L. E. Brus. Fast surface diffusion of large disk-shaped nanocrystal aggregates. *Nano Letters*, 1:219–222, 2001.
- [5] S. K. St. Angelo, C. C. Waraksa, and T. E. Mallouk. Diffusion of gold nanorods on chemically functionalized surfaces. *Adv. Mater.*, 5:400–402, 2003.
- [6] J. Weckesser, J. V. Barth, and K. Kern. Direct observation of surface diffusion of large organic molecules at metal surfaces: PVBA on Pd(110). *J. Chem. Phys.*, 113: 5351–5354, 1999.
- [7] R. Lüthi, E. Meyer, H. Haefke, L. Howald, W. Gutmannsbauer, and H.-J. Güntherod. Sled-type motion on the nanometer scale: Determination of dissipation and cohesive energies of C<sub>60</sub>. *Science*, 266:1979–1981, 1994.
- [8] B. Maier and J. O. Rädler. Conformation and self-diffusion of single DNA molecules confined to two dimensions. *Phys. Rev. Lett.*, 82:1911–1914, 1999.
- [9] B. Maier and J. O. Rädler. DNA on fluid membranes: A model polymer in two dimensions. *Macromolecules*, 33:7185–7194, 2000.
- [10] D. Nykypanchuk, H. H. Strey, and D. A. Hoagland. Brownian motion of DNA confined within a two-dimensional array. *Science*, 297:987–990, 2002.
- [11] I. Derényi, P. Tegzes, and T. Vicsek. Collective transport in locally asymmetric periodic structures. *Chaos*, 8:657–664, 1998.
- [12] R. D. Astumian and I. Derényi. Fluctuation driven transport and models of molecular motors and pumps. *Eur. Biophys. J.*, 27:474–489, 1998.
- [13] M. O. Magnasco. Forced thermal ratchets. *Phys. Rev. Lett.*, 71:1477–1481, 1993.
- [14] L. P. Faucheux, L. S. Bourdieu, P. D. Kaplan, and A. J. Libchaber. Optical thermal ratchet. *Phys. Rev. Lett.*, 74:1504–1507, 1995.

## Bibliography

- [15] A. van Oudenaarden and S. G. Boxer. Brownian ratchets: Molecular separations in lipid bilayers supported on patterned arrays. *Science*, 285:1046–1048, 1999.
- [16] N. Koumura, R. W. J. Zijlstra, R. A. van Delden, N. Harada, and B. L. Feringa. Light-driven monodirectional molecular motor. *Nature*, 401:152–154, 1999.
- [17] R. D. Astumian. Adiabatic theory for fluctuation-induced transport on a periodic potential. *J. Phys. Chem*, 100:19075–19081, 1996.
- [18] G. S. Bloom and S. A. Endow. Motor proteins 1: Kinesins. *Protein Profile*, 2:1109–1111, 1995.
- [19] J. R. Sellers and H. V. Goodson. Motor proteins 2: Myosins. *Protein Profile*, 2: 1323–1423, 1995.
- [20] M. J. Schnitzer, K. Visscher, and S. M. Block. Force production by single kinesin motors. *Nature Cell Biol*, 2:718–723, 2000.
- [21] S. Leibler and D. A. Huse. Porters versus rowers: A unified stochastic model of motor proteins. *J. Cell Biol.*, 121:1357–1368, 1993.
- [22] K. Kitamura, M. Tokunaga, A.H. Iwane, and T. Yanagida. A single myosin head moves along an actin filament with regular steps of 5.3 nanometers. *Nature*, 397: 129–134, 1999.
- [23] A. L. Wells, A. W. Lin, L.-Q. Chen, D. Safer, S. M. Cain, T. Hasson, B. O. Carragher, R. A. Milligan, and H. L. Sweeney. Myosin VI is an actin-based motor that moves backwards. *Nature*, 401:505–508, 1999.
- [24] M. Schliwa. Myosin steps backwards. *Nature*, 401:431–432, 1999.



# 5 Stimulated response of monodendron jacketed polymers modified with photo-switchable spiropyran

## 5.1 Introduction

Spirobenzopyran derivatives are well known photoresponsive organic compounds which can be reversibly isomerized by UV and visible light irradiation (Figure 5.1). Isomerization between the zwitter-ionic merocyanine and the neutral spiroform was utilized to prepare polymers with a photoresponsive conformation [1], in order to regulate the viscosity of polymer solutions [2], enzyme activities [3, 4], membrane potential [5–7], ion permeation using liquid membranes [8] and non linear optical (NLO) materials [9].

Photochromic molecules containing polymerizable organic functional groups (ethenyl, methacryloxy and trimethoxysilyl) have been incorporated by copolymerization in polymers and addition to polysiloxanes [10, 11]. Photostimulated conformational changes in polymer chains in solution can induce macroscopic changes in the shape and size of polymers and solids [1, 12–14]. The grafting of polymers containing spiropyran residues in the side chains on porous polymeric membranes lead to photocontrollable membranes. For example water permeation through the graft membrane [15] or the diameter of the pores in organic solutions (Figure 5.2) [16] can be controlled in this way. Furthermore, merocyanines are very sensitive to steric and polar effects and can thus be used to monitor the steric interaction and solubility in polymer molecules [17–19]. For a short review on the technological interest in these materials see reference [20].

In this project the idea was to synthesize copolymers containing spiropyran moieties in order to control the adsorption on a substrate by switching the spiropyran from the uncharged to the zwitter-ionic merocyanine isomer. By this it should be possible to control the motion of molecules on a substrate by light in contrast to the thermal activation described in Chapter 4.

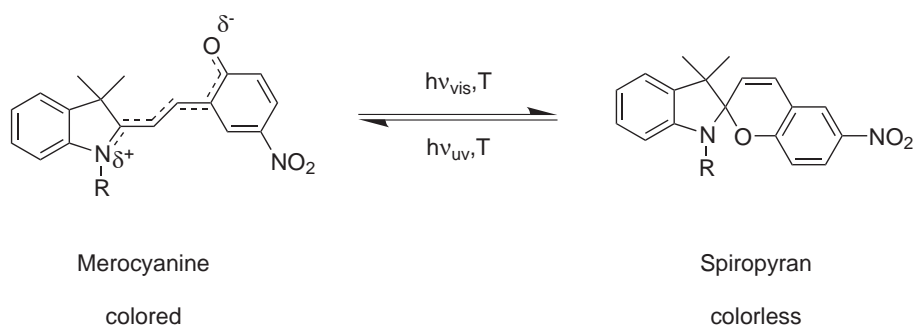


Figure 5.1: Photoswitching of spiropyrans

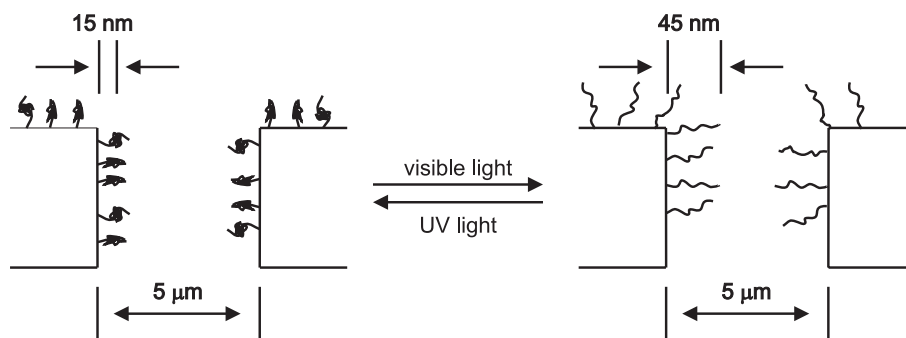


Figure 5.2: Photo-controllable membrane: The spiropyran residues in the side chains on a porous polymeric membrane can be selectively shrunk or extended and by this control the permeation [16]

Here the synthesis of a methacrylate functionalized nitrospiropyran and its copolymerization with a monodendron jacketed monomer is described. The successful synthesis was confirmed by GPC with UV detection and UV spectra of the monomer and polymer. Illumination of the polymer solutions by UV light prior to spin-coating on the substrate yielded aggregation of the macromolecules. In the experiments performed so far illumination of the molecules on the substrate during online SFM measurements did not affect the molecules.

## 5.2 Experimental part

### 5.2.1 Materials

1-( $\beta$ -methacryloxyethyl)-3,3-dimethyl-6-nitrospiro(indoline-2,2-[2H-1]benzopyran) was synthesized according to a procedure in literature [21]. Figure 5.3 shows the synthesis scheme. The formation of an imidazolidine, as described in [22], could be avoided by using of pyridine as acid scavenger [21]. 2-[2-{2-(2-(methacryloyloxy)ethoxy)ethoxy}ethoxy]ethyl 3,4,5-tris[(4-(*n*-dodecan-1-yloxy)benzyl)oxy]benzoate (12-ABG-4EO-MA) was synthesized according to the procedure in chapter 3.2.3. The statistical copolymer Poly(12-ABG-4EO-MA-co-Spiran-MA) (Figure 5.4) was done by radical polymerization in toluene using AIBN as initiator. A fraction of 8 mol-% Spiran-MA was utilized.

The synthesis of the spiropyran-monomer and the polymerization was carried out by M. Kraus (University of Ulm, Germany) [21].

THF (Uvasolv, 99,9 %) and toluene (Uvasolv, 99,9 %) from Merck were used as received. Freshly cleaved mica (BAL-TEC) was chosen as substrate for the SFM experiments.

### 5.2.2 Methods

Scanning force microscopy (SFM) was performed on a Digital Instruments Multimode scanning force microscope equipped with a Nanoscope IIIa controller or on an Asylum Research MFP-3D. Imaging was done in tapping mode using standard silicon cantilevers: Nanoworld Pointprobe NCH ( $k = 42 \text{ N/m}$ ,  $f_0 = 330 \text{ kHz}$ ) or FM ( $k = 2.8 \text{ N/m}$ ,  $f_0 = 70 \text{ kHz}$ ). The samples were prepared by means of a spin-coating procedure (2000 rpm) using dilute solutions of the polymer in toluene (0.1-0.5 g/l).

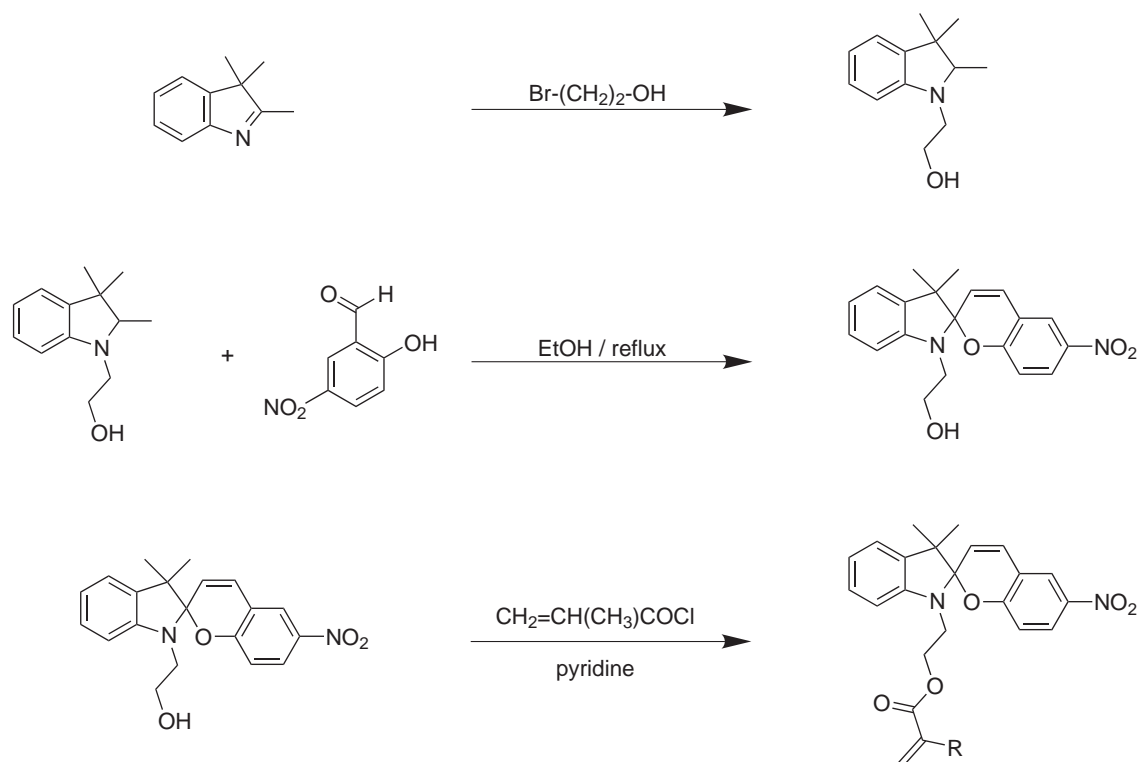


Figure 5.3: Synthesis of 1-( $\beta$ -methacryloxyethyl)-3,3-dimethyl-6-nitrospiro(indoline-2,2-[2H-1]benzopyran) (Spiran-MA)

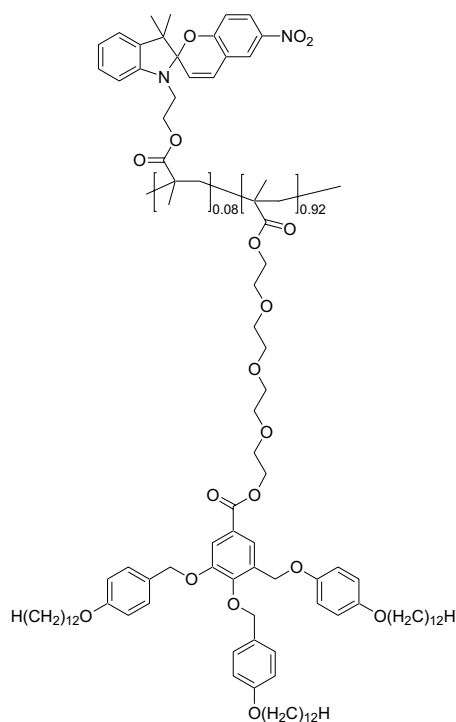


Figure 5.4: Structure and composition of Poly(12-ABG-4EO-MA-co-Spiran-MA)

UV/VIS measurements were conducted on a Perkin Elmer Lambda 16 spectrometer. 1 wt-% solutions of the monomer and polymer were prepared and measured in 10 mm standard cuvettes against THF as a reference.

Molecular weight and molecular weight distribution were determined by SEC in THF as solvent. The setup consisted of a Waters 600 pump and controller, Waters Ultrastaygel columns ( $10^5$ ,  $10^4$ ,  $10^3$  and  $500 \text{ \AA}$  pore sizes). Detection was done with a Waters 410 differential refractometer and a Waters 486 tunable absorbance detector driven in the UV-range at 366 nm. Calibration was done with narrow polystyrene standards from PSS (Mainz). For the calculation of molecular weight PSS WinGPC scientific software was used.

### 5.3 Results and discussion

The decision to modify the well known polymer 12-ABG-4EO-PMA (Chapter 3 and 4) with a spiropyran showed two general problems:

1. The nitro-group in the spiropyran-monomer can serve as a radical scavenger and therefore inhibit the polymerization or lead to low molecular weight polymers.
2. It is known [23–25] that the 12-ABG-4EO-MA monomer self-assembles in solution to cylindrical aggregates leading to an unexpected high rate of polymerization because of grouping together the polymerizable groups in the aggregates. This could disturb the statistical copolymerization of the 12-ABG-4EO-MA with the Spiran-MA.

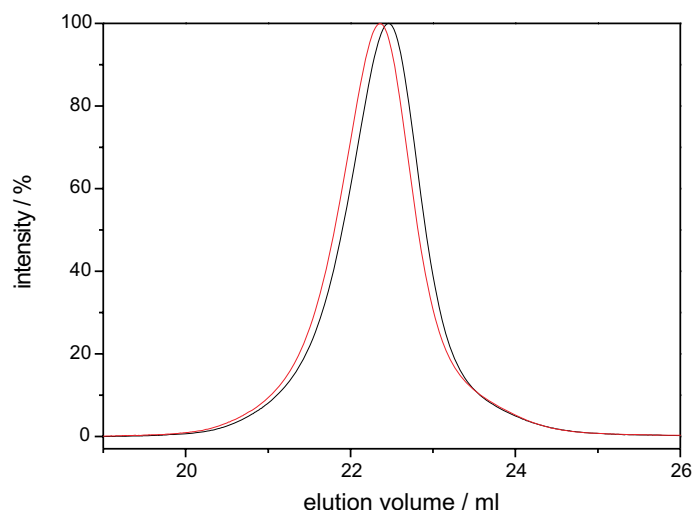


Figure 5.5: GPC spectra of Poly(12-ABG-4EO-MA-co-Spiran-MA) detected with  $R_i$  (red) and  $UV_{366\text{ nm}}$  (black)

Table 5.1: Molecular weight of Poly(12-ABG-4EO-MA-co-Spiran-MA) determined by SEC using polystyrene calibration

$M_n$ [kg/mol]	$M_w$ [kg/mol]	PD
101	252	2.5

Despite all expected problems the polymerization yielded high molecular weights and a moderate polydispersity (Table 5.1). Figure 5.5 shows the GPC traces of Poly(12-ABG-4EO-MA-co-Spiran-MA) detected with a refractive index and an UV detector selectively set on the absorption of the Spiro-MA monomer ( $\lambda = 366\text{ nm}$ ). The two traces match almost perfectly indicating that the Spiro-MA monomer is incorporated in the copolymer. The absence of any double peak, shoulder, tailing or other anomaly in the GPC-peaks is a good evidence that the Spiro-MA monomer is equally distributed in the resulting polymer.

UV-spectra of the Spiro-MA monomer and Poly(12-ABG-4EO-MA-co-Spiran-MA) (Figure 5.6a and b) after UV irradiation at 366 nm showed almost the identical absorption as the pure spiran-group. This proves that the switching from the spiro-MA monomer to the merocyanine form is still possible in the polymer.

First SFM experiments to elucidate the appearance of the copolymer showed no differences compared to the homo-polymer 12-ABG-4EO-PMA visualized in the chapters before. Figure 5.7a depicts an image of Poly(12-ABG-4EO-MA-co-Spiran-MA) on mica spin-coated from a toluene solution. In Figure 5.7b a high molecular weight fraction, obtained by GPC fractionation, on HOPG is seen. For the preparation of the copolymers on HOPG a variety of solvents (chloroform, THF, toluene) can be used with almost the same result as shown in Figure 5.7b. The situation is different on mica: only with toluene a distribution of isolated molecules was obtained. THF and chloroform dewet the mica

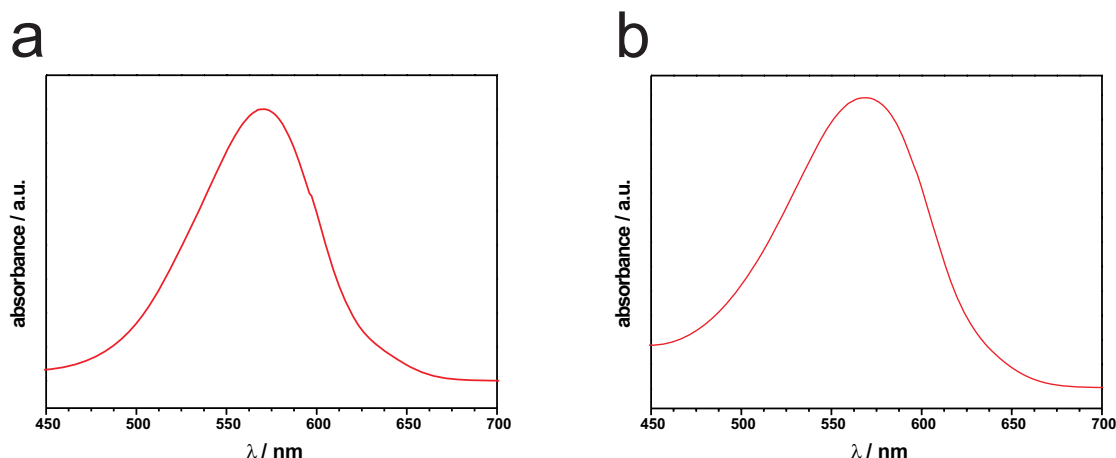


Figure 5.6: UV spectra of a) the Spiran-MA monomer and b) (Poly(12-ABG-4EO-MA-co-Spiran-MA) after irradiation with UV-light ( $\lambda = 366$  nm)

surface and collect the polymer molecules to unordered clusters.

In order to see if the isomerization of the spiropyran group has an influence on the copolymer the polymer solution was illuminated with UV light prior to the spin-coating procedure. For these experiments toluene solutions and mica as substrate were chosen because it is well known from the homopolymer 12-ABG-4EO-PMA that it is invariant on mica surfaces.

Figure 5.8 shows the images obtained without and with UV radiation. In this case UV-light with a wavelength of  $\lambda = 254$  nm was used and the irradiation was directly conducted in the glass pipette used for spin-coating. Figure 5.8a shows isolated molecules as seen before, whereas the copolymers from the illuminated solution showed aggregation (5.8b) to bigger clusters.

The situation was the same for a more diluted solution ( $c = 0.01$  g/l) using UV light with a wavelength of 366 nm (Figure (5.9)). Here the aggregates look even more distinct and also the adsorbed molecules per area increased.

The explanation of this effect is straight forward: Switching of the spiran groups in Poly(12-ABG-4EO-MA-co-Spiran-MA) to the zwitter-ionic merocyanine form by means of UV-radiation causes the occurrence of Coulomb-interactions. The unpolar solvent toluene is not able to stabilize the now charged molecules as individuals, therefore the polymer molecules saturate each other by aggregation in solution. The charge of the copolymer molecules also explains the improved adsorption on the strongly polar mica substrate.

All experiments performed so far by illumination of Poly(12-ABG-4EO-MA-co-Spiran-MA) on a substrate (HOPG and mica) during SFM operation as well as off-line, even at elevated temperatures ( $50^\circ\text{C}$ ), did not show any effect distinct from the behavior of the homo-polymer 12-ABG-4EO-PMA.

## 5.4 Conclusions

The synthesis of a copolymer containing a MA monomer with mini-dendritic side groups and a spiropyran-MA monomer is described. The statistical incorporation of the

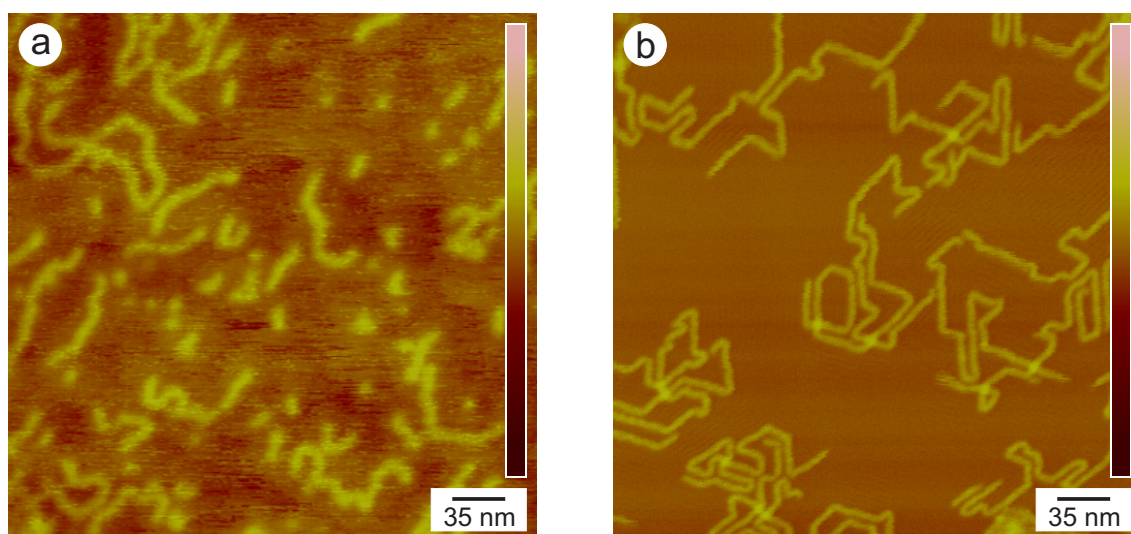


Figure 5.7: SFM tapping mode topography images of Poly(12-ABG-4EO-MA-co-Spiran-MA) spin-coated (2000 rpm) a) from toluene solution ( $c = 0.025$  g/l) on mica (z-range 5 nm) b) from chloroform solution on HOPG (high molecular weight sample, z-range 10 nm)

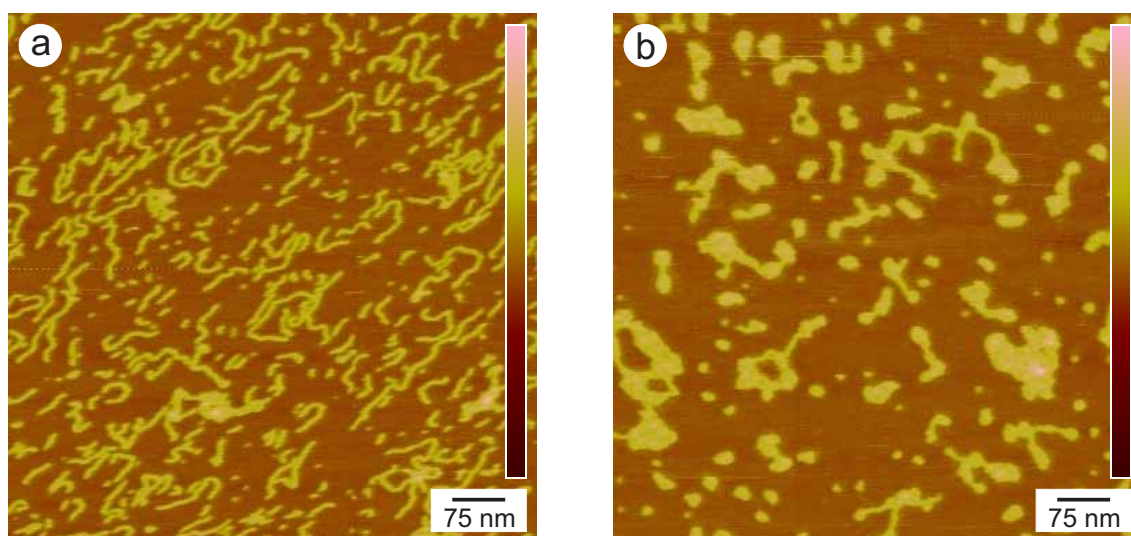


Figure 5.8: SFM tapping mode topography images of Poly(12-ABG-4EO-MA-co-Spiran-MA) a) spin-coated (2000 rpm) on mica from toluene solution ( $c = 0.025$  g/l) b) the solution was illuminated with UV-light ( $\lambda = 254$  nm) in a glass pipette for 45 sec before the spin-coating procedure (z-range 5 nm)

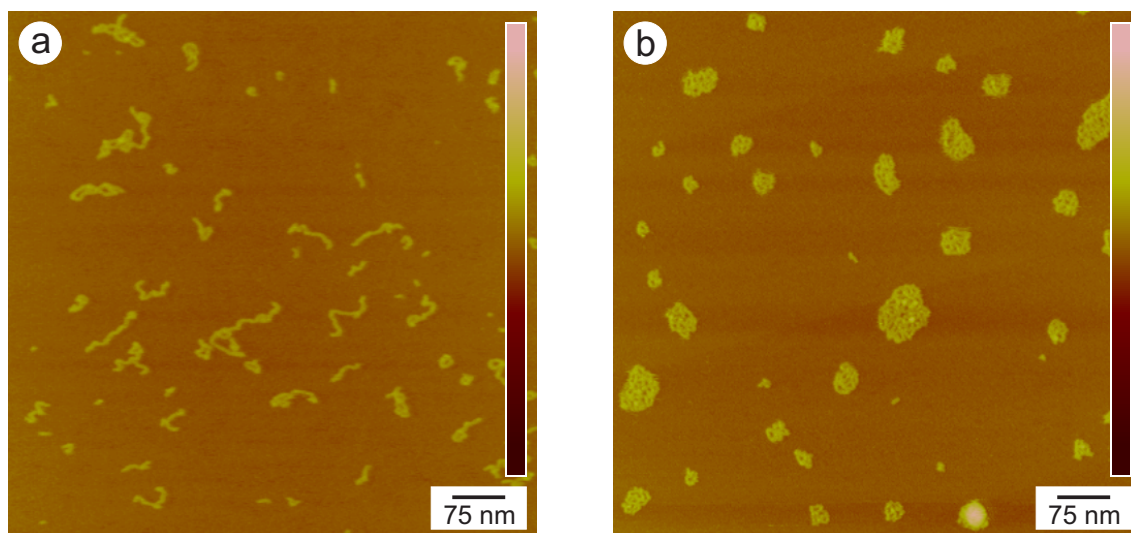


Figure 5.9: SFM tapping mode topography images of Poly(12-ABG-4EO-MA-co-Spiran-MA) a) spin-coated (2000 rpm) on mica from toluene solution ( $c = 0.01$  g/l) b) the solution was illuminated with UV-light ( $\lambda = 366$  nm) in a glass vial for 60 sec before the spin-coating procedure (z-range 10 nm)

spiropyran-MA monomer and the functionality of the spiropyran-unit in the copolymer was proven by GPC with UV detection and UV-measurements.

Furthermore it was shown that Poly(12-ABG-4EO-MA-co-Spiran-MA) can be switched in solution to the zwitter-ionic merocyanine form, yielding aggregation caused by Coulomb-interaction. The aggregated state could be transferred to mica substrates and visualized by scanning force microscopy.



# Bibliography

- [1] M. Irie, A. Menju, and K. Hayashi. Photoresponsive polymers. Reversible solution viscosity change of poly(methyl methacrylate) having spirobenzopyran side groups. *Macromolecules*, 12:1176–1180, 1979.
- [2] A. Menju, K. Hayashi, and M. Irie. Photoresponsive polymers. 3. Reversible solution viscosity change of poly(methacrylic acid) having spirobenzopyran pendant groups in methanol. *Macromolecules*, 14:755–758, 1981.
- [3] I. Karube, Y. Nakamoto, and S. Suzuki. Photocontrol of urease activity in spirocyan collagen membrane. *Biochim. Biophys. Acta*, 445:774–779, 1976.
- [4] K. Namba and S. Suzuki. Normal and reverse photochromism of 1-( $\beta$ -carboxyethyl)-3,3-dimethyl-6'-nitrospiro[indoline-2,2'-2*H*-benzopyran] in water-dioxane. *Bull. Chem. Soc. Jpn.*, 48:1323–1324, 1975.
- [5] S. Kato, M. Aizawa, and S. Suzuki. I. Light-induced potential changes across membranes incorporating a photochromic compound. *J. Membr. Sci.*, 1:289–300, 1976.
- [6] S. Kato, M. Aizawa, and S. Suzuki. II. Photo-induced potential changes across spirocyan-entrapped asymmetric membranes. *J. Membr. Sci.*, 2:39–47, 1977.
- [7] J. Anzai, A. Ueno, and T. Osa. High and rapid response in photo-induced potential changes across a poly(vinylchloride)/spirobenzopyran membrane. *J. Chem. Soc. Chem. Commun.*, pages 688–689, 1984.
- [8] T. Shimidzu and M. Yoshikawa. Photo-induced carrier mediated transport of alkali metal salts. *J. Membr. Sci.*, 13:1–13, 1983.
- [9] L. Kador, R. Fischer, R. Kasemann, S. Brück, and H. Dürr. Fine structure in the  $\chi^{(2)}$  signals of inorganic-organic nanocomposites. *J. Appl. Phys.*, 75:2709–2711, 1994.
- [10] C. B. McArdle, editor. *Applied Photochromic Polymer Systems*. Blackie, Glasgow, 1992.
- [11] A. Zelichenok, F. Buchholtz, S. Yitzchaik, J. Ratner, M. Safro, and V. Krongauz. Steric effects in photochromic polysiloxanes with spirooxazine side groups. *Macromolecules*, 25:3179–3183, 1992.
- [12] M. Irie, T. Iwayanagi, and Y. Taniguchi. Photoresponsive polymers. 7. Reversible solubility change of polystyrene having pendant spirobenzopyran groups and its application to photoresists. *Macromolecules*, 18:2418–2422, 1985.
- [13] M. Irie. Photoresponsive polymers. *Adv. Polym. Sci.*, 94:27–67, 1990.

- [14] A. Fissi, O. Pieroni, G. Ruggeri, and F. Ciardelli. Photoresponsive polymers. Photo-modulation of the macromolecular structure in poly(L-lysine) containing spiropyran units. *Macromolecules*, 28:302–309, 1995.
- [15] D. J. Chung, Y. Ito, and Y. Imanishi. Preparation of porous membranes grafted with poly(spiropyran-containing methacrylate) and photocontrol of permeability. *J. Appl. Polym. Sci.*, 51:2027–2033, 1994.
- [16] Y. S. Park, Y. Ito, and Y. Imanishi. Photocontrolled gating by polymer brushes grafted on porous glass filter. *Macromolecules*, 31:2606–2610, 1998.
- [17] P. H. Vandewyer, J. Hoefnagels, and G. Smets. Photochromic spiropyrans. *Tetrahedron*, 25:3251–3266, 1969.
- [18] R. Gautron. Photochromisme des indolinspiropyranes. *Bull. Soc. Chim. France*, 8: 3190–3200, 1968.
- [19] P. H. Vandewijer and G. Smets. Photochromic polymers. *J. Polym. Sci C*, 22:231–245, 1968.
- [20] H. Dürr. Photochromie – Stand und Entwicklungstendenzen. *Praxis d. Naturwissen. (Chemie)*, 40:22, 1991.
- [21] M. Kraus. *Functional Combocopolymers for Superhydrophobic and Superhydrophilic Surfaces*. PhD thesis, University of Ulm (Germany), 2002.
- [22] Y. A. Degutis and A. A. Shachkus. 1,2,3,9a-Tetrahydro-9H-imidazo[1,2-a]indoles. *Chem. Heterocyc. Comp.*, 23:191–194, 1987.
- [23] V. Percec, J. A. Heck, D. Tomazos, and G. Ungar. The influence of the complexation of sodium and lithium triflate on the self-assembly of tubular-supramolecular architectures displaying a columnar mesophase based on taper-shaped monoesters of oligoethylene oxide with 3,4,5-tris[*p*-(*n*-dodecan-1-yloxy)benzyloxy]benzoic acid and of their polymethacrylates. *J. Chem. Soc. Perkin Trans.*, 2:2381–2388, 1993.
- [24] V. Percec, W.-D. Cho, P. E. Mosier, G. Ungar, and D. J. P. Yeardley. Structural analysis of cylindrical and spherical supramolecular dendrimers quantifies the concept of monodendron shape control by generation number. *J. Am. Chem. Soc.*, 120:11061–11070, 1998.
- [25] V. Percec, W.-D. Cho, G. Ungar, and D. J. P. Yeardley. Von molekularen Kreissegmenten, Scheiben und Kegeln zu supramolekularen Zylindern und Kugeln mit an der Peripherie modifizierten Fréchet-Monodendren. *Angew. Chem.*, 112:1661–1666, 2000.

# 6 Reversible collapse of polymer brushes

## 6.1 Introduction

Scanning force microscopy (SFM) enables visualization of single macromolecules on a flat substrate, and controlled environmental conditions allow to examine the dynamics of macromolecules in situ. SFM has been employed to study the morphology of individual polymer molecules, e. g. DNA [1], RNA [2], and their complexes with proteins [3], surfactants [4], and other compounds. Ex situ visualizations of conformational changes of DNA molecules were carried out for macromolecules interacting with oppositely charged silanes [5], polymer nanoparticles [6], surfactants [7],  $Mg^{2+}$  cations (in ethanol) [8], spermidine [9, 10], polylysine [11, 12], poly(ethylene glycol)-poly(amidoamine) copolymer [13], lipospermine, and polyethylenimine [14]. Generally, the information obtained in these experiments was already available before from electron microscopy studies [15]. One of the main advantages of SFM in comparison with electron microscopy is the possibility to investigate in situ and to visualize in real-time the dynamics of molecule transformations. Thus, the condensation of DNA molecules could be observed in a water-alcohol mixture [16] directly by an SFM equipped with a liquid cell. The molecules collapsed at increasing alcohol concentration. SFM allowed firstly to follow the partially compacted macromolecules on the substrate [17], and secondly their partial unfolding as the alcohol concentration was decreased again. Another example concerns the in situ study of DNA interacting with oppositely charged polymer macromolecules [18], and with RNA polymerase [19]. Thomson et al. [20] visualized the dynamics of the adsorption of DNA onto mica at changing buffer conditions.

The reasons why most of these studies focus on DNA molecules are their size and rigidity. The lateral resolution in SFM is determined by the size of the tip-sample contact area, which is typically a spot with a diameter of one nanometer and more. To visualize clearly details of the conformation of an adsorbed macromolecule its lateral sizes (e. g. curvature radii) should be larger than the SFM lateral resolution. The rather stiff and thick DNA molecule satisfies these conditions and hence can be imaged rather easily by SFM.

Brush-like macromolecules are also suitable model compounds for SFM studies [21–24]. Brush polymers consist of a macromolecular backbone densely grafted by macromolecular side chains. The steric repulsion between the side chains imposes an effective rigidity of the brush macromolecule. At the same time the thickness facilitates good visibility in SFM. Interaction, i. e., adsorption of the side chains on a flat substrate enforces an extended 2D-conformation of the backbone [21, 24]. It has been shown [21], that a conformational collapse of the brush molecules can be induced by increasing the surface pressure on a Langmuir monolayer of such macromolecules on a water sub-phase. The brush molecules underwent a transition from an extended two-dimensional worm-like conformation to a compact globule. It was also shown that the transition could be reversed when the surface pressure was reduced again. The compacted molecules unfolded and resumed an extended conformation. At a critical pressure the collapsed and the extended state coexisted even within one molecule. The latter observation has been regarded as an indication that the

Table 6.1: Molecular characterization of poly(methacrylate)-*graft*-poly(*n*-butyl acrylate) brush molecules

name	macroinitiator DP	side chains DP	grafts per monomer in the backbone
PMA- <i>g</i> -PBuA(l)	pBPEM, 3700	<i>n</i> -BA, 30	1
PMA- <i>g</i> -PBuA(s)	pBPEM, 400	<i>n</i> -BA, 100	1

transition is of the first-order type. However, in order to image the molecular structure at the different states of compaction the monolayer film had to be transferred onto a substrate. This approach did not allow to observe the dynamics of the conformational transition of single molecules.

As earlier theoretically analyzed, the conformation of the brush molecules is determined by the balance of the interfacial interaction forces and entropic forces [21, 24]. Controlled variation of the environment, e. g. introduction of solvent vapor or changes in temperature, can shift this balance and effect conformational changes. Kumaki et al. [25] have revealed that poly(methyl methacrylate) blocks of PS-*b*-PMMA molecules deposited onto mica can transform into an extended conformation if the sample is exposed to water vapor saturated atmosphere. Apparently, the presence of a thin absorbed water layer can enhance the mobility of the chains and affect their conformational rearrangement. Balnois and Wilkinson [26] and Morozov et al. [27] have also reported that the morphology of macromolecules deposited onto mica can change significantly if the sample is exposed to humid air.

In this chapter poly(methacrylate)-*graft*-poly(*n*-butyl acrylate) (PMA-*g*-PBuA) brushes on mica were exposed to water and ethanol vapors and followed by in situ SFM imaging. It is demonstrated that the dynamics of the collapse to a globule and its reversion can be controlled and followed in real time. Finally, the system is extended to other substrates (HOPG, Si, SrTiO<sub>3</sub>), a variety of solvent vapors, and a general mechanism is proposed.

## 6.2 Experimental

### 6.2.1 Materials

The PMA-*g*-PBuA brush molecules were prepared by grafting *n*-butyl acrylate from a poly(2-(2-bromo propionyloxy)ethyl methacrylate) (pBPEM) macroinitiator using atom transfer radical polymerization reaction as described before [28]. The synthesis was done in the group of Prof. K. Matyjaszewski (Carnegie Mellon University, Pittsburgh, USA). The two samples employed in this study differed in the lengths of the macromolecular backbone and of the grafts as well. Table 6.1 summarizes the corresponding degrees of polymerization.

Milli-Q water (Milli-Q Plus 185), ethanol, chloroform, isopropanol, diethyl ether, ethyl acetate, ethylene glycol, dimethyl sulfoxide, N,N-dimethylformamide (DMF) and cyclohexanone of analytical grade (Merck) were used as received throughout the experiments.

Muscovite mica (BAL-TEC), highly oriented pyrolytic graphite (Plano), Silicon(113)-wafer (CrysTec) and SrTiO<sub>3</sub>(305) single crystals (CrysTec) were chosen as substrates on which the polymer molecules were deposited by spin-coating from a solution in chloroform



Figure 6.1: Experimental setup: Molecular Imaging PicoSPM with environmental chamber. The Petri-dish inside the chamber is used to deliver the solvent vapors. In the background is the vibration damping system based on bungee cords, mounted into a soundproof box

( $c = 0.002\text{--}0.02$  mg/ml; 2000 rpm; 25 s) using a WS400 spin processor (Laurell Technologies).

### 6.2.2 Scanning force microscopy in vapor atmospheres

SFM images were recorded by means of the acoustic mode with a ‘PicoSPM’ scanning probe microscope (Molecular Imaging, USA, Figure 6.1). In order to introduce solvent vapor to the atmosphere around the sample 0.3–0.7 ml of solvent or a mixture of solvents was injected into the microscope’s environmental chamber (volume of  $\approx 1.21$ ). The injection was performed without interruption of the scanning procedure through special inlets in the device panel. In order to replace the vapor by a dry atmosphere and to remove also traces of solvents from the sample surface, dry nitrogen (99.999 % purity, MTI Industrie Gase AG, Germany) was blown through the chamber. SFM images were collected with an information density of  $512 \times 512$  points at 1 Hz scanning frequency. Silicon FM-W cantilevers (NanoWorld, Switzerland) with a resonance frequency of 68–87 kHz were used.

## 6.3 Results and discussion

### 6.3.1 Collapse/decollapse dynamics of short PMA-*g*-PBuA brush molecules on mica in ethanol/water atmosphere

As deposited by the spin-coating procedure the polymer brushes attained a highly extended worm-like conformation, see e. g. Figures 6.2, 6.3a, 6.4a, 6.6a, and 6.7a. Generally, there was no significant difference for the molecular conformation on mica, silicon, SrTiO<sub>3</sub> or on HOPG, in spite of the very different polarities of these substrates. The substrates differ

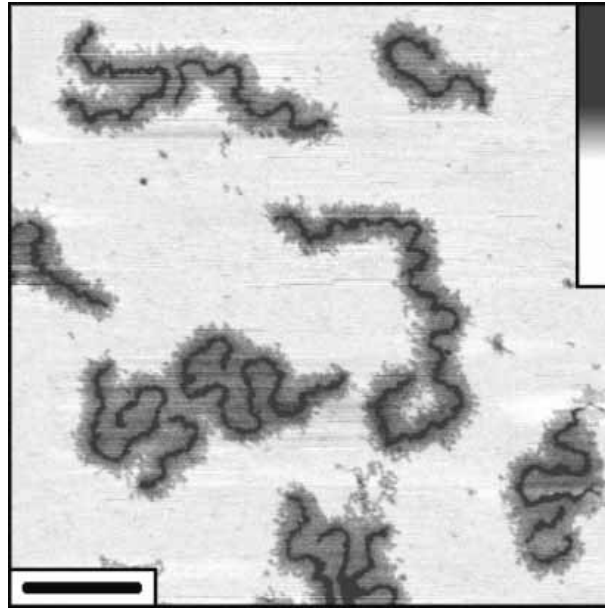


Figure 6.2: High-resolution SFM image of PMA-*g*-PBuA(1) brush molecules on mica. One can see the two-dimensional coronas of side chains surrounding the backbones. Bar size: 150 nm, grey scale: 5 nm

mostly in the efficiency by which they bind the molecules during the spin-coating process: at equal conditions, solution concentration, etc. more molecules were adsorbed on mica, silicon and SrTiO<sub>3</sub> than on HOPG. The drying procedure (solvent removal) did not affect the macromolecular conformation. In other cases, e. g. deposition of flexible single-chain macromolecules (such as RNA molecules of a tobacco mosaic virus [3, 29]), the drying procedure is rather critical and can result in significant changes of the macromolecular conformations as well as in aggregation [30]. The fact that macromolecules adsorbed mostly as separated individual polymer chains with only occasional intersection points indicates that the deposition of the molecules takes place by adsorption from solution and that the repulsion of the side chains in a good solvent (chloroform) causes an extended conformation of the macromolecules already in solution. In particular, in the case of the molecules with a long backbone and long side chains, adsorption is accompanied by a significant penalty in entropy. Thus, even in a good solvent, the interaction energy with the substrate must be strong [21, 24]. It was already shown [21], that the conformation of PMA-*g*-PBuA brushes on mica is essentially that of a flat 2D brush: the backbone is surrounded by a two-dimensional aureole of the side chains, see Figure 6.2. This results in a very small contact area (contact line) between the individual adsorbed brush molecules. Together with the small surface tension of chloroform only very small capillary forces can act between the molecules during solvent evaporation and the molecules conformation is little affected by the drying procedure.

This extended adsorbed state is stable in dry air and nitrogen atmosphere. Attempts to affect the collapse of the molecules by raising the temperature failed. Even at temperatures up to 200 °C, the molecules did not desorb from the mica substrate, but started to degrade. However, when we saturated the atmosphere over the sample by ethanol vapor, we observed a direct response of the molecular conformation already at room temperature. A series of

SFM images that depicts the collapse of the single isolated short brush molecules is shown in Figure 6.3a-e. The transformation has been observed in real time and the images in Figure 6.3 represent the most important stages. Figure 6.3a depicts the brush molecules as deposited and observed in dry atmosphere. Figure 6.3b was recorded directly during ethanol was injected into the sample chamber and the atmosphere started to become saturated by alcohol vapor. At the bottom of the image the molecules did not change yet compared to Figure 6.3a, on top, however, one recognizes a considerable increase in thickness which is explained by uptake of ethanol, i.e. swelling. The height in the SFM-profile increased from about 1.5–2.5 nm up to 3–5 nm.

After about 10 min, the swollen brushes started to contract forming hemispheric particles with a height of 4–8 nm (Figure 6.3c-d). Complete transformation to globules was observed after 20–30 min exposure to ethanol vapor. Because the molecules also gained mobility and started to diffuse along the surface they tended to aggregate to clusters of several molecules when the sample was exposed further to ethanol.

The transformation could be frozen at any state when the ethanol-saturated atmosphere was replaced by dry nitrogen (the sample chamber was purged with N<sub>2</sub>). Deswelling of the globules resulted in a decrease in height by 30–60 % but not in any change in the molecular conformation.

Images in Figure 6.3e-i depict the effect that was observed when water was subsequently introduced in the sample chamber following the drying procedure. Once the atmosphere got saturated by water vapor, the aggregated molecules started to separate and the individual molecules adopted again an extended conformation. Both the decomposition of aggregates and the straightening of the molecules is remarkable.

After several hours the molecules ceased and we assume that the extended worm-like slightly curved conformation is near to the equilibrium state. The curvature of the molecules is in agreement with the model recently proposed by Potemkin et al. [24]. Based on a scaling approach, the model demonstrates that a 2D-brush tightly adsorbed on a flat substrate will preferentially adopt a curved state with an uneven distribution of the side chains between the two sides of the backbone, provided that the side chains are long enough. The driving force is a gain in configurational entropy. The apparent distance between the worm-like molecules – only the backbone can be seen in the images – is larger than 25–30 nm, which corresponds well to the width of the corona of side chains as depicted in Figure 6.2. The height of the extended molecules within a water-saturated atmosphere was measured to be the same as the value in dry conditions. This indicates that the uptake of water or swelling of the brush molecules is small and negligible compared to the situation found for ethanol (Figure 6.3a-e).

For selected particular molecules we could compare the lengths before and after the ‘collapse-decollapse’ cycle. A decrease by not more than 5-10 % was measured, which can be explained by the redistribution of side chains from an even left/right distribution (as cast) to an uneven left/right distribution after equilibration by the ethanol/water vapor treatment.

### 6.3.2 Collapse/decollapse dynamics of long PMA-*g*-PBuA brush molecules on mica in ethanol/water atmosphere

The high molecular weight PMA-*g*-PBuA(1) brushes showed similar properties as the shorter molecules discussed before. However, due to the improved length, the transformation was more expressed but also the observation comprised further details. Figure

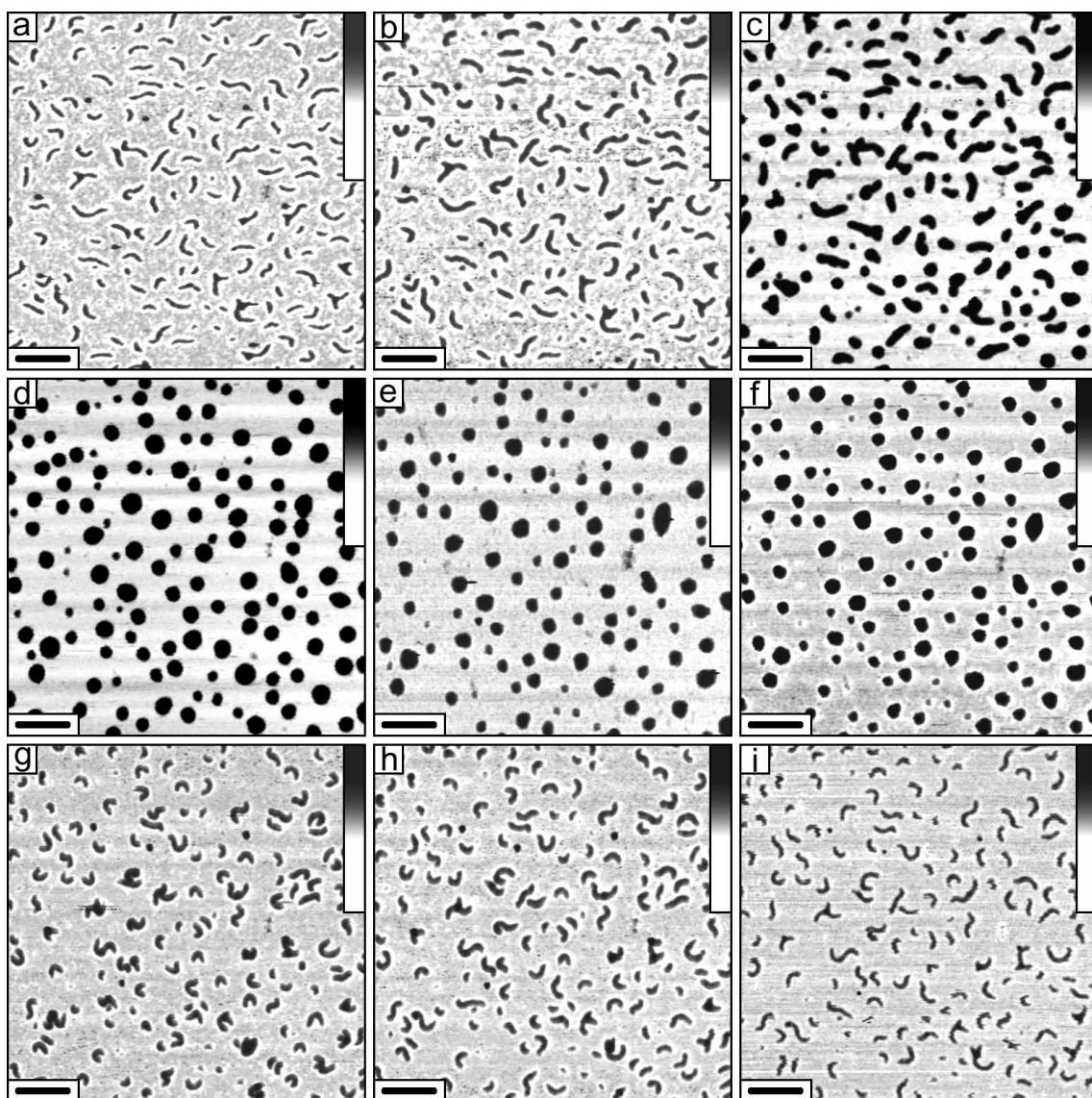


Figure 6.3: Sequence of SFM images that demonstrate the collapse/decollapse dynamics of PMA-*g*-PBuA(s) brush molecules on mica in an atmosphere with varying ethanol and water partial pressure. a: initial image of sample in dry N<sub>2</sub> atmosphere; b: image obtained during injection of ethanol abs. to the sample space; c,d: images obtained 14 min (c) and 23 min (d) after ethanol injection; e: image after the sample space was purged with dry N<sub>2</sub> again, molecules remain in the collapsed state; f: image obtained during injection of water to the sample space; g-i: images obtained 15 min (g), 24 min (h), and 1.5 h (i) after water injection. The temperature was kept constant at 24 °C corresponding to a partial vapor pressure of 7.4 kPa for ethanol and 3 kPa for H<sub>2</sub>O; bar size: 300 nm, grey scale: 10 nm



6.4 depicts a series of images taken at different times after the extended molecules were exposed to ethanol vapor. Initially, swelling of the individual molecules resulted in an increased width and height. Typically, the height of PMA-*g*-PBuA(l) brushes above the substrate was equal to 0.2–0.8 nm after spin-coating sample preparation (before exposure to ethanol vapor), see Figure 6.4a. As a result of the exposure to ethanol vapor the height increased to 1.5–4 nm, see Figure 6.4b-d. Collapse of the extended swollen chain could, however, only be achieved if besides ethanol (abs.) also a small amount of water was introduced into the sample atmosphere ( $P_{\text{H}_2\text{O}, 24^\circ\text{C}} = 3 \text{ kPa}$ ;  $P_{\text{ethanol}, 24^\circ\text{C}} = 37.4 \text{ kPa}$ ). Exposed to ethanol/water vapor the smaller molecules started to collapse preferentially at the chain end. This is seen in Figure 6.4c-e by the occurrence of small nodules at the ends of the chains. These nodules increase in size and move toward the center of the molecule as they ‘eat up’ the inner segments (see Figure 6.4e-h). The collapse stops with coagulation of two nodules to an individual globule.

If the distance between the molecules was small (i. e. the surface density was high), the collapse proceeded in a more complicated manner. In this case, the nearest strands of different molecules could stick together, and complex intermolecular aggregates were formed which finally tended to adopt a spherical shape. Further exposure to ethanol vapor resulted in further aggregation. Again the transformation could be frozen at any stage by venting the chamber with nitrogen. This allowed it to ‘freeze’ molecules in a partially compacted conformation, see Figure 6.4h and i (‘dumbbell-like’ conformation).

In ethanol vapor the sizes of globules formed from individual molecules were in the range of 6–12 nm. Drying with nitrogen resulted in 20–50 % decrease of the globule size.

The compaction process is going slower for the longer brushes than for the smaller ones. Typically, it took several hours starting from the injection of ethanol in the chamber.

Like in the case of the shorter brush molecules decollapse and re-extension of the compacted long brush molecules was observed in a water vapor saturated atmosphere. Figure 6.5 presents images taken at different stages of the decollapse process in real time. Before water was introduced the sample had been thoroughly dried in a nitrogen flow to remove any traces of ethanol. One can see how individual strands of the molecules crawl out of the globules and untwine. The molecules spread out across the surface increasing the distance between them and decreasing their curvature. The molecular motion stopped when the molecular strands were separated by a distance of 20–35 nm and had adopted a distinct curvature [24].

Like in the case of the smaller brushes the height values measured in dry atmosphere (in air and in nitrogen) and in water saturated atmosphere did not differ. Similarly no significant change in the contour length for dry and humidified molecules was observed. This indicates little uptake of water, i. e. swelling.

### 6.3.3 Collapse/decollapse experiments of PMA-*g*-PBuA brush molecules on HOPG, SrTiO<sub>3</sub> and silicon substrates in ethanol/water atmosphere

Attempts to study the same collapse-decollapse with HOPG as a substrate were performed. It was found, that on HOPG both the long and the short brush molecules thickened only slightly when the sample was exposed to ethanol vapor. However, the ethanol did not affect the collapse. At the same time the molecules gained some mobility and reorganized to form clusters and to align along the terraces of the HOPG layers. Thus, mobility can be introduced without collapse, provided the adsorption remains sufficiently strong. We believe that the reduced swelling and the stability of the extended conformation of the

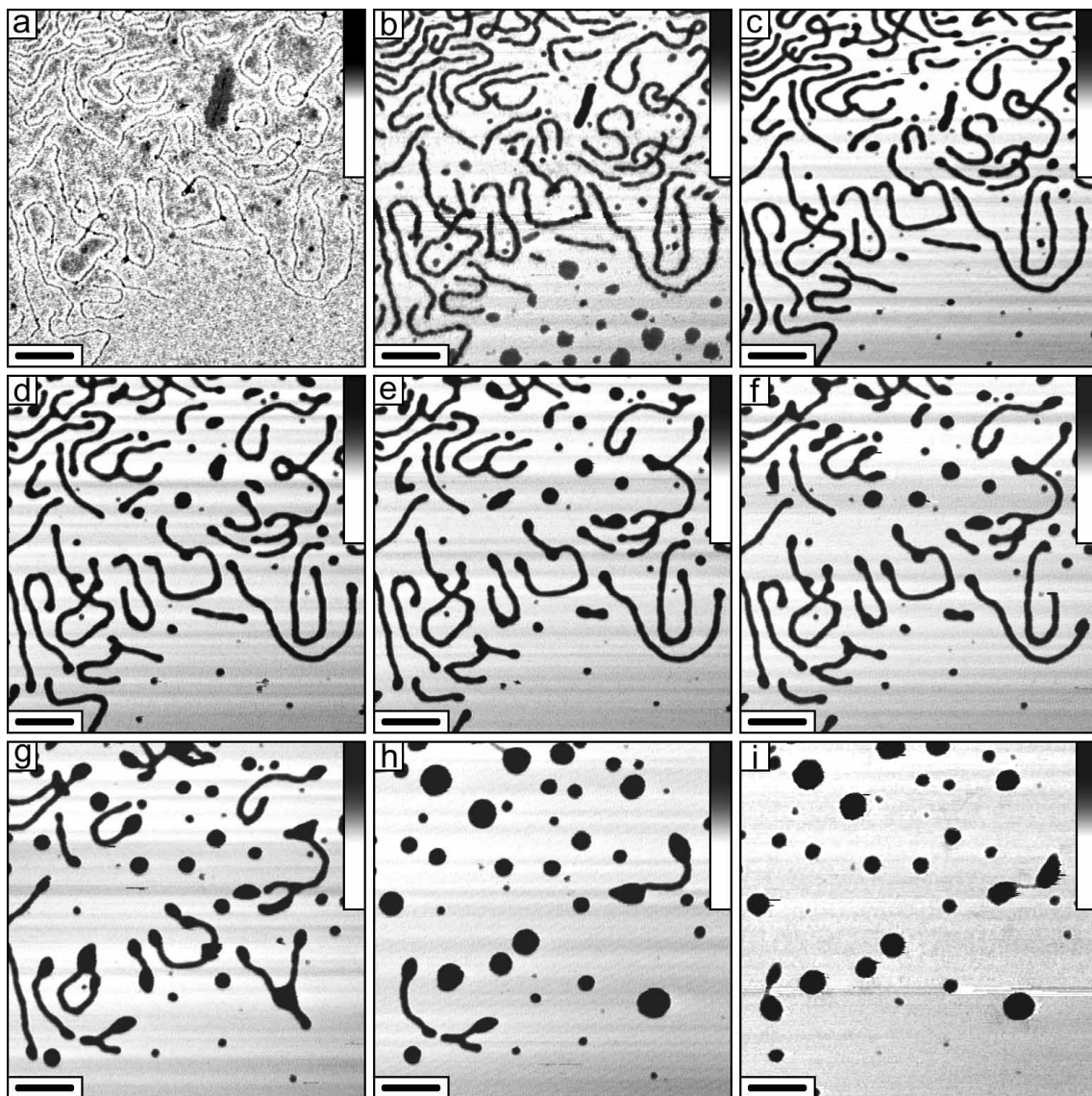


Figure 6.4: SFM visualization of the collapse dynamics for long PMA-*g*-PBuA(1) brush molecules on mica in ethanol vapor. a: initial image of the spin-coated sample thoroughly dried under nitrogen; b: image obtained in ethanol abs. vapor 18 min after injection of absolute ethanol. In the pure ethanol atmosphere, the molecules swelled but did not collapse yet. Only when one droplet of water was added into the chamber after 1.6 h the collapse of the individual molecules was observed; Figures c, d, and e depict images recorded 1.8 h (c), 2.1 h (d), and 3 h (e) after the first ethanol injection. At this water concentration the structural transformation stopped again at the state shown in Figure e and only when another droplet of water was added into the chamber 3.1 h after ethanol injection total collapse could be observed; f-h: images obtained 3.2 h (f), 3.4 h (g), and 3.5 h (h) after ethanol injection; i: final image of compacted molecules after drying with nitrogen flow. The temperature was kept constant at 24 °C. Bar size: 300 nm, grey scale: 10 nm

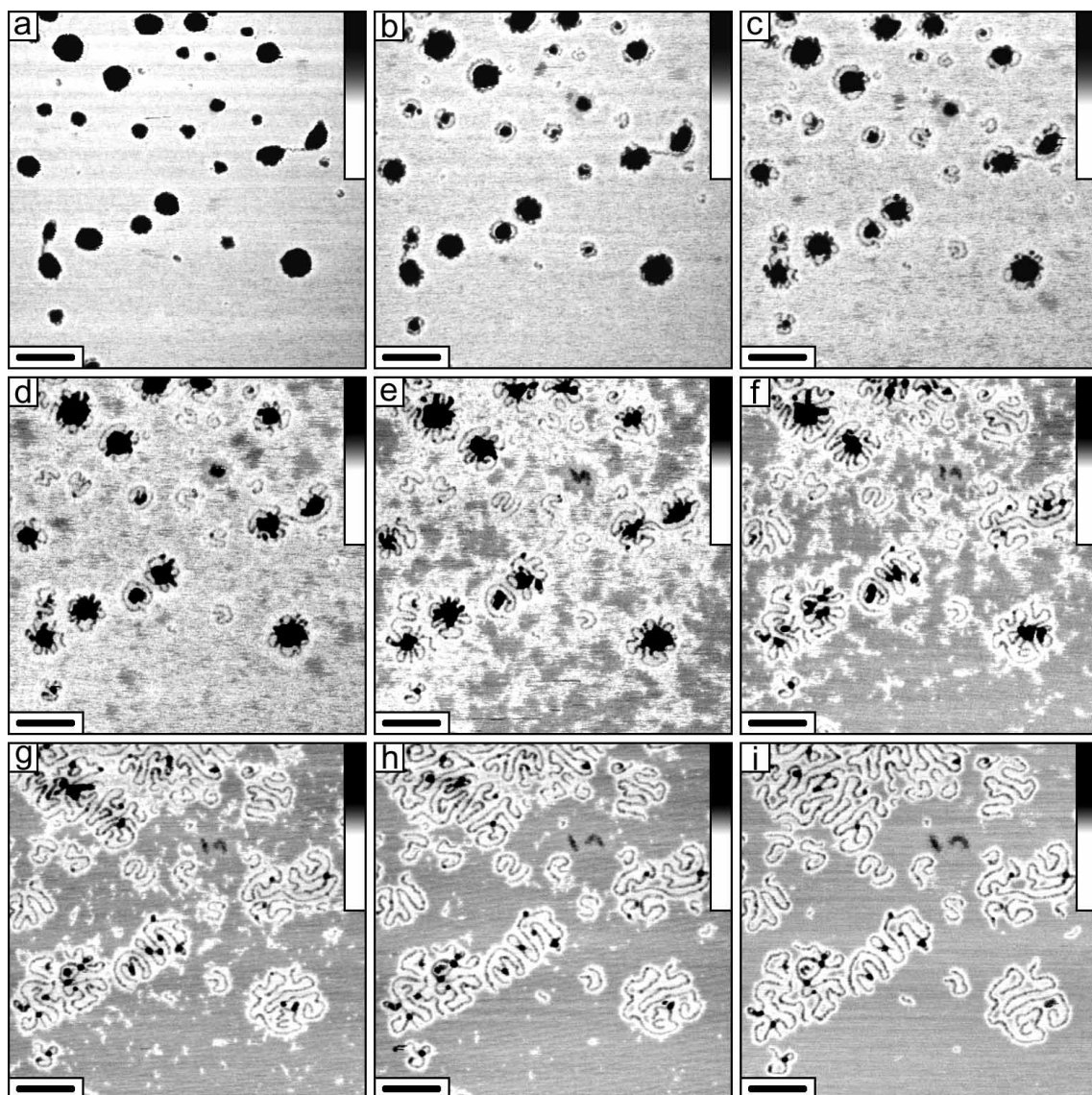


Figure 6.5: SFM visualization of the decollapse dynamics for long PMA-*g*-PBuA(1) brush molecules on mica in water vapor (the figure depicts the same section as Figure 6.4i after drying the sample with nitrogen flow). a-i: images obtained 13 min (a), 22 min (b), 30 min (c), 39 min (d), 1 h (e), 1.5 h (f), 2 h (g), 4 h (h), and 15 h (i) after water injection. The temperature was kept constant at 24 °C. Bar size: 300 nm, grey scale: 10 nm

brush molecules on HOPG is to be explained by the different interaction of water as well as of ethanol with the surface of HOPG in comparison to mica. Only in the latter case  $\text{H}_2\text{O}$  is expected to form a well defined ad-layer that can moderate the interaction of the brush molecules with the substrate strongly.

Mica as a strong polar substrate is the exact opposite to the non-polar HOPG. Furthermore mica has special properties because of its polyionic surface structure. Other polar substrates that are able to form a water ad-layer should show the same behavior as mica. In Figure 6.6 and 6.7 the experiments on  $\text{SrTiO}_3$  and silicon are shown and indeed similar observations were made. On  $\text{SrTiO}_3$  a slow collapse dynamics was observed (Figure 6.6a-d). The molecules collapsed only partially and the addition of a small amount of water did not enhance the collapse process (Figure 6.6e). After drying with nitrogen the sample was exposed to water vapor and the molecules started to separate and regained their extended conformation (Figure 6.6f-i).

The brush molecules on silicon swelled immediately after exposure to ethanol vapor (Figure 6.7b) and showed very fast aggregation within 30 minutes (Figure 6.7c-d). Also the decollapse process was observed when the sample was subsequently exposed to water vapor.

### 6.3.4 The role of water in the rod-globule transition

The critical role of water is also demonstrated by the following observation: when the sample with the brush molecules deposited on mica was extensively dried after spin-coating (under  $\text{N}_2$  flow) we observed thickening by the uptake of ethanol but the brush molecules did not start to collapse within at least 12 hours. This is the similar behavior as described above for HOPG. When we introduced, however, only a relatively small amount of water (see also the discussion of the result shown in Figure 6.4) into the sample space, the collapse occurred within few minutes for the brushes previously swollen in ethanol vapor during several hours.

It is concluded that swelling of the brush molecules is not sufficient to introduce the rod-globule transition, but that additionally an ad-layer of water must be formed at the surface of mica.

‘Lubrication’ or competitive desorption by water is also supported by the following observation. Attempts to flush the brush molecules from the mica substrate by putting a droplet of a solvent onto the rotating sample in the spin-coater, it was found that water was much more efficient in comparison to ethanol or even the good solvent, i. e. chloroform.

Systematic variation of the amount of water that was added to the ethanol revealed that injection of an 80 %/20 % vol. ethanol/water mixture into the environmental chamber was most efficient to affect a fast collapse of the long brush molecules. In this case complete collapse took place within 30 min, see Figure 6.8.

So far it is described that wet ethanol vapor favors the collapse while pure water vapor promotes extension. Now the question is addressed, which is the critical ethanol to water ratio for the transition from the extended to the globular state. Injection of ethanol/water mixtures with 20 % vol. or less of ethanol into the environmental chamber did not induce collapse. Injection of an ethanol/water mixture with 30 % vol. of ethanol (or more) induced collapse in half an hour. When the ethanol/water composition was 25 %/75 % vol. the molecules collapsed but did not form well-shaped globules. Moreover, during several hours in the same atmosphere the molecules were decollapsing very slowly. Such a kinetic effect should be pronounced near the critical composition. Hence, the critical composition is

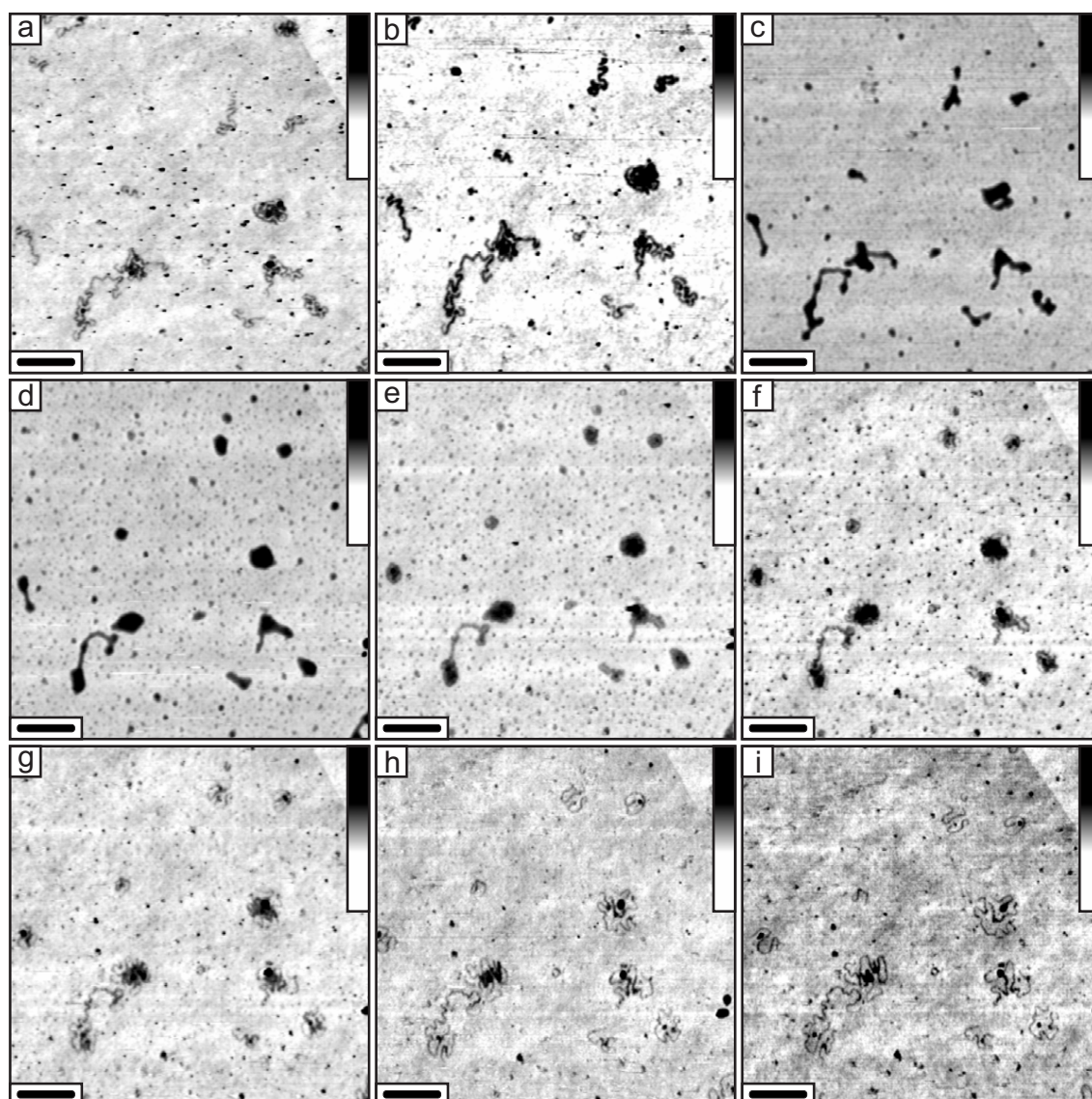


Figure 6.6: Sequence of SFM images that demonstrate the collapse/decollapse dynamics of PMA-*g*-PBuA(1) brush molecules on SrTiO<sub>3</sub> substrate in an atmosphere with varying ethanol and water partial pressure. a: initial image of the sample in dry N<sub>2</sub> atmosphere; b: image obtained during injection of ethanol abs. to the sample space; c,d: images obtained 31 min (c) and 13.7 h (d) after ethanol injection leading to partial collapse; e: a small amount of water was added and within 1.6 hours no changes occurred. Finally the sample was dried with dry N<sub>2</sub> again, the molecules remain in the partially collapsed state; f-i: images obtained 16 min (f), 47 min (g), 2.1 h (h) and 6.7 h (i) after water injection. The temperature was kept constant at 24 °C. Bar size: 300 nm, grey scale: 10 nm

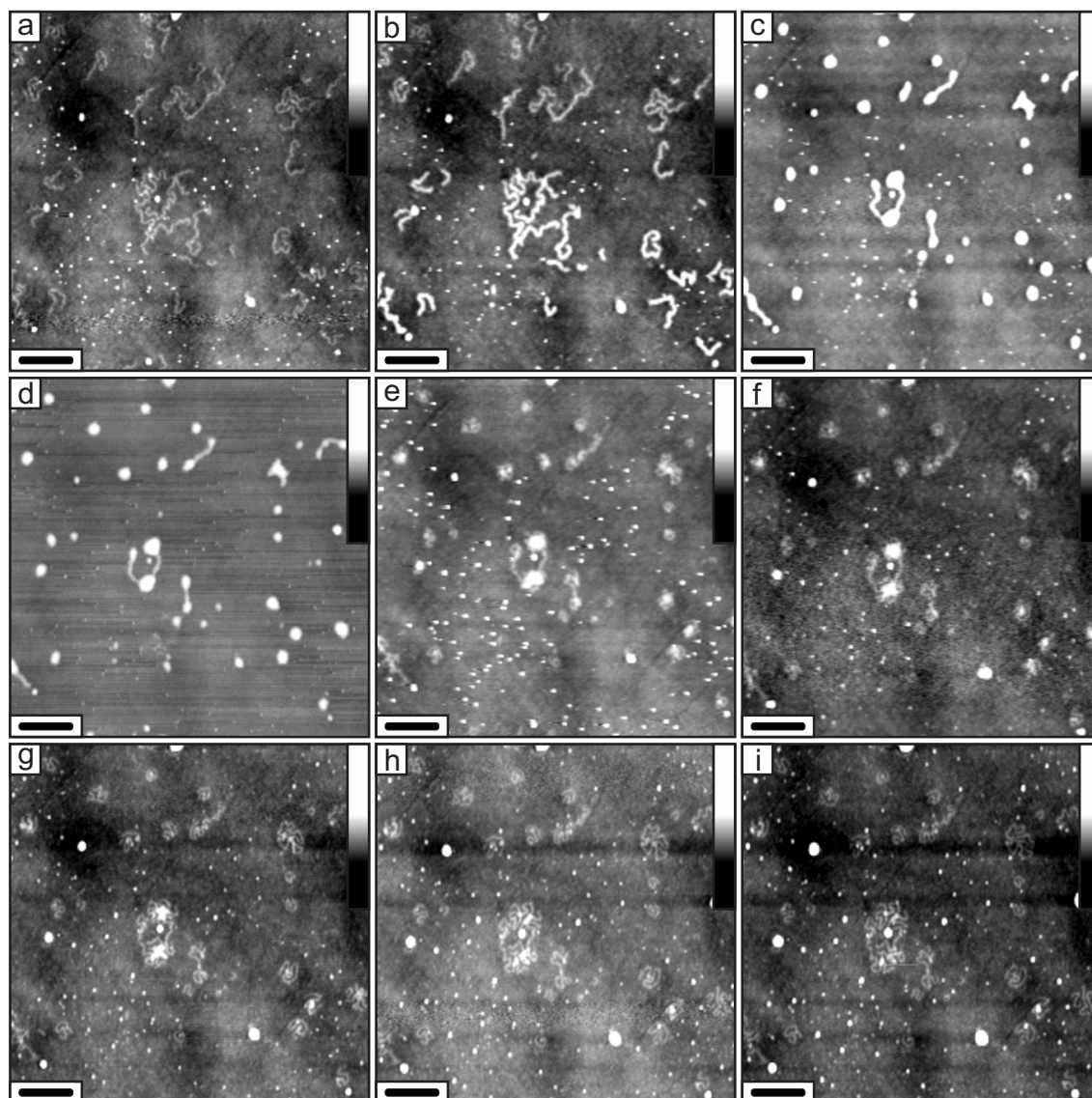


Figure 6.7: Sequence of SFM images that demonstrate the collapse/decollapse dynamics of PMA-*g*-PBuA(1) brush molecules on silicon substrate in an atmosphere with varying ethanol and water partial pressure. a: initial image of the sample in dry N<sub>2</sub> atmosphere; b: image obtained during injection of ethanol abs. to the sample space; c,d: images obtained 15 min (c) and 31 min (d) after ethanol injection. Fast collapse without addition of water; e: image after the sample space was purged with dry N<sub>2</sub> again, molecules remain in the collapsed state; f-i: images obtained 46 min (f), 1.6 h (g), 4.3 h (h) and 7.6 h (i) after water injection. The temperature was kept constant at 24 °C. Bar size: 300 nm, grey scale: 10 nm

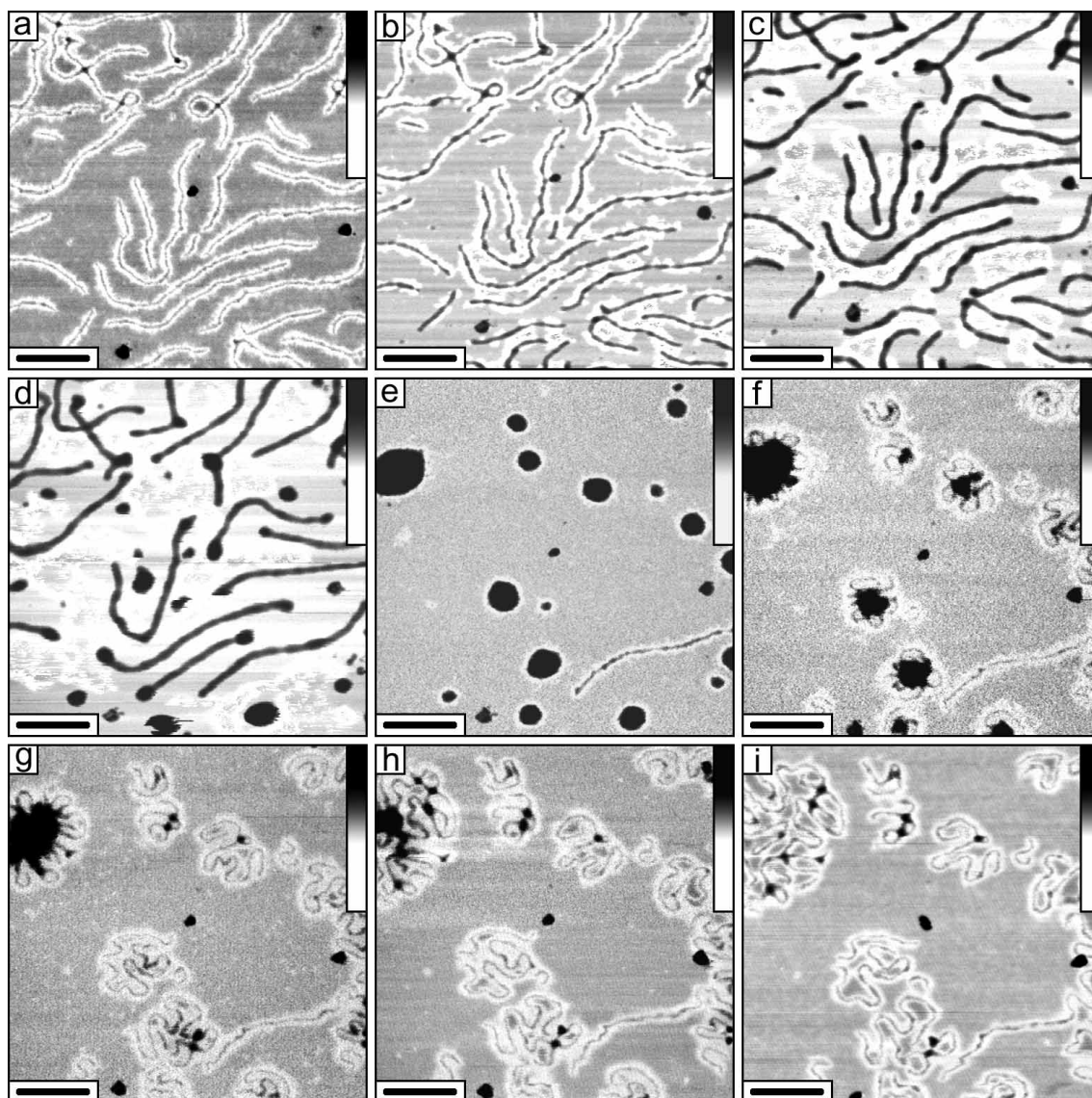


Figure 6.8: SFM visualization of the collapse/decollapse dynamics for long PMA-*g*-PBuA(1) brush molecules on mica in ethanol/water vapor. a: initial image of the dry sample as spin-cast; b-d: images obtained 9 min (b), 18 min (c) and 26 min (d) after injection of 80 %/20 % ethanol/water mixture; e: image of compacted molecules after purging with dry nitrogen; f-i: images recorded 17 min (f), 35 min (g), 1 h (h) and 16 h (i) after water injection. The temperature was kept constant at 24 °C. Bar size: 250 nm, grey scale: 10 nm

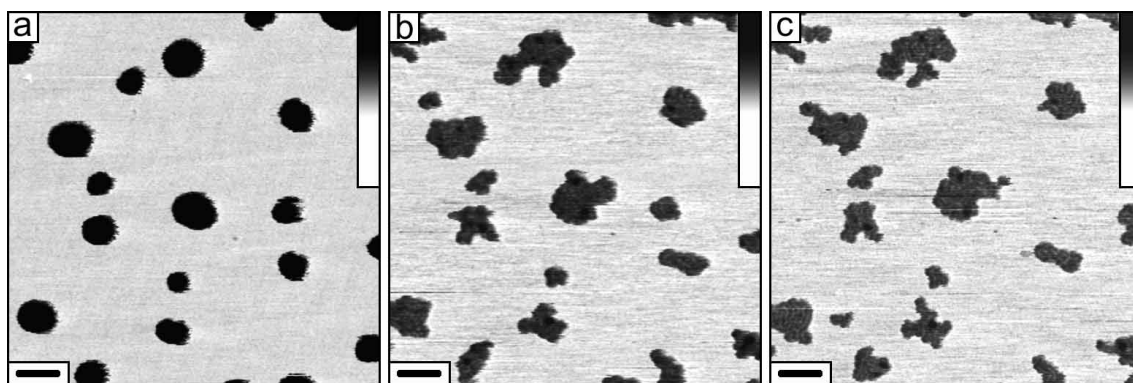


Figure 6.9: SFM images of collapsed and partially collapsed long PMA-*g*-PBuA(1) brush molecules after equilibration under ethanol/water vapor of different composition. a: image at 30 % vol. of ethanol (60 h after mixture injection); b: after 24 h at 25 % vol. of ethanol (the same place), and c: after 8 h at 20 % vol. of ethanol (the same place). The temperature was kept constant at 24 °C. Bar size: 300 nm, grey scale: 10 nm

estimated to be about 30 % vol. of ethanol content. The delayed decollapse can be explained by the different vapor pressures. Ethanol is more volatile than water and depending on the relative amounts of ethanol/water in the vapor, water adsorption at the mica surface can be delayed. Injection of a liquid mixture into the chamber, will initially result in a relatively higher concentration of ethanol in the vapor phase than in equilibrium. But after the equilibration, the ethanol concentration in the film adsorbed at the mica surface will reflect the composition of the liquid introduced to the sample space. So, it is concluded, that the critical composition for the adsorbed film is also about 30 % vol. of ethanol. Figure 6.9 presents equilibrated structures for the long brush molecules adsorbed on mica after they had been exposed to ethanol/water vapor of different composition.

The observation of a critical ethanol/water composition and the fact that the collapse was only observed on mica but not on the less strongly interacting HOPG is considered a key point for the explanation of the experimental observation. Water is a very poor and ethanol is still a non-solvent for the PMA-*g*-PBuA brush molecules [31]. Therefore, it is natural to expect, that both of them should induce a condensation of macromolecules in the bulk (i. e. in the three-dimensional case). In the two-dimensional case (in ultrathin layers adsorbed onto mica) water behaves like a ‘two-dimensionally’ good solvent for the brushes, whereas ethanol is still a ‘two-dimensionally’ poor solvent. For the mixture of these two solvents the transition point is near 30 % vol. of ethanol. What could be the possible reason for the observed difference in molecular behavior in ‘two-dimensional’ water and ethanol?

It is suggested that the difference in surface tensions of water and ethanol determines the observed phenomena. Indeed, surface tension of pure water (71.9 mN/m) is much higher than that of ethanol (22.2 mN/m). Surface tension of a water/alcohol mixture decreases monotonically with an increase of ethanol content (Figure 6.10) and is equal to about 35 mN/m at 30 % vol. of ethanol concentration [32]. Surface tension of poly(*n*-butyl acrylate) is found in the range of 31–34 mN/m [31], and this range is very close to the value for water/ethanol mixture at the point of transition from collapse to decollapse. It is



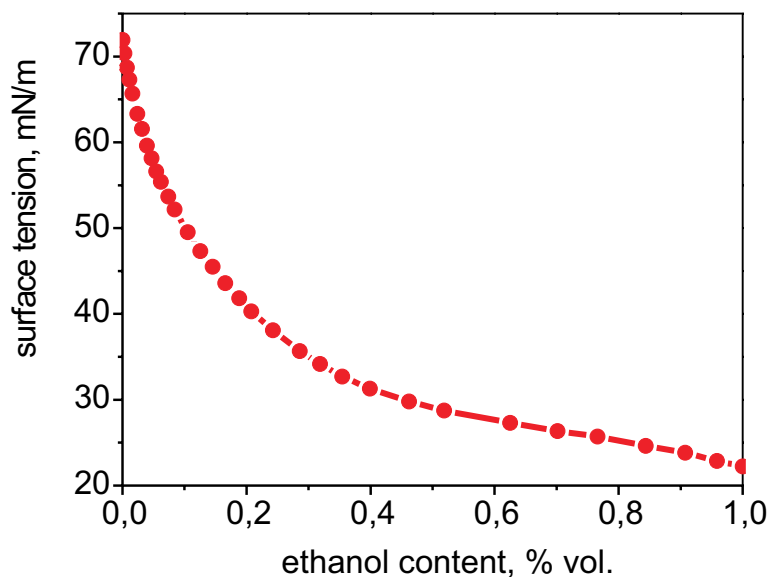


Figure 6.10: Surface tension of ethanol/water mixtures at 20 °C

natural to make the conclusion about the relationship between surface tension and driving forces of the observed collapse/decollapse processes.

To prove the assumption that the surface tension is the key parameter that decides whether a collapse or decollapse dynamics is observed, a variety of solvent vapors was tested. The solvents and the corresponding surface tensions are given in table 6.2. On the left side are the solvents listed that have a lower surface tension as poly(*n*-butyl acrylate). On the right side the solvents with higher surface tension.

### 6.3.5 Collapse/decollapse experiments of PMA-*g*-PBuA brush molecules on mica in different solvent vapors

Figure 6.11 shows the collapse/decollapse dynamics for PMA-*g*-PBuA(s) molecules on mica in saturated ethyl acetate/ethylene glycol atmosphere. The polymer molecules show the same swelling and collapse behavior with ethyl acetate as with ethanol vapor. Also the decollapse dynamics in ethylene glycol is very similar to the one observed with water vapor. The decollapse is by a factor of 5–10 slower compared to the situation with water vapor.

In the Figures 6.12, 6.13, and 6.14 the collapse/decollapse dynamics for PMA-*g*-PBuA(l) molecules on mica in saturated Isopropanol/DMSO, diethyl ether/DMF, and ethyl acetate/cyclohexanone atmosphere is shown. In all three cases the addition of the low surface tension solvent induces only the swelling of the polymer brushes. After adding a small amount of water a fast collapse was observed, supporting the theory that a thin ad-layer of water is necessary for the collapse process. As in the previous experiment with the short brush molecules, the decollapse was also slowed down by a factor of 5–10. Especially slow was the decollapse dynamics with cyclohexanone vapor, because of the surface tension of cyclohexanone (34 mN/m) being just slightly above the one of poly(*n*-butyl acrylate) (31–34 mN/m).

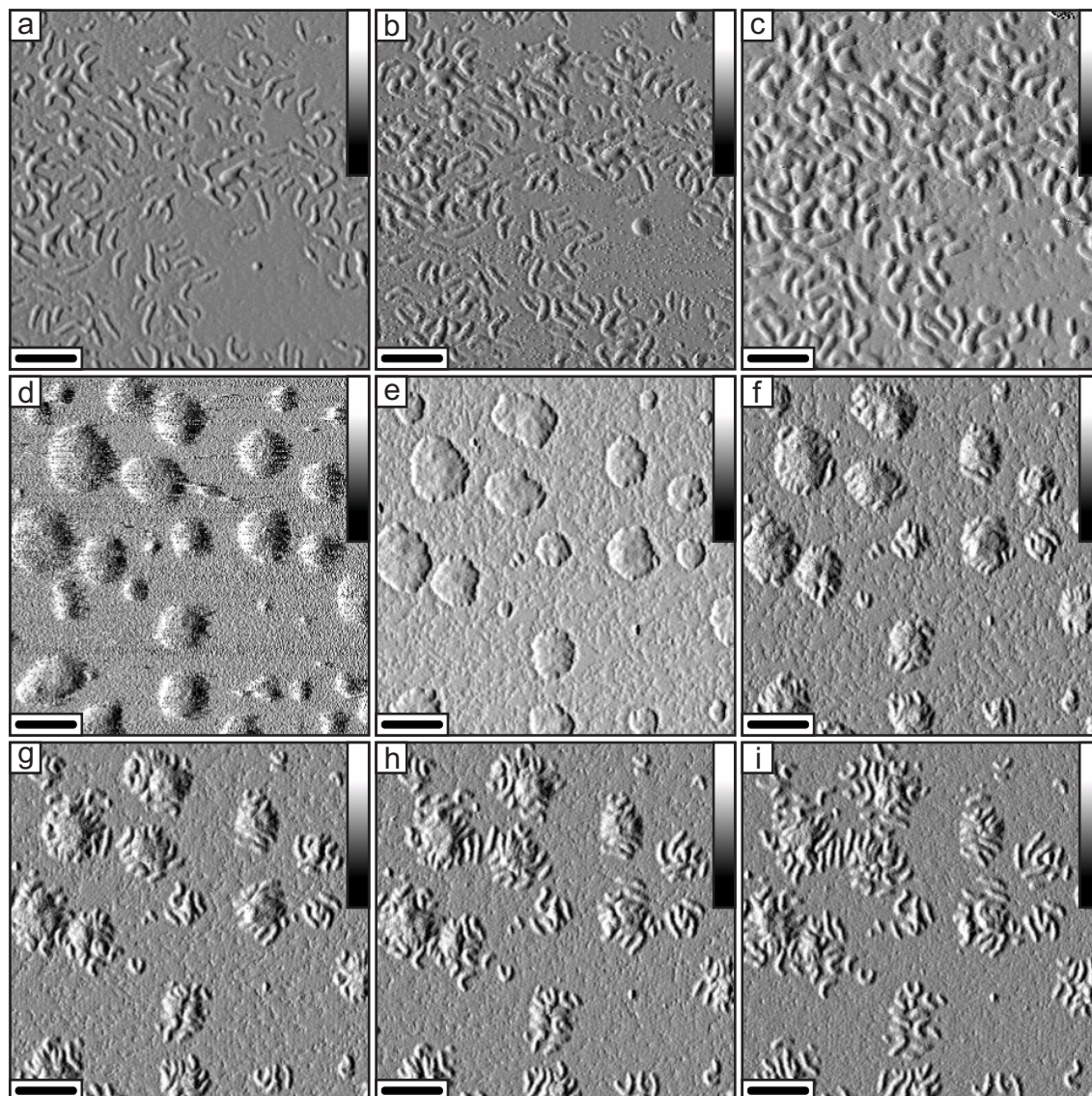


Figure 6.11: Sequence of SFM images that demonstrate the collapse/decollapse dynamics of PMA-*g*-PBuA(s) brush molecules on mica in saturated ethyl acetate/ethylene glycol atmosphere. a: initial image of the sample in dry N<sub>2</sub> atmosphere; b-d: images obtained 15 min (b), 61 min (c) and 91 min (d) after ethyl acetate injection; e: image after the sample space was purged with dry N<sub>2</sub> again, molecules remain in the collapsed state; f-i: images obtained 6 h (f), 8.7 h (g), 11.5 h (h) and 16.2 h (i) after ethylene glycol injection. The temperature was kept constant at 24 °C. Bar size: 250 nm, grey scale: 1.5 nm (amplitude signal)

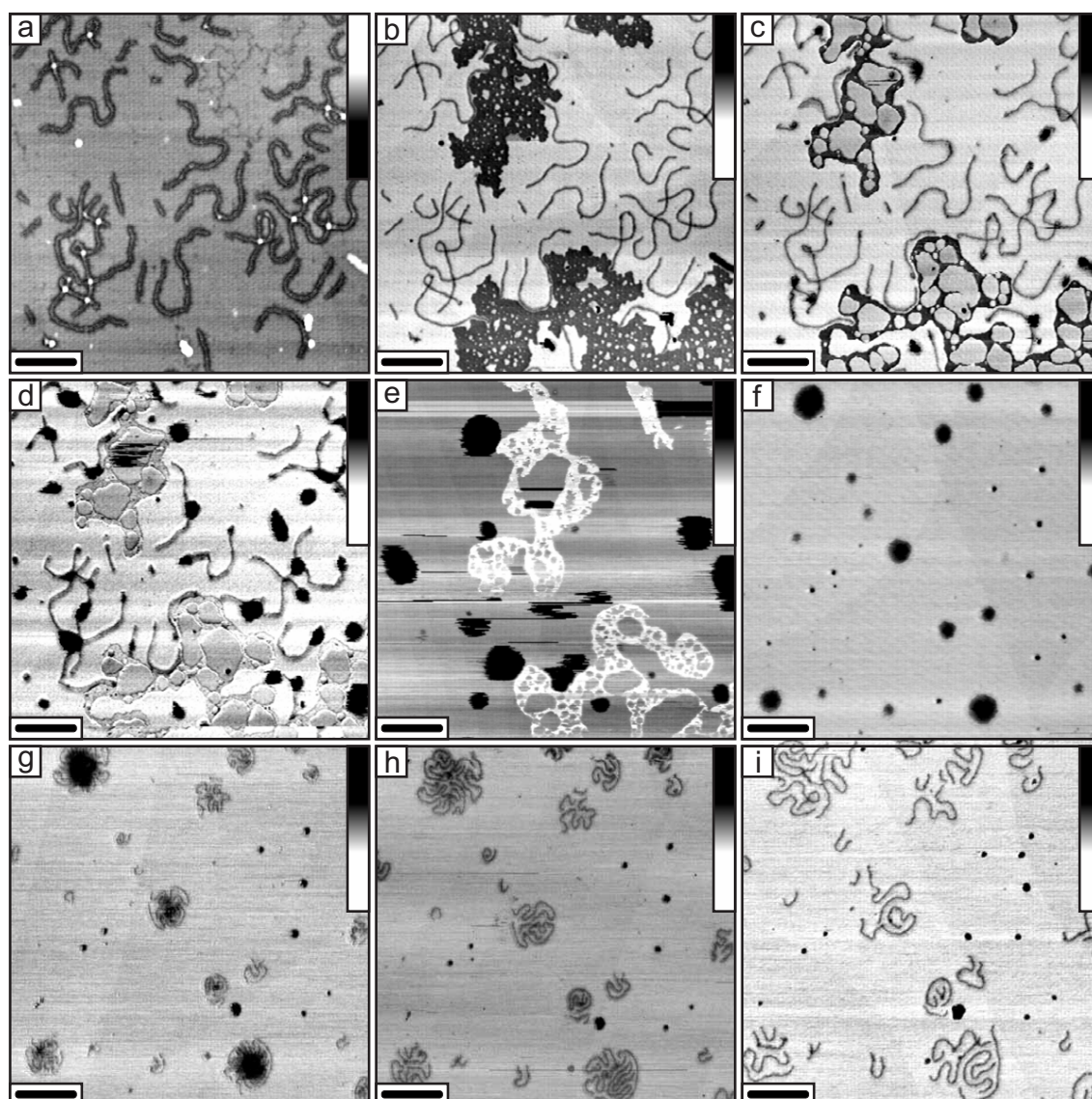


Figure 6.12: Sequence of SFM images that demonstrate the collapse/decollapse dynamics of PMA-*g*-PBuA(1) brush molecules on mica in saturated isopropanol/DMSO atmosphere. a: initial image of the sample in dry N<sub>2</sub> atmosphere; b: image obtained 2.1 h after injection of isopropanol. The molecules swell but do not collapse; c-e: images obtained 44 min (c), 1.1 h (d) and 3.3 h (e) after a small amount of water was added. The molecules collapse completely; f: image after the sample space was purged with dry N<sub>2</sub> again, molecules remain in the collapsed state (new area); g-i: images obtained 3.1 h (g), 4.8 h (h) and 20.3 h (i) after DMSO injection. The temperature was kept constant at 24 °C. Bar size: 300 nm, grey scale: 10 nm

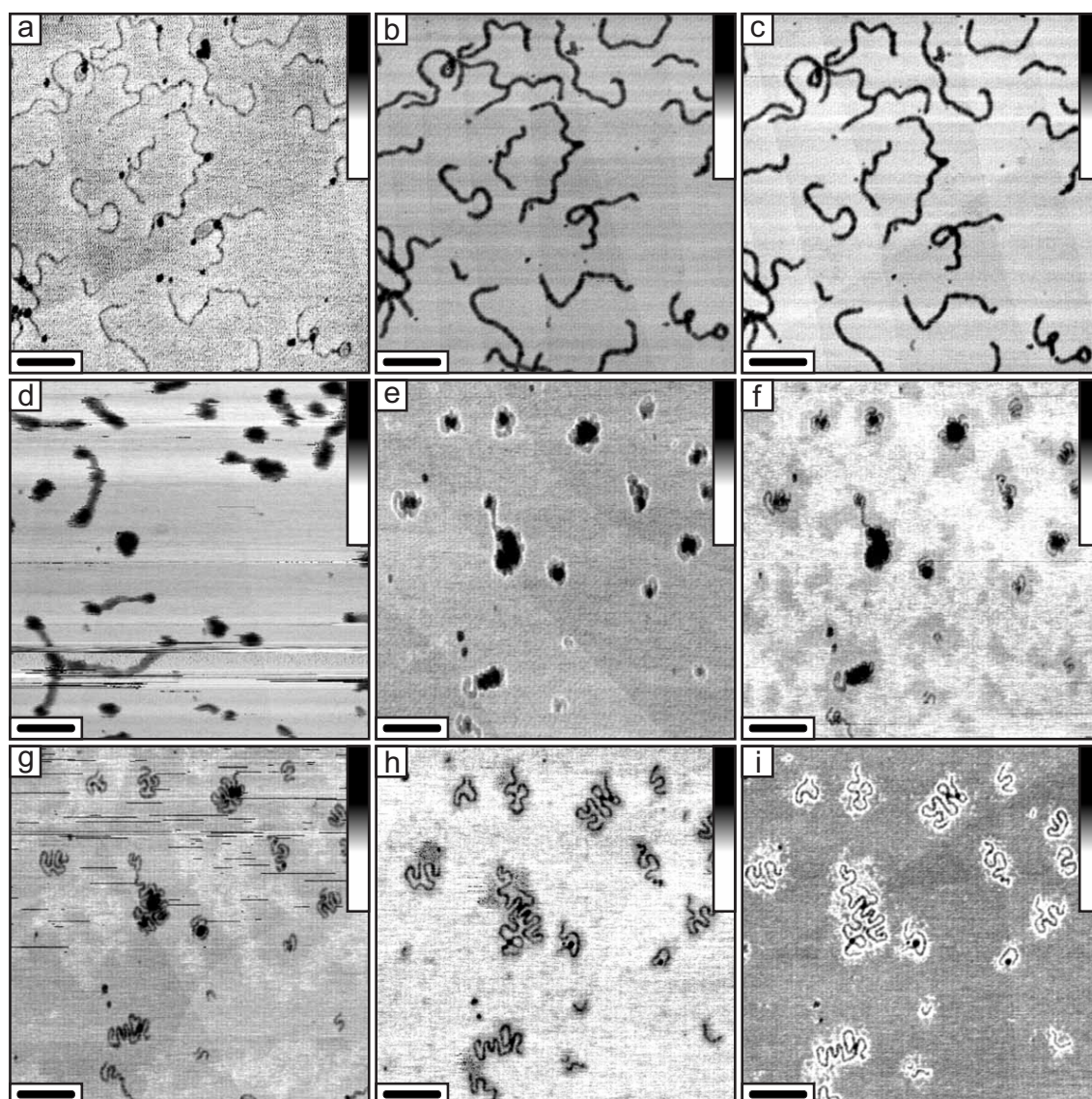


Figure 6.13: Sequence of SFM images that demonstrate the collapse/decollapse dynamics of PMA-*g*-PBuA(1) brush molecules on mica in saturated diethylether/DMF atmosphere. a: initial image of the sample in dry N<sub>2</sub> atmosphere; b,c: images obtained 25 min (b) and 58 min (c) after diethylether injection. The molecules swell but do not collapse; d: image obtained 9 min after a small amount of water was added. Immediate collapse of the brush molecules occurred; e: image after the sample space was purged with dry N<sub>2</sub> again, molecules remain in the collapsed state (new area); f-h: images obtained 1.2 h (f), 3 h (g) and 13 h (h) after DMF injection; i: Image after drying the sample with N<sub>2</sub>. The temperature was kept constant at 24 °C. Bar size: 300 nm, grey scale: 10 nm.

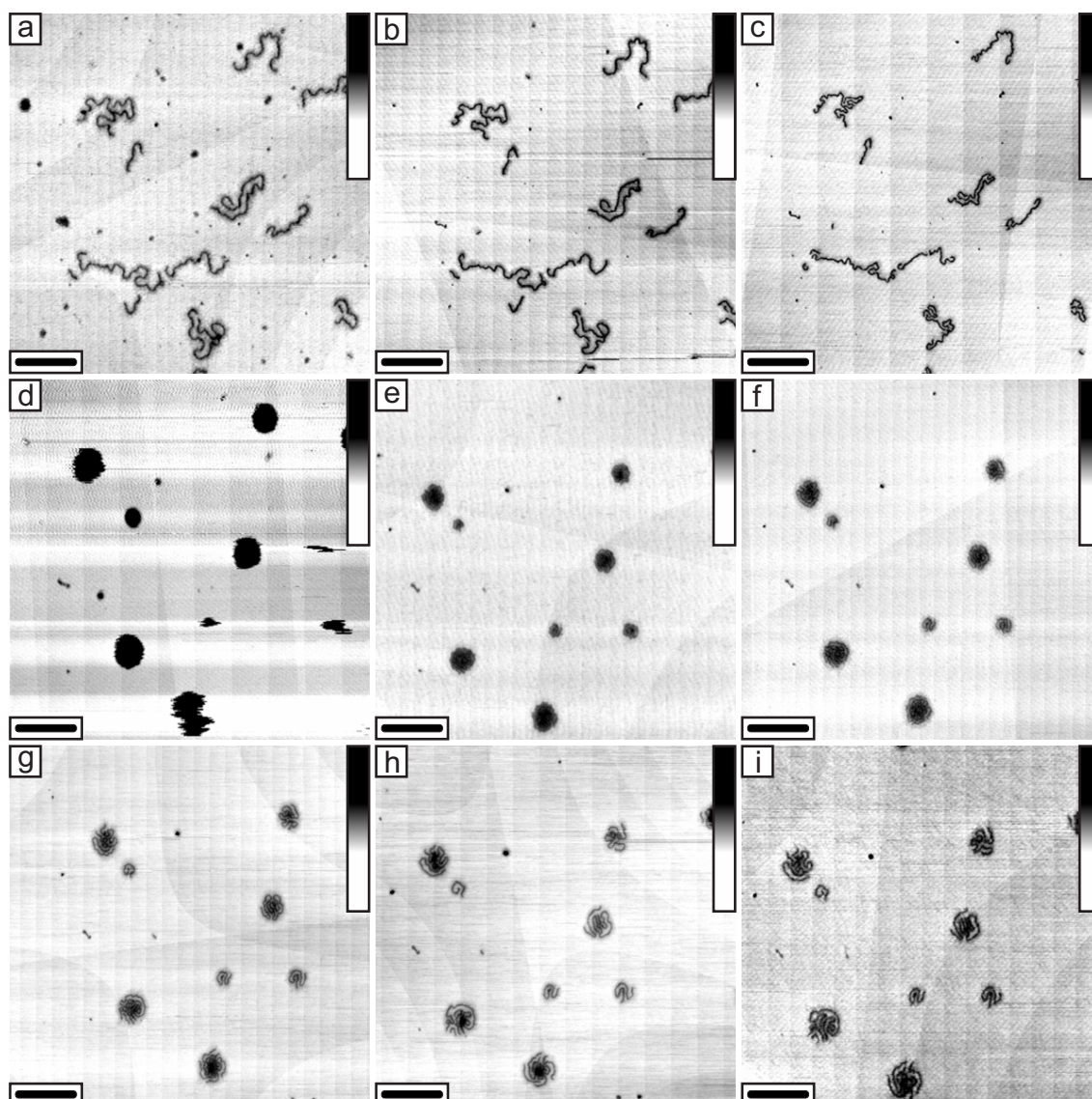


Figure 6.14: Sequence of SFM images that demonstrate the collapse/decollapse dynamics of PMA-*g*-PBuA(l) brush molecules on mica in saturated ethylacetate/cyclohexanone atmosphere. a: initial image of the sample in dry N<sub>2</sub> atmosphere; b,c: images obtained 17 min (b) and 1.8 h (c) after ethylacetate injection. The molecules swell but do not collapse; d: image obtained 8 min after a small amount of water was added. Immediate collapse of the brush molecules occurred; e: image after the sample space was purged with dry N<sub>2</sub> again, molecules remain in the collapsed state; f-i: images obtained 25 min (f), 5.1 h (g), 19 h (h) and two days (i) after cyclohexanone injection. The temperature was kept constant at 24 °C. Bar size: 250 nm, grey scale: 10 nm.

Table 6.2: Surface tension of the solvents used for the collapse and decollapse dynamics of the brush molecules. On the left side are the solvents listed with a lower surface tension as poly(*n*-butyl acrylate) (31–34 mN/m). On the right side the solvents with higher surface tension.

collapse		decollapse	
vapor	surface tension mN/m	vapor	surface tension mN/m
ethyl acetate	23.2	water	72.0
ethanol	22.0	ethylene glycol	47.0
isopropanol	18.3	dimethyl sulfoxide	43.0
diethyl ether	16.5	N,N-dimethyl formamide	36.3
		cyclohexanone	34.0

### 6.3.6 Model explanation

The following model explanation of the observed phenomena is presented: Side chains of the investigated brushes consist of poly(*n*-butyl acrylate), which have a slightly amphiphilic nature and are characterized by a surface tension close to that of a water/alcohol mixture at the transition point (30 % vol. of ethanol). This value is higher than that for pure ethanol and lower than that for pure water. Therefore, if a polymer brush is surrounded by an ultrathin (with nanometer-scale thickness) adsorbed liquid layer, the forces arising due to surface tension gradient will influence quite differently depending on the environment. If the layer consists of a liquid with high surface tension (water, mixtures with high water content, and others), the resulting forces should promote a flat ‘monolayer of side chains’. In this case the forces will be applied to the side chains of the brushes, and will be directed ‘outward’ the whole molecule, which, as a result, will be stretched and extended. The decollapse process will finish, when such ‘monolayer of side chains’ is created for every molecular ‘patch’.

These surface tension forces should be regarded as some additive to the total balance of macromolecule–solvent interaction. In the case of the two-dimensional solvent this additive has to be quite important, and may even change the solvent quality. In the described example the water is a poor solvent in the bulk, but due to its high surface tension it acts as a good solvent for the brushes in ultrathin layers.

Ethanol, isopropanol, diethyl ether, and ethyl acetate remain poor solvents in ultrathin layers, because they have much smaller surface tensions. The increase of ethanol content in ethanol/water mixtures and, consequently, the decrease of surface tension in the adsorbed layer reduces the surface tension additive in the whole macromolecule–solvent interaction balance. When the surface tension gradient forces (directed ‘outward’ the molecule) begin to be too small and cannot flatten the macromolecule conformation anymore (in a layer with high ethanol content), the conformation is determined by other contributions to the macromolecule–solvent interaction balance. This is why we observe compaction of adsorbed molecules, if the concentration of ethanol is increased in mixtures or if solvents with low

surface tension are used for sample exposure.

The described model is quite simple and the real situation is most probably more complicated. The model does not take into account the detailed balance of side chains interaction in water and the used solvents. Exposure to the pure low surface tension solvents is not enough to induce collapse, small amounts of water have to be injected for this purpose. The collapse was never observed on a graphite substrate. This may be explained now by an absence of adsorbed layers on the hydrophobic graphite substrate. Some other factors may also be important, because the system is very complex and includes several interacting components: deposited brushes, substrate (in the case of mica even with dissociating  $K^+$  cations), vapor environment, and ultrathin adsorbed layers of water and the used solvents. The situation is complicated also by the fact, that adsorbed ultrathin liquid layers (e. g. water [33, 34] and ethanol [35] on mica) demonstrate specific properties, that are not typical for those liquids in the bulk.

Nevertheless, the proposed model seems to be quite appropriate as a first explanation of the dynamics of single molecular processes on a substrate. The model explains the general reason, why a ‘three-dimensionally’ poor solvent, i. e. water, may become a ‘two-dimensionally’ good solvent being confined in ultrathin adsorbed layer. The results demonstrate the fundamental difference between macromolecule-solvent interaction in the bulk and in two-dimensional (ultrathin) films.

## 6.4 Conclusions

Cylindrical poly(methacrylate)-*graft*-poly(*n*-butyl acrylate) brush molecules deposited onto mica, silicon, and  $SrTiO_3$  substrates were transformed reversibly from a two-dimensional extended worm-like state to a compact globular state. The transformation is affected by changing the molecular adhesion to the substrate by adsorbing of solvent vapors from the surrounding atmosphere as an ultrathin film. The dynamics of the conformational transition has been visualized in real-time by scanning force microscopy operated at controlled vapor atmosphere. When the brush molecules were exposed to solvent vapors with a lower surface tension than poly(*n*-butyl acrylate) (e. g. ethanol), the macromolecules, adsorbed in an extended conformation, swell and crawl up to form compact hemispheres. Without traces of water the macromolecules showed only swelling and the addition of small amounts of water was necessary to induce the collapse. When the collapsed macromolecules are exposed afterwards to solvent vapors with a surface tension higher than poly(*n*-butyl acrylate) (e. g. water), they extended again to a worm-like conformation. The non-polar HOPG substrate is not able to adsorb ultrathin water layers and no collapse/decollapse dynamics was observed.

A simple model explanation of the observed phenomena is proposed: The macromolecule/solvent interaction in ultrathin films fundamentally differs from the interaction in bulk, because in the two-dimensional case the contribution of surface tension forces is of great importance.

If the polymer brush is surrounded by an ultrathin adsorbed liquid layer with high surface tension, the forces arising due to the surface tension gradient will be directed ‘outward’ and promote a flat ‘monolayer of side chains’ resulting in an extended conformation. For solvents with low surface tensions the forces acting on the *n*-butyl acrylate side chains due to the surface tension gradient (directed ‘outward’) are too small to keep the brush molecules in the extended state and they subsequently collapse to hemispheres.





# Bibliography

- [1] T. Thundat, D. P. Allison, R. J. Warmack, G. M. Brown, K. B. Jacobson, J. J. Schrick, and T. L. Ferrell. Atomic force microscopy of DNA on mica and chemically modified mica. *Scanning Microscopy*, 6:911–918, 1992.
- [2] Y. L. Lyubchenko, B. L. Jacobs, and S. M. Lindsay. Atomic force microscopy of reovirus dsRNA: A routine technique for length measurements. *Nucl. Acids Res.*, 20: 3983–3986, 1992.
- [3] Y. F. Drygin, O. A. Bordunovaa, M. O. Gallyamov, and I. V. Yaminsky. Atomic force microscopy examination of tobacco mosaic virus and virion RNA. *FEBS Lett.*, 425: 217–221, 1998.
- [4] V. G. Sergeev, O. A. Pyshkina, M. O. Gallyamov, I. V. Yaminsky, A. B. Zezin, and V. A. Kabanov. DNA-surfactant complexes in organic media. *Progr. Colloid Polym. Sci.*, 106:198–203, 1997.
- [5] Y. Fang and J. H. Hoh. Cationic silanes stabilize intermediates in DNA condensation. *FEBS Lett.*, 459:173–176, 1999.
- [6] K. B. Thurmond II, E. E. Remsen, T. Kowalewski, and K. L. Wooley. Packaging of DNA by shell crosslinked nanoparticles. *Nucl. Acids Res.*, 27:2966–2971, 1999.
- [7] A. S. Andreeva, M. O. Gallyamov, O. A. Pyshkina, V. G. Sergeev, and I. V. Yamin-skii. Morphology of DNA-surfactant complexes after their passing through the water-chloroform interface as studied by atomic force microscopy. *Russ. J. Phys. Chem.*, 73:1858–1863, 1999.
- [8] Y. Fang, T. S. Spisz, and J. H. Hoh. Ethanol-induced structural transitions of DNA on mica. *Nucl. Acids Res.*, 27:1943–1949, 1999.
- [9] Y. Fang and J. H. Hoh. Early intermediates in spermidine-induced DNA condensation on the surface of mica. *J. Am. Chem. Soc.*, 120:8903–8909, 1998.
- [10] Z. Lin, C. Wang, X. Feng, M. Liu, J. Li, and C. Bai. The observation of the local ordering characteristics of spermidine-condensed DNA: atomic force microscopy and polarizing microscopy studies. *Nucl. Acids Res.*, 26:3228–3234, 1998.
- [11] H. G. Hansma, R. Golan, w. Hsieh, C. P. Lollo, P. Mullen-Ley, and D. Kwoh. DNA condensation for gene therapy as monitored by atomic force microscopy. *Nucl. Acids Res.*, 26:2481–2487, 1998.
- [12] R. Golan R. Golan, L. I. Pietrasanta, W. Hsieh, and H. G. Hansma. DNA toroids: Stages in condensation. *Biochemistry*, 38:14069–14076, 1999.

- [13] B. J. Rackstraw, A. L. Martin, S. Stolnik, C. J. Roberts, M. C. Garnett, M. C. Davies, and S. J. B. Tendler. Microscopic investigations into PEG-cationic polymer-induced DNA condensation. *Langmuir*, 17:3185–3193, 2001.
- [14] D. D. Dunlap, A. Maggi, M. R. Soria, and Lucia Monaco. Nanoscopic structure of DNA condensed for gene delivery. *Nucl. Acids Res.*, 25:3095–3101, 1998.
- [15] V. A. Bloomfield. Condensation of DNA by multivalent cations: considerations on mechanism. *Biopolymers*, 31:1471–1481, 1991.
- [16] S. V. Mikhailenko, V. G. Sergeyev, A. A. Zinchenko, M. O. Gallyamov, I. V. Yaminsky, and K. Yoshikawa. Interplay between folding/unfolding and helix/coil transitions in giant DNA. *Biomacromolecules*, 1:597–603, 2000.
- [17] M. O. Gallyamov, O. A. Pyshkina, V. G. Sergeyev, and I. V. Yaminsky. T4 DNA condensation in water-alcohol media. *Surf. Invest.*, 16:1177–1182, 20001.
- [18] A. L. Martin, M. C. Davies, B. J. Rackstraw, C. J. Roberts, S. Stolnik, S. J. B. Tendler, and P. M. Williams. Observation of DNA-polymer condensate formation in real time at a molecular level. *FEBS Lett.*, 480:106–112, 2000.
- [19] M. Guthold, X. Zhu, C. Rivetti, G. Yang, N. H. Thomson, S. Kasas, H. G. Hansma, B. Smith, P. K. Hansma, and C. Bustamante. Direct observation of one-dimensional diffusion and transcription by escherichia coli RNA polymerase. *Macromolecules*, 31:9413–9415, 1998.
- [20] N. H. Thomson, S. Kasas, B. Smith, H. G. Hansma, and P. K. Hansma. Reversible binding of DNA to mica for AFM imaging. *Langmuir*, 12:5905–5908, 1996.
- [21] S. S. Sheiko, S. A. Prokhorova, K. L. Beers, K. Matyjaszewski, I. I. Potemkin, A. R. Khokhlov, and M. Möller. Single molecule rod-globule phase transition for brush molecules at a flat interface. *Macromolecules*, 34:8354–8360, 2001.
- [22] M. Gerle, K. Fischer, S. Roos, A. H. E. Müller, M. Schmidt, S. S. Sheiko, S. Prokhorova, and M. Möller. Main chain conformation and anomalous elution behavior of cylindrical brushes as revealed by GPC/MALLS, light scattering, and SFM. *Macromolecules*, 32:2629–2637, 1999.
- [23] H. G. Börner, K. Beers, K. Matyjaszewski, S. S. Sheiko, and M. Möller. Synthesis of molecular brushes with block copolymer side chains using atom transfer radical polymerization. *Macromolecules*, 34:4375–4383, 2001.
- [24] I. I. Potemkin, A. R. Khokhlov, S. Prokhorova, S. S. Sheiko, M. Möller, K. L. Beers, and K. Matyjaszewski. Spontaneous curvature of comb-like polymers at a flat interface. *Macromolecules*, submitted, 2003.
- [25] J. Kumaki, Y. Nishikawa, and T. Hashimoto. Visualization of single-chain conformations of a synthetic polymer with atomic force microscopy. *J. Am. Chem. Soc.*, 118:3321–3322, 1996.
- [26] E. Balnois and K. J. Wilkinson. Sample preparation techniques for the observation of environmental biopolymers by atomic force microscopy. *Colloids Surf. A*, 207:229–242, 2002.

- [27] V. N. Morozov, T. Y. Morozova, and N. R. Kallenbach. Atomic force microscopy of structures produced by electrospraying polymer solutions. *Int. J. Mass. Spectrom.*, 178:143–159, 1998.
- [28] K. L. Beers, S. G. Gaynor, K. Matyjaszewski, S. S. Sheiko, and M. Möller. The synthesis of densely grafted copolymers by atom transfer radical polymerization. *Macromolecules*, 31:9413–9415, 1998.
- [29] M. O. Gallyamov, E. V. Dubrovin, and I. V. Yaminsky. Micromechanics of nucleic acids. *Phys. Low-Dim. Struct.*, 5/6:7–12, 2002.
- [30] S. S. Sheiko and M. Möller. Visualization of macromolecules – A first step to manipulation and controlled response. *Chem. Rev.*, 101:4099–4123, 2001.
- [31] J. Brandrup and E. H. Immergut, editors. *Polymer Handbook*. A Wiley-Interscience publication, third edition, 1999.
- [32] R. Strey, Y. Viisanen, M. Aratono, J. P. Kratochvil, Q. Yin, and S. E. Friberg. On the necessity of using activities in the gibbs equation. *J. Phys. Chem. B*, 103:9112–9116, 1999.
- [33] J. Hu, X.-D. Xiao, d. F. Ogletree, and M. Salmeron. Imaging the condensation and evaporation of molecularly thin films of water with nanometer resolution. *Science*, 268:267–269, 1995.
- [34] P. B. Miranda, L. Xu, Y. R. Shen, and M. Salmeron. Icelike water monolayer adsorbed on mica at room temperature. *Phys. Rev. Lett.*, 81:5876–5879, 1998.
- [35] V. Franz and H.-J. Butt. Confined liquids: Solvation forces in liquid alcohols between solid surfaces. *J. Phys. Chem. B*, 106:1703–1708, 2002.

*Bibliography*

# 7 Self-assembly of eicosylperfluorotetradecane

## 7.1 Introduction

Diblock molecules consisting of short hydrocarbon chains covalently linked to fluorocarbon chains are model compounds, because the synthetic pathway guarantees monodispersity in contrast to the long chain analogues. This advantage was explored in a number of fundamental studies where the precision in the molecular structure is of importance e. g. conformational studies related to the helical structure of the fluorocarbon chains [1], crystallization [2] ... Besides the strong incompatibility [3] between the two building blocks, the peculiarity of such compounds originates in the molecular structure, which is a flexible hydrocarbon chain with a Van-der-Waals diameter that is 25 % smaller than a rigid helical fluorocarbon chain [1]. The antagonistic nature of the two building units and the crystallization ability of each block results in distinct self-assembled structures. Self-assembly in bulk [2, 4–6], in solution [7–9] as well as at liquid interfaces [10–15] has been extensively studied in the last two decades.

Yet, the unexplored aspect is the self-assembly in dilute solution and structure formation in a molecularly thin layer. This chapter focuses on the effect of the solvent polarity on the self-assembled structure. To that purpose the self-assembly of the eicosylperfluorotetradecane,  $F(CF_2)_{14}(CH_2)_{20}H$ , abbreviated as  $F_{14}H_{20}$ , in dilute solution and on a solid substrate is investigated. Molecularly thin layers were deposited from dilute solution. Mica, silicon dioxide or water surfaces were used as substrates to track the effect of the support on the molecular ordering. Scanning force microscopy (SFM) was utilized to probe the molecular ordering of  $F_{14}H_{20}$  as function of the solvent polarity. X-ray reflectivity was used to measure the film thickness and to probe the distribution of the electronic density along the solid interface. The obtained SFM images are compared with X-ray reflectivity data to evaluate the molecular packing of both the fluorocarbon and the hydrocarbon layer. In addition grazing incidence x-ray diffraction (GIXD) allowed to establish the liquid nature of the in-plane packing. A model of the molecular structure of the self-assembled objects is proposed and contrasted to recent studies. Furthermore, the environmental chamber of the SFM was used to record in situ the structural changes of the organized layers upon exposure to organic solvent vapors. The structural transition was found to be stable and reversible, which supports the molecular model of the self-assembled structure.

## 7.2 Experimental part

### 7.2.1 Materials

The  $F_{14}H_{20}$  sample was synthesized according to the procedures reported in reference [16] and [17] by Jens Höpken (University of Twente, The Netherlands). Three types of solvents were used: selective solvents for either the fluorinated block i. e. perfluorodecalin, per-

fluorohexane, or for the hydrocarbon block i. e. decalin, xylene, chloroform, and solvents that are able to dissolve both parts of the molecule i. e. hexafluoroxylyene. Perfluorodecalin (Aldrich, 95 %, mixture of cis and trans), perfluorohexane (Aldrich, 99 %), decahydronaphthalene (decalin, Merck, 98 %, mixture of cis and trans), xylene and chloroform both of analytical grade (Merck, > 99.8 %) and 1,3-bis(trifluoromethyl)benzene (hexafluoroxylyene, HFX, Apollo Scientific) have been used as received.

Solutions of  $F_{14}H_{20}$  with concentrations of 1 g/l and 0.1 g/l have been prepared. To ensure complete dissolution of the compound the solutions were heated up to 120 °C or close to the boiling point for 30 min and subsequently the flasks were put aside to cool down to room temperature. In the case of decalin, dilution of the 1 g/l solution was necessary to avoid gel formation. Dilution was also required in the cases of perfluorodecalin and perfluorohexane to avoid precipitation.

Mica and silicon dioxide were used as substrates. A monomolecular layer was prepared either by Langmuir-Blodgett (LB) deposition or by spin-coating technique. The LB experiments have been performed on a Lauda FW2 Langmuir trough with a surface area of 927 cm<sup>2</sup> operated at 22 °C using milli-Q water as sub-phase. A defined volume of the solution was deposited at the air water interface. Compression of the monolayers started after two to four hours delay to ensure homogenous spreading of the solution and complete evaporation of the solvent. During compression, the surface area was reduced by 5 % per minute. Transfer onto the substrate followed at constant surface pressure by lowering the subphase. In the spinning procedure, 2000 rpm was found to produce monolayers that cover homogeneously the substrate.

### 7.2.2 Methods

Scanning force microscopy (SFM) was performed on the following devices:

1. Digital Instruments Multimode scanning force microscope equipped with a Nanoscope IIIa controller. Imaging was done in tapping mode using standard silicon cantilevers: Nanoworld Pointprobe NCH ( $k = 42 \text{ N/m}$ ,  $f_0 = 330 \text{ kHz}$ ) or FM ( $k = 2.8 \text{ N/m}$ ,  $f_0 = 70 \text{ kHz}$ ).
2. Molecular Imaging Picoforce scanning force microscope equipped with a Digital Instruments Nanoscope IIIa controller and an environmental chamber, which allows imaging under controlled vapor atmosphere. The scanning was done in the acoustic mode using standard silicon cantilevers: Nanoworld Pointprobe FM ( $k = 2.8 \text{ N/m}$ ,  $f_0 = 70 \text{ kHz}$ ).

X-ray reflectivity. The films were investigated by specular x-ray reflectivity using a triple-axis reflectometer with copper  $K_{\alpha_1}$ -radiation (wavelength  $\lambda = 0.154 \text{ nm}$ ) from a rotating anode x-ray generator (Rigaku RU-300H). The beam was collimated by a parabolic graded multi-layer mirror and a pre-sample slit of 0.1 mm. At specular reflectivity the momentum transfer  $q = k_{out} - k_{in}$  is perpendicular to the film ( $z$ -direction), i. e.  $|q| = q_z = (4\pi/\lambda)\sin\Theta$ , where  $\Theta$  is the angle of incidence. Hence the reflected intensity is sensitive to the electron density profile in the latter direction, averaged over the footprint of the incident beam. The density profile was determined by comparing calculated and experimental reflectivity [18]. Calculations were based on a parameterized molecular model in which the two sub-layers are approximated by a box-like function. The box function was characterized by thickness and density, convoluted with a Gaussian probability describing the interfacial roughness.

The best-fit curve to the data was determined by a minimization procedure leading to the density and roughness profile along the film normal. The total thickness is directly determined by the interference oscillations (Kiessig fringes) between x-rays reflected from the top and the bottom of the film.

Grazing incidence x-ray diffraction (GIXD) was performed at the interface diffractometer of the DUBBLE beamline BM26 at the European Synchrotron Radiation Facility (ESRF, Grenoble, France) at a wavelength of  $\lambda = 0.779 \text{ \AA}$ . In GIXD an x-ray beam is incident on a surface at a small glancing angle  $\alpha < \alpha_c$  where  $\alpha_c$  is the critical angle for total external reflection. Under these conditions an evanescent wave is generated that propagates along the film-air interface with an intensity exponentially decaying with depth. This wave can be considered as incident beam for 2D x-ray diffraction, giving information about the 2D structure in the plane of the film [19]. The penetration depth of the x-rays depends on  $\alpha$ , which was set to  $0.105^\circ$ . This is slightly below the critical angle of silicon ( $0.11^\circ$ ) and well above the critical angle of the  $F_{14}H_{20}$  layer ( $0.107^\circ$  and  $0.076^\circ$  for  $CF_2$  and  $CH_2$ , respectively). As a result the whole thickness of the film contributed to the observed scattering. Note that over the (large) footprint of the incident beam the sample can be considered as a 2D ‘powder’, and rotation of the sample does in principle not influence the results. The resolution was 70 mdeg and 35 mdeg in the horizontal and vertical direction, respectively.

## 7.3 Results and discussion

### 7.3.1 SFM Imaging

#### Non-selective solvent

Figure 7.1a shows a SFM image of a monomolecular layer of  $F_{14}H_{20}$  as cast from a solution of HFX on a mica substrate. The film consists of a discrete assembly of toroidal objects that are arranged in a hexagonal lattice. The toroidal objects have a diameter of ca. 80 nm and a height of  $3.0 \pm 0.5 \text{ nm}$ . A ribbon that has a 3 nm height and  $35.0 \pm 3.0 \text{ nm}$  width forms the skeleton of the torus. The ribbon binds at lengths of 30–60 nm with defined angle ( $105^\circ$ – $130^\circ$ ) to form open or closed toroids (see the arrows in Figure 7.1a and the scheme in Figure 7.2).

To address the effect of the preparation method on the morphology, a defined volume of the solution was deposited at the air–water interface on a LB-trough. After complete evaporation of the solvent, the mono-film was compressed up to  $4.9 \text{ mN/m}$ ; the corresponding surface area per molecule was  $23.8 \text{ \AA}^2$ . The floating film was then transferred onto mica or silicon wafer. Figure 7.1b depicts a 2-dimensional assembly of uniform sized toroids (‘donut’-like structure) with a periodicity of 60 nm. The LB technique allows higher coverage of the substrate compared to the spin-coated film. Apparently, lateral compression of the self-assembled objects produces toroids with faceted edges and hexagonal symmetry. Besides that, the dimensions of the toroids are conserved and the preparation method does not influence the self-assembly. Similar structures have been observed by Kato et al. [10–12] for partially perfluorinated long-chain acids.

#### Selective solvent

Decalin was used as a good solvent for the hydrocarbon block and spin-coating was chosen to coat the mica surface with a homogenous layer of  $F_{14}H_{20}$ . Figure 7.3a depicts the

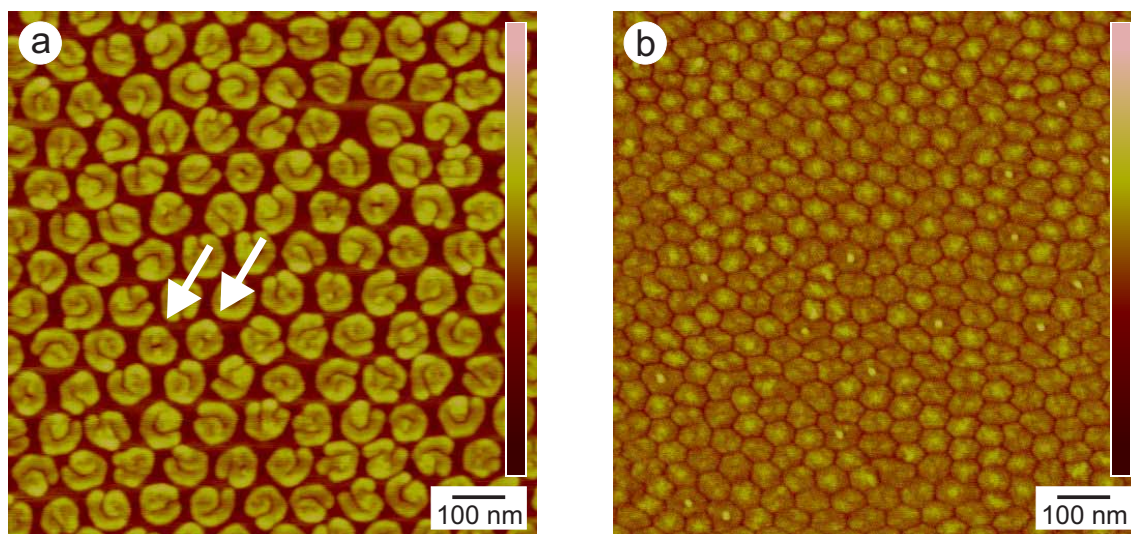


Figure 7.1: SFM tapping mode topography images of  $F_{14}H_{20}$  prepared from HFX solution (1 g/l) on mica by a) spin-coating (2000 rpm) and b) LB-film deposition, transferred at a surface pressure of 4.9 mN/m. The arrows in the left image indicate closed toroids (z-range 5 nm)



Figure 7.2: Ribbons are rolled up to toroids



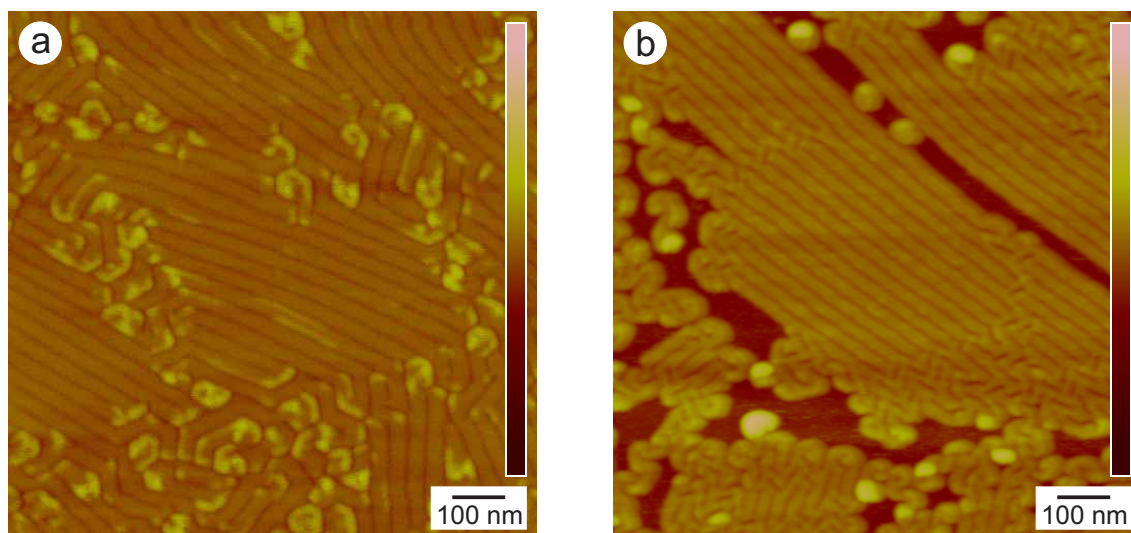


Figure 7.3: SFM tapping mode topography images of  $F_{14}H_{20}$  prepared from decalin solutions on mica by a) spin-coating (2000 rpm),  $c = 1$  g/l and b) LB-film preparation: spread from decalin solution with concentration of 0.1 g/l and transferred at a surface pressure of 4.6 mN/m (z-range 10 nm)

surface morphology of the spin-coated film. For comparison, Figure 7.3b displays the surface morphology of a film that was prepared by LB deposition on the mica surface. The transfer was achieved at a surface pressure of 4.6 mN/m, which corresponds to an area per molecule of  $24.1 \text{ \AA}^2$ . The spin-coating process produces a more homogenous coverage of the surface compared to the LB deposition. However, in both cases the samples showed similar structures consisting of aligned ribbons with a height of  $3.0 \pm 0.5$  nm and width of  $35 \pm 3$  nm. In some areas of the sample, toroidal structures coexist with the ribbons. Note that the characteristic size of the ribbons is exactly the same as for the ribbons forming the toroids obtained from the non-selective solvent HFX.

Selective dissolution of the fluorinated block resulted in elongated structures as well. Figure 7.4 shows the morphology of the spin-cast films from dilute solution of hexafluoroxylene (Figure 7.4a) and from perfluorodecalin (Figure 7.4b). The low coverage of the surface is due to the dilution of the solution, which was necessary to prevent precipitation. The self-assembled structures consist mainly of ribbons with the same dimensions as described above (height  $3.0 \pm 0.5$  nm, width  $35 \pm 5$  nm). However, the ribbons exhibit the tendency to bend and to create branches. Furthermore, in some areas of the sample, isolated toroidal objects coexist with the elongated structures.

So far, we can summarize the experimental data as following: Selective solvents promote the formation of extended ribbons while non-selective ones restrain the ribbons to be bent in definite geometry.

### In situ SFM measurements

To address the question whether the structure exists already in the solution or it is formed upon casting, in situ SFM investigations were performed. The as cast samples were exposed to organic solvent vapors during the SFM scan, and the structural transformations were recorded in real time. The results are displayed in Figure 7.5, two snap shots were selected

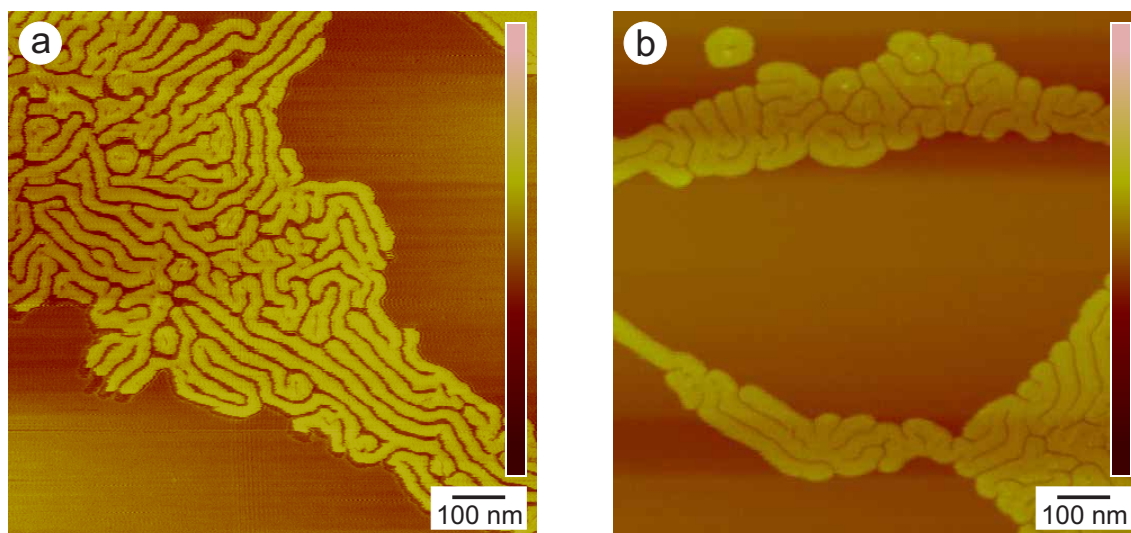


Figure 7.4: SFM tapping mode topography images of  $F_{14}H_{20}$  on mica prepared by spin-coating (2000 rpm) from a) perfluorohexane solution ( $c = 0.1$  g/l) b) perfluorodecalin solution ( $c = 0.1$  g/l) (z-range 10 nm)

that capture the main feature of the structural transformation. Figure 7.5a shows the surface morphology of the as cast sample from decalin solution. Nicely isolated ribbons were obtained. Figure 7.5b shows the same area of the sample in the course of the treatment with HFX vapor during 10 hours. The micrographs demonstrate the occurrence of the transition from extended ribbons to bent ones. The inset in the image (bottom left corner) magnifies the bent structure. These results demonstrate explicitly the effect of the solvent selectivity on the structure and support strongly the idea of the existence of the structure in the solution.

The opposite situation is given by treating the sample with an organic vapor that dissolves selectively either the hydrogenated part or the fluorinated one. For the initial state a toroidal morphology was chosen that was cast from dilute HFX solution (Figure 7.6a). While the surface was scanned in the condition that allows resolved images, perfluorodecalin vapor was generated in the SFM chamber. Figure 7.6b shows, elongated structures that were created within 40 minutes of vapor treatment. Even though some of the toroidal structure persists, the morphological transformation triggered by the solvent vapor is unambiguous in the micrograph (Figure 7.6b).

However, it turned out to be more difficult to observe the same transformation when the sample was exposed to a good solvent for the hydrogenated part e. g. decalin. In this case, the morphological change towards elongated structures was observed only in the scanning area. It seems that the hydrocarbon block is hidden by the fluorinated block so that it is difficult to swell the hydrogenated part, unless the SFM tip disturbs locally the structure. Note that in all cases, the structures could be transformed reversibly from bent structure to elongated one or vice-versa. Hence, we conclude that both self-assembled structures are thermodynamically stable and are formed in solution.

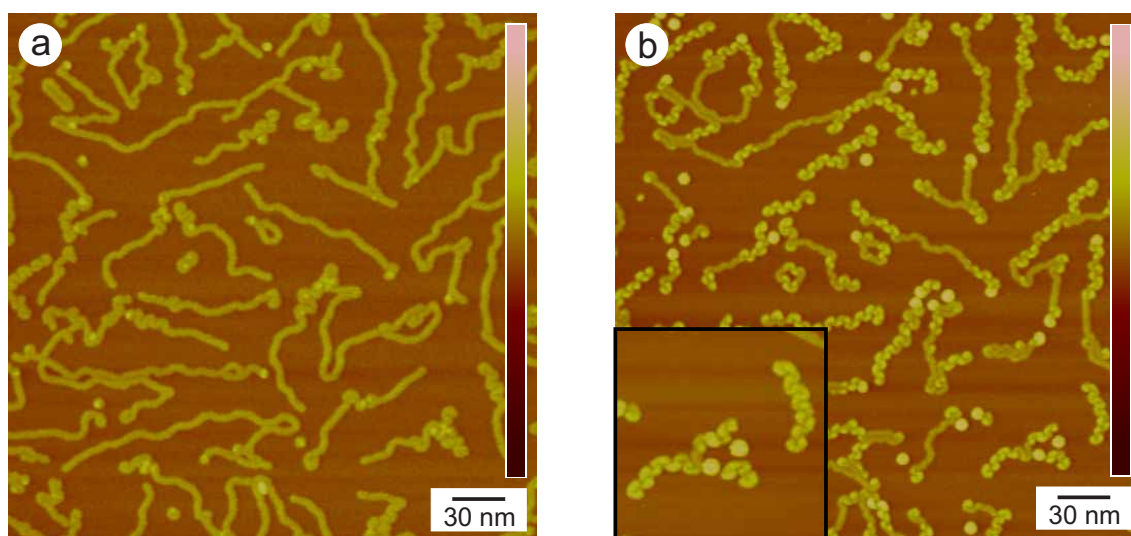


Figure 7.5: SFM tapping mode topography images of  $F_{14}H_{20}$  on mica a) film as cast from decalin solution ( $c = 0.1$  g/l) b) after exposure to HFX vapor for 10 hours (z-range 15 nm)

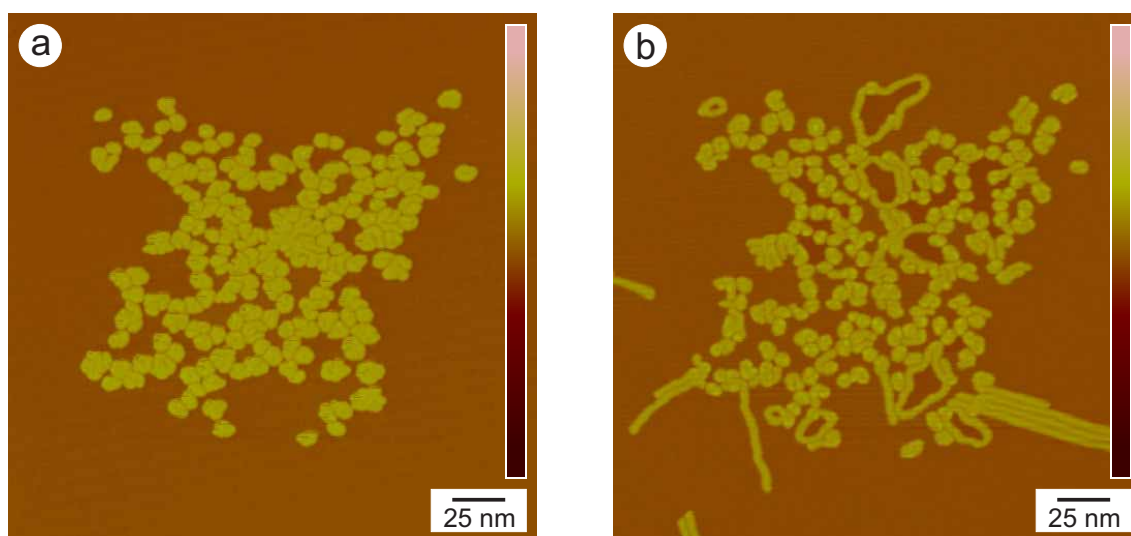


Figure 7.6: SFM tapping mode topography images of  $F_{14}H_{20}$  on mica a) film as cast from HFX solution ( $c = 0.1$  g/l) b) after exposure to perfluorodecalin vapor for 40 minutes (z-range 15 nm)

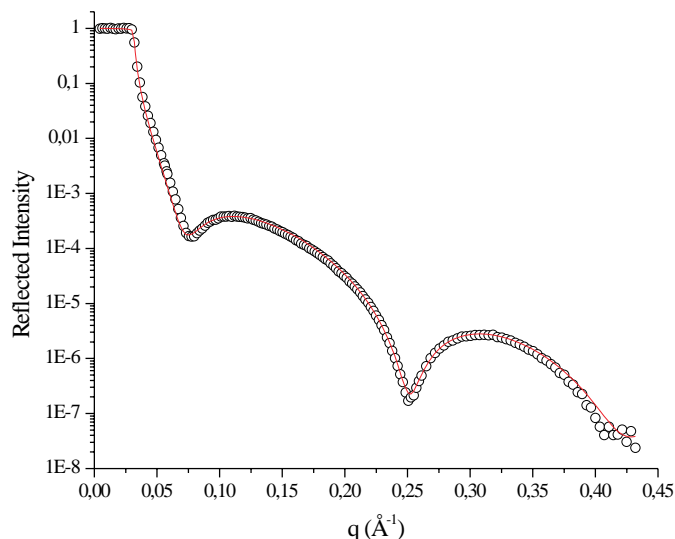


Figure 7.7: X-ray results for a monolayer of semi-fluorinated alkane  $F_{14}H_{20}$ . Experimental data (circles) and fitting (full line) to a double-layer model

### 7.3.2 X-ray reflectivity

In order to propose a molecular model of the self-assembled structure rigorous investigation of the molecular details of the self-assembled layer with complementary techniques is needed. X-ray reflectivity was used to probe the inner structure of the monolayer; the thickness and the density distribution along the interfaces were derived. Mono-layers of  $F_{14}H_{20}$  were prepared from low-concentration solutions in different solvents on silicon substrate. The LB technique was chosen to ensure optimum coverage of the surface. SFM was used to control the quality of the transfer and only samples with relatively high coverage ( $> 90\%$ ) were investigated by x-ray reflectivity. Figure 7.7 shows the reflected x-ray intensity of a film prepared from a HFX solution (donuts). From the interference fringes, unambiguously a total film thickness of  $3.76 \pm 0.05$  nm was derived, which exceeds by 25% the SFM data. The discrepancy was attributed to the indentation artifact of tapping SFM and the x-ray value was taken as the correct layer thickness. This value is smaller than the length of the extended molecule, i. e. 4.19 nm (see Figure 7.8), but consistent with a monolayer with a tilt angle of  $143^\circ$  at the linkage between the fluorocarbon and the hydrocarbon chain segments. The single-frequency oscillations in the x-ray reflectivity effectively exclude thicknesses of more than a monolayer.

The Van-der-Waals diameter of the fluorinated and hydrogenated parts are 0.6 and 0.48 nm, respectively. This results from the fact that a  $-(CF_2)_n-$  sequence cannot exist in a planar zigzag configuration, as it is possible for  $-(CH_2)_n-$ . Instead, the  $-(CF_2)_n-$  sequence adopts a 15/7 helix [20], leading to a rigid rod-like structure. To obtain an optimum packing this difference is expected to lead to a tilted structure. Assuming a close-packed arrangement of the molecules, a calculation of the tilt angle gives  $\alpha = 143^\circ$ . Using this angle, the vertical projection of the hydrocarbon block length is 2.04 nm. Added to the length of the fluorinated part (1.64 nm) this gives 3.68 nm for the thickness of the

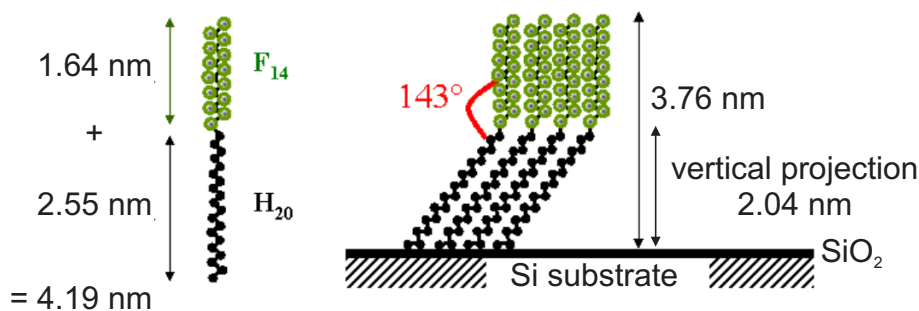


Figure 7.8: Scheme illustrating the packing of the semi-fluorinated molecules

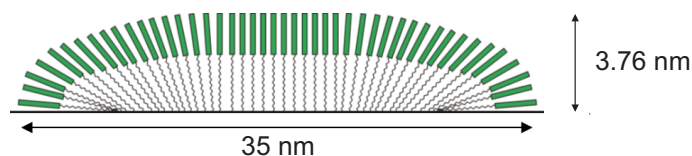


Figure 7.9: Packing of the semi-fluorinated alkanes perpendicular to the plane defined by the kink

monolayer, in excellent agreement with the x-ray reflectivity result.

The tilt angle allows a dense packing of both blocks within the plane defined by the kink, compensating for the larger width of the fluorocarbon segment. In the plane perpendicular to the kink, long range ordered dense packing of the alkyl chains is not possible. In this direction the difference in Van-der-Waals diameter between the hydrogenated and the fluorinated parts leads to a mismatch. Evidently this restricts the width of the patterns to a stable constant value  $w \approx 35$  nm, corresponding to a commensurability length of about 50 molecules. The simplest model would be as in Figure 7.9. Such a model is in principle possible as the GIXD results indicate that in the present monolayer structures crystallization is strongly suppressed. Note that Figure 7.9 does not indicate the kinks. These can have either a ‘forward’ or a ‘backward’ direction along the ribbons and do not show up in this projection.

Nevertheless, there are several problems associated with this picture. Table 7.1 gives the thickness, density and roughness of the upper fluorinated layer and the lower hydrogenated layer respectively. The roughness of the interface between the two layers is quite extended compared to the roughness of the top (fluorocarbon–air) and bottom (hydrocarbon–SiO<sub>2</sub>) interface. In the model of Figure 7.9 one would expect that any variation in the central interface would be accompanied by a similar variation in the fluorocarbon–air interface. Secondly SFM results indicate that the top of the structure is quite flat and shows no evidence of the continuous bending associated with this picture. The only way to smooth exclusively the central interface is via the dynamics of the molecules, in particular a combination of translations along the layer normal coupled to a variation of the kink-angle, so that the end-point approximately stays in place.

Table 7.1: Fitting parameters corresponding to the mono-layer structure of  $F_{14}H_{20}$  proposed in Figure 7.8

	layer thickness	electron density	interface roughness
	d [Å]	$\delta \times 10^6$	$\sigma$ [Å]
<b>Si</b>	$\infty$	7.57	7.0
<b>SiO<sub>2</sub></b>	8.0	6.80	4.5
<b>CH<sub>2</sub></b>	20.9	0.90	11.5
<b>CF<sub>2</sub></b>	16.4	5.31	3.0

### 7.3.3 Gracing incidence x-ray reflectivity

Figure 7.10 shows typical GIXD patterns that indicate broad liquid-like peaks with some internal structure. In this figure three regions are indicated corresponding to (from left to right):  $-(CF_2)_n-$  close-packed as well as liquid-like,  $-(CH_2)_n-$  liquid-like and  $-(CH_2)_n-$  close-packed. Evidently all these elements are present.

Figure 7.11 indicates fits to either two or three Lorentzians. The width corresponds to correlations lengths in the order of 0.7–0.8 nm, typical for liquids: crystallization is strongly suppressed. Figure 7.12 shows a specific measurement in which an indication of crystallization was observed. The  $q$ -value corresponds to close-packed alkane chains. However, this result did not reproduce at other positions on the sample. The experimental peaks evidently show some structure in the form of local maxima/shoulders, which makes the fitting somewhat arbitrary. The most probable interpretation seems to be as follows:

1. The GIXD shows at least two liquid peaks, corresponding evidently to the hydrogenated and fluorinated parts in a liquid-like state.
2. In order to explain the broad spectrum we assume that in the two liquid states still some distribution of distances occurs. Otherwise the total broad distribution can hardly be understood. This idea reflects the model of Figure 7.9, in which one could expect different spacings at the edges of the ‘ribbons’.
3. The extra peaks should probably not be interpreted as a third broad distribution, but rather as additional crystalline peaks from small local regions. This is in particular needed to reproduce the full distribution in the region of close-packed  $-(CH_2)_n-$ . According to results for Langmuir mono-layers of fatty acids [15, 28] crystalline peaks can occur around either  $q \approx 0.15\text{--}0.152 \text{ nm}^{-1}$  or  $q \approx 0.16\text{--}0.165 \text{ nm}^{-1}$ . The first value is in agreement with the crystalline peak of Figure 7.12, the latter one with a local maximum in Figure 7.10.

Hence, we assume that crystallization is largely, but not fully suppressed. In the literature for various systems peaks have been observed for both, the  $-(CF_2)_n-$  and for the  $-(CH_2)_n-$  close-packed segments. These were interpreted as crystalline, but were not resolution-limited. This means that some broadening occurs due to limited ranges of the crystalline regions. Hence it is quite possible that similar effects occur here.

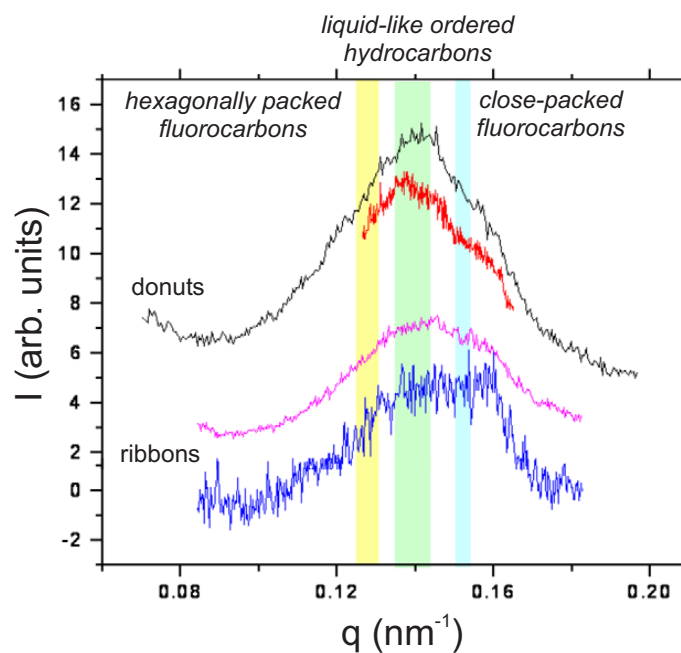


Figure 7.10: Comparison of the experimental GIXD-curves for two samples with ‘donut’-structure (black and red) and two samples with ‘ribbon’-structure (magenta and blue). The highlighted areas represent literature findings [1, 12, 20–27] for peak positions of hexagonally packed fluorocarbons (yellow), liquid-like order of hydrocarbons (green) and close-packed hydrocarbons (blue)

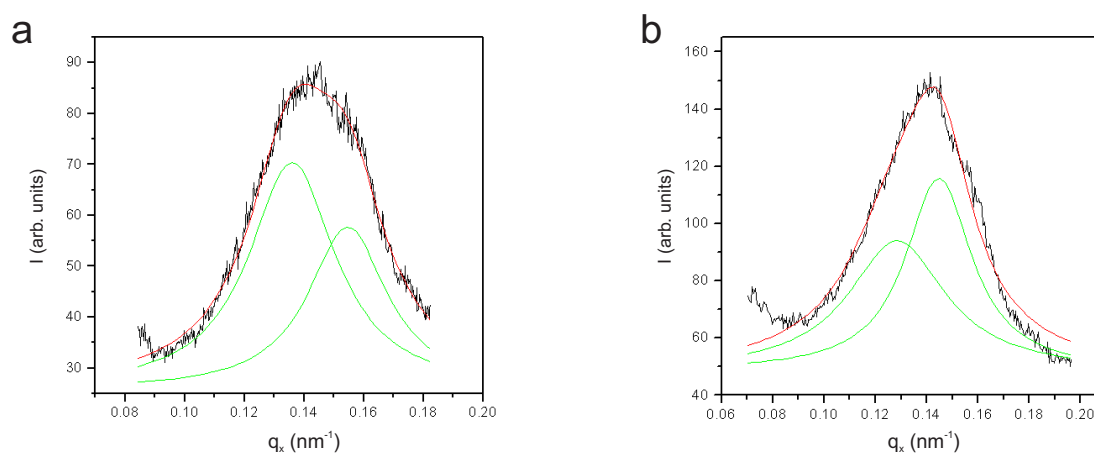


Figure 7.11: Fitting of Lorentzians to the GIXD intensities a) ‘ribbon’-sample b) ‘donut’-sample

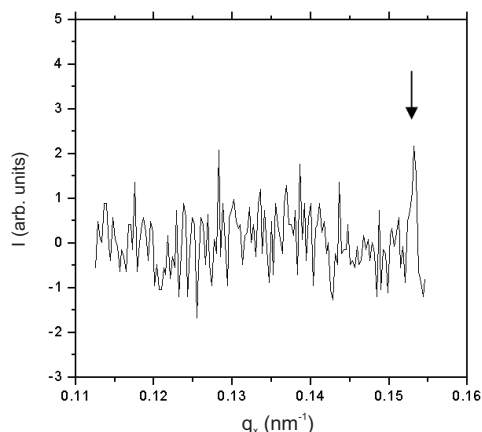


Figure 7.12: Crystalline peak in the ‘ribbon’-sample

## 7.4 Conclusions

Solvents that are not selective for one of the blocks of the semifluorinated alkanes lead to the formation of open or closed toroidal structures whereas solvents selective for one of the blocks prefer the self-assembly to elongated ribbons. The in situ SFM experiments in organic solvent vapors show that the structures can be transformed from elongated ribbons to curved structures and vice versa in thin liquid films and therefore acknowledging that the observed structures are formed already in solution.

The height of 3.7 nm measured by x-ray reflectivity gives a bending angle of  $143^\circ$  between the hydrocarbon and the perfluorinated block.

From the results so far it seems that the ribbon pattern is the natural way to accommodate a monolayer of  $\text{F}_{14}\text{H}_{20}$ . This is nicely explained by the difference between the closed packing along the long direction and the packing problem in the transverse direction. The latter leads to a constant width that is also preserved in the ‘donut’ structure. The packing in the ‘donut’ structure and the driving force for rolling up the ribbons is not yet understood.

GIXD measurements yielded that the internal structure of the formed films shows predominantly liquid-like behavior with small crystalline domains inside.



# Bibliography

- [1] C. W. Bunn and E. R. Howells. Structures of molecules and crystals of fluorocarbons. *Nature*, 174:549–551, 1954.
- [2] O. Gang, J. Ellmann, M. Möller, H. Kraack, E. B. Sirota, B. M. Ocko, and M. Deutsch. Surface phases of semi-fluorinated alkane melts. *Europhys. Lett.*, 49:761–767, 2000.
- [3] R. D. Dunlap, R. G. Bedford, J. C. Woodbrey, and S. D. Furrow. Liquid-vapor equilibrium for the system: Perfluoro-*n*-hexane–*n*-hexane. *J. Am. Chem. Soc.*, 81: 2927–2930, 1959.
- [4] J. F. Rabolt, T. P. Russell, and R. J. Twieg. Structural studies of semifluorinated *n*-alkanes. 1. Synthesis and characterization of  $F(CF_2)_n(CH_2)_mH$  in the solid state. *Macromolecules*, 17:2786–2794, 1984.
- [5] T. P. Russell, J. F. Rabolt, R. J. Twieg, and R. L. Siemens. Structural characterization of semifluorinated *n*-alkanes. 2. Solid-solid transition behavior. *Macromolecules*, 19: 1135–1143, 1986.
- [6] J. Höpken and M. Möller. On the morphology of (perfluoroalkyl)alkanes. *Macromolecules*, 25:2482–2489, 1992.
- [7] C.-Y. Ku, P. L. Nostro, and S.-H. Chen. Structural study of the gel phase of a semifluorinated alkane in a mixed solvent. *J. Phys. Chem.*, 101:908–914, 1997.
- [8] M. P. Turberg and J. E. Brady. Semifluorinated hydrocarbons: Primitive surfactant molecules. *J. Am. Chem. Soc.*, 110:7797–7801, 1988.
- [9] Y. Ishikawa, H. Kuwahara, and T. Kunitake. Self-assembly of bilayer membranes in organic solvents by novel “amphiphilic” compounds. *J. Am. Chem. Soc.*, 111: 8530–8531, 1989.
- [10] Y. Ren, K.-i. Iimura, A. Ogawa, and T. Kato. Surface micelles of  $CF_3(CF_2)_7-(CH_2)_{10}COOH$  on aqueous  $La^{3+}$  subphase investigated by AFM and IR spectroscopy. *J. Phys. Chem. B*, 105:4305–4312, 2001.
- [11] T. Kato, M. Kameyama, M. Ehara, and K.-i. Iimura. Monodisperse two-dimensional nanometer size clusters of partially fluorinated long-chain acids. *Langmuir*, 14:1786–1798, 1998.
- [12] Y. Ren, K.-i. Iimura, and T. Kato. Surface micelles of  $F(CF_2)_m(CH_2)_{22}COOH$  on the aqueous cadmium acetate solution investigated in situ and ex situ by infrared spectroscopy. *J. Phys. Chem. B*, 106:1327–1333, 2002.

- [13] A. L. Simões Gamboa, E. J. M. Filipe, and P. Brogueira. Nanoscale pattern formation in Langmuir-Blodgett films of a semifluorinated alkane and a polystyrene-poly(ethylene oxide) diblock copolymer. *Nano. Lett.*, 2:1083–1086, 2002.
- [14] M. Maaloum, P. Muller, and M. P. Krafft. Monodisperse surface micelles of nonpolar amphiphiles in langmuir monolayers. *Angew. Chemie*, 114:4507–4510, 2002.
- [15] V. M. Kaganer, I. R. Peterson, R. M. Kenn, M. C. Shih, M. Durbin, and P. Dutta. Tilted phases of fatty acid monolayers. *J. Chem. Phys.*, 102:9412–9422, 1995.
- [16] J. Höpken. *Fluorocarbon-hydrocarbon molecules, structural components for self-organizing materials*. PhD thesis, University of Twente (The Netherlands), 1991.
- [17] J. Höpken, C. Pugh, W. Richtering, and M. Möller. Melting, crystallization and solution behavior of chain molecules with hydrocarbon and fluorocarbon segments. *Makromol. Chem.*, 189:911–925, 1988.
- [18] M. Tolan. *X-Ray Scattering from Soft-Matter Thin Films*. Springer, Berlin, 1999.
- [19] J. Als-Nielsen, D. Jacquemain, K. Kjaer, F. Leveiller, M. Lahav, and L. Leiserowitz. Principles and applications of grazing incidence x-ray and neutron scattering from ordered molecular monolayers at the air-water interface. *Phys. Rep.*, 246:251–313, 1994.
- [20] P. Marczuk and P. Lang. A structural x-ray study on semifluorinated alkanes (SFA): SFA revisited. *Macromolecules*, 31:9013–9018, 1998.
- [21] X. Z. Wu, E. B. Sirota, S. K. Sinha, B. M. Ocko, and M. Deutsch. Surface crystallization of liquid normal-alkanes. *Phys. Rev. Lett.*, 70:958–961, 1993.
- [22] S. W. Barton, B. Lin, F. Novak, A. Acero, and S. A. Rice. Structural transitions in a monolayer of fluorinated amphiphile molecules. *J. Chem. Phys.*, 96:1343–1351, 1992.
- [23] W. Mahler, D. Guillon, and A. Skoulios. Smectic liquid crystals from (perfluorodecyl)decane. *Mol. Cryst. Liq. Cryst. Lett.*, 2:111–119, 1985.
- [24] D. L. Dorset. Perfluoroalkanes. A model for the hexagonal methylene subcell? *Chem. Phys. Lip.*, 20:13–19, 1977.
- [25] E. S. Clark and L. T. Muus. Partial disordering and crystal transitions in polytetrafluoroethylene. *Z. Krist.*, 117:119–127, 1962.
- [26] Z. Huang, A. A. Acero, N. Lei, S. A. Rice, Z. Zhang, and M. L. Schlossman. Structural studies of semifluorinated hydrocarbon monolayers at the air/water interface. *J. Chem. Soc. Faraday Trans.*, 92:545–552, 1996.
- [27] P. Marczuk, P. Lang, G. H. Findenegg, S. K. Mehta, and M. Möller. Gibbs films of semi-fluorinated alkanes at the surface of alkane solutions. *Langmuir*, 18:6830–6838, 2002.
- [28] M. C. Shih, T. M. Bohanon, J. M. Mikrut, P. Zschack, and P. Dutta. X-ray-diffraction on the superliquid region of the phase diagram of a Langmuir monolayer. *Phys. Rev. A*, 45:5734–5737, 1992.

# 8 Micellization of 16-arm star-block copolymers

## 8.1 Introduction

Microphase separating block copolymers with two incompatible blocks A and B can organize to mesomorphic bulk morphologies consisting of regularly packed spheres, cylinders and lamellae, depending on the volume ratio of the two blocks [1–3]. Block copolymers dissolved in a selective solvent, i. e., a good solvent for one of the blocks but a precipitant for the other, tend to form supramolecular assemblies, the micelles. Micelles are of spherical shape, if  $DP_{corona} > DP_{core}$ , where DP is the degree of polymerization of the corona and core forming block, respectively. Such associates have also been called star-type micelles. Numerous reports deal with the determination of micellar parameters as the size, the critical micelle concentration (cmc) and the number of associated molecules for spherical associates [4–11].

Non-spherical associate structures of high molecular weight block copolymers in solution are rarely observed. In 1980, Canham et al. described for the first time the formation of worm like micelles from poly(styrene)-*b*-poly(butadiene)-*b*-poly(styrene) triblock copolymers in ethyl acetate, being a poor solvent for the butadiene block [12]. The existence of cylindrical micelles in solution was also described for poly(styrene)-*b*-poly(isoprene) in dimethylacetamide [13] and for poly(ethylene oxide)-*b*-poly(propylene oxide)-*b*-polyethylene oxide in aqueous media [14].

Eisenberg and coworkers reported a rich variety of associate structures for block copolymers in aqueous solution. Evaluation of the structures was performed by electron microscopy on dried films, assuming that the self-organization was not affected substantially by the drying procedure. Two families of block copolymers were used, namely, poly(styrene)-*b*-poly(acrylic acid) and poly(styrene)-*b*-poly(ethylene oxide) [15–20]. By decreasing the degree of polymerization of the water soluble block (PAA and PEO, respectively) the morphology of the aggregates changed from spherical to rod-like and to lamellar or vesicular and finally to large compound vesicles (LCV) and large compound micelles (LCM). Also, hollow tubes and bicontinuous structures have been found.

Comparison of spherical and cylindrical micelles shows that the volume occupied by one polymer molecule must transform from a conical shape in the case of spherical micelles into something that looks more than a truncated cone in the case of cylindrical micelles. Additionally, the base of the cone must adopt a more ellipsoidal shape (Figure 8.1) in order to pack nicely into a cylinder.

The transition from spheres to cylinders can be explained by evaluating the energetic balances. The Gibbs Free Energy describes the balance between enthalpic and entropic contributions.

$$\Delta G = \Delta H - T\Delta S$$

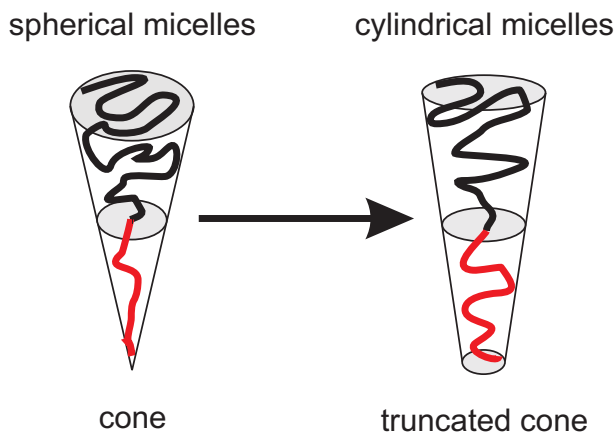


Figure 8.1: Transformation of the volume occupied by a single molecule in spherical and cylindrical micelles. The shape transforms from a cone to a truncated cone with a more flattened (ellipsoidal) shape

At the critical conditions, where cylindrical micelles are formed is

$$\Delta G_{cylinders} < \Delta G_{spheres}$$

whereas  $\Delta G_{cylinders} = \Delta H_{cylinders} - T\Delta S_{cylinders}$  and  $\Delta G_{spheres} = \Delta H_{spheres} - T\Delta S_{spheres}$ .

There are several possibilities how a system can be influenced in order to shift the equilibrium to cylindrical micelles:

1. Variation of the block lengths in favor of longer core blocks. The more voluminous core blocks favor a truncated core shape and therefore the cylindrical shape [21, 22].
2. Changing of the solvent quality or mixing of solvents. Highly selective solvents favor a spherical shape. Less selective solvents allow the core block more swelling and to adopt a truncated cone shape. Adding small amounts of a good solvent for the core block reduces the selectivity of the solvent and leads to the situation that selectively the core block is swollen because of an accumulation of the added solvent in the core [16, 19, 23]. Even insoluble polymers can be dissolved in solvent mixtures and one of the solvents can be removed by dialysis [17, 22].
3. The formation of cylindrical micelles can also be promoted by increasing the concentration. Formation of spheres at low concentrations is favored by entropy. Using a selective solvent for one block there is a small but negative contribution from the solvent-soluble block interaction to  $\Delta H$ . Upon transformation to cylinders, the interfacial area between the core and corona block is reduced giving a favorable enthalpic contribution for the transformation. In total,  $\Delta H_{spheres \rightarrow cylinders}$  can be considered to be small and must be negative. The  $\Delta S$  between spheres and cylinders can be described by three contributions  $\Delta S = \Delta S_{core} + \Delta S_{corona} + \Delta S_{association}$ . At a change in the morphology from spheres to cylinders, the first term will be positive because of less stretching of the core forming unit, the second will be negative, because the corona chains must expand in order to pack very densely and the third one will also be negative because of a higher degree of association of chains. At higher

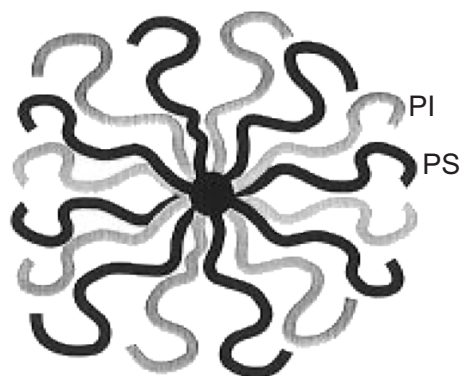


Figure 8.2: Miktoarm star-copolymers of the  $A_8B_8$ -type with 8 polystyrene and 8 polyisoprene arms.

concentrations, the entropic penalty from a reduced dispersion and interaction with the solvent becomes smaller and cylinders are formed.

4. Adopting of the polymer structure. Besides varying the block lengths of the polymer the structure itself can be adopted in order to prefer a truncated conical and therefore a cylindrical shape. Studies with linear triblock copolymers (ABA) [12, 14], stars with three ( $A_2B$ ) [24] and more arms [25] have been investigated. And even studies of polymers with more sophisticated shapes, like H-shape and  $\pi$ -shape [26, 27] and graft copolymers [28] have been performed.
5. Adding of stabilization agents. Partial neutralization of PS-P2VP with  $\text{HAuCl}_4$  led to the formation of cylindrical micelles whereas the pure PS-P2VP showed spherical micelles [29].

Here the micellization of star block copolymers with 8 PS and 8 PI arms was investigated by scanning force microscopy. Three samples with different block lengths were used. In order to obtain cylindrical micelles the approach of increasing the polymer concentration and changing the solvent quality was chosen.

## 8.2 Experimental

### 8.2.1 Materials

Miktoarm star-copolymers of the  $A_8B_8$ -type (Figure 8.2) with eight PS and eight PI arms have been synthesized in the group of Prof. N. Hadjichristidis (University of Athens, Greece) using anionic polymerization and controlled chlorosilane chemistry as described in [30]. The appropriate amount of living PSLi was reacted with a chlorosilane dendrimer having 16 active Si-Cl bonds in order to produce an 8-arm star. The remaining chlorosilane bonds were reacted with excess PILi arms of the desired molecular weight. The fractionated final products were characterized by SEC, LALLS and NMR. Table 8.1 gives the molecular weights measured by LALLS of the three used star-copolymers. The bulk properties of these star copolymers was studied in [31].

Cyclohexane ( $\geq 99.5\%$ ), methyl ethyl ketone (MEK,  $\geq 99\%$ ), toluene ( $\geq 99.9\%$ ), all three of analytical grade, and octane ( $\geq 99\%$ ), all from Merck, were used as received.

Table 8.1: Molecular characterization of the polystyrene (PS) and polyisoprene (PI) arms and the miktoarm star-copolymers of the  $A_8B_8$ -type. Molecular masses [g/mol] were determined by LALLS in THF at 25 °C.

	VS1	VS2	VS3
<b>VS, <math>M_w \times 10^{-4}</math></b>	33.0	71.0	89.4
<b>VS, PD</b>	1.07	1.05	1.05
<b>PS arm, <math>M_w \times 10^{-4}</math></b>	2.09	4.36	4.36
<b>PS, PD</b>	1.06	1.03	1.03
<b>PI arm, <math>M_w \times 10^{-4}</math></b>	2.02	4.82	7.12
<b>PI, PD</b>	1.06	1.07	1.05

### 8.2.2 Methods

Scanning force microscopy was performed using a Digital Instrument Multimode SPM equipped with a Nanoscope IIIa controller operating in the tapping mode. Nanosensors Pointprobe NCH single crystal silicon cantilevers with a resonance frequency of ca. 300 kHz and a spring constant of ca. 40 N/m were used. The microscope was operated in air at room temperature.

### 8.2.3 Sample preparation

All solutions have been prepared by heating to 50 °C for 24 hours, slowly cooled down to room temperature and given another 24 hours relaxation time in order to ensure complete dissolution and equilibration of the formed micelles. Polymer micelles were deposited on mica (BAL-TEC) by spin-coating from solutions ( $c = 0.2\text{--}5.0$  mg/ml; 2000 rpm; 20 s) using a homebuilt device. Spin-coating was chosen as a fast deposition method in order to preserve the structures formed in solution.

## 8.3 Results and discussion

### 8.3.1 Micellization from octane solutions

For the first micellization experiments octane was chosen as a solvent. It is a highly selective solvent, good for the PI and poor for the PS block. As expected for diblock copolymers also the star block copolymers formed uniform spherical micelles (Figure 8.3) throughout the whole tested concentration range (0.5–5.0 g/l). The uniform dimensions of the micelles supports that the aggregates shown in the micrographs reflect the equilibrium structure in solution and were not formed upon solvent evaporation during the spin-coating process. Already at concentrations larger than about 1.5–2.0 g/l multi-layer formation occurred and complicated the evaluation of the micellar shape, showing the main draw-back of using SFM as visualization tool.

The measured dimensions of the micelles are given in Table 8.2 and are compared with the viscometric and hydrodynamic radius in decane from [32]. VS1 formed the smallest micelles with a diameter of 26.1 nm. The polymer VS2 with PS and PI arms twice as

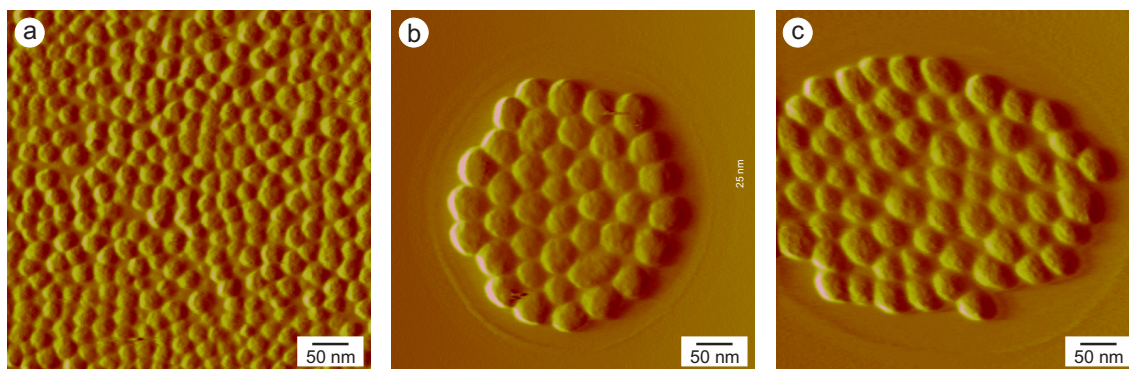


Figure 8.3: Spherical micelles of VS1, VS2, VS3 spin-coated from octane solutions on mica substrates (amplitude images). The used concentrations were a) 1.0, b) 0.7 and c) 0.5 g/l

Table 8.2: Dimensions of the micelles in octane by SFM compared with the viscometric and hydrodynamic values from viscosimetry and DLS in decane

	VS1	VS2	VS3
<b>diameter [nm], SFM</b>	26.1	46.5	44.1
<b>height [nm], SFM</b>	23.2	37.8	33.7
<b>molecules per micelles<sup>a</sup></b>	17	43	30
<b><math>R_h</math> [nm], DLS [32]</b>	40.2	79.0	70.2
<b><math>R_v</math> [nm], viscosimetry [32]</b>	30.2	68.6	64.9

a) calculated using the diameter value from SFM, assuming a spherical shape

long as VS1 formed micelles with almost double size: 46.5 nm. The largest star diblock copolymer, VS3, with the same PS arm size as VS2 and longer PI arms shows a slightly smaller micellar size than VS2: 44.1 nm. The sizes of the micelles found in solution by viscosimetry and DLS are by a factor of 2–3 larger but show the same relative size scaling (Table 8.2). The difference in size is reasonable because the values determined by SFM are for the dried state, whereas DLS and viscosimetry give the dimensions in the dissolved swelled state. The number of molecules incorporated in a single micelle is about one order of magnitude smaller compared to linear PS-*b*-PI diblock copolymers [9]. However if one takes into account that each star copolymer contains 8 PS and 8 PI arms the number of polymer chains is in the same range.

### 8.3.2 Micellization from cyclohexane solutions

In order to obtain cylindrical micelles cyclohexane as a less selective solvent was examined. Cyclohexane is a good solvent for the PI block and a  $\Theta$ -solvent for PS at 35 °C [33] and therefore should allow more swelling of the inner PS block.

For the polymer VS1 in the concentration range from 0.2–0.9 g/l spherical micelles, with

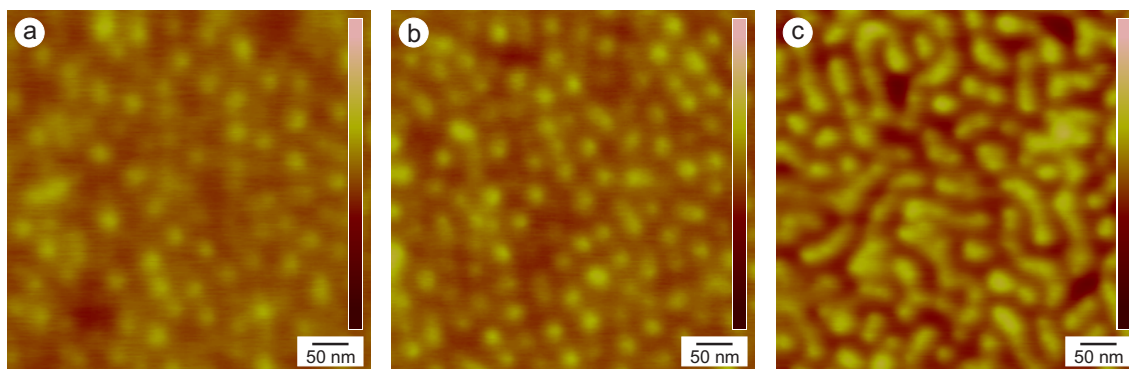


Figure 8.4: SFM topography images of micelles on mica substrate formed from polymer VS1 in cyclohexane solutions. At lower concentrations a) 0.5 and b) 0.9 g/l spherical micelles are formed, whereas at c) 1.0 g/l the morphology changed to cylindrical micelles

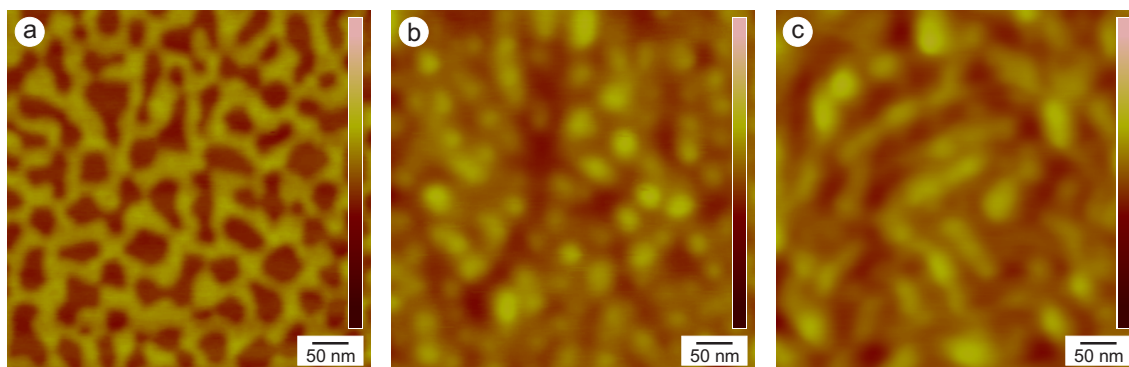


Figure 8.5: SFM topography images of aggregates on mica formed from polymer VS2 in cyclohexane solutions. The concentrations are a) 0.2, b) 1.0 and c) 5.0 g/l. At concentrations below 0.5 g/l no micelles were formed, at higher concentrations the morphology changed over spherical to cylindrical (above 2.0 g/l)

a diameter of 23.4 nm, have been observed (Figure 8.4a and b). Starting from  $c = 1.0$  g/l elongated micelles, with the same diameter and lengths up to 150 nm were formed and coexisted with a few spherical micelles (Figure 8.4c). Increasing the concentration to 5.0 g/l did not enhance the formation of cylindrical shaped micelles.

In the case of VS2 the polymer was deposited as a film with a height of ca. 2.9 nm on the substrate and no micelles were observed at a concentration of 0.2 g/l (Figure 8.5a). In the concentration range of 0.5 g/l to about 2.0 g/l cylindrical micelles with a diameter of 28.3 nm were formed (Figure 8.5b). This means that the critical micelle concentration for this system must be somewhere between 0.2–0.5 g/l. At concentrations above 2.0 g/l mainly micelles with cylindrical shapes were formed (Figure 8.5c). The diameter is the same as for the spherical aggregates, the length of the cylinders goes up to 200 nm.

Polymer VS3 with soluble PI arms twice the size as polymer VS2 did not form micelles at a concentration of 0.2 g/l. At  $c = 0.5$  g/l only a few isolated micelles in a film of the remaining polymer (height 3.5 nm) was visible (Figure 8.6a), indicating that the cmc is



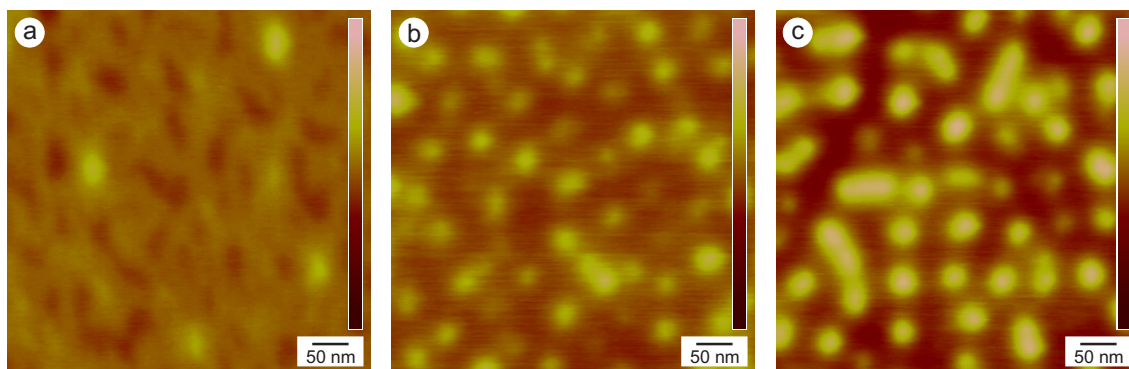


Figure 8.6: SFM topography images of aggregates on mica formed from polymer VS3 in cyclohexane solutions. The concentrations are a) 0.5, b) 0.9 and c) 1.0 g/l. At  $c = 0.5$  g/l the formation of micelles started (cmc) and from concentrations higher than 1.0 g/l a few di- and tri-meres were formed

just slightly below 0.5 g/l. Already at  $c = 0.6$  g/l mostly spherical micelles were visible and their shape did not change up to 0.9 g/l (Figure 8.6b). The average diameter was 29.3 nm. Increasing the concentration above 0.9 g/l showed some elongated aggregates (Figure 8.6c) that looked like dimers or, in some rare cases, like trimers of the spherical micelles. But the main species were spherical aggregates. Further increase of the concentration to 5.0 g/l did not enhance the morphology in the direction towards cylindrical micelles.

The experiments from cyclohexane solutions showed that increasing the concentration shifted the equilibrium towards cylindrical micelles. The longer the soluble PI block was, the higher was the critical micelle concentration. Increasing the fraction of the soluble corona PI block hampered the formation of cylindrical micelles and delivered predominantly spherical shaped micelles.

Another example supporting the formation of cylindrical micelles at increased concentrations is shown in Figure 8.7. Here a solution of VS2 in cyclohexane (0.76 nm) was prepared on a mica substrate by dipping the substrate into a cyclohexane solution with a dipping speed of 5 mm/min. The comparable slow evaporation of the solvent in contrast to the spin-coating process led to a reorganization of the micelles during the preparation process when the concentration increases. As a result cylindrical micelles have been observed at a concentration of 0.76 g/l that have been observed in the spin-coating approach only at concentrations beyond 2.0 g/l. Additionally the problem of high surface coverage could be avoided. Nevertheless the evaporation speed is uncontrolled and therefore the formed aggregates showed extreme deviation from the results shown in Figure 8.7. Also the results depend strongly on the dipping speed. As a consequence the sample preparation by dipping is not suitable for transferring the equilibrium structure from the solution onto the substrate.

### 8.3.3 Micellization from solvent mixtures

In the next approach a co-solvent was added to cyclohexane in order to further decrease the selectivity of the solvent. Two solvents have been investigated: first toluene as a non-selective solvent and second methyl ethyl ketone as a selective solvent for the PS block. The polymer VS2 was chosen for the experiments and the concentration was kept constant

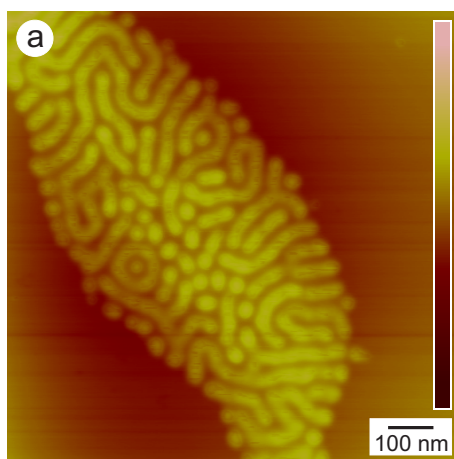


Figure 8.7: SFM topography image of polymer VS2 transferred from a cyclohexane solution ( $c = 0.76$  g/l) onto mica by dipping with  $v = 5$  mm/min

at 1.0 g/l, where in pure cyclohexane spherical micelles have been formed. All co-solvent fractions are given as volume percent.

Figure 8.8a shows the spherical micelles in pure cyclohexane solution. Addition of 1% of toluene led to the formation of elongated structures that resembled connected spherical micelles (Figure 8.8b). Already at 2% toluene content no micelles have been observed, instead phase separation patterns, similar to those of diblock copolymers in non-selective solvents, were seen. The pattern reached the most regular appearance at a 5% toluene content (Figure 8.8c). At 10% toluene content also these pattern disappeared and a corrugated film was deposited on the mica substrate.

The second co-solvent MEK is selective for the inner PS block and therefore should be accumulated in the core block and lead to enhanced swelling of this block. Addition of small amounts of MEK led, as in the case of toluene, to the transformation from spheres (Figure 8.9a, pure cyclohexane) to connected spheres (Figure 8.9b, 2% MEK). Further increase of the MEK content to 5% showed the formation of cylindrical micelles with lengths of several hundred nanometers. Only a few spherical micelles coexisted. The diameter of the cylinders shrunk to 23.1 nm compared to the diameter of 28.3 nm of the spherical micelles or connected spheres, respectively. The cylindrical micelles were present at MEK contents up to 20%, above no micelles have been observed.

## 8.4 Conclusions

The three investigated star-block copolymers formed spherical micelles in the highly selective solvent octane over the whole probed concentration range (0.2–5.0 g/l). The critical micelle concentration is below 0.2 g/l. The results confirm the data accumulated by studies in decane using DLS and viscometry [32].

In the less selective solvent cyclohexane the cmc increases from  $< 0.2$  g/l (VS1), 0.2–0.5 g/l (VS2) to 0.5 g/l (VS3) according to the increasing chain length of the soluble PI block. In the same order the tendency to form cylindrical shaped micelles at higher concentrations decreased. VS1 and VS2 formed cylindrical micelles with a length to diameter ratio of up to 10:1 at concentrations above 0.9 g/l and about 2.0 g/l, respectively. The

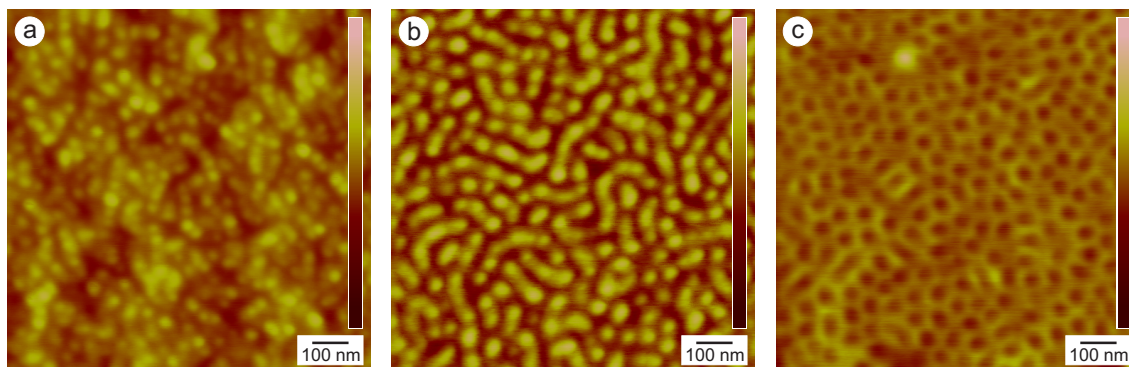


Figure 8.8: SFM topography images of aggregates on mica formed from polymer VS2 in cyclohexane/toluene mixtures. The polymer concentration was 1.0 g/l and the toluene contents were 0 %, 1 % and 5 % by volume. The aggregates transformed from spherical micelles via connected spheres to a regularly phase separated pattern

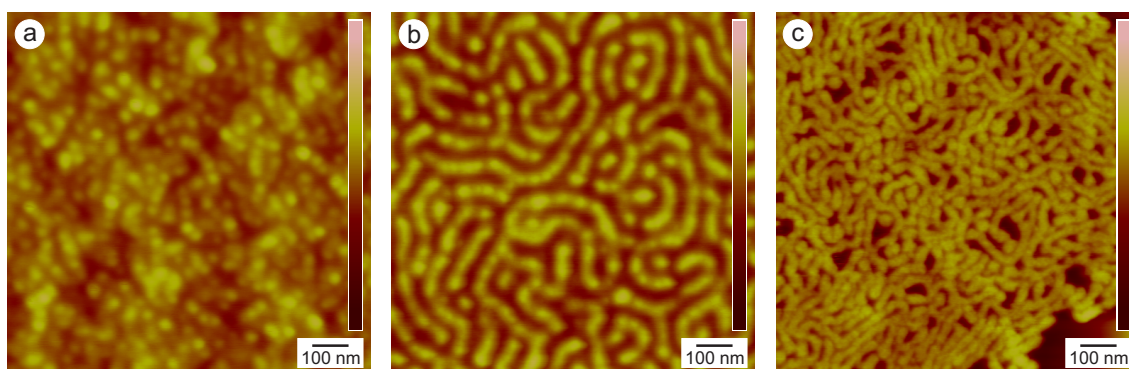


Figure 8.9: SFM topography images of aggregates on mica formed from polymer VS2 in cyclohexane/MEK mixtures. The polymer concentration was 1.0 g/l and the toluene contents were 0 %, 2 % and 5 % by volume. The aggregates transformed from spherical micelles via connected spheres to cylindrical micelles

cylinders coexisted with a few spherical aggregates. Polymer VS3 formed according to the chain length ratio of PS:PI of almost 1:2 spherical star-micelles and only a few dimeric or trimeric aggregates at higher concentrations.

Adding a small amount of a good solvent for the core block showed the desired effect of cylinder formation. At the beginning of cylinder formation the aggregates looked like connected spheres. The system was quite sensitive and only slightly higher amounts of co-solvent destroyed the cylinder structure (cyclohexane/toluene-system). Adding of MEK to cyclohexane showed the longest cylinders. The diameter of the cylinders reduced significantly compared to the spherical micelles at lower MEK content.

The concept of using only slightly selective solvents and increasing the concentration in order to shift the equilibrium towards cylindrical micelles could be proven. Transferring the micelles on a solid substrate and investigating by SFM is possible but it limits the observable concentration range by formation of multi-layers. Mixing solvents in order to improve the swelling of the core block also enhances the formation of elongated shaped micelles.

In all cases the cylindrical micelles coexisted with a few round aggregates and only exceeded a length to diameter ratio of 10:1 in the case of mixed cyclohexane/MEK solutions. Finally, one can say that the miktoarm star structure  $A_8B_8$  is an alternative for linear diblock copolymers to form cylindrical micelles.

# Bibliography

- [1] F. S. Bates. Polymer-polymer phase behavior. *Science*, 251:898–905, 1991.
- [2] M. W. Matsen and F. S. Bates. Unifying weak- and strong-segregation block copolymer theories. *Macromolecules*, 29:10091–1098, 1996.
- [3] F. S. Bates and G. H. Fredrickson. Block copolymer thermodynamics: Theory and experiment. *Annu. Rev. Phys. Chem.*, 41:525–557, 1990.
- [4] K. Schillén, A. Yekta, S. Ni, J. P. S. Farinha, and M. A. Winnik. Characterization of polyisoprene-*b*-poly(methyl methacrylate) diblock copolymer micelles in acetonitrile. *J. Phys. Chem. B*, 103:9090–9103, 1999.
- [5] I. Astafieva, X. F. Zhong, and A. Eisenberg. Critical micellization phenomena in block polyelectrolyte solutions. *Macromolecules*, 26:7339–7352, 1993.
- [6] Z. Gao and A. Eisenberg. A model of micellization for block copolymers in solutions. *Macromolecules*, 26:7353–7360, 1993.
- [7] K. Khougaz, Z. Gao, and A. Eisenberg. Determination of the critical micelle concentration of block copolymer micelles by static light scattering. *Macromolecules*, 27:6341–6346, 1994.
- [8] S. Förster, M. Zisenis, E. Wenz, and M. Antonietti. Micellization of strongly segregated block copolymers. *J. Chem. Phys.*, 104:9956–9970, 1996.
- [9] P. Bahadur, N. V. Sastry, S. Marti, and G. Riess. Micellar behaviour of styrene-isoprene block copolymers in selective solvents. *Coll. Surf.*, 5:337–346, 1985.
- [10] S. Pispas, S. Allorio, N. Hadjichristidis, and J. W. Mays. Micellization of  $\omega$ -functionalized poly(styrene-*b*-isoprene) copolymers in *n*-decane. *Macromolecules*, 29:2903–2908, 1996.
- [11] D. Nguyen, C. E. Williams, and A. Eisenberg. Block ionomer micelles in solution. 1. Characterization of ionic cores by small-angle X-ray scattering. *Macromolecules*, 27:5090–5093, 1994.
- [12] P. A. Canham, T. P. Lally, C. Price, and R. B. Stubbersfield. Formation of worm-like micelles from a polystyrene-polybutadiene-polystyrene block copolymer in ethyl acetate. *J. Chem. Soc. Faraday I*, 76:1857–1867, 1980.
- [13] C. Price, E. K. M. Chan, A. L. Hudd, and R. B. Stubbersfield. Worm-like micelle formation by a polystyrene-*b*-polyisoprene block copolymer in N,N'-dimethylacetamide. *Polym. Commun*, 27:196–198, 1986.

- [14] K. Schillén, W. Brown, and R. M. Johnsen. Micellar sphere-to-rod transition in an aqueous triblock copolymer system. A dynamic light scattering study of translational and rotational diffusion. *Macromolecules*, 27:4825–4832, 1994.
- [15] H. Shen, L. Zhang, and A. Eisenberg. Thermodynamics of crew-cut micelle formation of polystyrene-*b*-poly(acrylic acid) diblock copolymers in DMF/H<sub>2</sub>O mixtures. *J. Phys. Chem. B*, 101:4697–4708, 1997.
- [16] Y. Yu and A. Eisenberg. Control of morphology through polymer-solvent interactions in crew-cut aggregates of amphiphilic block copolymers. *J. Am. Chem. Soc.*, 119: 8383–8384, 1997.
- [17] K. Yu, L. Zhang, and A. Eisenberg. Novel morphologies of “crew-cut” aggregates of amphiphilic diblock copolymers in dilute solution. *Langmuir*, 12:5980–5984, 1996.
- [18] Y. Yu, L. Zhang, and A. Eisenberg. Morphogenic effect of solvent on crew-cut aggregates of amphiphilic diblock copolymers. *Macromolecules*, 31:1144–1154, 1998.
- [19] K. Yu and A. Eisenberg. Bilayer morphologies of self-assembled crew-cut aggregates of amphiphilic PS-*b*-PEO diblock copolymers in solution. *Macromolecules*, 31:3509–3518, 1998.
- [20] L. Zhang, H. Shen, and A. Eisenberg. Phase separation behavior and crew-cut micelle formation of polystyrene-*b*-poly(acrylic acid) copolymers in solutions. *Macromolecules*, 30:1001–1011, 1997.
- [21] J. Tao, S. Stewart, G. Liu, and M. Yang. Star and cylindrical micelles of polystyrene-*block*-poly(2-cinnamoyl ethyl methacrylate) in cyclopentane. *Macromolecules*, 30: 2738–2745, 1997.
- [22] L. Zhang and A. Eisenberg. Multiple morphologies and characteristics of “crew-cut” micelle-like aggregates of polystyrene-*b*-poly(acrylic acid) diblock copolymers in aqueous solutions. *J. Am. Chem. Soc.*, 118:3168–3181, 1996.
- [23] L. J. M. Vagberg, K. A. Cogan, and A. P. Gasto. Light-scattering study of starlike polymeric micelles. *Macromolecules*, 24:1670–1677, 1991.
- [24] A. Ramzi, M. Prager, D. Richter, V. Efstratiadis, N. Hadjichristidis, R. N. Young, and J. B. Allgaier. Influence of polymer architecture on the formation of micelles of miktoarm star copolymers polyethylene/poly(ethylenepropylene) in the selective solvent decane. *Macromolecules*, 30:7171–7182, 1997.
- [25] D. K. Polyakov, G. M. Ignat’eva, E. A. Rebrov, N. G. Vasilenko, S. S. Sheiko, M. Möller, and A. M. Muzafarov. Star-shaped multi-arm poly(styrene-*block*-isoprene). *Polym. Sci. Ser. A*, 40:876–883, 1998.
- [26] S. Pispas, N. Hadjichristidis, and J. W. Mays. Micellization of model graft copolymers of the H and  $\pi$  type in dilute solution. *Macromolecules*, 29:7378–7385, 1996.
- [27] H. Iatrou, L. Willner, N. Hadjichristidis, A. Halperin, and D. Richter. Aggregation phenomena of model PS/PI super-H-shaped block copolymers. influence of the architecture. *Macromolecules*, 29:581–591, 1996.

- [28] M. Pitsikalis, J. Woodward, J. W. Mays, and N. Hadjichristidis. Micellization of model graft copolymers in dilute solution. *Macromolecules*, 30:5384–5389, 1997.
- [29] J. P. Spatz, S. Mößmer, and M. Möller. Metastabile inverse Kugelmicellen und micellare Drähte aus Blockcopolymeren. *Angew. Chem.*, 108:1673–1676, 1996.
- [30] A. Avgeropoulos, Y. Poulos, and N. Hadjichristidis. Synthesis of model 16-Miktoarm (Vergina) star copolymers of the  $A_8B_8$  type. *Macromolecules*, 29:6016–6078, 1996.
- [31] F. L. Beyer, S. P. Gido, Y. Poulos, A. Avgeropoulos, and N. Hadjichristidis. Morphology of Vergina Star 16-arm block copolymers and scaling behavior of interfacial area with graft point functionality. *Macromolecules*, 30:2373–2376, 1997.
- [32] S. Pispas, Y. Poulos, and N. Hadjichristidis. Micellization behavior of  $(PS)_8(PI)_8$  Miktoarm (Vergina) Star copolymers. *Macromolecules*, 31:4177–4181, 1998.
- [33] J. E. Mark, editor. *Polymer Data Handbook*. Oxford University Press, online edition, 1999.

*Bibliography*



# A Visualization of the gelation process of a new class of semicarbazide-organogelators by scanning force microscopy

## A.1 Introduction

Organogels consist of solvents and organic minor components that form percolating supramolecular structures confining the solvent. The obtained elastic or viscoelastic systems exhibit thermoreversible or even mechanoreversible structure formation. Examples of organogelators for aqueous [1] and organic [2] systems have been reviewed. Organogelators have been early discovered [3] and were applied during the first half of the 20<sup>th</sup> century as thickeners to generate artificial greases and lubricants. Other applications concerned wood furniture repair kits, adhesives, inks and ointment bases. Between 1960 and 1980 the organogel research virtually rested. The scientific interest was then renewed (e. g. [4]) and has gained large interest. Although the thickening effect is still a matter of concern – e. g. for the preparation of drop-free wall paints and greases [5] – the actual research is more directed towards the supramolecular features of organogels.

Percolation theory states elongated thin objects to form three dimensional percolating structures at rather low volume fractions [6, 7], and by means of the ‘random contact theory’ the percolation threshold volume fraction  $\Phi^*$  was related to the aspect ratio of the cylinders [8]:  $\Phi^* = K_{cylinder} \cdot \frac{D}{L}$  (D = cylinder diameter, L = cylinder length,  $K_{cylinder} \approx 4.2$ ).

In fact the most effective organogelators, gelling solutions below contents of 1 wt%, are known to self-assemble to cylinder- or ribbon-like solid aggregates from solution. In many cases well defined aggregates with narrow diameter distributions [4] or peculiar superstructures like ribbons [9], rolled up multi-layer sheets [10], bundles of fibres [11] or helices [12] have been observed. This multitude of supramolecular architectures makes organogels to valuable sources for new structures applied in supramolecular chemistry. New opportunities concern the use of the supramolecular fibres as templates to create porous materials, the construction of supramolecular transport channels as well as the preparation of new supramolecular/macromolecular hybrid systems. Table A.1 summarises industrially realized applications and some possible future directions of organogel research.

Employing organogels in supramolecular chemistry requires to control structure and functionality of the fibrous aggregates. Hence, rational concepts are needed to obtain molecular defined objects which are limited in two-dimensionally growth. The few papers that address this subject try to construct the interaction between the associating molecules in great detail [25]. Despite its success the approach only applies for a specific molecular structure and lacks for generality.

In our group a simplified geometric concept without perfectly considering packing and interactions was developed. In this approach approximately flat, amphiphilic molecules consisting of small polar and bulky non-polar parts were used. In a non-polar environment the molecules will aggregate to minimize the unfavorable contact between polar and

Table A.1: Realized applications of organogels and possible future directions [13–24]

Property	Application	Industrial Examples	Academical Examples
<i>Thermoreversibility</i>	‘smart’ thickeners	Lubricants Greases Napalm	Solid Electrolytes Solar Cells
<i>Thixotropy/ Shear thinning</i>		Inks Wall Paints	Pharmacy
<i>Structural definition</i>	supramolecular chemistry	—	Templates Tectons
<i>Functionality</i>	adaptive Materials switchable Materials	—	New Polymers Functional Membranes

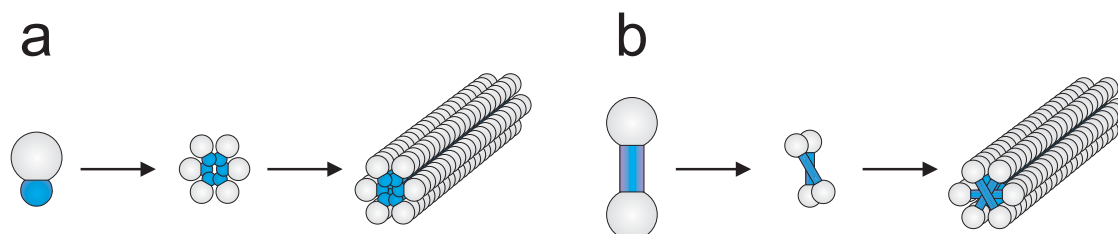


Figure A.1: Schematic sketch of elementary fibril formation with a) wedge- and b) dumb-bell shaped organogelators

non-polar regions. Caused by the different space requirements of the molecular parts the association should be driven towards ‘core–shell’ structures with the polar, strongly associative groups confined to the inner part of the aggregates. The task of the large non-polar molecular end is to prevent lateral growth of the aggregates by steric shielding effects. From the specific shape of the molecules the preferred formation of cylinder-like supramolecular objects is expected (Figure A.1a).

Rod-formation was shown with the examples of wedge-shaped, ‘dipolar’ amphiphilic molecules like tris(alkoxy)benzamides [11], N-sorbitoyl-3,4,5-tris(alkoxy)benzamides [26] and crown ether amphiphiles [21]. The obtained fibres were molecularly defined, and contained polar functional groups in their interior. Fibres derived from polymerisable crown ether amphiphiles have been used as supramolecular ion transport channels [23, 24].

Subsequently, the concept was extended to molecules that can be regarded as covalently linked dimers of such wedge-shaped amphiphiles (Figure A.1b). It was assumed that linking together two wedge-shaped amphiphiles to a gelator molecule containing one single associative core will increase the thermal and mechanical stability of the resulting gels.

Bis(semicarbazides) of the general structure  $\mathbf{Y-CO-NH-NH-CO-NH-X-NH-CO-NH-NH-CO-Y}$  have been chosen as the highly associative molecular core. Y represents

(alkoxy)phenyl units, and X denotes either an aromatic or an aliphatic moiety. Such cores have been selected because of i) their ability to form up to 12 hydrogen bonds per molecule, ii) their simple preparation and iii) their large structural variability.

Here the effect of changing the molecular geometry of the bis(semicarbazide) core X, from a linear 1,4-phenyl- to a U-shaped 1,8-naphthyl-geometry on the gelation properties is compared by scanning force microscopy. Furthermore the process of gelation is visualized.

## A.2 Experimental part

### A.2.1 Methods

Scanning force microscopy (SFM) was performed in air on a Digital Instruments Multi-mode SPM with a Nanoscope IIIa controller operating in the tapping mode at a resonance frequency of ca. 330 MHz. Silicon probes (Nanosensors) with a spring constant of ca. 42 N/m were used.

Thermo gravimetric analysis (TGA) was performed on a Perkin-Elmer TGS-2. The heating runs were performed under nitrogen atmosphere, taking the onset temperature of the weight loss as the decomposition temperature  $T_{decomp}$  ( $dT/dt = 10$  K/min).

DSC measurements were performed, using a PERKIN-ELMER DSC 7 unit, equipped with a TAS 7 data processor. The device was calibrated against cyclohexane, water and indium standards. 4–5 mg of each sample were sealed in PERKIN-ELMER pressure pans and heated with a rate of 10 K/min.

Molecular Modelling was performed with MacroModel 7.1 [27], using the Merck Molecular Force Field (MMFF) [28]. The structure was refined further by means of the Truncated Newton conjugate gradient method [29] until the final gradient was below 0.005 kJ/Å.

### A.2.2 Gel preparation

#### ‘Hot gelation’ procedure

The bis[(alkoxy)benzoyl]semicarbazides ( $25.0 \pm 0.5$  mg) and the solvent ( $975.0 \pm 0.5$  mg) were weighted into screw cap vials (1.5 ml, LabTop) and, after closing the vial, heated until a clear solution was obtained. If no complete dissolution was observed, the vials were heated for at least 15 minutes. On standing at ambient temperature (cooling rate at 40 °C: 6 K/min), the samples gelled within a few minutes. For slow cooling, the sample vials were put into a styropor block (cooling rate at 40 °C: 2 K/min). Gelation was taken to be finished, if the sample vials could be turned upside down without observing any flow of the mixture inside.

#### ‘Cold gelation’ procedure

1 ml of the solvent was injected into a precursor solution of bis[(alkoxy)benzoyl]semicarbazide ( $25.0 \pm 0.5$  mg) in DMAc ( $50.0 \pm 0.5$  mg) at ambient temperature. After vigorous agitation the sample was allowed to stand without further mechanical stress until gelation occurred.

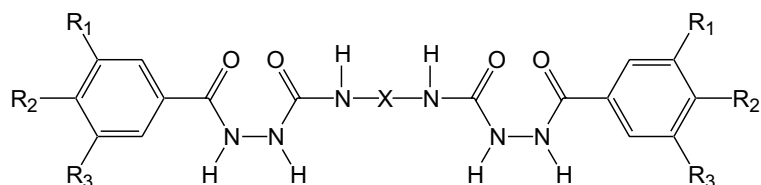


Figure A.2: General structure of bis[[(alkoxy)benzoyl]semicarbazides].

X = 1,4-phenyl-, 2,4-toluy-, 2,6-toluy-, 1,8-naphthyl-, 1,6-hexamthylene-;

R<sub>i</sub> = C<sub>n</sub>H<sub>2n+1</sub>O-, H-

Table A.2: Synthesised bis(semicarbazides)

name	X	R <sub>1</sub>	R <sub>2</sub>	R <sub>3</sub>
<b>1,4-PDI-8</b>	1,4-PDI	C <sub>8</sub> H <sub>17</sub> O-	C <sub>8</sub> H <sub>17</sub> O-	C <sub>8</sub> H <sub>17</sub> O-
<b>1,8-NDI-12</b>	1,8-NDI	C <sub>12</sub> H <sub>25</sub> O-	C <sub>12</sub> H <sub>25</sub> O-	C <sub>12</sub> H <sub>25</sub> O-

1,4-PDI = 1,4-phenyl, 1,8-NDI = 1,8-naphthyl

### A.2.3 Materials

The solvents used for the gelation experiments N,N-dimethylformamide (DMF), ethanol, 2-hydroxy-ethyl methacrylate (HEMA), tetrahydrofuran (THF), chloroform, *n*-hexyl methacrylate (HMA), styrene, toluene, *tert*-butyl acetate (*t*-BuAc), *n*-hexane and tri(isopropyl)benzene (TiPrB) (all of technical grade) were used as received.

### A.2.4 Synthesis of bis[(alkoxy)benzoyl]semicarbazides

The (alkoxy)benzoyl semicarbazides were prepared from Dr. Uwe Beginn and his coworkers (University of Ulm, Germany) by reaction of isocyanates with N-(alkoxy)benzoyl hydrazides that have been obtained by aminolysis of methyl alkoxybenzoates with hydrazine hydrate [30, 31]. In a second step the hydrazides were coupled to a diisocyanate to obtain the ‘bis(semicarbazides)’ (Figure A.2). Both reaction steps worked fast and efficient. The overall yield of the bis(semicarbazides) was found in the range between 61 % and 92 % with respect to the starting methyl ester. The substitution pattern and the used cores for the two considered bis(semicarbazides) is summarized in Table A.2.

In the case of 1,4-PDI-8 the reaction mixture gelled due to the formation of the bis(semicarbazides). It was then found to be of advantage to suppress the gelation by addition of DMF prior to the work up of the reaction mixture.

## A.3 Results and discussion

### A.3.1 Thermal transitions

The thermal properties of the bis(semicarbazides) have been investigated by thermogravimetry (TGA) and differential scanning calorimetry (DSC). The results for the two here investigated bis(semicarbazides) are listed in Table A.3.

Table A.3: Thermal properties of the bis(semicarbazides)

name	$T_{decomp}/^{\circ}\text{C}$ (TGA)	$T_m/^{\circ}\text{C}^{\text{a}}$
<b>1,4-PDI-8</b>	$230 \pm 2$	220 (68.1)
<b>1,8-NDI-12</b>	$208 \pm 5$	199 (160)

a) DSC onset temperature, values in brackets: transition enthalpy in kJ/mol

The thermal stability of bis(semicarbazides) was mainly determined by the molecular core that separates the two semicarbazide units. With the 1,4-phenyl core the  $T_{decomp}$  exceeded  $220^{\circ}\text{C}$  and was in the case of 1,4-PDI-8  $230^{\circ}\text{C}$ , while compounds with toluyl- and naphthyl-core usually decomposed below  $212^{\circ}\text{C}$ .

### A.3.2 Gelation tests

Thermoreversible gelation was studied as a first indication for the self-ordering to supramolecular structures [32]. Formation of rod-like associates will cause gelation at rather low concentrations [6–8]. Table A.4 summarises qualitative tests with various solvents. The hot semicarbazide/solvent mixtures were cooled at a controlled rate ( $< 6$  K/min) to a temperature below the melting transition in order to induce gelation. Three types of gels have been distinguished: (i) transparent-clear gels, (ii) turbid-translucent gels, and (iii) opaque-white gels. Opaque gels were most frequently obtained from the polar solvents, while the non-polar liquids preferably yielded clear- or at least turbid-translucent gels.

The two extremes can be discussed with ethanol and *n*-hexane. Ethanol was found to be a bad solvent for both bis(semicarbazides). Although only partial solubility was observed during the solubility experiments, opaque gels were formed from ethanol solutions of 1,4-PDI-8 and 1,8-NDI-12. In this solvent the critical gelation concentration (cgc) was found to fall short of 1 wt%.

Both bis(semicarbazides) formed transparent-clear gels on cooling hot mixtures of hexane and gelator. 1,4-PDI-8 was not completely soluble in boiling hexane, but strongly swelled during the heating until all the solvent was taken up. Both bis(semicarbazide)/hexane gels could not be molten on re-heating the samples to the boiling temperature of *n*-hexane ( $69^{\circ}\text{C}$ ). Clear solutions of high viscosity were also found at  $20^{\circ}\text{C}$  for 1,8-NDI-12/toluene.

1,4-PDI-8 formed highly viscous solutions or gels even in boiling solvents making it difficult to obtain homogeneous mixtures. In particular the gels from chloroform were inhomogeneous after 1 hour of heating. The inhomogenities vanished after prolonged annealing ( $> 5$  days) at  $20^{\circ}\text{C}$ .

### A.3.3 Cold gelation

Gelation was most pronounced with less polar solvents like chloroform, styrene, toluene, and *n*-hexane since the solubility was rather limited in non-polar liquids. The observed orthogonality in solubility and gel formation offers intriguing opportunities to induce gel

Table A.4: Dissolution and gelation of bis(semicarbazide)/solvent mixtures (2.5 wt% semicarbazide). Each sample was annealed at 20 °C, than heated to the boiling point, and subsequently cooled to 20 °C

Solvent	1,4-PDI-8			1,8-NDI-12		
	RT <sup>1)</sup>	$\Delta$	RT <sup>2)</sup>	RT <sup>1)</sup>	$\Delta$	RT <sup>2)</sup>
Ethanol	i	i	Go	i	ps	Go
DMF	i	s	s	i	s	Go
HEMA	i	s	Gt	i	s	Go
THF	i	sw	Gt	s	s	Go
CHCl <sub>3</sub>	i	i	Gc	s	s	Go
HMA	i	s	Gc	i	s	Go
Styrene	i	sw	Gt	sw	s	Gt
Toluene	i	i	Gc	sw	s	s $\eta$
t-BuAc	i	i	Gc	i	s	Go
<i>n</i> -Hexane	i	i	Gt	sw	s	Gc

1) 20 °C, before heating, 2) after annealing for 15 minutes and cooling to 20 °C,  $\Delta$  = heating to the boiling temperature, i = insoluble, sw = swelling, ps = partially soluble, s = soluble, s $\eta$  = viscous solution, Gc = clear transparent gel, Gt = translucent gel, Go = opaque/white gel

Table A.5: ‘Cold’ gelation of toluene, *n*-hexane, and 1,3,5-tri(isopropyl)benzene by mixing with solutions of 1,4-PDI-8 in DMAc at 20 °C

$C_{1,4\text{-PDI-8}}$ [wt%] <sup>(a)</sup>	solvent added	$C_{\text{DMAc}}$ [wt%] <sup>(b)</sup>	$C_{1,4\text{-PDI-8}}$ [mol/L]	Observation at 20 °C (10 min)	Observation at 20 °C (15 h)
20,0	toluene	10,0	0,021	Gt	<i>S</i> $\eta$
33,3	toluene	5,0	0,021	Gt	Gt
33,3	toluene	1,7	0,007	Gc	Gc
33,3	<i>n</i> -hexane	6,2	0,026	Gc	Gc
33,3	<i>n</i> -hexane	2,2	0,009	Gc	Gc
33,3	TiPrB	3,0	0,012	Gc	Gc
33,3	TiPrB	1,5	0,006	Gc	Gc
33,3	TiPrB	0,75	0,004	Gc	Gc
33,3	TiPrB	0,38	0,002	<i>S</i> $\eta\eta$	Gc
33,3	TiPrB	0,19	0,001	<i>S</i> $\eta$	<i>S</i> $\eta\eta$

(a) concentration of 1,4-PDI-8 in the initial DMAc solution, (b) concentration after addition of solvent, *S* $\eta$  = viscous solution, *S* $\eta\eta$  = highly viscous solution, Gt = turbid/translucent gel, Gc = clear/transparent gel

formation by isothermal change of the solvent composition. At ambient temperature such ‘cold gelation’ might be of practical interest because of (i) the high rate of gelation, (ii) the reduced thermal load of the thickened liquid, (iii) the possibility to mix low viscous dissolved gelators to a solution, or dispersion that should be gelled or thickened, and (iv) the opportunity to produce gelator concentrations far beyond its thermodynamic solubility limit.

‘Cold’ gelation was done with ‘precursor’ solutions of the bis(semicarbazides) in *N,N*-dimethylacetamide (DMAc), a solvent that is able to break hydrogen-bonds. Exemplarily, the results for 1,4-PDI-8 are shown here in more detail. At 20 °C solutions of 50 wt% 1,4-PDI-8 in DMAc solidified within five minutes, while solutions containing 33 wt% remain stable for at least six hours. Below 20 wt% no gelation was observed. On adding toluene, 1,3,5-tri(isopropyl)benzene (TiPrB) or *n*-hexane to the cold DMAc solutions the gels were immediately formed. While the toluene gels were slightly turbid on exceeding a concentration of 1.5 wt% (12 mM), clear gels emerged from TiPrB and hexane. The critical gelation concentration was found to fall short of 0.5 wt% (4.2 mM) in each case.

The results of the dilution experiments are summarised in Table A.5.

### A.3.4 Gel morphology

The gel morphologies and fibre formation abilities of semicarbazide 1,4-PDI-8, and 1,8-NDI-12 have been investigated by scanning force microscopy. The two compounds were selected because of their opposite molecular shape. While 1,4-PDI-8 represented an example of a linear gelator molecule, 1,8-NDI-12 exhibited a U-turned molecular geometry.

All gels were prepared by means of the ‘cold’ solution technique from a precursor solution of 33 wt% semicarbazide in DMAc.

Figure A.3 depicts SFM scans of aggregates of 1,4-PDI-8 that have been deposited

on mica substrates under different conditions. In Figure A.3a a thick film of 1,4-PDI-8 was obtained by drying a droplet of a 1,4-PDI-8/toluene gel containing 3 wt% of 1,4-PDI-8. The substrate was completely covered and not expected to alter the structure of the uppermost layers. In this gel 1,4-PDI-8 formed a dense network of bundle like fibres with diameters around  $90 \pm 30$  nm. Since no substructure comparable to the dimensions of the individual molecules have been resolved the coverage of the substrate was reduced by spin-coating diluted solutions of 1,4-PDI-8 in toluene on freshly cleaved substrates. A viscoelastic solution of 0.25 wt% 1,4-PDI-8 in toluene was diluted to 0.025 wt%, and 0.0025 wt%, respectively. Immediately to dilution the mixtures were spin-coated on the substrate to avoid alterations of the gels original structure due to re-equilibration processes. In Figure A.3b (0.25 wt% 1,4-PDI-8/toluene) two layers on top of each other can be distinguished. The top layer appeared to consist of fibres (diameters 20–50 nm, height:  $5 \pm 1$  nm) similar to that of Figure A.3a, while in the down most layer the fibres showed a more ‘flattened’ habit. Further dilution to 0.025 wt% yielded specimen without the second coverage layer clearly demonstrating the strong effect of the substrate on the fibres (Figure A.3c). The bundles, up to several 100 nm in width, were flattened by the strong adsorption on mica and partly even torn apart. The vertical extension of the structures was uniform with a height of 3–4 nm.

Further dilution experiments with the 0.24 wt% 1,4-PDI-8/toluene gel to obtain 0.0026 wt% 1,4-PDI-8 yielded thinner filaments of more uniform lateral diameters, ranging from 40 nm to less than 6 nm (Figure A.3d). Simultaneously the height of the ‘2d-fibres’ was reduced to 1.5 nm. This observation corresponds to the molecular dimensions of the semicarbazide molecule 1,4-PDI-8: Due to the strong polar nature of the mica surface the semicarbazide core should adsorb in a flat conformation, while the non-polar alkyl chains are directed towards the air interface. Since the length of the octyloxy chains is roughly 1 nm in their stretched conformation, and the closest approximation of aromatic units to the surface will be around 0.3 nm, a thickness of the monolayer of 1.3 nm is to be expected.

Similar observations were made with diluted gels, spin-coated on HOPG. Figure A.4a depicts the SFM micrograph of a 0.1 wt% solution of 1,4-PDI-8 in toluene, showing a two dimensional network of flat fibrous bundles adsorbed on the graphite. In this case it was possible to resolve the fibril sub-structure of the surface bundles (A.4b) to consist of parallel elementary fibres exhibiting a lateral periodicity of  $d = (5.5 \pm 0.7)$  nm, and a height of  $h = (1.2 \pm 0.2)$  nm.

An attempt was made to follow the time evolution of the supramolecular aggregates during the gelation process. A ‘cold gelation’ sequence, starting from a 16 wt% precursor solution of 1,4-PDI-8 in DMAc was performed to yield a final mixture of 0.4 wt% 1,4-PDI-8/2.0 wt% DMAc in toluene. After mixing the precursor solution and toluene, the solutions were taken and spin-coated on mica. It was assumed that the spin-coating would immediately quench the gelation and impede further growth or alteration of the gel structure, since the time scale of spin-coating (milliseconds) is much shorter than the time scale of structure evolution (minutes). Due to the resulting thick layer of dried gel the substrate will not influence the top layers of gel fibres visualised by SFM. One minute subsequent to mixing of precursor solution and toluene, a dense layer made up from elongated primary aggregates was found. The aggregates measure between 250 and 500 nm in length, their diameters are distributed between 50 and 100 nm (Figure A.5a). Five minutes after mixing ‘short’ fibrils varying in diameter from 60 to 100 nm were established. The fibrils length is in the range of 800–1200 nm. Though the fibrils crossed each other at many points only Van-der-Waals contacts, i. e. no evidence for the presence of permanent connections, were



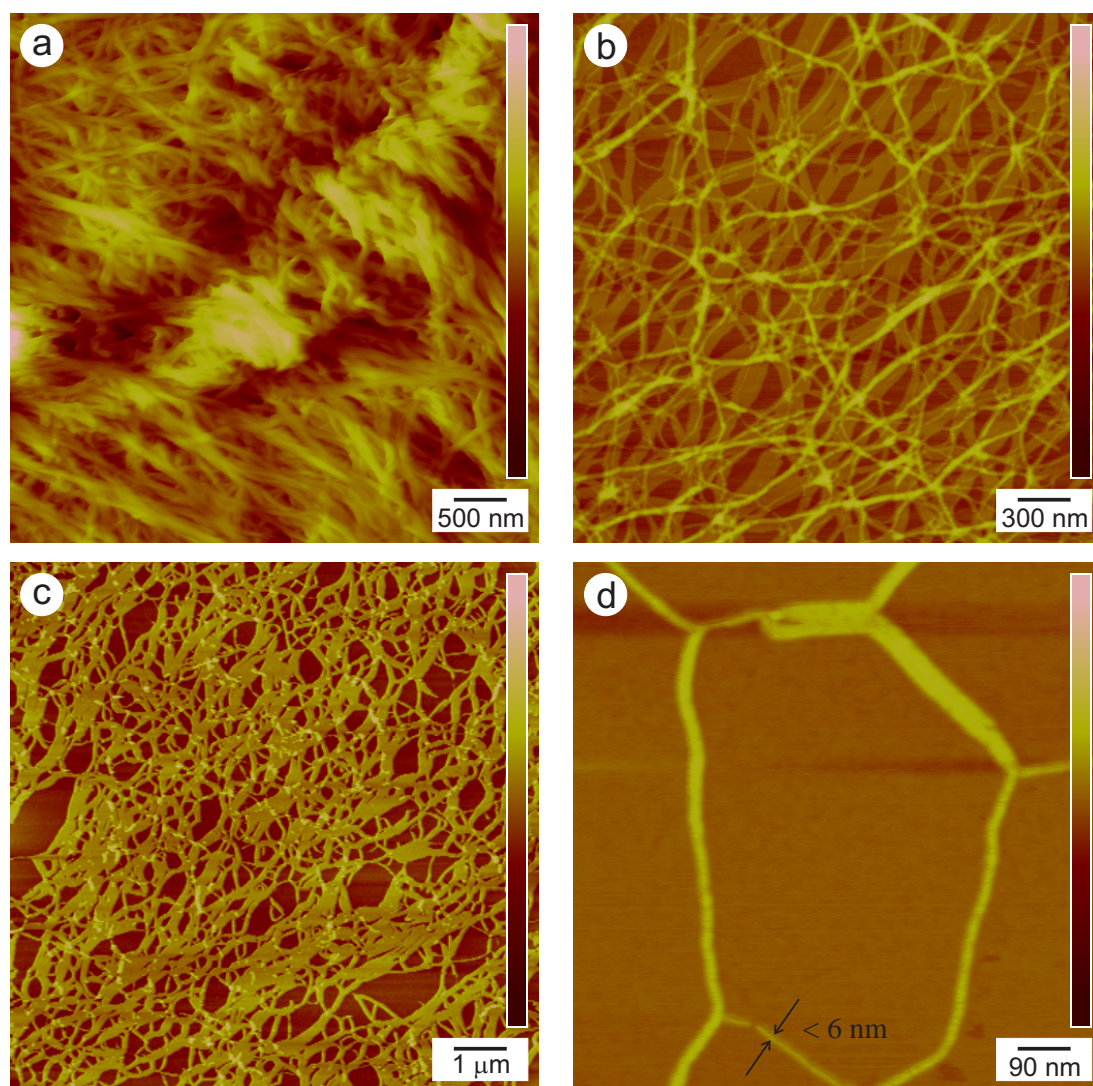


Figure A.3: SFM tapping mode topography micrographs of 1,4-PDI-8/DMAc/toluene systems deposited on mica. a) dried gel (3.0 wt% 1,4-PDI-8; z-range 500 nm), b) spin-coated gel (0.25 wt% 1,4-PDI-8; 0.5 wt% DMAc; z-range 50 nm), c) spin-coated viscoelastic solution (0.025 wt% 1,4-PDI-8; 0.05 wt% DMAc; z-range 15 nm), d) spin-coated solution (0.0025 wt% 1,4-PDI-8; 0.005 wt% DMAc; z-range 20 nm)

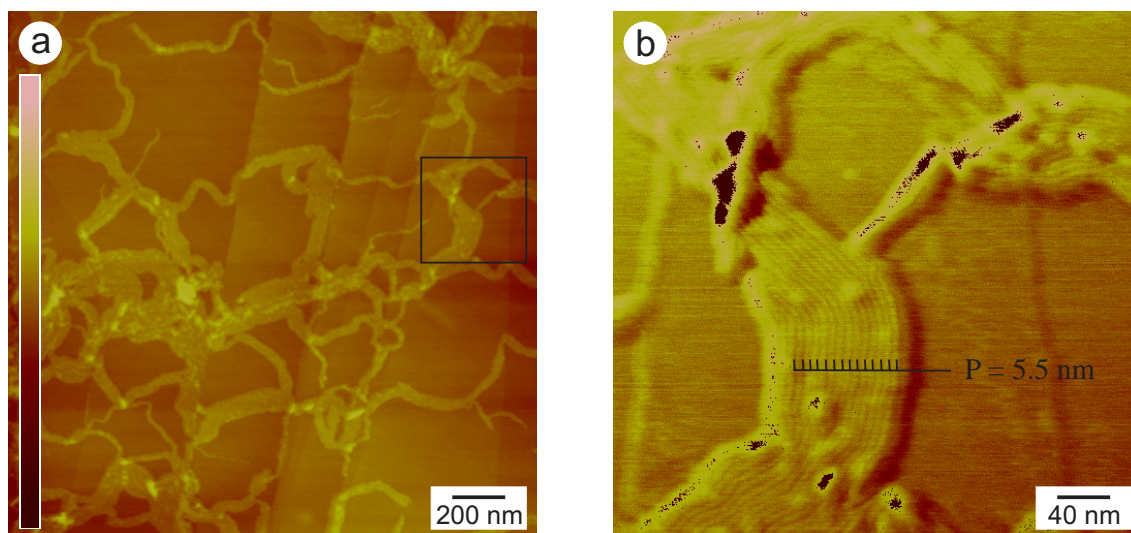


Figure A.4: SFM tapping mode micrographs of a 1,4-PDI-8/DMAc/toluene gel (0.1 wt% 1,4-PDI-8; 0.2 wt% DMAc) spin-coated on HOPG. a) Overview (topography, z-range 20 nm), b) Resolution of the fibril substructure of the surface bundles (phase signal)

observed. 30 minutes after mixing the length of the primary fibrils exceeded the side length of the scanning window (5000 nm), while its diameters virtually remained unchanged. Simultaneously many additional small fibres (diameter = 30–60 nm, Figure A.5c) have been grown in the interstices of the larger fibers, filling the voids between the thicker fibres.

Repeating this experiment with a final concentration of 0.25 wt% 1,4-PDI-8/0.5 wt% DMAc in toluene (Figure A.6) showed the presence of primary fibres (50–100 nm diameter) even after 1 minute. Two hours after mixing SFM revealed a fully developed network with fibres of fairly infinite lengths. According to the rheology experiments this mixture started to thicken with an induction period of 5–8 minutes, reaching its final modulus at 40–60 minutes.

Thick films of dried gels arising from the ‘U’-shaped gelator molecule 1,8-NDI-12 (0.5 wt%) in hexane are depicted in Figure A.7. The observed aggregates were elongated but irregularly shaped, exhibiting diameters in the range of 30–50 nm, and aspect ratios of  $[d/L]_{1,8\text{-NDI-12}} = 10 \pm 3$ . This value was considerably lower than obtained from fibres with the linear gelator 1,4-PDI-8 ( $[d/L]_{1,4\text{-PDI-8}} \gg 100$ ). Additionally, the crystallites appeared strongly bent, and curved (Figure A.7a). Dilution of the 1,8-NDI-12/hexane gels, and spin-coating on mica did not result in the resolution of individual elementary fibres. Instead the associates remained broad and fragmented (Figure A.7b). Even the smallest structures exhibited lateral dimensions of  $45 \pm 5$  nm. Furthermore the substrate seemed to be covered by a flat layer of gelator molecules as indicated by the dark shadowed zones between the aggregates. By means of diluting, and subsequent spin-coating it was obviously not possible to preserve the characteristic gel structure during the sample preparation. This may be in connection to the enhanced solubility, i. e. the higher critical gelation concentration of 1,8-NDI-12 with respect to compound 1,4-PDI-8. Probably the strong interaction between the high-energy surface of mica and the dissolved single molecules of 1,8-NDI-12 caused the partial disintegration of the gel forming structures.

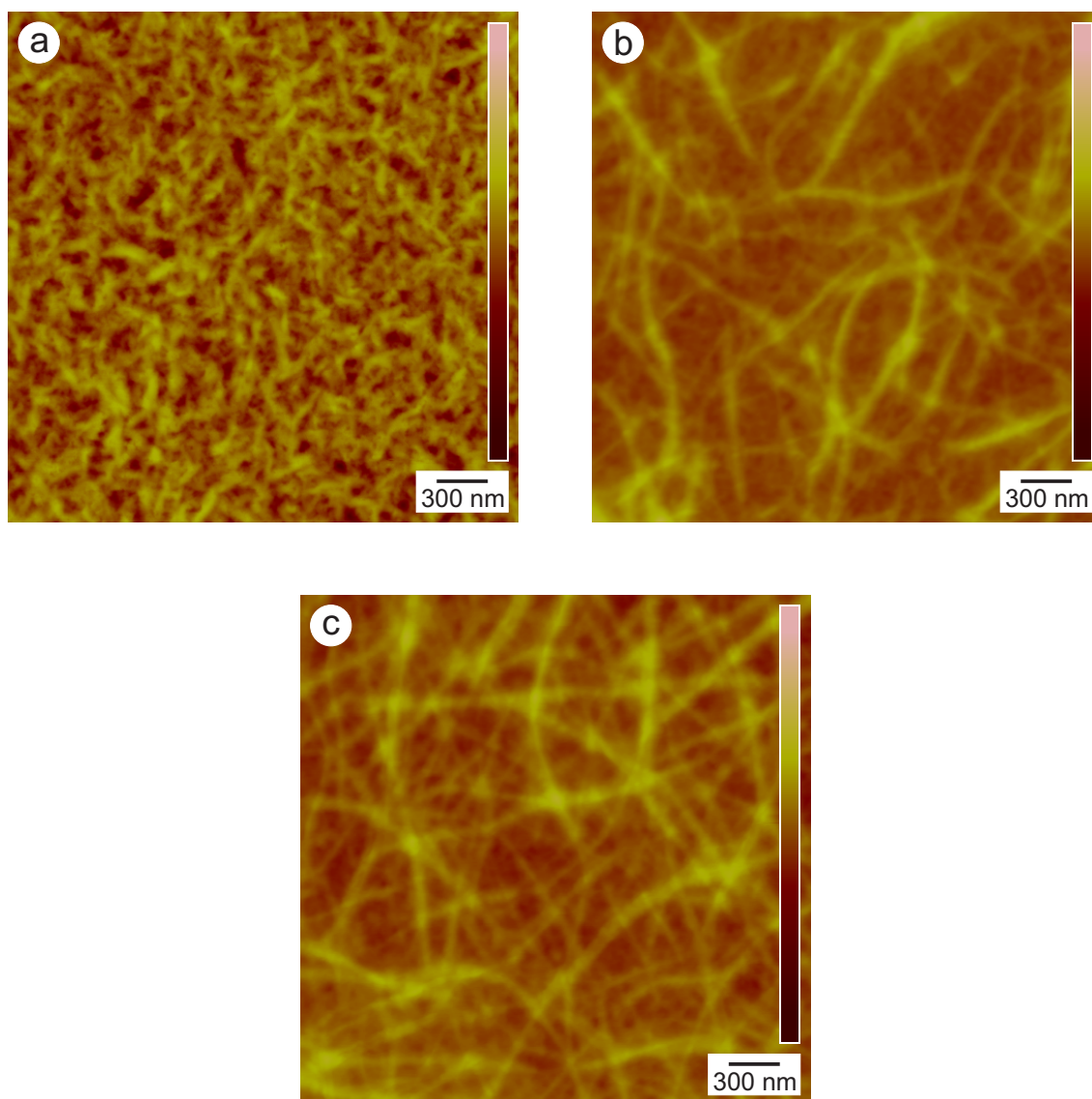


Figure A.5: SFM tapping mode topography micrographs of the time evolution of the supramolecular aggregates during the gelation process. A gel consisting of 0.4 wt% 1,4-PDI-8, 2.0 wt% DMAc in toluene was spin-coated on mica. After a) 1 min (z-range 50 nm), b) 5 min (z-range 150 nm), c) 30 min (z-range 200 nm)

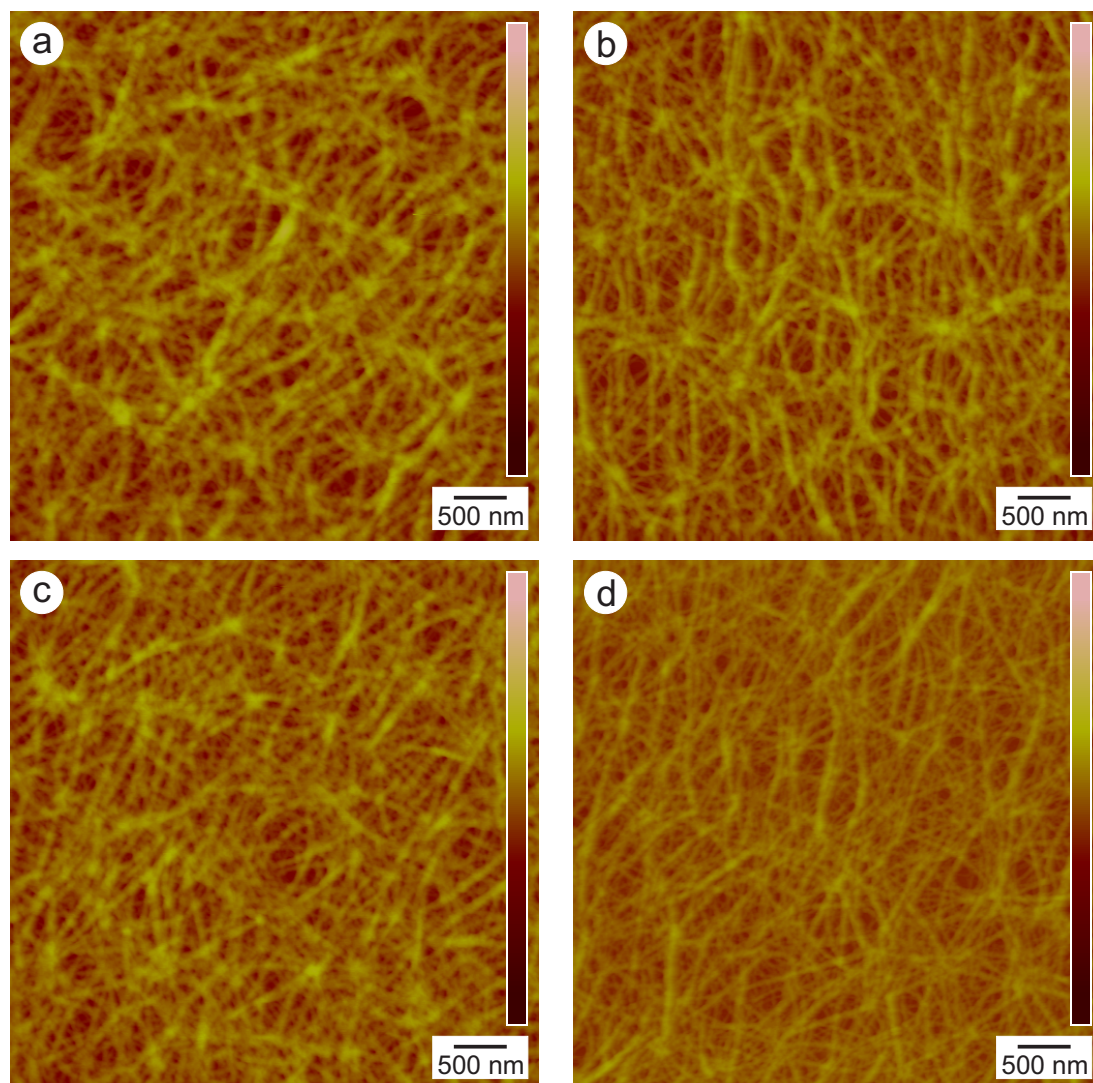


Figure A.6: SFM tapping mode topography micrographs of the time evolution of the supramolecular aggregates during the gelation process. A gel consisting of 0.25 wt% 1,4-PDI-8, 0.5 wt% DMAc in toluene was spin-coated on mica. After a) 1 min, b) 10 min, c) 30 min, d) 2 hours (z-range 200 nm)

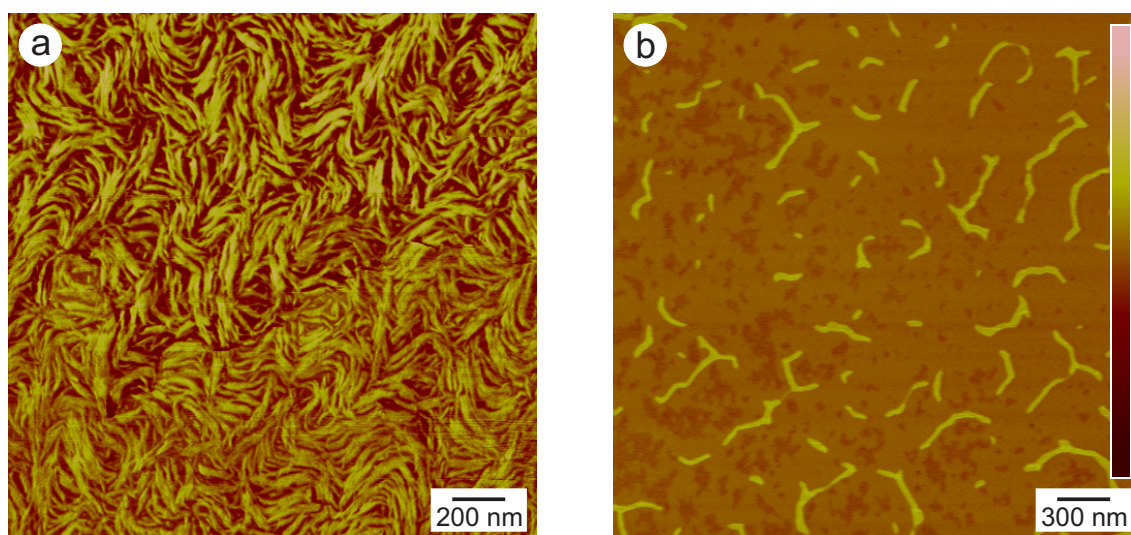


Figure A.7: SFM tapping mode micrographs of 1,8-NDI-12/*n*-hexane systems deposited on mica. a) dried gel (0.5 wt% 1,8-NDI-12, phase image), b) spin-coated solution (0.02 wt% 1,4-PDI-8, topography, z-range 20 nm)

### A.3.5 Modelling

Molecular modelling studies were performed with MacroModel 7.1 [27] using the MMFF force field [28]. To derive a packing model of semicarbazide 1,4-PDI-8 in the gelled state the molecules were assumed to adopt the transoid conformation depicted in Figure A.8a. This assumption is justified by experimental studies on molecular conformations of hydrazides [33], and semicarbazides. With the transoid conformation the molecules were found to assemble to linear stacks independently of the starting configuration. The calculated CPK model of a stacked linear tetramer is depicted in Figure A.8b indicating a lateral extension of 4.8 nm, and an axial stacking distance of 0.6 nm. These values are compatible to the dimensions of the elementary fibres resolved in Figure A.4. Within these stacks two independent ribbons of hydrogen bonds were distinguished: Each semicarbazide moiety forms six H-bonds, three to its upper-, and three to its lower next neighbour. The N-H donor units interact in two different manners with the carbonyl oxygen atom since the urea-oxygen atom is always found to form two H-bonds, while the hydrazide oxygen atom only accepts one H-atom. With 12 hydrogen bonds per molecule sticking together the stacks their enthalpy of association must exceed the thermal energy by far. In fact, molecular modelling experiments simulating the stepwise disintegration of a tetramer of 1,4-PDI-8 in the presence of water, or chloroform, suggested the enthalpy of association  $\Delta H_{ass}$  to be in the range of  $190 \pm 20$  kJ/mol. In vacuo the dissociation was connected to a  $\Delta H_{ass}$  of 370 kJ/mol, obviously caused by the lack of solvent shielding effects.

## A.4 Conclusions

Bis[(alkoxy)benzoyl]semicarbazides, prepared from (alkoxy)benzoyl hydrazides and diisocyanates, represent a new, and versatile class of high efficient organogelators. The gelation properties can be tuned with high accuracy by variation of (i) the central molecular core,

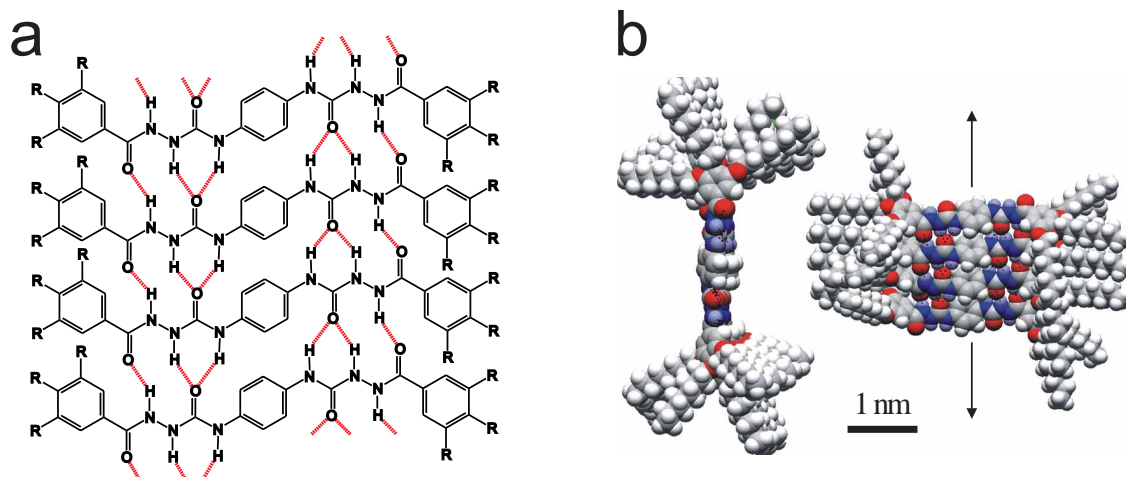


Figure A.8: Proposed model of the molecular arrangement of 14 molecules in the elementary fibrils. (a) Schematic depiction of the hydrogen bond network, (b) Calculated CPK model

(ii) the number of the alkyl chains, and (iii) the length of the alkyl chains attached to the bis[benzoyl]semicarbazide moiety. The procedure of ‘cold’ gelation is an easy applicable and versatile technique for industrial purposes.

It was shown that scanning force microscopy is a powerful tool to get detailed insight in the fibril structures of the formed gels. The size of the elementary fibers determined by SFM is in the same range as expected from the molecular size and from the molecular modelling. The improved gelation of 1,4-PDI-8 compared to 1,8-NDI-12 is due to the formation of infinite long fibers of the linear gelation agent. The U-shaped 1,8-NDI-12 formed elongated curved structures with a maximum length of several hundred nanometers.

Time resolved SFM of the gelation process of 1,4-PDI-8 showed that in an initial fast step a network of thick bundles of fibers is formed. In a second slower process the interstices between these bundles are filled with thinner fibers.

# Bibliography

- [1] J.-H. Fuhrhop and J. Köning. *Membranes and Molecular Assemblies: The Syneknetic Approach*. The Royal Society of Chemistry, Cambridge, U. K., 1994.
- [2] P. Terech and R. G. Weiss. Low molecular mass gelators of organic liquids and the properties of their gels. *Chem. Rev.*, 97:3133–3159, 1997.
- [3] A. Lipowitz. Versuche und Resultate über die Löslichkeit der Harnsäure. *Ann. Chem. Pharm.*, 38:348–355, 1841.
- [4] B. Pfannemüller and W. Welte. Amphiphilic properties of synthetic glycolipids based on amide linkages. I. electron microscopic studies on aqueous gels. *Chem. Phys. Lip.*, 37:227–240, 1985.
- [5] E. R. Booser. 'Lubrication and Lubricants' in 'Encyclopedia of Chemical Technology', volume 15. Wiley-Interscience, New York, 4th edition, 1995.
- [6] M. Sinclair, K. C. Lim, and A. J. Heeger. Gelation of rodlike macromolecules. *Phys. Rev. Lett.*, 51:1768–1771, 1983.
- [7] A. L. R. Bug, S. A. Safran, and I. Webman. Continuum percolation of permeable objects. *Phys. Rev. B*, 33:4716–4724, 1986.
- [8] A. P. Philipse. The random contact equation and its implications for (colloidal) rods in packings, suspensions, and anisotropic powders. *Langmuir*, 12:1127–1133, 1996.
- [9] J.-H. Fuhrhop and W. Helfrich. Fluid and solid fibers made of lipid molecular bilayers. *Chem. Rev.*, 93:1565–1582, 1993.
- [10] J.-H. Fuhrhop, D. Spiroski, and C. Boettcher. Molecular monolayer rods and tubules made of  $\alpha$ -(l-lysine), $\omega$ -(amino) bolaamphiphiles. *J. Amer. Chem. Soc.*, 115:1600–1601, 1993.
- [11] U. Beginn, S. Sheiko, and M. Möller. Self-organization of 3,4,5-tris(octyloxy)benzamide in solution and embedding of the aggregates into methacrylate resins. *Macromol. Chem. Phys.*, 201:1008–1015, 2000.
- [12] T. Gulik-Krzywicki, C. Fouquey, and J.-M. Lehn. Electron microscopic study of supramolecular liquid crystalline polymers formed by molecular-recognition-directed self-assembly from complementary chiral components. *Proc. Natl. Acad. Sci. USA*, 90:163–167, 1993.
- [13] K. Hanabusa, K. Hiratsuka, M. Kimura, and H. Shirai. Easy preparation and useful character of organogel electrolytes based on low molecular weight gelator. *Chem. Mater.*, 11:649–655, 1999.

- [14] W. Kubo, K. Murakoshi, T. Kitamura, Y. Wada, K. Hanabusa, H. Shirai, and S. Yanagida. Fabrication of quasi-solid-state dye-sensitized TiO<sub>2</sub> solar cells using low molecular weight gelators. *Chem. Lett.*, 27:1241–1242, 1998.
- [15] J. L. Schaller, B. Briggs, and M. Briggs. Progesterone organogel for premenstrual dysphoric disorder. *J. Amer. Acad. Child Adolesc. Psychiatry*, 39:546–547, 2000.
- [16] H. Gankema, M. A. Hempenius, M. Möller, G. Johansson, and V. Percec. Gel template leaching: An approach to functional nanoporous membranes. *Macromol. Symp.*, 102: 381–390, 1996.
- [17] R. J. H Hafkamp, B. P. A. Kokke, I. M. Danke, H. P. M. Geurts, A. E. Rowan, M. C. Feiters, and R. J. M. Nolte. Organogel formation and molecular imprinting by functionalized gluconamides and their metal complexes. *Chem. Commun.*, pages 545–546, 1997.
- [18] W. Gu, L. Lu, G. B. Chapman, and R. G. Weiss. Polymerized gels and ‘reverse aerogels’ from methyl methacrylate or styrene and tetraoctadecylammonium bromide as gelator. *Chem. Commun.*, pages 543–544, 1997.
- [19] Y. Ono, Y. Kanekiyo, K. Inoue, J. Hojo, and S. Shinkai. Evidence for the importance of a cationic charge in the formation of hollow fiber silica from an organic gel system. *Chem. Lett.*, 28:23–24, 1999.
- [20] C. Geiger, M. Stanescu, L. Chen, and D. G. Whitten. Organogels resulting from competing self-assembly units in the gelator: Structure, dynamics, and photophysical behavior of gels formed from cholesterol-stilbene and cholesterol-squaraine gelators. *Langmuir*, 15:2241–2245, 1999.
- [21] U. Beginn, G. Zipp, and M. Möller. Self-organization of liquid crystalline 3,4,5-tris[(11- methacryloyl-undecyl-1-oxy)-4-benzyloxy] benzoates in low-shrinkage methacrylate mixtures. *J. Polym. Sci. A: Polym. Chem.*, 38:631–640, 2000.
- [22] K. Inoue, Y. Ono, Y. Kanekiyo, K. Hanabusa, and S. Shinkai. Preparation of new robust organic gels by *in situ* cross-link of a bis(diacetylene) gelator. *Chem. Lett.*, 28: 429–430, 1999.
- [23] U. Beginn, G. Zipp, and M. Möller. Functional membranes containing ion-selective matrix-fixed supramolecular channels. *Adv. Mater.*, 12:510–513, 2000.
- [24] U. Beginn, G. Zipp, A. Mourran, P. Walther, and M. Möller. Membranes containing oriented supramolecular transport channels. *Adv. Mater.*, 12:513–516, 2000.
- [25] J. H. van Esch and B. L. Feringa. New functional materials based on self-assembling organogels: From serendipity towards design. *Angew. Chem. Int. Ed.*, 39:2263–2266, 2000.
- [26] U. Beginn, S. Keinath, and M. Möller. New carbohydrate amphiphiles, 2 Gel formation and gel morphologies. *Macromol. Chem. Phys.*, 199:2379–1284, 1998.
- [27] F. Mohamadi, N. G. J. Richards, W. C. Guida, R. Liskamp, M. Lipton, C. Caulfield, G. Chang, T. Hendrickson, and W. C. Still. MacroModel – An integrated software



- system for modeling organic and bioorganic molecules using molecular mechanics. *J. Comput. Chem.*, 11:440–467, 1990.
- [28] T. A. Halgren. Merck molecular force field. I. Basis, form, scope, parameterization, and performance of MMFF94. *J. Comput. Chem.*, 17:490–519, 1996.
- [29] J. W. Ponder and F. M. Richardson. An efficient newton-like method for molecular mechanics energy minimization of large molecules. *J. Comput. Chem.*, 8:1016–1024, 1987.
- [30] U. Beginn. *Synthese und Charakterisierung neuer nieder- und hochmolekularer supramolekularer Mesogene*. PhD thesis, University of Bayreuth (Germany), 1994.
- [31] C. K. Lai, C.-H. Tsai, and Y.-S. Pang. Discotic metallomesogens: mesophase crossover of columnar rectangular to hexagonal arrangements in bis(hydrazinato)nickel(ii) complexes. *J. Mater. Chem.*, 8:1355–1360, 1998.
- [32] U. Beginn and B. Tartsch. Bis[(alkoxy)benzoylsemicarbazides] - a new class of powerful organogelators. *J. Chem. Soc. Chem. Commun.*, 19:1924–1925, 2001.
- [33] H. Paulsen and D. Stoye. "The Chemistry of Hydrazides" in "The Chemistry of Functional Groups: The Chemistry of Amides". Interscience Publishers, London, 1970.

*Bibliography*

# B Gold nanoparticles with covalently attached polymer chains

## B.1 Introduction

Over recent years thiol-stabilized gold nanoparticles (Au-NPs) have attracted increasing interest [1, 2] because of their potential in divergent fields such as nanoelectronics and -optics as well as DNA diagnostics [3–6].

Alkanethiolate-stabilized Au-NPs of narrow size distribution are easy to synthesize and of relatively high stability [7]. The shell of these organic–inorganic hybrid materials can be functionalized by site-exchange reactions thus allowing the controlled change of the properties of the particles and the adjustment of the surface for further reactions [8–10].

Au-NPs modified with polymer chains covalently bound to the surface by ‘grafting from’ reaction have been described in only two examples [11, 12]. ‘Grafting from’ by the use of the so-called ‘living’/controlled radical polymerization in accord with the mechanism of atom transfer radical polymerization (ATRP), which was first described in 1995 [13], is promising but has not been applied to Au-NPs yet. It has, however, been shown that ATRP is a suitable method for preparing polymer layers covalently bound to the surface of different solid materials and even for the generation of block copolymer grafts [14–17].

A polymer shell is interesting for the control of surface properties, for an increase in chemical and/or thermal stability, and, if functional monomers are used, for the provision of functional groups in the bound polymer chains for further modification. Here it is shown that grafting from ATRP is an efficient synthetic route to attach polymer chains covalently to nanoparticles, and scanning force microscopy is used as visualization tool.

## B.2 Experimental

### B.2.1 Materials

Dodecanethiol-protected gold colloids were prepared according to the method in reference [7]. The synthesis was carried out at room temperature with a threefold molar excess of dodecanethiol to tetrachloroauric acid. Compound **1** and the thiol-initiator **2** (Figure B.1) were synthesized according to the methods in reference [16] and [18].

The site exchange process of the dodecanethiol protecting the gold nanoparticle with the thiol-initiator, the grafting from ATRP and the cleavage of the polymer chains are described in [18].

The whole synthesis was carried out by Stefan Nuß in the laboratories of Prof. M. L. Hallensleben at the University of Hannover, Germany.

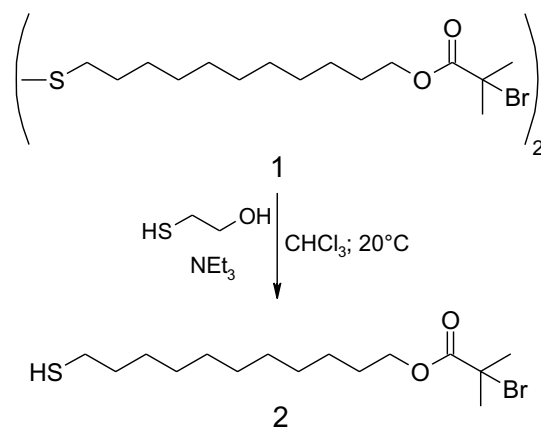


Figure B.1: Synthesis of thiol-initiator **2**. This molecule can be attached to a gold surface by the thiol functionality and contains a  $\alpha$ -bromoester moiety as an initiator unit for ATRP

## B.2.2 Methods

TEM images were recorded on a Philips CM-300 microscope working at 300 kV. SFM measurements were performed on a Digital Instruments Multimode SPM with a Nanoscope IIIa controller in tapping mode. The resonance frequency dependent on the Si-cantilever ( $K \approx 42$  N/m, Nanosensors) was set to about 330 kHz. Samples were prepared by spin-casting of a dilute CHCl<sub>3</sub> or THF solution with a concentration of 0.01 mg/ml at 2000 rpm on mica as a substrate. GP chromatograms were recorded on a Spectra-Physics SP 8100 (polystyrene calibration). Thermogravimetric measurements were carried out on a Netzsch TG 209.

## B.3 Results and discussion

The C<sub>12</sub>S residues on dodecanethiol-stabilized Au-NPs are replaced by thiol-initiator **2** by means of site-exchange reactions. Compound **2** is synthesized starting from the known compound **1** [16] (Figure B.1) by cleavage of the disulfide bond. Compound **2** contains a thiol group, which serves as an anchor to bind **2** to the surface of the Au-NPs, and a  $\alpha$ -bromoester moiety, which is suitable as an initiator group for the ATRP. Thus the site-exchange reaction leads to Au-NPs functionalized on the surface with initiator moieties for a 'living'/controlled radical polymerization. The ratio of **2** to surface-bound dodecanethiol can be varied within narrow ranges and be confirmed by <sup>1</sup>H-NMR spectroscopy. In combination with thermogravimetric analysis (TGA) measurements the number of initiator groups per mg Au-NP can be calculated, which allows the preselection of a defined initiator/catalyst ratio for the polymerization.

ATRP starting from initiator-modified Au-NPs was carried out with Cu<sup>I</sup>Br/Me<sub>6</sub>tren (Me<sub>6</sub>tren = tris(2-dimethylaminoethyl)amine) (Figure B.2). This catalytic system allows the polymerization of *n*-butyl acrylate at room temperature [19]. Dynamic processes at the surface such as desorption of initiator molecules or thermal initiation of the monomer are suppressed to a large extent under these reaction conditions. The organic part of this new organic-inorganic hybrid can be as much as 90% w/w (TGA) after the polymerization.

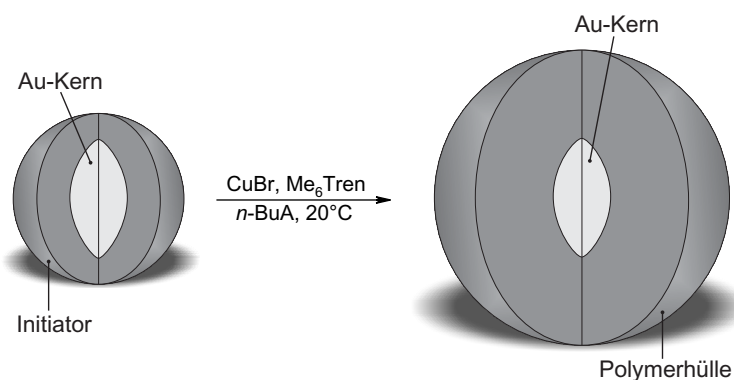


Figure B.2: Generation of a polymer shell around the Au-NPs; *n*-BuA = *n*-butyl acrylate

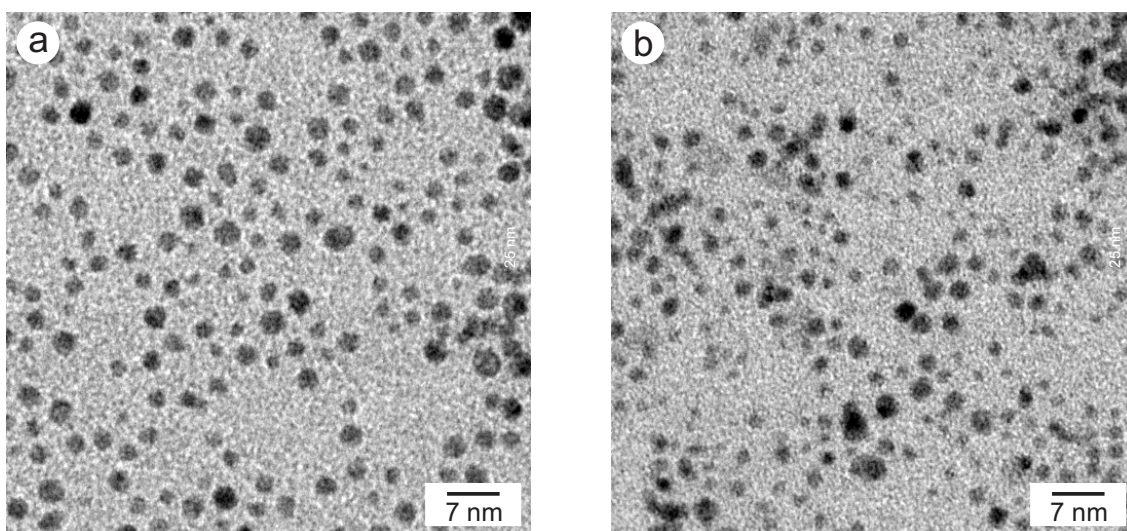


Figure B.3: TEM images of a) dodecanethiol-stabilized, and b) polymer-coated Au-NPs

The  $^1\text{H-NMR}$  spectrum and glass transition temperature of the surface-bound polymer chains (determined by dynamic difference calorimetry) are almost identical with those obtained from investigations on free poly(*n*-butyl acrylate).

Transmission electron microscopy (TEM) investigations reveal that the Au-NPs are still individual particles after the graft polymerization (Figure B.3). The size distribution of the Au-NPs is unaffected by the grafting process; the average diameter is about 2 nm.

The high energy impact during TEM measurements almost completely destroys the attached polymer. However, scanning force microscopy (SFM) investigations convincingly demonstrate the successful grafting of the Au-NPs (Figure B.4). The gold cores are depicted by the white protrusions in the SFM images; the polymer chains are shown in gray. Figures B.4a and b clearly demonstrate that the polymer chains are bound to the gold cores, which confirms the success of the grafting-from ATRP. Figure B.4b also shows that different numbers of chains of varying lengths are attached to the Au-NP and that even unbound chains are present.

The different number of chains on the surface may be the result of the statistical site-exchange reaction of dodecanethiol against compound **2**, but may also be caused by the

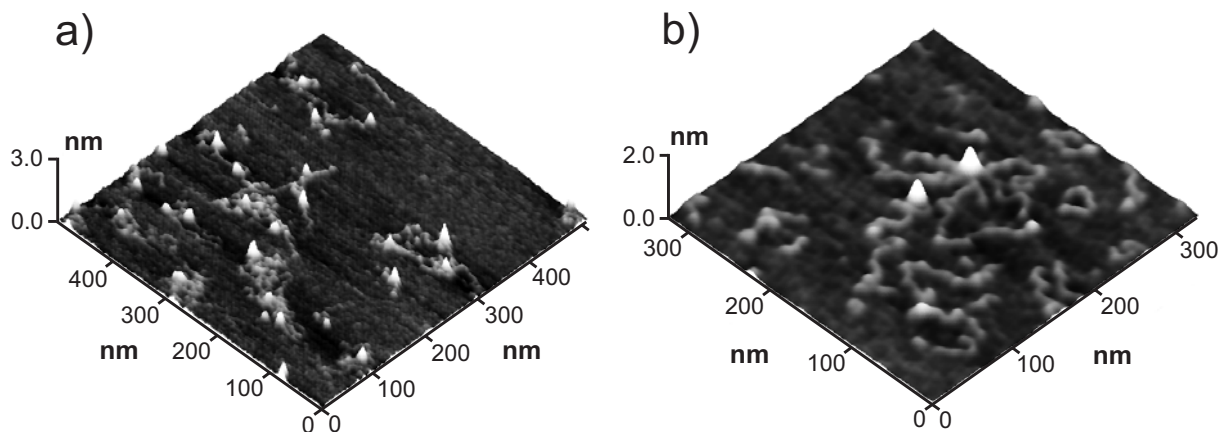


Figure B.4: SFM images of Au-NPs with tethered polymer chains spin-casted onto mica from a) chloroform, and b) THF solution.

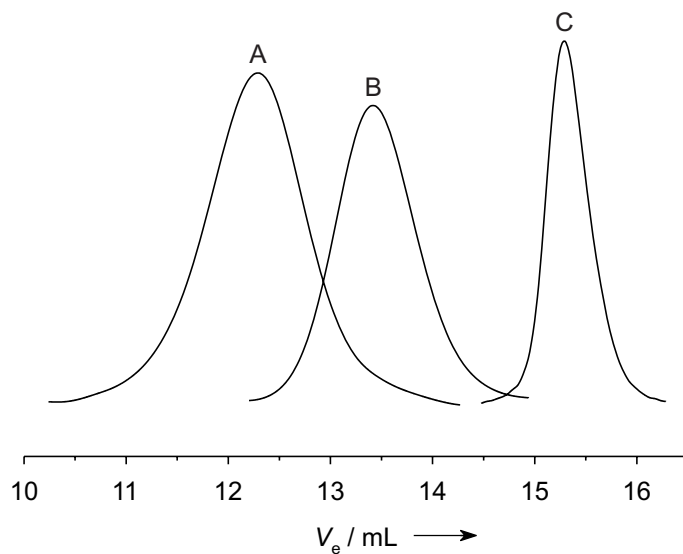


Figure B.5: GPC chromatograms of A) polymer-grafted Au-NPs ( $M_n = 206,000$  g/mol,  $PD = 1.63$ ), B) cleaved polymer ( $M_n = 75,000$  g/mol,  $PDI = 1.25$ ), and C) dodecanethiol-stabilized Au-NPs ( $M_n = 4,700$  g/mol,  $PDI = 1.14$ ); molecular mass relative to polystyrene standard;  $V_e$  = elution volume

size distribution of the Au-NPs itself. This finding from the SFM investigation is in good agreement with GPC results (Figure B.5). The polymer-grafted Au-NPs give a relatively broad distribution (chromatogram A, polydispersity index (PDI) = 1.63) compared to that for the cleaved polymer (chromatogram B, PDI = 1.25), showing that the single polymer chains undergo controlled growth also on the surface. The monomodal distribution of trace A can be regarded as proof for the interpretation that the ‘free’ polymer chains in Figure B.4b are a result of the spin-casting process during the preparation of the SFM samples.

The GPC traces can be compared only qualitatively, since calibrations were carried out with a polystyrene standard, and the chemical structure of the materials is different. However, the polymer-grafted Au-NPs (chromatogram A) show a much shorter elution time than the dodecanethiol stabilized Au-NPs (chromatogram C) and the detached polymer chains (chromatogram B). This is due to an increase of the hydrodynamic radii and of the molecular weight as a result of the grafting reaction. From the molecular weights one can estimate an average degree of grafting of three polymer chains per gold core, which is in full agreement with the results of SFM investigations (see Figure B.4).

## B.4 Conclusions

Au-NPs can be grafted with polymer chains by the ATRP mechanism in a simple sequence of reactions. SFM showed the superiority over TEM to visualize the tethered polymer chains of the Au-NPs. No free polymer chains are formed during the grafting reaction and the Au-NPs remain unchanged in size and size distribution.





# Bibliography

- [1] A. C. Templeton, W. P. Wuelfing, and R. W. Murray. Monolayer-protected cluster molecules. *Acc. Chem. Res.*, 33:27–36, 2000.
- [2] R. L. Whetten, J. T. Khoury, M. M. Alvarez, S. Murthy, I. Vezmar, Z. L. Wang, P. W. Stephens, C. L. Cleveland, W. D. Luedtke, and U. Landman. Nanocrystal gold molecules. *Adv. Mater.*, 8:428–433, 1996.
- [3] L. He, M. D. Musick, S. R. Nicewarner, F. G. Salinas, S. J. Benkovic, M. J. Natan, and C. D. Keating. Colloidal Au-enhanced surface plasmon resonance for ultrasensitive detection of DNA hybridization. *J. Am. Chem. Soc.*, 122:9071–9077, 2000.
- [4] W. P. McCormell, J. P. Novak, L. C. Brousseau III, R. R. Fuieler, R. C. Tenent, and D. L. Feldheim. Electronic and optical properties of chemically modified metal nanoparticles and molecularly bridged nanoparticle arrays. *J. Phys. Chem. B*, 104: 8925–8930, 2000.
- [5] J. J. Storhoff, A. A. Lazarides, R. C. Mucic, C. A. Mirkin, R. L. Letsinger, and G. C. Schatz. What controls the optical properties of DNA-linked gold nanoparticle assemblies. *J. Am. Chem. Soc.*, 122:4640–4650, 2000.
- [6] S. Chen, R. S. Ingram, M. J. Hostetler, J. J. Pietrom, R. W. Murray, T. G. Schaaff, J. T. Khoury, M. M. Alvarez, and R. L. Whetten. Gold nanoelectrodes of varied size: Transition to molecule-like charging. *Science*, 280:2098–2101, 1998.
- [7] M. J. Hostetler, J. E. Wingate, C.-J. Zhong, J. E. Harris, R. W. Vachet, M. R. Clark, J. D. Londono, S. J. Green, J. J. Stokes, G. D. Wignall, G. L. Glish, M. D. Porter, N. D. Evans, and R. W. Murray. Alkanethiolate gold cluster molecules with core diameters from 1.5 to 5.2 nm: Core and monolayer properties as a function of core size. *Langmuir*, 14:17–30, 1998.
- [8] M. J. Hostetler, A. C. Templeton, and R. W. Murray. Dynamics of place-exchange reactions on monolayer-protected gold cluster molecules. *Langmuir*, 15:3782–3789, 1999.
- [9] A. C. Templeton, M. J. Hostetler, E. K. Warmoth, S. Chen, C. M. Hartshorn, V. M. Krishnamurthy, M. D. E. Forbes, and R. W. Murray. Gateway reactions to diverse, polyfunctional monolayer-protected gold clusters. *J. Am. Chem. Soc.*, 120:4845–4849, 1998.
- [10] M. J. Hostetler, S. J. Green, J. J. Stokes, and R. W. Murray. Monolayers in three dimensions: Synthesis and electrochemistry of  $\omega$ -functionalized alkanethiolate-stabilized gold cluster compounds. *J. Am. Chem. Soc.*, 118:4212–4213, 1996.

- [11] R. Jordan, N. West, A. Ulman, Y.-M. Chou, and O. Nuyken. Nanocomposites by surface-initiated living cationic polymerization of 2-oxazolines on functionalized gold nanoparticles. *Macromolecules*, 34:1606–1611, 2001.
- [12] K. J. Watson, J. Zhu, S. T. Nguyen, and C. A. Mirkin. Hybrid nanoparticles with block copolymer shell structures. *J. Am. Chem. Soc.*, 121:462–463, 1999.
- [13] T. E. Patten and K. Matyjaszewski. Atom transfer radical polymerization and the synthesis of polymeric materials. *Adv. Mater*, 10:901–915, 1998.
- [14] H. Böttcher, M. L. Hallensleben, Stefan Nuß, and Hellmuth Wurm. ATRP grafting from silica surface to create first and second generation of grafts. *Polym. Bull.*, 44: 223–229, 2000.
- [15] J.-B. Kim, M. L. Bruening, , and G. L. Baker. Surface-initiated atom transfer radical polymerization on gold at ambient temperature. *J. Am. Chem. Soc.*, 122:7616–7617, 2000.
- [16] R. R. Shah, D. Merreceyes, M. Husemann, I. Rees, N. L. Abbott, C. J. Hawker, and J. L. Hedrick. Using atom transfer radical polymerization to amplify monolayers of initiators patterned by microcontact printing into polymer brushes for pattern transfer. *Macromolecules*, 33:597–605, 2000.
- [17] M. Husseman, E. E. Malmstro1m, M. McNamara, M. Mate, D. Mecerreyes, D. G. Benoit, J. L. Hedrick, P. Mansky, E. Huang, T. P. Russell, and C. J. Hawker. Controlled synthesis of polymer brushes by “living” free radical polymerization techniques. *Macromolecules*, 32:1424–1431, 1999.
- [18] S. Nuß, H. Böttcher, H. Wurm, and M. L. Hallensleben. Goldnanopartikel mit kovalent angebundenen Polymerketten. *Angew. Chem.*, 113:4137–4139, 2001.
- [19] J. Xia, S. G. Gaynor, and K. Matyjaszewski. Controlled/“living” radical polymerization. Atom transfer radical polymerization of acrylates at ambient temperature. *Macromolecules*, 31:5958–5959, 1998.

# C Sterically terminated polymerization leading to polymers with defined shape and uniform molecular weight

## C.1 Introduction

Due to the used polymers for the main part of this thesis there was a close cooperation with the group of Prof. Dr. V. Percec (University of Pennsylvania, Philadelphia, USA). Several other polymer samples have been synthesized in his group and were investigated here in Ulm by scanning force microscopy. This appendix will deal with one of these compounds.

Polymers with minidendritic side groups have been widely used to create macromolecules with defined shapes [1–4]. Typically these polymers form cylinders. Diameters of 5 nm and more in combination with a defined shape simplifies the visualization with SFM and makes this type of molecules to model compounds similar to DNA strands but with an order of magnitude smaller sizes. Additionally the different chemistry of these synthetic polymers gives complementary results.

Studies of the polymerization kinetic of oxanorbonenes substituted with minidendritic side groups using ring opening metathesis polymerization showed a very interesting behavior [5, 6]: After initiation the reaction propagated with a certain speed. Soon the reaction rate was decreasing. But when the resulting polymer reached a certain molecular weight the reaction went on with a second faster rate of propagation. The explanation of this effect is straight forward. When the reaction starts and the first monomers react with each other the reactive center is shielded more and more by the big dendritic side groups (see Figure C.1). In this stage the polymer adopts a spherical shape with the reactive center in the middle making it harder and harder for new monomers to continue the polymerization. The reaction rate is decreasing. Further propagation is only possible if the polymer readjusts its shape from spherical to cylindrical. Then the reactive center is only shielded from one side and can be freely reached from the other side resulting in a second higher rate of propagation.

If the used monomer possesses an extremely high degree of branching in the minidendritic side group the bulkiness of the side-groups does not allow the system to transform into the cylindrical conformation and to continue the polymerization. As a result the reaction stops at a certain degree of polymerization yielding spherical particles with uniform molecular weight. The Polymerization is sterically terminated but the reactive center inside the sphere is chemically active. Addition of a second small monomer that is able to penetrate in the shell formed by the minidendritic side groups should be able to reach the reactive center and to continue the reaction. The result is a sphere with a chain growing out of it – a tadpole.

Here the system 345-345-ON (Figure C.3a) showed exactly the effect of steric terminated polymerization as discussed in the latter paragraph. Addition of di-ethoxy substituted oxanorbornene as a small monomer resulted in increased molecular weight (Figure C.2).

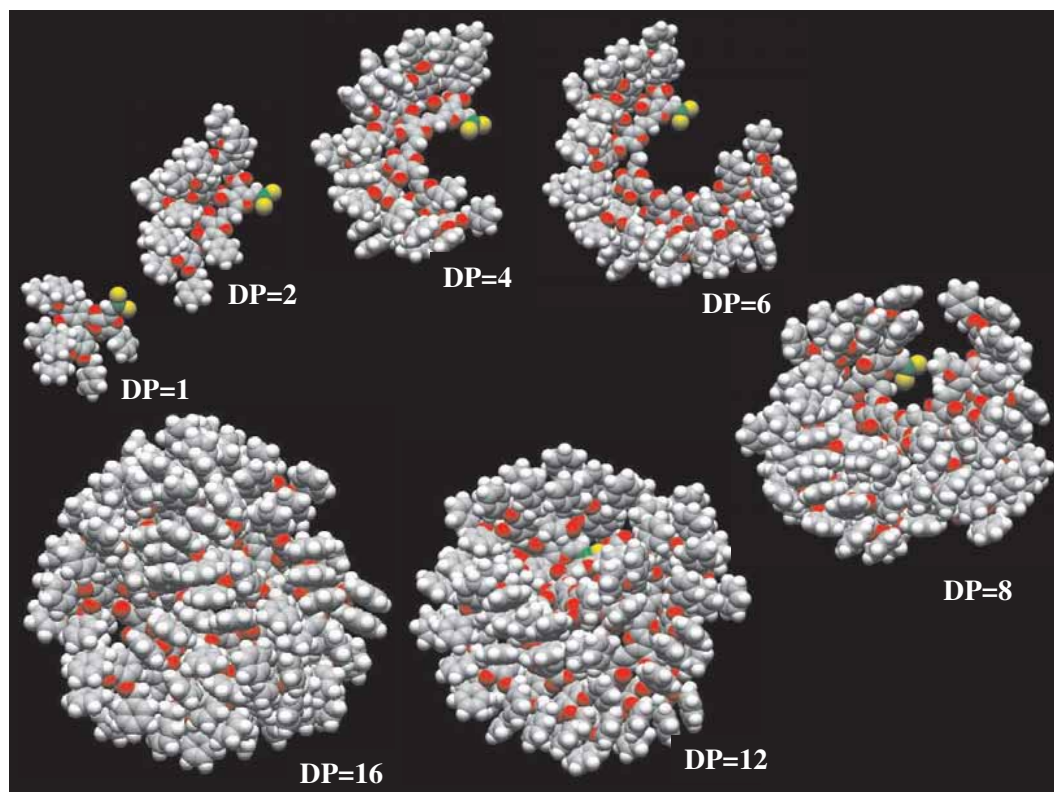


Figure C.1: Molecular modelling of P(345-345-ON) with different degree of polymerization, showing the encapsulation of the reactive center. The modelling was performed on a Silicon Graphic Indi computer with Macromodel Version 5.0 from Columbia University and CSC Chem3D from Cambridge Scientific Computing, Inc.

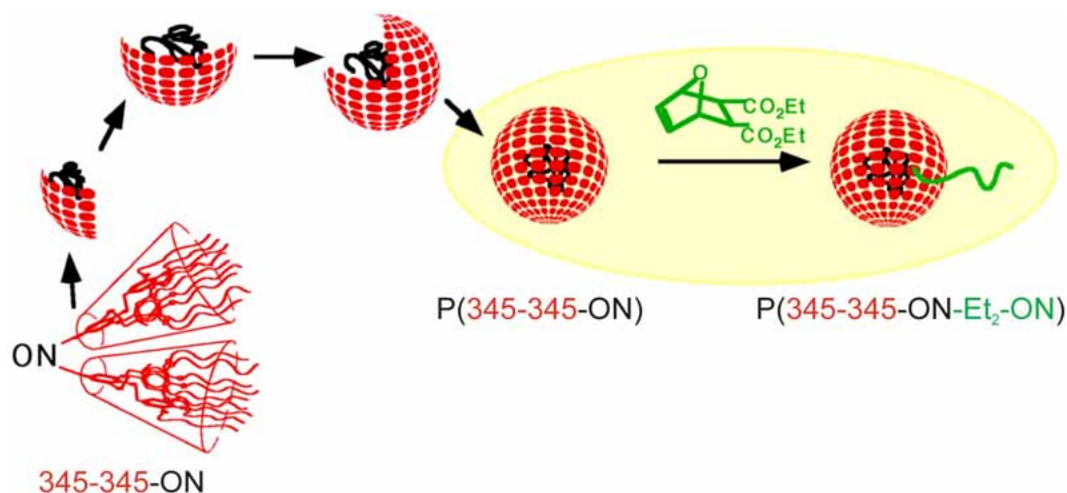


Figure C.2: Polymerization of 345-345-ON stops after formation of a sphere, the encapsulated reactive center is able to react with a small monomer, that can diffuse through the shell

The aim was to visualize the resulting polymers P(345-345-ON) – the sphere – and P(345-345-ON-Et<sub>2</sub>-ON) – the tadpole – by SFM to prove the above theory.

## C.2 Experimental part

### C.2.1 Materials

THF (Uvasolv, 99,9 %), toluene (Uvasolv, 99,9 %) and *n*-hexane (Uvasolv 98,5 %) all from Merck were used as received. Mica plates (BAL-TEC) and HOPG (Agar Scientific Limited) were freshly cleaved before use.

The polymer compounds Poly(*exo,exo*-5,6-bis[[[3,4,5-tris(3,4,5-(dodecyl-1-oxy)benzyloxy)]benzyloxy]carbonyl]-7-oxabicyclo[2.2.1]hept-2-ene) abbreviated as P(345-345-ON) – spherical shape – and Poly(*exo,exo*-5,6-bis[[[3,4,5-tris(3,4,5-(dodecyl-1-oxy)benzyloxy)]benzyloxy]carbonyl]-7-oxabicyclo[2.2.1]hept-2-ene-*block-exo,exo*-5,6-di-ethoxy-7-oxabicyclo[2.2.1]hept-2-ene) abbreviated as P(345-345-ON-Et<sub>2</sub>-ON) – tadpole shape – (Figure C.3) were synthesized by Dr. Marian N. Holerca in the group of Prof. Dr. V. Percec in the Roy & Diana Vagelos Laboratories, University of Pennsylvania. The synthesis is described elsewhere [5, 7, 8].

### C.2.2 Methods

The polymer samples were prepared on the substrates by spin-coating of dilute polymer solutions (0.5–0.005 g/l) with 2000 rpm.

Scanning force microscopy was performed using a Digital Instrument Multimode SPM equipped with a Nanoscope IIIa controller operating in the tapping mode. Nanoworld Pointprobe NCH single crystal silicon cantilevers with a resonance frequency of ca. 300 kHz and a spring constant of ca. 40 N/m were used. The microscope was operated in air at room temperature.

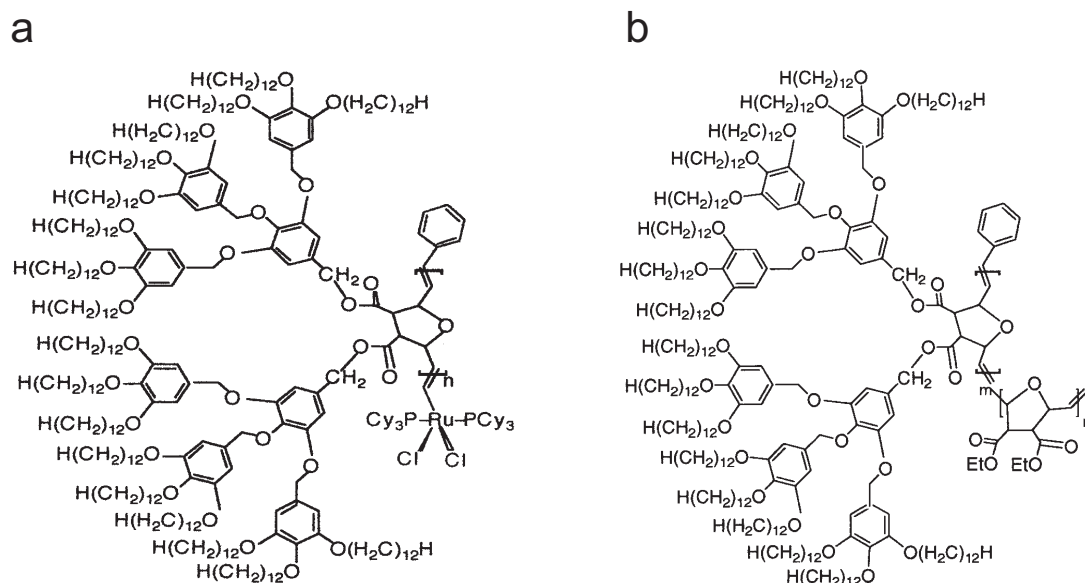


Figure C.3: Chemical structure of a) P(345-345-ON) and b) P(345-345-ON-Et<sub>2</sub>-ON)

For the visualization of the freely distributed single molecules a Molecular Imaging Picoscan SPM operating in the acoustic mode was used. The measurements were performed with Nanoworld Pointprobe FM single crystal silicon cantilevers with a resonance frequency of ca. 70 kHz and a spring constant of ca. 3 N/m. The microscope was operated in dry nitrogen atmosphere at room temperature.

### C.3 Results and discussion

Figure C.4 shows a SFM image of P(345-345-ON) on HOPG. The molecules do not exhibit a spherical shape as expected, but a defined flattened ellipsoidal shape. The size is not completely uniform but shows some distribution. Part of the size variation can be explained by overlapping of the molecules. Molecules lying partly underneath others are visualized as smaller molecules, even if they have the same size.

The average size of the ellipsoids is: length ca. 10.5 nm, width ca. 5.7 nm and height ca. 1.8 nm. Table C.1 gives the molecular weight of the molecules determined by different methods. The molecular mass from SFM was calculated from the volume assuming a density of 1 g/cm<sup>3</sup>. The molecular weight from all methods is in the same range and belongs to a degree of polymerization (DP) of 5–15. This is close to the theoretically expected DP of 16 from molecular modelling (Figure C.1). The low polydispersity obtained by MALDI-TOF-MS could not be confirmed by SFM.

Figure C.5 shows a SFM image of P(345-345-ON-Et<sub>2</sub>-ON). Here the substrate was changed to mica in order to achieve a strong adsorption of the polar tails, which are expected to be hard to visualize because of their small size. Again ellipsoidal shaped features are visible on the image with the same size as in the case of P(345-345-ON). These ellipsoids are grouped together and are surrounded by a multitude of disordered polymer chains. Because of the high density of these thin polymer chains it was not

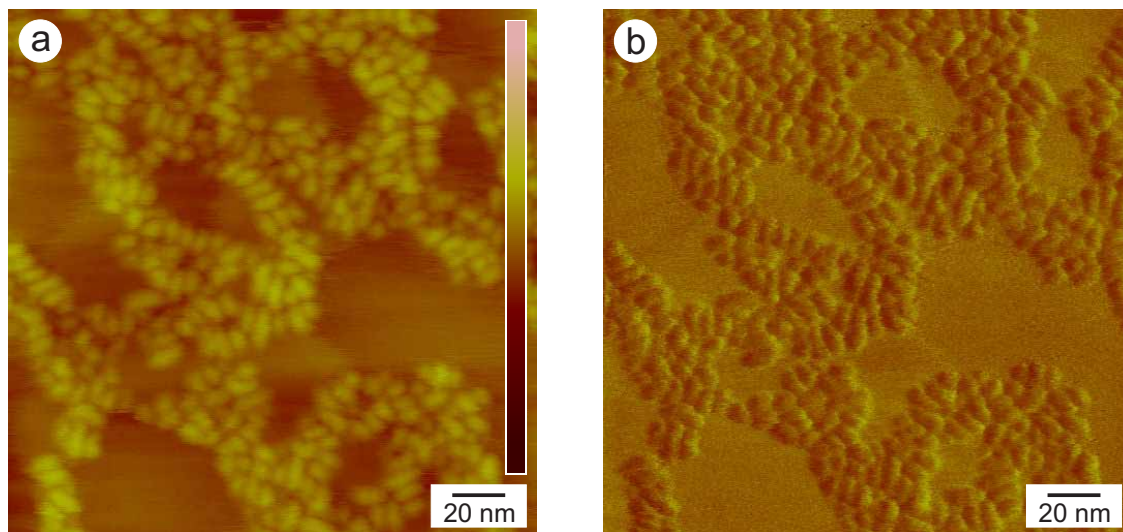


Figure C.4: SFM tapping mode images of P(345-345-ON) spin-coated from hexane solution  $c = 0.46$  g/l on HOPG: a) topography (z-range 7 nm) and b) phase

Table C.1: Molecular weight of P(3,4,5-3,4,5-G<sub>2</sub>-ON) determined by SFM, SEC, and MALDI-TOF-MS

method	molecular mass [g/mol]	polydispersity
<b>SFM<sup>a</sup></b>	20,000–60,000	–
<b>SEC<sup>b</sup></b>	28,400	1.04
<b>MALDI-TOF-MS<sup>c</sup></b>	60,419	1.0009

a) assuming a density of 1 g/cm<sup>3</sup> b) polystyrene calibration  
c) private communication with Prof. V. Percec

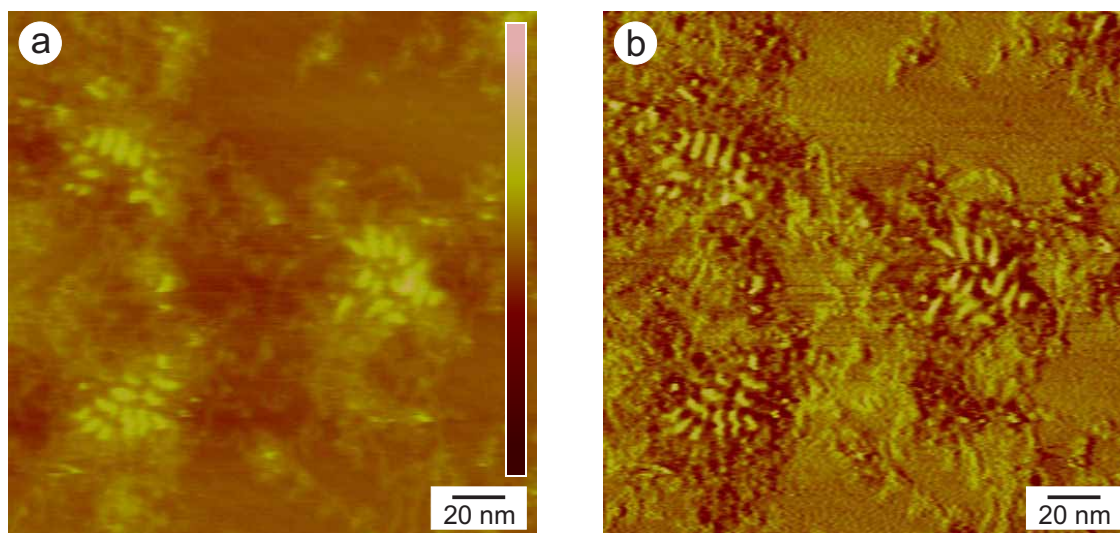


Figure C.5: SFM tapping mode images of P(345-345-ON-Et<sub>2</sub>-ON) spin-coated from THF solution  $c = 0.05$  g/l on mica: a) topography (z-range 10 nm) and b) phase

possible to sharply image these by SFM. This arrangement resembles the aggregation how it is found in micelles. Here the dense packed hydrophobic sphere with a low surface area is worse soluble in THF than the more hydrophilic long and flexible tail of the tadpole molecule. Even at very low concentrations down to 0.001 g/l the aggregation could not be suppressed.

The weight of the head was again calculated from SFM data to 20,000–60,000 g/mol and the length of the tail is varying from ca. 40–70 nm. The molecular number average weight from SEC (PS calibration) of the whole molecule is 140,000 g/mol.

In order to have an arrangement of single distributed molecules of P(345-345-ON-Et<sub>2</sub>-ON) on the substrate a variety of different solvents (THF, chloroform, hexane and toluene), preparation methods (spin-casting, dipping and LB-film deposition) and concentrations was tried. The most successful approach was spin-casting of very diluted toluene solutions on mica as substrate. Additionally a SFM setup was used which allowed to work in dry nitrogen atmosphere in order to eliminate the omnipresent water layer on the sample and therefore to improve the imaging of small features. In the top left and bottom right of Figure C.6 a single molecule is visible. In between an aggregate of two or three molecules can be seen. The head of the tadpole can be recognized nicely in the topography image by the bright spot whereas the polymer chain growing from the head is better visible in the phase image. The head dimensions are the same as in the two images before and the tail has a length of 40–50 nm.

## C.4 Conclusions

The polymerization of 345-345-ON – a monomer with a highly branched minidendritic side-group – leads to the formation of particles with defined shape and a small size distribution which can be visualized by SFM on HOPG and mica, respectively. The shape of the polymer molecules is not spherical as expected but more ellipsoidal. The molar mass determined by SFM (20,000–60,000 g/mol) covers the range of the SEC, MALDI-TOF-MS and the



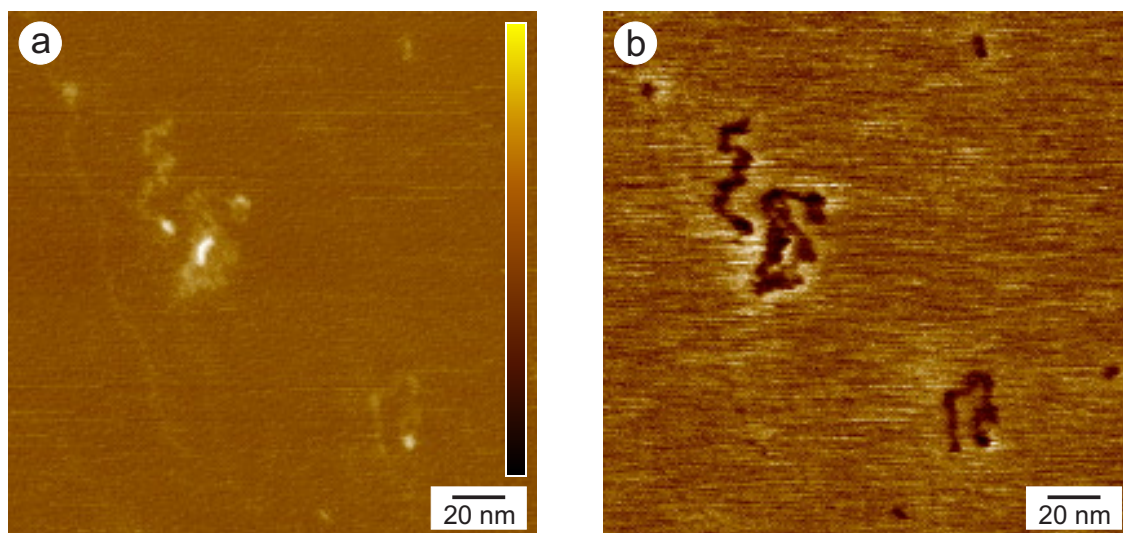


Figure C.6: SFM tapping mode images of P(345-345-ON-Et<sub>2</sub>-ON) spin-coated from toluene solution  $c = 0.005$  g/l on mica: a) topography (z-range 2 nm) and b) phase images

theoretical predicted values. The size distribution given by SFM is larger than the almost mono-dispers values from the other methods.

P(345-345-ON-Et<sub>2</sub>-ON) could be visualized as tadpole shaped molecules. The head of the tadpole is again ellipsoidal and has the same dimensions as P(345-345-ON); the tail has a length of 40–70 nm.

The finding of the expected tadpole shape by SFM, except for the bigger size distribution and the more ellipsoidal shape of the head, proves the mechanism of sterically terminated polymerization with still active reactive center inside.



# Bibliography

- [1] V. Percec, C.-H. Ahn, G. Ungar, D. J. P. Yearley, M. Möller, and S. S. Sheiko. Controlling polymer shape through the self-assembly of dendritic side-groups. *Nature*, 391:161–164, 1998.
- [2] A. D. Schlüter and J. P. Rabe. Dendronized polymers: Synthesis, characterization, assembly at interfaces, and manipulation. *Angew. Chem. Int. Ed.*, 39:864–883, 2000.
- [3] V. Percec, W.-D. Cho, P. E. Mosier, G. Ungar, and D. J. P. Yearley. Structural analysis of cylindrical and spherical supramolecular dendrimers quantifies the concept of monodendron shape control by generation number. *J. Am. Chem. Soc.*, 120:11061–11070, 1998.
- [4] V. Percec, W.-D. Cho, M. Möller, S. A. Prokhorova, G. Ungar, and D. J. P. Yearley. Design and structural analysis of the first spherical monodendron self-organizable in a cubic lattice. *J. Am. Chem. Soc.*, 122:4249–4250, 2000.
- [5] V. Percec and M. N. Holerca. Detecting the shape of complex macromolecules during their synthesis with the aid of kinetics. A new lesson from biology. *Biomacromolecules*, 1:6–16, 2000.
- [6] W. Buchowicz, M. N. Holerca, and V. Percec. Self-inhibition of propagating carbenes in ROMP of 7-oxa-bicyclo[2.2.1]hept-2-ene-5,6-dicarboxylic acid dendritic diesters initiated with  $\text{Ru}(=\text{CHPh})\text{Cl}_2(\text{PCy}_3)(1,3\text{-dimesityl-4,5-dihydroimidazol-2-ylidene})$ . *Macromolecules*, 34:3842–3848, 2001.
- [7] V. Percec and D. Schlueter. Mechanistic investigations on the formation of supramolecular cylindrical shaped oligomers and polymers by living ring opening metathesis polymerization of a 7-oxanorbornene monomer substituted with two tapered monodendrons. *Macromolecules*, 30:5783–5790, 1997.
- [8] V. Percec, D. Schlueter, J. C. Ronda, G. Johansson, G. Ungar, and J. P. Zhou. Tubular architectures from polymers with tapered side groups. Assembly of side groups via a rigid helical chain conformation and flexible helical chain conformation induced via assembly of side groups. *Macromolecules*, 29:1464–1472, 1996.

*Bibliography*

## Summary

The aim of this thesis was to study the organization, manipulation and motion of brush polymers on different substrates by means of scanning force microscopy. In this context also low molecular weight substances as for example the perfluoroalkyl alkanes were studied in detail.

The main part of this work is concentrated on one specific type of polymer: the monodendron jacketed linear chains, namely 12-ABG-4EO-PMA. This is a polymer with a methacrylate backbone in which each methacrylate monomer exhibits a minidendritic unit with three dodecyl-chains at the end. Thus the polymer has a brush-like structure that however is too fine to be visualized by scanning force microscopy.

This polymer plays the main role in the chapters 3, 4 and 5 that intertwine one into another at several points.

At the beginning the synthesis of the polymer was conducted in order to have larger amounts of the material available for the studies.

It was shown that 12-ABG-4EO-PMA shows a different way of adsorption on different materials. Whereas on mica an unspecific adsorption of flat laying molecules was observed resulted on highly ordered pyrolytic graphite as well as on tungsten selenide an epitaxial organization of flat laying molecules with long straight segments that bend at  $60^\circ$  and  $120^\circ$  angles. The straight segments are oriented parallel to the three axes defined by the crystal structure of the topmost atom layer. The epitaxial organization is ascribed to the atom distances in the crystal lattice, that is in the case of graphite and tungsten selenide in the range of a C–C single bond of the outstanding alkyl-chains of the polymer and much larger in the case of the mica substrate.

Annealing of the samples up to ca.  $60^\circ\text{C}$  enhanced the epitaxial organization of the molecules and led to the formation of bigger aggregates or clusters. The molecules remained flat on the substrate but had to change their position or shape for the reorganization. Already at this point a certain mobility of the polymer molecules on the substrate is stated. In the case of mica as substrate no changes of the samples were present up to  $200^\circ\text{C}$ , when the polymers started to degrade.

Further was shown that the monodendron jacketed macromolecules could be moved on the substrate by the tip of the scanning force microscope. For that purpose a special equipped scanning force microscope with enhanced control of the tip position was used. The outcomes are in agreement with the adsorption experiments: translation of polymer molecules was possible on HOPG and tungsten selenide whereas on mica no variation was observed under the same conditions. Intensified conditions by exerting higher forces on the macromolecules led to intersection of the macromolecules. The mildest conditions for successful manipulation were found for graphite. A little more force was necessary for tungsten selenide thus a stronger adsorption on the substrate is concluded. Furthermore the tendency of the polymers to orient epitaxial on tungsten selenide after a successful manipulation was larger compared to HOPG.

This manipulation technique was exploited to prepare completely straight molecules of 12-ABG-4EO-PMA on graphite in order to study the folding of the molecules in in-

situ SFM-experiments. Parts of the macromolecule formed kinks with  $60^\circ$  angles but the tendency to move around on the substrate was at  $40^\circ\text{C}$  already higher than the tendency to fold. The velocity was not reduced until the molecules encountered other molecules and folded by forming bigger clusters.

In a second experiment a molecule fixed on a step in the graphite was studied. The temperature had to exceed  $60^\circ\text{C}$  in order to force the molecules to bend in  $120^\circ$  or  $180^\circ$  angles yielding a compaction of the molecule. Once parts of the molecule came into contact with each other these structures appeared to be stable under the used conditions and did never release.

In parallel to these experiments the motion of single molecules of 12-ABG-4EO-PMA and of molecular clusters was studied by in-situ SFM experiments in the temperature range of  $30\text{--}48^\circ\text{C}$ . The experiments showed motion of the clusters similar to statistical diffusion processes. For each cluster the diffusion coefficient was calculated and the way of motion was analyzed. The main results are: The velocity increases with reduced cluster size and higher temperature. Molecules that collide with others stick together and exhibit a high shape persistence. Molecules coming into contact with defects in the substrate get caught by these and either quit moving or start a one-dimensional guided motion along the step in the graphite. The energy source for the diffusive motion is the thermal excitation as well as the energy transferred to the molecules by the oscillating tip of the scanning force microscope.

Special motion modes have been identified: molecular clusters with bar shaped conformation containing parallel chains exhibit diffusion predominantly rectangular to the parallel chains. All observed motion modes are explained by a segment motion model. This model separates the macromolecules in uniform segments and analyzes which segments are coupled together for a basic step of motion. For translation of a single segment only a small energy is necessary to desorb from the substrate. Coupled segments have to desorb from the substrate all at once for one single step and therefore a higher energy is needed. Coupling is induced by parallel aligned chains or crossovers. This explains why large clusters or crossovers move slower. Additionally the number of coupled segments can be different for translation in a certain direction and therefore lead to oriented diffusion as for the bar shaped clusters described. For translation at right angle only a part of the molecule has to desorb from the substrate and two kinks are formed. The rest of the molecule can follow in further steps. For displacement along the chain all the segments have to desorb at the same time and therefore must be treated as coupled segments. This leads to the oriented diffusion perpendicular to the chain axes. The different ways of coupling the segments together in two clusters of same size can significantly influence their mobility.

The external stimulation of the mobility of macromolecules on the substrate was also investigated by incorporating photo-switchable groups in 12-ABG-4EO-PMA. A comonomer with photo-switchable spiropyran was synthesized and copolymerized with the existing monomer 12-ABG-4EO-MA. The success of the synthesis and the activity of the spiropyran was confirmed by size exclusion chromatography with UV-detection. A reaction of the polymer molecules on the external stimulation with UV-light on different substrates in in-situ SFM experiments could not be established. Choosing mica as substrate to freeze the state after the spin coating procedure the copolymer showed the same appearance as the 12-ABG-4EO-PMA homopolymer. Irradiation of the solution with UV-light immediate before spin coating resulted obviously in the formation of aggregates in solution. These aggregates were found and visualized by SFM on the mica substrate.

Another way of stimulation and resulting reaction is shown for polymer brushes with

butylacrylate side chains. These polymers consist also of a methacrylate backbone and each monomer possesses exact one butylacrylate side chain. The side chains are significantly longer and thicker in contrast to the three short alkyl chains in 12-ABG-4EO-PMA. The side chains of the brush polymers could be visualized in high resolution SFM images.

The worm-like brush polymers have been deposited on mica substrates and exposed to ethanol vapor resulting in a collapse to dense packed spherical aggregates. Venting of the chamber to remove the ethanol vapor and exposure to humid air resulted in spreading of brush polymers on the substrate. This behavior could be shown over several cycles. By applying ethanol/water mixtures for the experiments it was proven that ethanol/water mixtures with more than 30 % of ethanol resulted in collapse of the brush polymers whereas higher water contents led to the decollapse. The characteristic parameter for this transition is the surface tension of the used solvents. The solvent vapors come down onto the substrate and form a thin liquid film. This film is in concurrence with the butylacrylate side chains of the brush polymer. Solvents with a smaller surface tension as the side chains push the chains aside resulting in the collapse of the polymer. In the opposite case the side chains win and the result is a spread worm-like brush polymer. The surface tension of poly(butylacrylate) is 31–34 mN/m. The validity of this concept and the collapse could be proven for the following solvents with lower surface tension: ethyl acetate, ethanol, isopropanol, diethyl ether and ethanol/water mixtures with more than 30 % ethanol content. Spreading of the brush polymers was observed with the following high surface tension compounds: water, ethylene glycol, dimethyl sulfoxide, dimethyl formamide and cyclohexanone. Another requirement for the transformation is a polar substrate. Mica, strontium titanate and silicon (with oxide layer) have been proven to be suitable, whereas the transformation did not work on HOPG because no thin film of the solvent was formed on the substrate.

In the following the organization of perfluoroalkyl alkanes on different substrates was studied. Independent of the nature of the substrate the organization to 35 nm wide stripes was observed when the film was prepared from selective solvents for either block. Using the non-selective solvent hexafluoroxylyene a donut or snail shell structure of rolled up stripes was observed. The height of the structures was determined by grazing incidence x-ray reflectivity to 3.76 nm resulting in a kink of the molecule between the two blocks of 143°. The formation of the stripe structure is explained by the different sizes of the two blocks when packing the molecules together. The perfluoroalkyl block has a larger diameter as the alkyl block leading to packing mismatch. In one direction, along the stripes, this tension can be released by tilting the alkyl chains leading to a broadening of the alkyl chains. In the direction at right angle no compensation of the tension is possible and the structure breaks up leading to the width of 35 nm of the stripes. For the formation of the rolled up structures exists no explanation up to now. The grazing incidence x-ray reflectivity experiments yielded for the internal structure a liquid-like behavior with small crystalline domains.

In the last chapter the micellization of polystyrene-polyisoprene-star-blockcopolymers was investigated with the aim to find conditions for the formation of cylindrical micelles. All three used star-polymers had eight equal polystyrene and eight equal polyisoprene arms, but different composition of PS and PI. The formation of cylindrical micelles was favored by less selective solvents, high polymer concentrations and short soluble blocks. It was shown that the addition of a few percent of a good solvent for the insoluble block led to swelling of this block and supports the formation of cylindrical micelles.

In the appendix of this work are three further projects described. In these projects

## *Summary*

the main work was done by other scientists and were completed by SFM imaging. These projects are integrated because of the time spent on it or because of the high quality of the results.

The first project deals with the gelation of new dumbbell shaped gelators based on semicarbazide chemistry. The structure of fiber networks of the dried gel could be visualized by scanning force microscopy and thinnest fibers with diameters below 6 nm could be revealed according to the dimensions of the single gelator molecules. The difference in gelation for two gelators with straight and curved molecular shape was visualized. Time resolved SFM experiments showed that in the beginning of the gelation thick main fibers were formed that in the continued gelation process were interconnected with fine fibers.

In the second project butylacrylat chains were grafted from functionalized gold nanoparticles. Scanning force microscopy images showed that the synthesis was successful and most particles had a few long polymer chains.

In the third project monomers with mini-dendritic side groups were used similar to those in the chapters 3 and 4, but here with more branched side groups with nine alkyl chains at the end. This high branching leads to a early termination of the polymerization reaction by sterical reasons, because the monomers are not any more able to reach the shielded reaction center. Addition of new small monomers without the minidendritic side group are able to continue the reaction because of their ability to penetrate through the shielding. The result is a polymer with a shape similar to a tadpole. The tadpole structure was confirmed by SFM images and the tendency to form micelles in selective solvents was shown.



# Zusammenfassung

Ziel der Arbeit war es die Anordnung, Manipulation und die Bewegung von Bürstenpolymeren auf verschiedenen Substraten mittels der Rasterkraftmikroskopie zu untersuchen. In diesem Zusammenhang wurden auch niedermolekulare Substanzen, wie zum Beispiel die Perfluoroalkylalkane, näher betrachtet.

Der wesentliche Teil der Arbeit konzentriert sich auf einen ganz bestimmten Polymertypus: die monodendron ummantelten linearen Ketten, namentlich 12-ABG-4EO-PMA. Dabei handelt es sich um Polymere mit Methacrylat Rückgrad wobei jeder Methacrylat-Monomer eine minidendritische Einheit enthält, die am Ende drei Dodecylketten trägt. Somit liegt eine Bürstenartige Struktur vor, die jedoch zu fein ist um mittels der Rasterkraftmikroskopie visualisiert zu werden.

Dieses Polymer spielt die entscheidende Rolle in den Kapiteln 3, 4 und 5 welche auch immer wieder ineinander übergreifen.

Zunächst ist die Synthese des Polymers beschrieben welche durchgeführt wurde um größere Mengen des Polymers für die Studien zur Verfügung zu haben.

Es wurde gezeigt das dieser Polymer auf unterschiedlichen Substraten unterschiedliche Adsorption zeigt. Während auf Glimmer eine unbestimmte Adsorption flach liegender Makromoleküle gefunden wird erhält man auf hochorientiertem pyrolitischen Graphit, als auch auf Wolframselenide, eine epitaktische Anordnung der flach liegenden Makromoleküle mit langen geraden Segmenten die in charakteristischen  $60^\circ$  und  $120^\circ$  Winkeln abknicken. Die geraden Segmente liegen parallel zu den drei durch die Kristallstruktur definierten Achsen der obersten Atomschicht. Die epitaxielle Anordnung wird auf die Atomabstände in den Kristallgittern zurückgeführt, die im Fall von Graphit und Wolframselenid in der Größenordnung einer C–C Einfachbindung der außenliegenden Alkylketten des Polymers liegen und für Glimmer deutlich größer sind.

Durch erwärmen der Proben bis ca.  $60^\circ\text{C}$  wurde diese epitaxielle Anordnung gefördert und die Moleküle schlossen sich zu größeren Aggregaten oder Clustern zusammen. Dabei blieben Sie immer noch flach auf dem Substrat liegen, mußten dazu allerdings Ihre ursprüngliche Position oder Anordnung aufgeben. Es ist also bereits hier eine gewisse Mobilität der Polymere zu beobachten gewesen. Im Fall von Glimmer als Substrat war keine Veränderung der Proben bis  $200^\circ\text{C}$  zu beobachten, darüber setzte ein Abbau der Polymere ein.

Es wurde weiterhin gezeigt, daß sich die monodendron umantelten Makromoleküle durch die Spitze des Rasterkraftmikroskops auf den Substraten verschieben lassen. Hierzu wurde ein speziell dafür ausgerüstetes Rasterkraftmikroskop mit Überwachung der Positionierung der Spitze eingesetzt. Die erhaltenen Ergebnisse stehen in Einklang mit den Adsorptionsexperimenten: auf HOPG und Wolframselenid ist die Verschiebung der Polymere möglich, wohingegen auf Glimmer unter vergleichbaren Bedingungen keine Veränderung zu beobachten ist. Verschärfung der Bedingungen durch Erhöhung der Kräfte auf die Moleküle führte zum zertrennen der Polymere auf dem Glimmer-Substrat. Die mildesten Bedingungen für erfolgreiche Manipulationen galten für Graphit. Auf Wolframselenid mußten etwas höhere Kräfte angewendet werden woraus auf eine stärkere Adsorption auf dem Substrat

geschlossen wird. Weiterhin war die Tendenz zur epitaxialen Anordnung auf Wolframselelenid nach einem erfolgreichen Manipulationsschritt größer.

Diese Manipulationstechnik wurde ausgenutzt um komplett ausgestreckte Moleküle von 12-ABG-4EO-PMA auf Graphit zu präparieren um dann die Faltung des Moleküls unter thermischem Einfluß in einem in-situ Rasterkraftmikroskopie-Experiment zu beobachten. Teile des Makromoleküls knickten in  $60^\circ$  Winkeln ab, jedoch war die Tendenz zur Wanderung auf dem Substrat bereits bei  $40^\circ\text{C}$  größer als die Tendenz sich zusammen zu falten. Erst beim Zusammenstoß mit anderen Molekülen und dem Ausformen größerer Cluster wurde die Geschwindigkeit herabgesetzt und die Anlagerung am Cluster fand statt.

In einem zweiten Experiment wurde ein auf einer Stufe im Graphit fixiertes Polymerelement beobachtet. Erst ab Temperaturen über  $60^\circ\text{C}$  kam es zur Ausbildung von Knicken mit  $120^\circ$  und  $180^\circ$  welche zur Anlagerung von Teilen der Polymerkette aneinander führte. Kam es erst einmal zum Kontakt einzelner Segmente des Makromoleküls so waren diese Kontaktpunkte unter den gegebenen Umständen stabil und wurden nicht wieder aufgelöst.

Parallel zu diesen Experimenten wurde die Bewegung von einzelnen Molekülen 12-ABG-4EO-PMA sowie von Molekülclustern auf Graphit in in-situ Rasterkraftmikroskopie-Experimenten, im Temperaturbereich von  $30\text{--}48^\circ\text{C}$ , untersucht. Die Experimente zeigten das eine der statistischen Diffusion ähnliche Bewegung statt findet. Für die einzelnen Cluster wurden Diffusionskoeffizienten berechnet und deren Bewegung analysiert. Die wesentlichen Erkenntnisse sind: Die Geschwindigkeit der Bewegung nimmt mit abnehmender Clustergröße und zunehmender Temperatur zu. Moleküle welche zusammenstoßen bleiben aneinander kleben und weisen eine große Formbeständigkeit auf. Moleküle welche mit Defekten im Substrat in Kontakt kommen bleiben daran hängen oder werden davon geleitet, indem sie eine eindimensionale Diffusion entlang einer Kante im Graphit ausführen. Der Energielieferant für die Diffusionsbewegung ist die thermische Anregung sowie die Energie die durch die oszillierende Spitze des Rasterkraftmikroskops auf die Polymere übertragen wird.

Es wurden auch spezielle Bewegungsmoden ausfindig gemacht: Molekülcluster, die bevorzugt stäbchenförmige Gestalt mit parallelen Ketten aufweisen zeigen Diffusion bevorzugt rechtwinklig zu den parallelen Ketten. Erklärt werden können all diese Bewegungsmoden mit einem Segment-Bewegungs-Modell. Dieses Modell zerlegt die Moleküle in gleichartige Segmente und untersucht welche davon für einen elementaren Bewegungsschritt miteinander gekoppelt sind. Für die Translation eines einzelnen Segments muß nur eine kleine Energie zur Desorption vom Substrat aufgebracht werden. Gekoppelte Segmente müssen jedoch für einen Schritt gleichzeitig von Substrat desorbieren und benötigen somit mehr Energie. Kopplung kommt durch parallel zueinanderliegende Ketten oder Kreuzen von Ketten zustande. Dies erklärt warum größere Cluster oder Kreuzungspunkte sich langsamer fortbewegen. Auch kann die Anzahl der gekoppelten Segmente sich für die Bewegung in eine bestimmte Richtung unterscheiden und somit zur orientierten Bewegung führen, wie für die stäbchenförmigen Cluster beschrieben. Für die Bewegung quer zur Kette muß nur ein Teil des Moleküls desorbieren und es kommt zur Ausbildung von Knicken. Der Rest des Moleküls kann dann in einzelnen Schritten hinterher ziehen. Für Bewegungen längs der Kette ist es jedoch nötig, daß alle Segmente gleichzeitig desorbieren und somit als gekoppelt betrachtet werden müssen, was zur bevorzugten gerichteten Bewegung rechtwinklig zur Kettenrichtung führt. Durch die Unterschiedliche Kopplung der Segmente in gleich großen Clustern können diese sich auch merklich in ihrer Beweglichkeit unterscheiden.

Die externe Stimulation der Bewegung auf dem Substrat wurde auch durch die Einbringung von photoschaltbaren Gruppen in 12-ABG-4EO-PMA untersucht. Dazu wurde ein Comonomer mit einem photoschaltbaren Spiropyran synthetisiert und mit dem bereits vorhandenen Monomer 12-ABG-4EO-MA copolymerisiert. Der Erfolg der Synthese und die Aktivität des Copolymers konnten durch Gelpermeationschromatographie mit UV-Detektion nachgewiesen werden. Eine Veränderung durch externe Stimulation mittels UV-Licht in in-situ Rasterkraftmikroskopieexperimenten auf verschiedenen Substraten konnte nicht beobachtet werden. Wurde jedoch Glimmer als Substrat gewählt um den Zustand nach dem Spincoaten der Proben einzufrieren, so zeigte das nicht bestrahlte Polymer das selbe Erscheinungsbild wie der 12-ABG-4EO-PMA Homopolymer. Wurde die Lösung jedoch unmittelbar vor dem Spincoaten mit UV-Licht bestrahlt, so kam es augenscheinlich zur Aggregation in Lösung und diese Aggregate wurden dann auf dem Glimmersubstrat wiedergefunden.

Eine andere Art der Stimulierung und damit verbundenen Reaktion wurde für Polymerbürsten mit Butylacrylat Seitenketten gezeigt. Dieser Polymer besitzt ebenfalls ein Methacrylat Rückgrad und jeder Monomer besitzt genau eine Butylacrylatseitenkette. Die Seitenketten sind deutlich länger und dicker im Gegensatz zu den drei kurzen Alkylketten von 12-ABG-4EO-PMA. Die Seitenketten der Bürstenpolymer konnten in hochauflösenden Rasterkraftmikroskopieaufnahmen abgebildet werden.

Die wurmartig auf dem Glimmersubstrat abgeschiedenen Bürstenpolymere wurden Ethanol-Dämpfen ausgesetzt und kollabierten dabei zu dichten kugelähnlichen Gebilden. Vertreiben der Ethanol-Dämpfe und Einbringung von hoher Luftfeuchtigkeit führte zum Ausspreiten der Bürstenpolymere auf dem Substrat. Dieser Vorgang konnte über mehrere Zyklen wiederholt werden. Durch die Verwendung von Ethanol/Wasser Gemischen für die Experimente konnte gezeigt werden, daß eine Ethanol/Wasser Gemisch mit mehr als 30 % Ethanol den Kollaps der Bürstenmoleküle bewirkt wohingegen höhere Wasseranteile zur Ausspreitung der Makromoleküle führen. Die wesentliche Kenngröße für diesen Prozeß ist die Oberflächenspannung der verwendeten Lösungsmittel. Die Lösungsmitteldämpfe schlagen sich auf dem Substrat nieder und bilden dort einen dünnen Film. Dieser Film steht in Konkurrenz mit den Butylacrylat-Seitenketten des Bürstenpolymers. Besitzt der Lösungsmittelfilm eine kleinere Oberflächenspannung als die Seitenketten so verdrängt er diese und der Bürstenpolymer kollabiert. Im umgekehrten Fall gewinnen die Seitenketten und verdrängen das Lösungsmittel zu Gunsten eines ausgespreizten Bürstenpolymers. Polybutylacrylat hat eine Oberflächenspannung von 31–34 mN/m. Die Gültigkeit des Konzepts und der Kollaps wurde durch folgende Lösungsmittel mit niedrigerer Oberflächenspannung gezeigt: Ethylacetat, Ethanol, Isopropanol, Diethylether und Ethanol/Wasser-Gemische mit mehr als 30 % Ethanol-Gehalt. Ausspreiten war möglich mit Wasser, Ethylenglykol, Dimethylsulfoxid, Dimethylformamid und Cyclohexanon, alle mit höherer Oberflächenspannung. Eine weitere Voraussetzung für die Transformation ist ein polares Substrat. Glimmer, Strontiumtitanat und Silizium (mit Oxidschicht) haben sich als geeignete Substrate herausgestellt, wohingegen die Transformation auf Graphit nicht möglich war, da es hier nicht zur Ausbildung des Lösungsmittelfilmes kommt.

Im folgenden wurde die Adsorption von Perfluoralkylalkanen auf verschiedenen Substraten untersucht. Unabhängig vom Substrat wurden für selektive Lösungsmittel, sowohl für den Alkyl-Block als auch für den perfluorierten Block, eine Anordnung in Streifen mit ca. 35 nm Breite beobachtet. Wird das nicht selektive Lösungsmittel Hexafluoroxylol verwendet so erhält man eine Donut oder Schneckenhaus ähnliche Struktur aus

aufgerollten Streifen. Die Höhe der beobachteten Strukturen wurde aus Gracing Incidence Röntgenuntersuchungen zu 3.76 nm bestimmt und setzt damit einen Knick der Moleküle zwischen beiden Blöcken mit  $143^\circ$  voraus. Die Streifenstruktur kann durch die unterschiedliche Größe der beiden Blöcke erklärt werden. Beim Ausbilden der Strukturen werden die Moleküle dicht aneinander gepackt. Dabei kommt es zu Spannungen da der Perfluoroalkyl-Block einen größeren Durchmesser als der Alkylblock hat. In eine Richtung, längs der Streifen, wird dies ausgeglichen durch Schrägstellung der Alkylketten da dies ebenfalls zu einer Verbreiterung der Alkylketten in eine Richtung führt. In die Richtung rechtwinklig dazu ist keine Kompensation der Spannungen möglich, es kommt zum Abbruch der Struktur und der Streifenbreite von 35 nm. Für die Ausbildung der aufgerollten Struktur gibt es bisher noch keine Erklärung. Die Gracing Incidence Röntgenexperimente liefern für den inneren Aufbau der Strukturen ein flüssiges Verhalten mit kleinen kristallinen Bereichen.

Im letzten Kapitel wurde die Mizellisierung von Polystyrol-Polyisopren-Sternblockcopolymeren untersucht mit dem Ziel Bedingungen für zylindrische Mizellen zu finden. Alle drei verwendeten Sternpolymere hatten acht gleich lange Polystyrol und acht gleich lange Polyisopren Arme, jedoch unterschiedliche Anteile an PS und PI. Die Bildung von zylindrischen Micellen wurde begünstigt durch wenig selektive Lösungsmittel, hohe Konzentrationen und einen kurzen löslichen Block. Weiterhin konnte gezeigt werden, daß das Hinzufügen weniger Prozent eines guten Lösungsmittels für den unlöslichen Block diesen anschwellen läßt und die Bildung zylindrischer Mizellen unterstützt.

Im Anhang der hier vorliegenden Arbeit sind noch drei weitere Projekte beschrieben. Bei diesen Projekten wurde die Hauptarbeit von anderen Wissenschaftler verrichtet und hier durch Rasterkraftmikroskopische Aufnahmen ergänzt. Diese Projekte sind aufgrund der investierten Zeit oder der Güte der Ergebnisse in diese Arbeit integriert.

Das erste Projekt behandelt die Gelbildung von neuen hantelförmigen Gelatoren auf Semicarbazid Basis. Die Struktur aus vernetzten Fäden der getrockneten Gele konnte abgebildet werden und feinste Fasern mit Durchmessern unter 6 nm wurden gefunden, entsprechend der Dimensionen der einzelnen Gelmoleküle. Die Unterschiede im Gelierverhalten zweier Gelatoren mit gerader und gekrümmter Molekülform konnten aufgezeigt werden. In zeitlich aufgelösten Experimenten konnte gezeigt werden, daß bei der Gelierung erst dicke Hauptstränge ausgebildet werden und diese dann durch feine Verästelungen weiter vernetzt werden.

Im zweiten Projekt wurden, ausgehend von funktionalisierten Goldnanopartikeln, Butylacrylat Ketten polymerisiert. Rasterkraftmikroskopische Aufnahmen konnten zeigen, daß die Synthese erfolgreich war, meist waren jedoch nur sehr wenige aber recht lange Polymerketten am einzelnen Nanopartikel zu finden.

Im dritten Projekt wurden Monomere mit minidendritischen Seitengruppen verwendet, ähnlich wie Sie in dieser Arbeit in den Kapiteln 3 und 4 verwendet wurden, allerdings mit stärker verzweigten Seitengruppen mit 9 Alkylketten. Diese starke Verzweigung führt zu einem frühen Abbruch der Polymerisationsreaktion aus sterischen Gründen, da die Monomere das schnell stark abgeschirmte Reaktionszentrum nicht mehr erreichen können. Die Hinzugabe von anderen kleinen Monomeren ohne die minidentrische Seitenkette führt zur Fortsetzung der Polymerisationsreaktion, da diese die Abschirmung durchdringen können und die Reaktion fortsetzen. Als Resultat erhält man dann Polymere die der Gestalt einer Kaulquappe ähneln. Die Kaulquappen ähnliche Struktur der Polymere konnte auf Rasterkraftmikroskopiebildern gezeigt werden, ebenso wie die Tendenz zur Bildung von Micellen in selektivem Lösungsmittel.

# Dankwort

Die vorliegende Arbeit entstand in der Zeit vom Juni 1999 bis Oktober 2003 in der Abteilung Organische Chemie III / Makromolekulare Chemie der Universität Ulm.

An dieser Stelle möchte ich namentlich all denen herzlich danken, die an der Entstehung dieser Arbeit beteiligt waren:

- Prof. Dr. Martin Möller für die interessante Themenstellung und die wissenschaftliche Betreuung. Durch ihn habe ich die Welt des Nanokosmos und der Rasterkraftmikroskopie kennengelernt.
- Prof. Dr. Virgil Percec, daß ich in seinem Labor in Philadelphia die Synthese der monodendritischen Polymere durchführen konnte. Die genauen Syntheseanleitungen von Dr. Marian N. Holerca waren dabei von unschätzbarem Wert.
- Prof. Dr. Sergei S. Sheiko für die Betreuung und seine nie endende Diskussionsbereitschaft.
- Dr. Svetlana A. Prokhorova als Zimmerkameradin die mir das Meiste beigebracht hat, was ich über die Rasterkraftmikroskopie weiß.
- Dr. Sergei N. Magonov und Dr. Debra Cook für die schöne Zeit in Santa Barbara und die Möglichkeit auf modernstem Equipment Manipulationsexperimente an einzelnen Molekülen durchzuführen.
- Dr. Hans Börner, Dr. Kathryn L. Beers und Prof. Dr. Krzysztof Matyjaszewski für die Synthese und Bereitstellung der Bürstenpolymere die sich als hochinteressante Modellsubstanzen für die Rasterkraftmikroskopie bewährt haben.
- Dr. Ahmed Mourran für die wissenschaftliche Diskussion und die gute Kameradschaft.
- Dr. Marat O. Gallyamov der mich sehr stark bei den AFM-Experimenten mit Lösungsmitteldämpfen unterstützt hat.
- Prof. Dr. Nikos Hadjichristidis für die Überlassung der Sternpolymere.
- Dr. Yaelle Serero und Prof. Dr. Wim de Jeu für die Unterstützung und Röntgenuntersuchungen an den Fluoralkanen.
- Dr. Michael Kraus als Freund und für die Synthese der Spiropyran-Copolymere.
- Dr. Uwe Beginn der die meiste Arbeit an den Semicarbazid-Gelen durchgeführt hat und die Proben für die Untersuchung mittels Rasterkraftmikroskopie zur Verfügung gestellt hat.
- Stefan Nuß und Prof. Dr. Manfred L. Hallensleben für die Bereitstellung der Polymer-modifizierten Gold-Nanopartikel.

## *Dankwort*

- Dr. Ulrich Ziener für die Korrektur der vorliegenden Arbeit.
- Mike Wendel für die GPC-Messungen meiner nicht immer ganz einfachen Polymere.
- Dr. Ute Schmidt für die Unterstützung bei den Arbeiten mit dem Molecular Imaging Gerät und diverse Grillparties.
- Meinen Kollegen, die ganz wesentlich zu einem positiven Umfeld während meiner Promotion beigetragen haben. Insbesondere erwähnen möchte ich Manfred Jaumann, Olli Mayer, Silke Riethmüller, Marcell Ott, Thomas Ameringer, Jürgen Groll, Krystyna Albrecht und Christoph Hartmann.
- Meinen Eltern die mich immer unterstützt und an mich geglaubt haben.
- Zum Schluß meiner Frau Petra für Ihre Liebe und Ihre Geduld.

# Lebenslauf

## **Bernd Tartsch**

geboren am 5. Juni 1971 in Giengen/Brenz  
verheiratet, ein Sohn

## **Schulbildung**

- 1977–1981 Grundschule in Giengen  
1981–1990 Margarethe Steiff Gymnasium in Giengen  
8. Mai 1990 Allgemeine Hochschulreife

## **Zivildienst**

- 1990–1991 Betreuung von psychisch kranken Menschen in der  
Arbeitstherapie, Reha Zentrum Heidenheim

## **Hochschulstudium**

- 1992–1995 Diplom-Chemie an der Universität Ulm  
29. August 1995 Vordiplom  
1995–1999 Lehramt für Chemie und Physik an der Universität Ulm  
Zulassungsarbeit in der Sektion Schwingungsspektroskopie  
bei Prof. Dr. Andreas Ruoff  
31. Mai 1999 Staatsexamen Lehramt Chemie und Physik

## **Promotion**

- 1999–2003 in der Abteilung Organische Chemie III/Makromolekulare  
Chemie an der Universität Ulm bei Prof. Dr. Martin Möller

## **Berufliche Erfahrungen**

- 1999–2003 Betreuung des Praktikums Makromolekulare Chemie in der  
Abteilung Organische Chemie III an der Universität Ulm  
10/99–12/99 Polymersynthese in den Roy & Diana Vagelos Laboratories  
bei Prof. Dr. Virgil Percec an der University of Pennsylvania,  
Philadelphia, PA, USA  
02/02–03/02 Forschungsaufenthalt bei Digital Instruments, Santa Barbara, CA, USA  
seit 11/03 Technical Sales Specialist, Viscotek GmbH